



HAL
open science

Biophysical approach of neuronal shapes

Céline Braini

► **To cite this version:**

Céline Braini. Biophysical approach of neuronal shapes. Biophysics. Université Grenoble Alpes, 2016. English. NNT : 2016GREAY091 . tel-01736978

HAL Id: tel-01736978

<https://theses.hal.science/tel-01736978>

Submitted on 19 Mar 2018

HAL is a multi-disciplinary open access archive for the deposit and dissemination of scientific research documents, whether they are published or not. The documents may come from teaching and research institutions in France or abroad, or from public or private research centers.

L'archive ouverte pluridisciplinaire **HAL**, est destinée au dépôt et à la diffusion de documents scientifiques de niveau recherche, publiés ou non, émanant des établissements d'enseignement et de recherche français ou étrangers, des laboratoires publics ou privés.

THÈSE

Pour obtenir le grade de

DOCTEUR DE LA COMMUNAUTE UNIVERSITE GRENOBLE ALPES

Spécialité : **Physique pour les sciences du vivant**

Arrêté ministériel : 7 août 2006

Présentée par

Céline BRAINI

Thèse dirigée par **Catherine VILLARD**

préparée au sein de l'**Institut Néel**, de l'**Institut Curie** et de
l'**Institut Pierre Gilles de Gennes (IPGG)**
dans l'**Ecole Doctorale de Physique de Grenoble**

Approche biophysique des formes neuronales

Thèse soutenue publiquement le **16 décembre 2016**,
devant le jury composé de :

Giovanni CAPPELLO

Directeur de recherche au LiPhy, Président du jury

Alexander VERKHOVSKI

Maître d'enseignement et de recherche à l'EPFL, Rapporteur

François AMBLARD

Directeur de recherche à l'Institut Curie et à l'UNIST, Rapporteur

Pierre-Etienne WOLF

Directeur de recherche à l'Institut Néel, Examineur

Zsolt LENKEI

Directeur de recherche à l'ESPCI, Examineur

Catherine VILLARD

Directeur de recherche à l'Institut Curie, Directeur de thèse



REMERCIEMENTS

Cette thèse a été un tel tourbillon de lieux, de projets, de sciences, qu'elle m'a permis de croiser le chemin d'un grand nombre de personnes. Mais comme le calme après une tempête déchaînée, où l'on découvre plein de trésors cachés alors échoués sur la plage, quand je repense à ces trois années de thèse je (re)découvre toutes les rencontres aussi intéressantes scientifiquement qu'humainement que j'ai pu faire et toutes les belles amitiés que je me suis faites. Tous ces liens tissés ont pour la majorité participé à tisser ma thèse, chacun à sa façon, et c'est pourquoi j'aimerais tous vous remercier comme il se doit.

Je voudrais commencer par remercier celle qui a rendu tout cela possible, ma directrice de thèse. Merci Catherine. Merci pour tout. Comme le dit très bien cette jolie tasse-neurone, "Catherine la meilleure directrice de thèse de l'année", mais pour bien plus qu'une année! Merci pour ton soutien, de m'avoir aidé à aller jusqu'au bout. Mais aussi merci de m'avoir invité dans cette belle aventure scientifique, et de m'avoir laissé des libertés, de m'avoir laissé m'amuser, parce que la science c'est avant tout une passion, et je l'ai bien découvert avec toi! Merci d'avoir été un si bon modèle, peut-être trop bon parfois! Je reviendrai toujours avec plaisir pour une bonne tasse de thé!

Je remercie ensuite chaleureusement les membres du jury, Giovanni Cappello, Sasha Verkhovski, François Amblard, Etienne Wolf et Zsolt Lenkei d'avoir accepté d'évaluer mon travail. Merci d'avoir fait le déplacement pour venir m'écouter. Malgré les nombreuses péripéties de ma thèse et l'écriture dans un temps réduit, j'espère que mon travail a su vous intéresser. Merci pour vos retours qui ont apporté un œil nouveau à mon travail, qui ont permis de déceler des choses très intéressantes dans nos recherches et qui nous ont donné de nouvelles pistes à explorer. Merci!

Merci également à toutes les différentes équipes et structures qui m'ont hébergé et permis d'effectuer ce travail. Merci à l'équipe Thermodynamique et biophysique des Petits Systèmes (TPS) dirigée par Olivier Bourgeois ainsi qu'à l'équipe Micro et NanoMagnétisme (MNM) dirigée par Stéfania Pizzini de l'Institut Néel. Je tiens à remercier aussi Alain Schuhl, Pierre-Etienne Wolf et Klaus Hasselbach pour leur accueil dans cet Institut et tout l'équipe administrative, en particulier Christine Martinelli et Elodie Bernard. Merci à Maxime Dahan pour son accueil dans l'UMR 168. Merci à Jean-Louis Viovy et Stéphanie Descroix pour leur chaleureux accueil dans l'équipe MMBM, à l'Institut Curie. Et je remercie également toute l'équipe administrative de l'Institut Curie, Françoise, Karen,

Laurence et bien sûr Brigitte. Merci également aux membres de l'Ecole Doctorale de Physique de Grenoble pour leur patience et leur aide, et pour leur écoute concernant les demandes de cours spécifiques. Merci d'avoir intégré les Labels à notre formation, et j'en profite pour remercier toute l'équipe du Label REI. Enfin merci aux différentes entreprises, labos, chercheurs qui nous ont accueilli temporairement ou avec qui nous avons collaboré. Je pense notamment à Nir Gov, merci pour ta collaboration très fructueuse avec notre équipe. Et merci à Oriade, Lyncée Tec, à l'IBS et à l'IBENS pour leur accueil.

Et maintenant tous les autres! Attention la liste est longue!

Ne sachant pas par où commencer, je vais simplement commencer par le commencement. Grenoble. L'Institut Néel. Le Creta. A tous les membres du Creta, qui a été mon labo d'accueil, de coeur, pendant mon stage de Master et ma première année de thèse, mais aussi qui m'a accueilli avec bonheur à chacune de mes missions de Paris, merci. Merci André de m'y avoir accueilli. Merci Laureline, Sophie, Patricia, Isabelle, Paul, Pierre-Fred, Arnaud et Arnaud, Guillaume, Nathaniel, Benjamin, Anne-Claire, Hervé, Yoann et Yohan, Myriam, Johnny, Beilun, Ben. Je pense notamment à notre superbe équipe de football! Merci pour ces déjeuners sushi ou au Katmandou, pour ces départs cantine à 11h30, pour ces déjeuners à la cafèt du Creta sous l'oeil critique de Guillaume et Arnaud, pour ces livraisons de Comté. Merci à tous les thésards, aux séminaires non-permanents, aux sessions bières-poster qui étaient nos points de rassemblement dans ce grand Institut et qui me permettait de voir ceux et celles que je voyais peu, je pense notamment à Zhihua, Elodie, Ketty, Marine, Karim.

Un peu plus loin dans l'Institut Néel, j'aimerais remercier Grégory et Anne, qui ont passé beaucoup de temps sur mon projet, à imaginer et à construire de nouvelles pièces, merci! Je remercie également Jean-Luc Mocellin pour ses conseils en électronique. Merci à l'équipe de Nanofab, qui m'a supportée toutes ces années. Un petit pincement au coeur en imaginant que je ne remettrai pas les pieds de sitôt dans cette magnifique salle blanche.. Merci Bruno, Thierry et Thierry, Gwenaëlle et un grand merci à Seb! Et voilà je ne vous embêterai plus avec mes innombrables masques et notre occupation de la salle blanche pour notre travail à la chaîne. Merci à toute l'équipe de Biofab et à toute la petite équipe Biophysique de Néel également. Je suis malheureusement partie quand Biofab ouvrait, mais j'ai eu la chance de quand même pouvoir profiter de ce nouveau lieu de biophysique. Merci Cécile, Antoine, à Gaël, Manu, Clotilde (pour ton prêt de badge !), Hervé, Jean-Luc et un grand merci à Valérie qui a repris en main le microscope holographique. Merci pour ces discussions et pour tes lumières sur l'optique. Merci également à Nora et Thibaut pour m'avoir permis d'utiliser le coin microfluidique, et merci encore Nora de m'avoir suivi dans l'organisation de ce premier parcours Biophysique pour la Fête de la Science.

Un grand merci à David Eon pour son aide pour les mesures d'ellipsométrie. Et merci également à mon parrain de thèse Julien Pernot pour ses conseils et son support.

Je ne pourrais pas finir la page Grenoble sans remercier mes collègues thésardes, mais surtout amies, et même voisines (!) Meriam, Pauline et Xueying (alias Sydney). Merci les filles! J'ai été heureuse de faire l'aventure "thèse" à vos côtés, dans les meilleurs moments comme dans les pires! Merci pour tous ces beaux souvenirs, de la randonnée à la gastronomie (tunisienne, chinoise et les bons produits du marché Saint Bruno. Je n'oublierai jamais nos soirées Mah-Jong. XieXie ! Saha Saha pour nos thèses! (Voilà je viens de trouver un premier défaut à LaTeX, c'est compliqué d'écrire en chinois et en arabe..).

Et je peux encore moins finir cette partie sans remercier mon équipe: Soha pour ton sourire, ta bonne humeur (plein de bonheur à toi et Ahmad, et à Jude (Hey Jude!) et Rachel qui découvrent ce monde avec la plus merveilleuse des mamans!); Beilun mon compagnon de stage, le roi du foot et du go, je te souhaite le meilleur aussi et j'espère recroiser ton chemin! Et Caterina, celle que je peux sans conteste appeler mon mentor, mais aussi mon amie. Merci de m'avoir tout appris, je n'oublierai jamais ces heures passées là-haut au microscope, et notre travail à la chaîne à Nanofab (111 lamelles ! 111!). Je suis contente que l'on ait gardé contact, que la science nous rassemble encore (cf Mechanobiology au Vietnam) et je suis sûre que l'on se recroisera encore.

Ma deuxième année de thèse a été aussi l'année des changements, changement de ville et de labo. Cela aurait pu être compliqué, stressant, cela aurait pu mal se passer.. Mais en intégrant la superbe équipe de Jean-Louis Viovy, je ne vois pas comment cela aurait pu mal se passer! Merci Jean-Louis de ton accueil! Tu as vraiment construit une équipe formidable. Merci à Bastien pour ton accueil, toujours le premier à accueillir les nouveaux, ne change pas! Merci à mes co-bureaux, dans le meilleur bureau du monde, à Vélan, que j'espère n'avoir pas trop distrait de sa rédaction en pleurant devant mes neurones mourants, encore à Bastien avec qui la musique était toujours bonne et qui a fait naître le merveilleux Og. Mais aussi aux anciens du bureau, à Karla, et Sylvain. Karla merci pour tous ces moments passés en dehors du labo, j'espère vraiment aller au Guatemala avec toi! Realmente eres un buen amiga! (Donde.. esta.. la biblioteca !?) Sylvain, merci pour tout ce que tu m'as appris, sur le volume mais sur la Recherche aussi! Ton départ a fait un grand vide que même Sylvain la plante n'a pas comblé (ou presque). A mes nouvelles co-bureaux merci les filles! Petra, j'ai été très heureuse de te rencontrer, j'ai beaucoup appris, merci pour nos discussions, un grand merci pour ton aide! Un jour on retournera faire du cheval en Corse! Laura, je suis vraiment heureuse que tu sois ma co-bureau! Je ne vais pas dire que je t'apprécie autant que Bonnie apprécie Châtaigne (oui, bon parce que c'est quand même vachement fort), mais je suis trop super contente

de t'avoir rencontré! Merci pour les cadeaux-chats et vivement le Mud Day! Sarah, on ne se connaît pas depuis longtemps, mais je t'adore déjà! Je pense aussi à Cécile qui a aussi été ma co-bureau un court moment, un jour je viendrai faire du roller avec toi! Et Madison, merci pour tes attentions, tes encouragements! J'espère que le Miracle Morning te réussit toujours aussi bien et que Loki se porte à merveille!

Et merci à tous les autres Viovy's! Merci Steph pour ta gentillesse et pour ton accueil dans l'équipe! Je pense aussi en particulier aux Girls, Ezgi, Miza, Floriane! Un grand merci à Floriane pour toute l'aide que tu m'as apporté! Tu es la nouvelle Neuron-Girl et je souhaite que tout se passe bien pour toi! (avec plein de Frozen Yoghourt!) Merci Lauriane (continue les gâteaux, surtout à la châtaigne!), Amel (Happy Tea and Happy water power! Et merci pour le chocolat!!), Marine, Iago Iago (Gracias a nuestro profesor!), Julien, Ayako, Claire, JB, Lucile, Ismail & Charles et bien sûr la team Italia: Davide, Marco, notre chère Giulia, et un spécial Grazie pour Ivan et Angelo pour votre aide sur le projet Volume! Grande grande grazie Angelo per il tuo aiuto!! Petite dédicace pour notre team Tarot aussi!

Merci aussi à tous ceux de Curie, merci à Rémy, Francis et Eric de l'atelier, un grand merci en particulier à Eric pour son aide pour la "Boiboite"! Merci à tous ceux que j'ai rencontré et qui ont illuminé ce passage à Curie, merci Fahima, John, Majdou, Susu, Rodrigo, Mélanie, Fanny, Kotrina, Feng, Momo, Jens, Thanh, Quentin, Perrine.. un grand merci à Sarah pour ton interprétation magnifique de mon rôle dans le film! Tu étais ché-niale!

Merci à toute l'équipe de l'IPGG. Perrine, Manon, Meriam, Sylvia, Charlotte, les Guillaume (merci de m'avoir supporté moi et mes demandes "spécifiques neurones")! Merci aux membres de l'équipe Piel avec qui j'ai pu collaborer, merci Matthieu pour les discussions sur la méthode d'exclusion de fluorescence, un grand merci à la magnifique Team Volume, Clotilde, Larisa, mais aussi Olivier de l'Institut Langevin, notre master en optique, c'est beau ce qu'on fait! (Force et honneur Clotilde!). Merci YanJun pour tes conseils sur la Chine, merci Rafaele pour ta bonne humeur quand je venais toujours demander "où est Clotilde?", gracias Pablo por su aliento y consejos!

En voyageant jusqu'au Vietnam pour la conférence Mechanobiology, j'ai pu y rencontrer des personnes intéressantes, scientifiquement et humainement. Merci Emrah pour ton petit coup de pouce pendant ma période de rédaction, merci Minerva pour ta bonne humeur et ton amitié (Espero beber un vaso de mojito fresquito en la playa con usted otra vez mi super amiga espanola!!). Merci Cesar pour tes petits cours d'astronomie et tes conseils pour mon futur télescope. J'ai aussi été super contente de vous rencontrer Si-

mon, Thao, Charlotte, Ian, Maxime, Morgane et les autres, la superbe "Mechanobiology Dream Team"! Merci à mes compagnons de voyage aussi, Caterina que j'ai eu la chance de retrouver, Ilaria, Daniela, Anastasiya, Delphine.. !

Enfin j'aimerais remercier mes amis, mes colocs, ma famille. Yaël, Marine, merci les filles d'être venues aussi souvent me voir à Paris! Ces petites bulles de bonheur, de folies, de bubble tea m'ont beaucoup aidé! Grâce à vous les restos japonais et coréens de Paris n'ont plus de secrets pour moi! Merci aussi Nono, Christine, Reda (DDR-chinois?!) pour tous ces bons moments passés à Paris! Merci Sandrine pour ces soirées sushi, il faut vraiment qu'on se refasse ça bientôt! Merci Claire d'avoir eu le courage de rester tout le long de ma soutenance, quel courage! Merci José d'avoir fait de même, et de m'avoir supporté pendant l'écriture! Muchas gracias!! Merci à mes colocs, Elie et Aurélien, de m'avoir supporté et de m'avoir aidé à avoir tout de même des moments de détente durant l'écriture! Merci aussi à Sam, notre cher coloc adoptif!

Et au risque de paraître folle, je vais aussi remercier le dernier colocataire, celui qui ne quitte jamais l'appartement: merci Châtaigne! Tu es un chat, mais pas n'importe lequel, et tu m'as bien aidé surtout pendant cette période d'écriture et pour cela je te dis merci!

Et merci à ma famille, mes parents, Nico et Sarah, Guy et Nicole, Martine et Kyri, les cousines (!), Simon et la petite Lily, Patrick, Alain, Mireille et aussi Barbara, Alain et Xavier, la famiglia de Corsica, merci pour tout votre support, vos encouragements! Dorénavant je pourrais rentrer plus souvent à Strasbourg et on commandera encore plus souvent du couscous! A vous tous j'aimerais dédier cette thèse, à Pépé et Mémé surtout, partis trop tôt à mon goût.. Merci d'être toujours là.

SUMMARY

The thesis deals with the control and the measurement of neuronal shapes *in vitro*, "control" by using adhesive micropatterns allowing to constrain cells shape in two dimensions, "measurement" by using either interferometry or fluorescence measurements in microfluidic chambers to gain knowledge on cell dry mass and volume.

The biological question at the heart of this thesis is the regulation by neurons of various morphological characteristics such as length, dry mass or volume, as well as how these characteristics arise from the cytoskeleton organization and dynamics. We quantified these different parameters in primary hippocampal neurons using micropatterning during the early stages of neurite growth until the establishment of the axo-dendritic polarity.

In **Chapter 2**, we present how shaping neurons allows a precise control over axo-dendritic polarization and neurite lengthening. In particular, we discuss the influence of neurite width on neurite growth and on the density of microtubules.

Chapter 3 is dedicated to the measurement of neuronal dry mass using an interferometric technique. We show in particular that the density of dry mass locally and the total neuritic dry mass seem to be conserved in the early stages of growth independently of the neuritic width. Lastly, the development of microfluidic tools combined with the exclusion method is presented in **Chapter 4**. Our first result indicates that neurite height are regulated independently of neurite width, and pave the way to the study of the biophysical mechanisms that underlies neuronal growth.

Key words: neuron, adhesive patterns, cellular shapes, volume, interferometry, microfluidic

RÉSUMÉ

Le sujet de cette thèse porte sur la maîtrise et la mesure des formes neuronales *in vitro*, "maîtrise" par l'emploi de micropatterns adhésifs permettant un contrôle des formes cellulaires en deux dimensions, "mesure" par notre volonté d'accéder à la masse sèche ainsi qu'au volume de la cellule par l'emploi de deux techniques complémentaires faisant appel à l'interférométrie ou à des mesures de fluorescence en chambre microfluidique.

La question biologique au coeur de cette thèse est celle de la régulation par le neurone de diverses caractéristiques morphologiques comme sa longueur, sa masse sèche ou son volume, mais aussi de comprendre comment ces caractéristiques surviennent de l'organisation et de la dynamique du cytosquelette. Nous avons quantifié ces différents paramètres dans des cultures primaires de neurones hippocampiques en utilisant des micropatterns pendant les premiers stades de la croissance neuritique jusqu'à l'établissement de la polarisation axo-dendritique.

Dans le **Chapitre 2**, nous présentons comment la maîtrise des formes neuronales nous donne un contrôle précis sur la polarisation axo-dendritique et sur les longueurs neuritiques. En particulier, nous discutons l'influence de la largeur neuritique sur la croissance des neurites et sur la densité de microtubules.

Le **Chapitre 3** est dédié à la mesure de la masse sèche des neurones avec une technique d'interférométrie. Nous montrons en particulier que la densité de masse sèche locale et la masse sèche neuritique totale dans les premiers stades de croissance semble être conservée indépendamment de la largeur neuritique. Finalement, le développement d'outils microfluidiques combinés avec la méthode d'exclusion de fluorescence est présenté au **Chapitre 4**. Notre premier résultat indique que la hauteur neuritique est régulée indépendamment de la largeur des neurites, cela ouvre la voie à l'étude des mécanismes biophysiques qui sous-tendent la croissance neuronale.

Mots clés: neurone, motifs d'adhésion, formes cellulaires, volume, interférométrie, microfluidique

CONTENTS

Remerciements	i
Summary	vii
Résumé	ix
1 General Introduction	1
1 A brief history of the brain	3
1.1 From heart to brain	4
1.2 Brain cells	5
1.3 Neuronal diversity	6
1.4 Generic neuronal morphology	7
2 Neuronal compartments: shapes and functions	9
2.1 Axon and dendrites	10
2.2 Axonal size: role and dynamics	17
2.3 The growing neuron: growth cone and actin waves	19
2.4 The sick axon	23
3 Biophysical bottom-up approaches of neuronal shapes	27
3.1 Hippocampal and cortical model	29
3.2 Control of neuronal shapes	30
3.3 Measuring cell shapes: toward 3D imaging	33
3.4 Context and objective of this thesis	39
2 Constraining neuronal shape in 2D	41
1 Introduction	42
2 Methods	42
2.1 Micropatterning	42
2.2 Cell culture	47
2.3 Fixation and immunofluorescence	49
3 Growth and polarization	51
3.1 Contributions	51
3.2 Neurite length	51
3.3 Polarization	53
3.4 Fine tuning of length and polarization	55
3.5 Discussion	58

4	Cytoskeleton response to geometrical constrains at the neurite level	60
4.1	Microtubules (MTs)	60
5	Conclusion and outlooks	62
5.1	Summary of most important findings	62
5.2	Outlooks	63
3	Mass measurement with Digital Holographic Microscope (DHM)	65
1	Introduction	66
2	Contributions	66
3	Methods	66
3.1	Microfabrication	66
3.2	Cell culture	68
3.3	Phase measurement	68
3.4	Experimental improvements for noise reduction	70
3.5	Analysis: custom Matlab program	72
4	From phase to dry mass	74
4.1	From phase and cell dry part RI relationship...	74
4.2	...to dry part RI and cell dry mass relationship	75
5	Results	77
5.1	Neurite tapering	78
5.2	Local neurite dry mass as a function of the distance to the soma .	79
5.3	Local neurite dry mass as a function of the neurite width	79
5.4	Total neurite dry mass	81
6	Accuracy of dry mass measurement with DHM	85
6.1	Phase variation due to birefringence	85
6.2	Hypothesis and validations	86
7	Refractive index and cell volume: preliminary results	87
7.1	Decoupling Procedure (DP)	87
7.2	Medium preparation and characterization	88
7.3	Custom-made medium replacing system and closed perfusion cham- ber	90
7.4	Preliminary result	90
8	Conclusion and outlooks	92
8.1	Summary of the most important findings	92
8.2	Outlooks	93
4	Volume measurement with the Fluorescent eXclusion method (FXm)	95
1	Introduction	96
2	Contributions	96
3	Chip for neuronal volume measurement	96

3.1	Chamber design	96
3.2	Microfabrication	97
4	Characterization	102
4.1	Pillars height	102
4.2	Roof roughness	102
4.3	Roof flatness	104
4.4	Control of the fluorescence contamination	105
5	From fluorescence intensity to height	107
5.1	Conversion law	107
5.2	Choice of objectives	109
5.3	Measuring volumes and heights	111
6	Cell culture	114
6.1	Surface fonctionnalization	114
6.2	Seeding	115
6.3	Imaging medium	115
7	Results	116
7.1	Neurite tapering	116
7.2	Neurites slices volume and dry mass as function of the width: toward neurite RI ?	117
7.3	Actin waves	118
7.4	Coupling FXm and micropatterning	121
8	Conclusion and prospects	123
8.1	Main findings	123
8.2	Outlooks	123
5	General conclusion	125
6	Résumé de la thèse en français	127
1	Introduction générale	127
1.1	Une brève histoire du cerveau	128
1.2	Compartiments neuronaux: formes et fonctions	129
1.3	Approches biophysiques "bottom-up" des formes neuronales	130
1.4	Contexte et objectifs de la thèse	131
2	Contrainte des formes neuronales en 2D	132
2.1	Résumé	132
2.2	Conclusions principales	132
3	Mesure de masse sèche avec le Microscope Holographique Digital (DHM)	133
3.1	Résumé	133
3.2	Conclusions principales	133
4	Mesure de volume avec la Méthode d'eXclusion de Fluorescence	134

4.1	Résumé	134
4.2	Conclusions principales	135
5	Conclusion générale	136
7	Appendices	139
1	Appendix 1: Model calculation of neurites length and polarization	139
2	Appendix 2: "Diver" design and technical scheme	142
3	Appendix 3: Matlab program for Phase analysis	142
3.1	Main program: dhm5201601.m	142
3.2	Routine to analyze neurite on the right of the soma: dhmright5.m	144
3.3	Routine to analyze neurite on the left of the soma: dhmleft5.m . . .	148
3.4	Routine to sum results from the different parts of a neurite: dhm- sum5.m	152
3.5	Routine to calculate the mean values for a group of neurons: moyenne.m	153
3.6	Decoupling procedure routine	159
3.7	Subsidiary routines used	163
4	Appendix 4: Theoretical and experimental comparisons between water and PBS phase measurements	167
4.1	Theoretically	167
4.2	Experimentally	167
4.3	Error estimation	168
5	Appendix 5: Electronic circuitry for the custom-made medium replacing system	169
6	Appendix 6: Technical schemes of the custom-made closed perfusion chamber	169
7	Appendix 7: Matlab program for FXm analysis	172
8	Appendix 8: Conditioned medium	173
	Bibliography	174

GENERAL INTRODUCTION

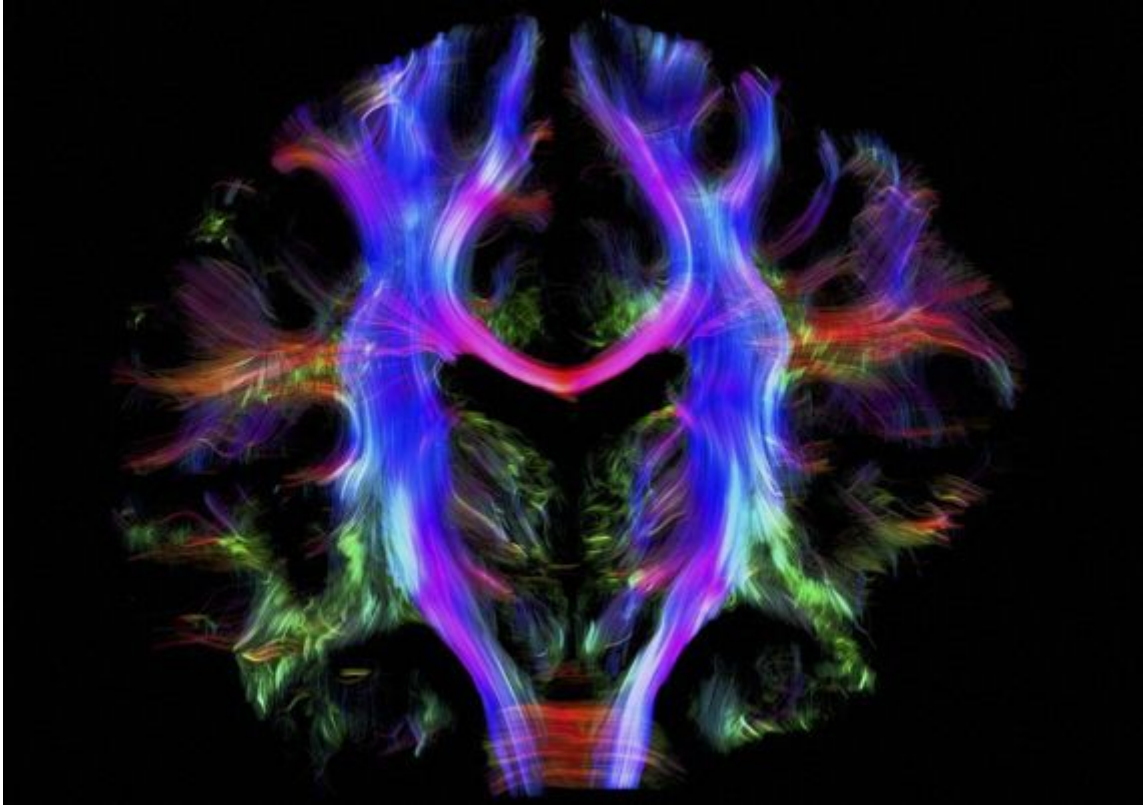
The brain remains the most complex and extraordinary machine in the known universe. Its main building blocks, neurons, are numerous (120 billions) and show a wide diversity of morphologies and functions.

During my PhD project, I investigated neuronal shapes through the use of diverse biophysical approaches. (i) With micropatterning to constrain cells shape, I explored issues such as the axo-dendritic polarization. (ii) Using an interferometry method, I studied the repartition of the dry mass into the different neuronal compartments. (iii) Lastly, I performed volume and height measurements to get insights into neuronal morphologies evolutions at the 3D level.

In **Chapter 1**, I will first introduce the different elements of my PhD, focusing on the actors of neuronal morphologies. I will then introduce the three techniques that I developed: micropatterning, Digital Holography Microscopy (DHM) and Fluorescence eXclusion method (FXm). The development of these biophysical tools as well as results that have been obtained about neuronal shapes, and notably about neuronal growth and polarization, will be detailed in **Chapters 2, 3 and 4**.

My Phd project was also conducted in a unique context. I started my PhD in the fundamental physics environment of the Néel Institute in Grenoble, before moving to the Curie Institute in Paris, at the beginning of my second year of Phd, and finally, like the whole team of Jean-Louis Viovy, to the Institut Pierre Gilles de Gennes, for my third and last year. These different scientific environments, and in particular the possibility to integrate the microfluidic tools in my researches from the second year, have strongly contributed to the final content of this thesis.

1 A brief history of the brain



Wiring the human brain, Alfred Anwander
Wellcome image awards 2016

"The Astonishing Hypothesis is that "You", your joys and your sorrows, your memories and your ambitions, your sense of personal identity and free will, are in fact no more than the behavior of a vast assembly of nerve cells and their associated molecules. As Lewis Carroll's Alice might have phrased it: "you're nothing but a pack of neurons." This hypothesis is so alien to the ideas of most people alive today that it can be truly called astonishing".

F. Crick, *The Astonishing Hypothesis*, 1994

States of Mind: Tracing the edges of consciousness
Wellcome Collection - 4 Feb. - 16 Oct. 2016 - London

1.1 From heart to brain

The heart was associated to the origin of mental activity for a long time and in many cultures. This point of view was illustrated by the heart-soul theory [1] of the Greek philosopher Aristotle (384–322 BC), the tradition in Ancient Egypt (3100–332 BC) that scooped and discarded the brain during mummification while carefully preserving the heart [2], and the hinduist belief of an atomic sized soul situated in the heart developed in the Bhagavad-Gita (Vth to IInd century BC) [3], among others. This theory is not so surprising since the heart is the most representative organ of mental activity, expressing it in a noticeable way all along our life and leading to the use, until now, of some expressions like "A broken heart" instead of "A broken brain". Nevertheless little by little, throughout centuries, a lot has been discovered. Notably at the Renaissance, when falls the prohibition by the Church to dissect bodies, anatomists were able to establish the link between mental activity and brain. They were able to highlight connections between the brain and other organs while revealing the presence of nerves, as illustrated by the drawing of Leonard de Vinci (1452 - 1519) presented in **Figure 1.1**. Nowadays it is interesting to note that the brain supremacy is again disputed, as another player, the gut microbiota, has come into the game. Recent studies recognized its role in the determination of behavior and cognition [4]. The established central organization of mental activity around the only brain is thus challenged. However the brain remains the most complex and extraordinary machine in the known universe and is still considered as the organ mainly involved in the control of our every action, thought, feeling, making possible the existence of our inner world (i.e. developing imagination) as well as our perception of reality and the possibility

to interact with the outer world, for example developing empathy. It allows us to feel happiness, pain or love and most remarkably we have conscious awareness and the experience (or the illusion..) of free will. How consciousness arises from this biological machine is one of the most challenging questions that scientists from different areas, using different and specific approaches and techniques, try to address. However they seem all to agree that it comes from a defined - still complicated - object: a network of nerve cells communicating with one another through a hundred trillion interconnections mainly being located inside **the brain**.

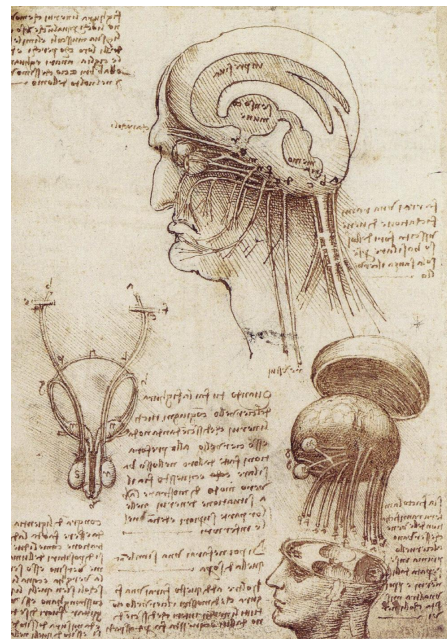


Figure 1.1 – Anatomical drawing by Leonard de Vinci (XVIth century).

1.2 Brain cells

As it was not always evident for human beings that the Sun is just another star among others, it was not always evident that the brain is just another - still special - organ among others, meaning composed of defined elements that are cells.

The first that proposed that the brain is a cellular machine was the father of neuroscience, the Spanish neuroanatomist Santiago Ramon y Cajal [5, 6] (1852 - 1934). This was not commonplace at all at this period, since the brain was seen as a continuous net rather than composed of connected but discrete entities, the brain cells. The cellular composition of the brain was difficult to assess compared to other tissues. Brain cells, unlike other cells, are **branched and hugely diverse in morphology**. It is using the staining method of the Italian anatomist Camillo Golgi (1843 - 1926) that this astonishing diversity of cells structures was revealed (see an example in **Figure 1.2**).

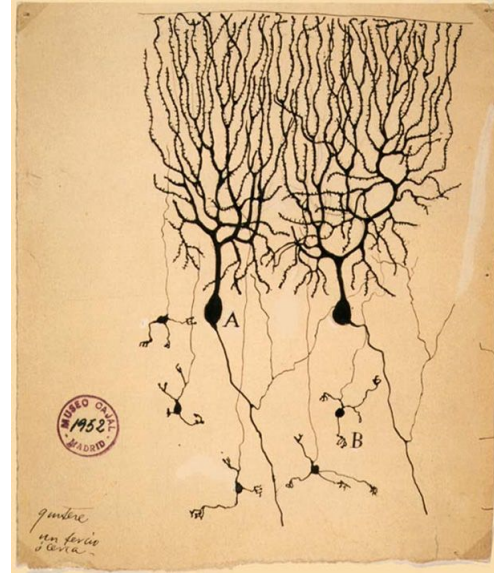


Figure 1.2 – *Drawing of Purkinje cells (A) and granule cells (B) from pigeon cerebellum by Santiago Ramón y Cajal, 1899.*

Two main types of cells specific to the brain were identified: neurons and glial cells. They are present in all the nervous system, composed of the Central Nervous System (CNS), which includes the brain and the spinal cord, and of the Peripheral Nervous System (PNS), which includes nerves and ganglia outside of the CNS. The brain contains 120 billions neurons, and, on contrary to the "glial cells are 10 times more numerous than neurons" general belief, it was recently assessed that the number of glial cells is of the same order of magnitude as the number of neurons [7]. Neurons are considered as the fundamental units of the nervous system because of their excitability. In this study we will focus on neurons from the CNS, although we will encounter on occasions glial cells whose types are numerous, as well as their roles in supporting neurons' survival.

1.3 Neuronal diversity

Neurons have a large diversity of morphologies, related to their function and location in the brain. About one hundred years ago, Ramon y Cajal identified many different types of neurons with various shapes and sizes as shown in **Figure 1.3**.

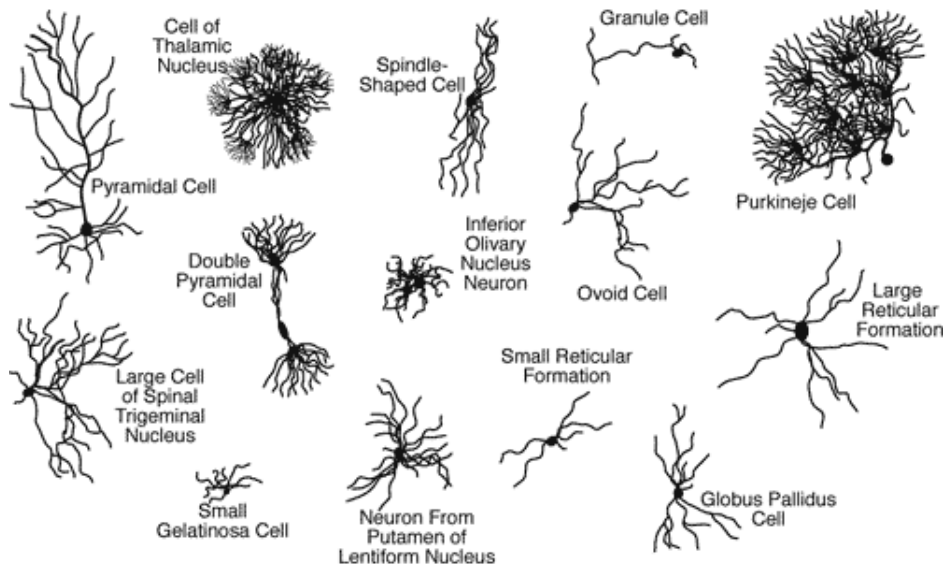


Figure 1.3 – *Diversity of morphologies and sizes among neurons, based on drawings made by Ramon y Cajal.*

The system is even more complex if we consider that one type of neuron can be present in different zones of the brain. Moreover a task can be controlled by different areas. About ten years ago the "Brainbow" neuroimaging technique was developed, allowing us to distinguish neighboring neurons of a given type using a combination of fluorescent proteins. This constitutes a real improvement since the time of Ramon y Cajal and the innovative but low efficient Golgi's staining method. The **figure 1.4** displays an example of a brainbow fly brain, where many individual neurons of only one targeted type can be observed.

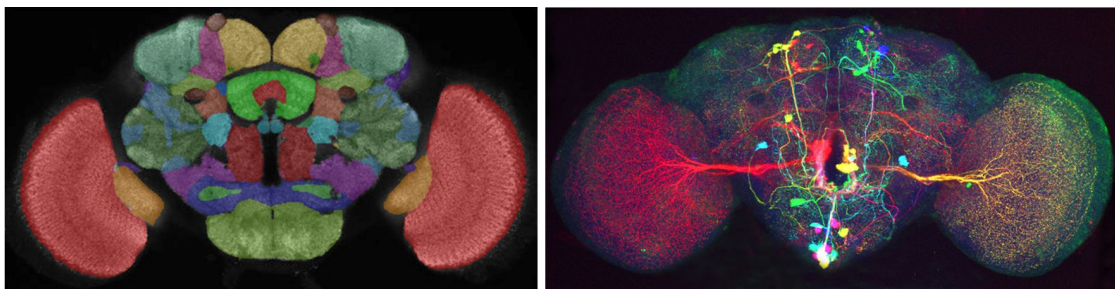


Figure 1.4 – **Left:** *Scheme of a fly brain [8].* **Right:** *Brainbow fly brain showing selectively labeled neurons that release octopamine [9].*

1.4 Generic neuronal morphology

Despite their diversity, all neuron types share similar morphological characteristics. A neuron is composed of the **cell body (soma)** and two types of processes (neurites) that are **dendrites** and **axons** as shown in **Figure 1.5**. Neurons exhibit a dendritic arborescence and usually one single axon, although some cell types do not follow this rule, like pseudounipolar neurons that display one axon that splits into two branches that serve both functions. One of these branches will be connected to periphery (skin, joint and muscle) and the other to the spinal cord. However, multipolar neurons constitute the majority of neurons in the brain. Soma diameter varies from $4\mu\text{m}$ (granule cell) to $100\mu\text{m}$ (motoneuron in the spinal cord) and the length of the whole neuron varies between a few micrometer to more than one meter for the longest motoneurons of the PNS. This length is mostly defined by the length of the axon.

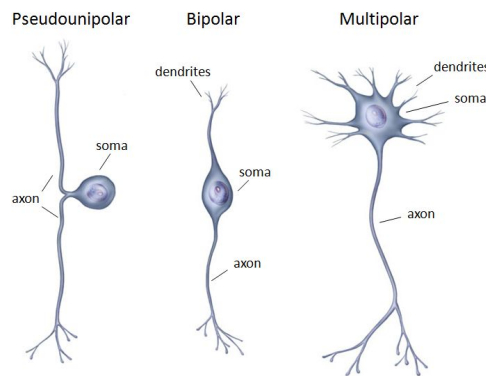


Figure 1.5 – *Pseudounipolar, bipolar and multipolar neurons. Adapted from Semay Johnston Medical Art.*

Information travels through the axon as an electrical signal as highlighted by Luigi Galvani (1737 - 1798) with his work on animal electricity and his experiment on frog's legs, where he induced an alive compartment on dead limbs. This experiment led to the discovery of the intrinsic electrical force of muscle and nerve cells responsible for muscle contractions and nerve conduction in living organisms [10]. In the collective memory, it is this operation which inspired the creation of the gothic masterpiece *Frankenstein* by the British novelist Mary Shelley [11].

In neurons information travels via a short-lasting electrical event called the action potential (AP). The unit of information represented by the AP is initiated inside the axon in the initial segment, a structure of a few tens of μm next to the soma, before being regenerated at the soma and finally sent back to the axon. The local inversion of membrane polarization associated to the AP is then conveyed distally along the axon, transducing chemical events within the physical gap separating adjacent neurons, the synapse. Small

change of membrane potential will be consequently generated within the post-synaptic dendrites, the whole process ensuring the transmission of electrical signal within neuronal networks. To complete this classical picture, we can mention the phenomena of neural backpropagation, i.e. the retroshooting of the AP back through to the dendritic arbor. The different phases of an action potential and its mechanism of propagation are presented in **Figure 1.6**.

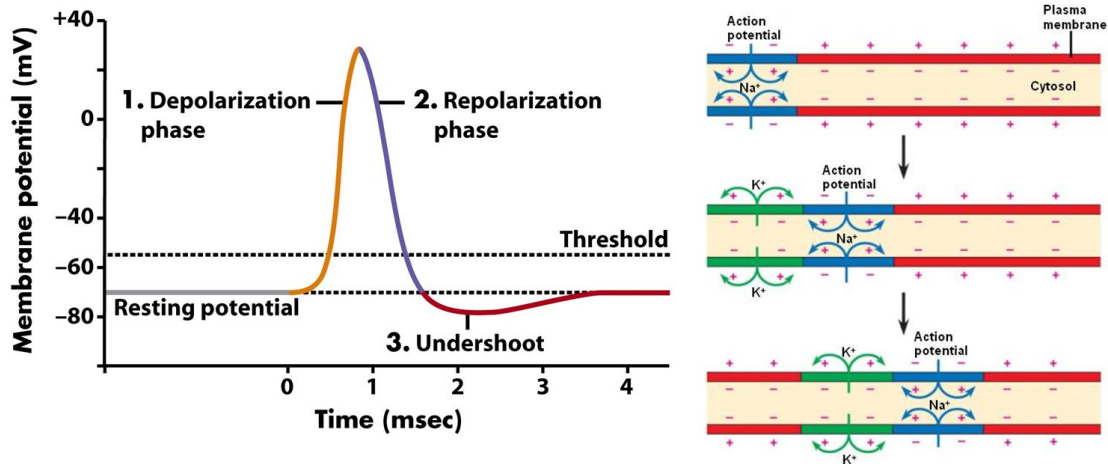
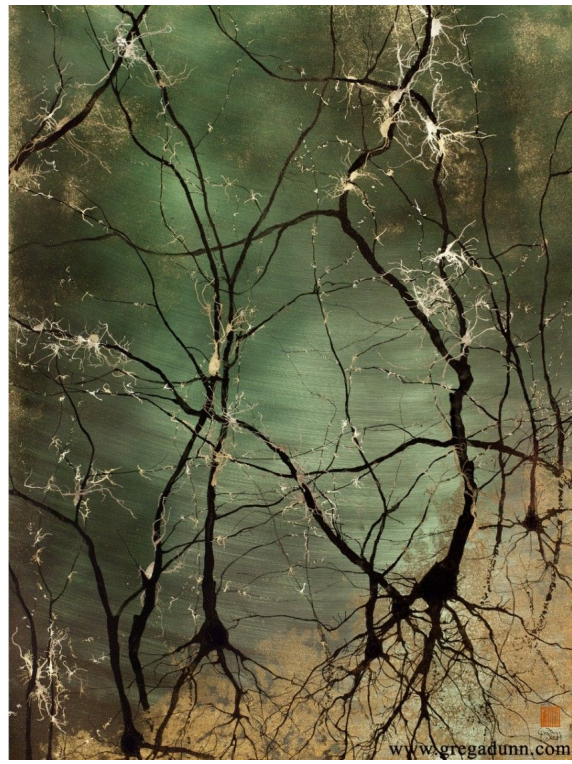


Figure 1.6 – **Left:** Action potential shape and phases [12]. **Right:** Propagation of the AP down the axon through a depolarization-repolarization process triggered by Na⁺ ions flowing in (depolarization) and K⁺ ions flowing out (repolarization). [13]

As highlighted in a seminal way by Cajal, neurons have very peculiar branched morphologies, providing an increased surface area. A more recent study showed that 97% of the surface area of a motoneuron (excluding the axon) is dendritic [14]. A spherical cell should have a diameter of 340 μ m to occupy the same volume. With 100 billion neurons connecting one to another and the evolutionary limit on head size, we can deduce how densely they are packed, while nevertheless ensuring long-range connectivity. As D. A. Sholl wrote: it is the *mode of connectivity* between neurons that is the most critical property of their diverse morphologies [15]. The establishment at the cellular and at the molecular level of the branched, compartmentalized and polarized morphology of neurons that support this connectivity will be addressed in the next section.

2 Neuronal compartments: shapes and functions



Spiny Stellate and Neural Migration, Greg Dunn, artist and neuroscientist

"The cerebral cortex is similar to a garden filled with innumerable trees, the pyramidal cells, that can multiply their branches thanks to an intelligent cultivation, sending their roots deeper and producing more exquisite flowers and fruits every day."

Ramon y Cajal, 1894

*States of Mind: Tracing the edges of consciousness
Wellcome Collection - 4 Feb. - 16 Oct. 2016 - London*

A neuron is an eukaryotic cell whose typical components are presented in **Figure 1.7**. As all animal cells, a neuron is delimited by the lipid bilayer forming the plasmic membrane. The membrane contains numerous transmembrane proteins making the link with the extracellular environment. The region of the neuron containing the nucleus is known as the cell body, or soma. The soma contains many other organelles like the centrosome or the Golgi apparatus involved in the nucleation or synthesis of various cell constituents. Another important part of an eukaryotic cell is its cytoskeleton composed of actin filaments, microtubules and intermediate filaments. The cytoskeleton plays a fundamental role in the regulation of cell shapes, mechanical properties, internal organization and trafficking. In neurons, the molecular organization and composition at the cellular or the sub-cellular levels is highly compartmentalized, and this process starts quite early in development. The specificities of dendrites and axons that are the two major compartments of neurons will be described in the next section.

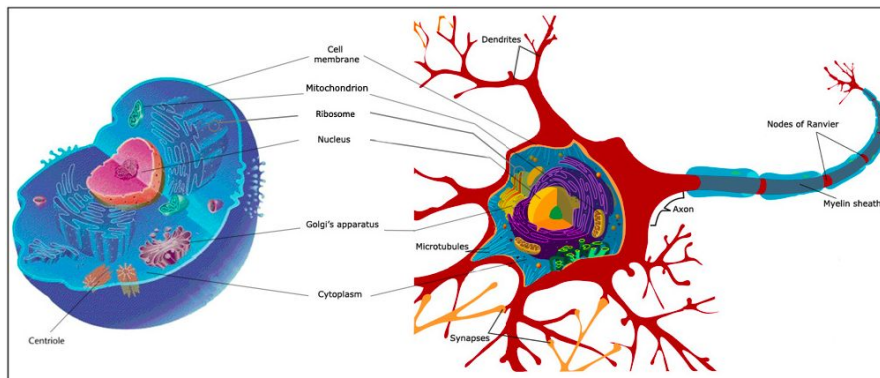


Figure 1.7 – *Common components between a typical eukaryotic animal cell (left), like glial cells, and a neuron (right). Adapted from Wikimedia Commons.*

2.1 Axon and dendrites

Mechanisms of neuronal polarization - the development stage where the cell specify one axon - are still not completely understood. However, differences between dendrites and axons are well identified. Some of these neuronal processes' characteristics are exposed here, from morphological differences at the cellular level to molecular specificities at the sub-cellular level.

2.1.1 Morphological differences

Diameters of CNS axons and dendrites in mammals are generally in the submicrometric range. However axons of different diameters have been identified in some regions of the CNS [16,17]. This is illustrated in **Figure 1.8** showing electron micrographs of regions containing thinner axons (mainly $\leq 0.5\mu\text{m}$). The opposite situation, i.e. the localization of thicker axons (mainly $\geq 1.5\mu\text{m}$), is displayed in **Figure 1.9**.

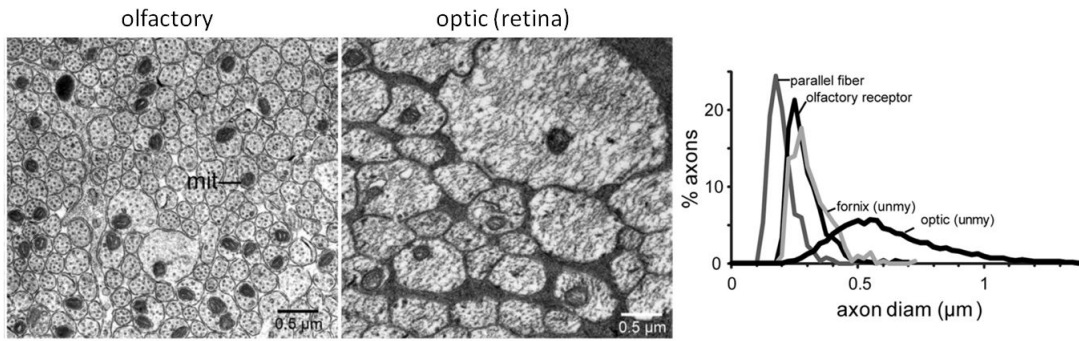


Figure 1.8 – Axons of thinner diameters. Electron micrographs: Olfactory receptor axons and axon segments of ganglion cells within the retina (guinea pig). The graph displays the percentage of axons versus axons diameters for different types of axons, including the two exemplified in the electron micrographs. Number of axons: $n=650$, 700, 300 and 10500 for parallel, olfactory, fornix and optic axons respectively. Adapted from [17].

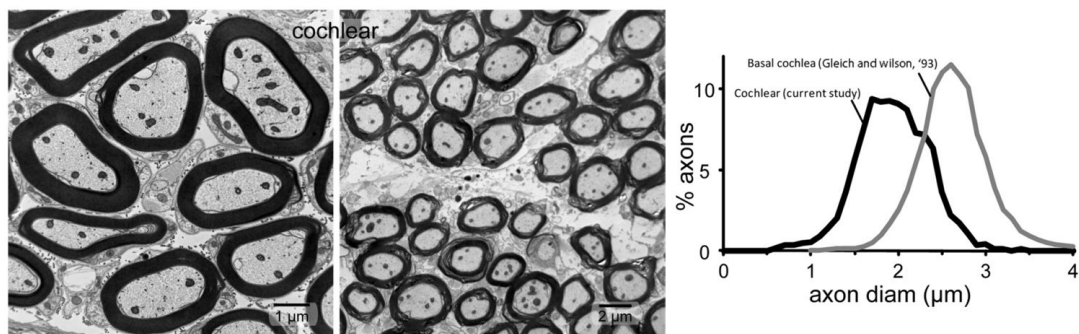


Figure 1.9 – Axons of thicker diameters. Electron micrographs: auditory axons (rat). The graph displays the percentage of axons versus axons diameters for the axons exemplified in the micrographs as well for fibers only from basal cochlea (guinea pig, replotted from Gleich and Wilson, 1993). Number of axons: $n=1700$ and 1800 for cochlear and basal axons respectively. Adapted from [17].

The difference between the diameters of axons and dendrites has been poorly studied. Nevertheless, it has been established that axons diameter is rather constant whereas dendrites are thicker near the soma and their diameter tapers gradually. This was observed in cultured hippocampus by Banker et al. [18] using electron microscopy to provide an estimate of the evolution with the distance to the soma of the relative size of axons and dendrites. This is illustrated in **Figure 1.10**. These data also suggest that besides being shorter, dendrites seem to be generally thicker compare to axons.

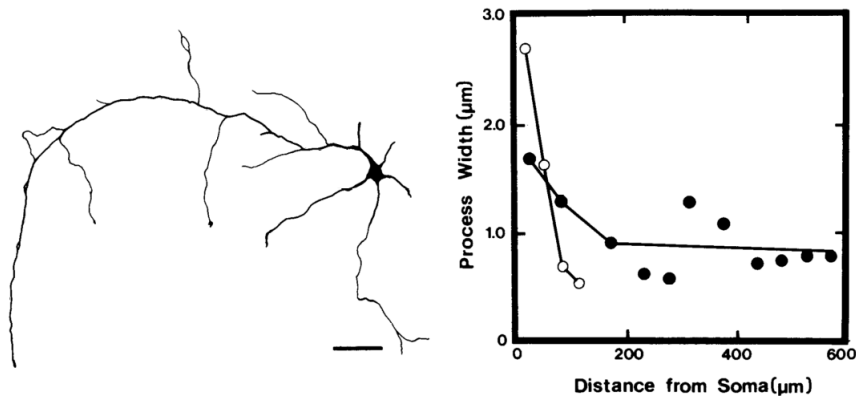


Figure 1.10 – *Width changes in dendrites and axon by electron microscopy. Left: Drawings illustrating the isolated neuron used for the study. Scale bar: 50 μm . Right: The change in width of the dendrites (open circles) and axon (solid circles) at increasing distances from the soma.*

However this is mostly at the sub-cellular level that the difference between axons and dendrites is significantly obvious thanks to the presence of specific molecular compositions and structures.

2.1.2 Actin and actin rings

Actin is a major cytoskeletal protein for the majority of cells. It exists as actin monomers, the Globular-Actin or G-Actin, which can polymerize to form Filamentous-Actin, or F-Actin, thanks to tight binding sites mediating head-to-tail interactions with two other actin monomers. These filaments are thin flexible fibers of about 7 nm in diameter and up to several micrometers in length. G-Actin and F-Actin, as presented in **Figure 1.11**, are both present in neurons and are major actors during their growth.

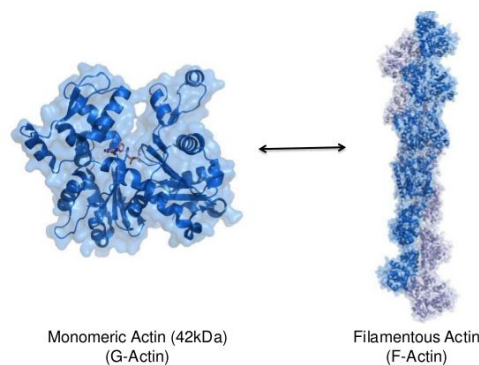


Figure 1.11 – *Actin structures. Monomeric or Globular-Actin (left) and Filamentous Actin (right) created by polymerization of several actin monomers. [19]*

Actin is organized in several specific structures in neurons, as reviewed very recently by Roy [20]. The actin organization at the neurite tips during neuronal growth, i.e. within a

structure named the growth cone (see the section **Growth cone**) is now well documented. In contrast, little was known about the neurite shaft until the paper of Xu et al. [21] showing, using super-resolution imaging, the presence of regularly spaced actin rings along the axon (**Figure 1.12 A**). Actin rings assembly starts as polarization begins (between 2 and 3 Days In Vitro (2/3 DIV) [22]. Later on, it was reported by D'Este et al. [23] that these structures were not specific only to axons and were also established in dendrites. Importantly, the spacing between actin rings corresponds to the length of an elongated protein named spectrin. In addition, another protein, i.e. adducin, is involved in the control of rings diameter, whose diameter is typically found around around 400nm [24] (**Figure 1.12 B**). The periodic distribution of spectrin and actin is seen at DIV2–3, whereas the presence of adducin in the rings is only visible at DIV8 [22], presumably to stabilize the actin-spectrin lattice as axons mature.

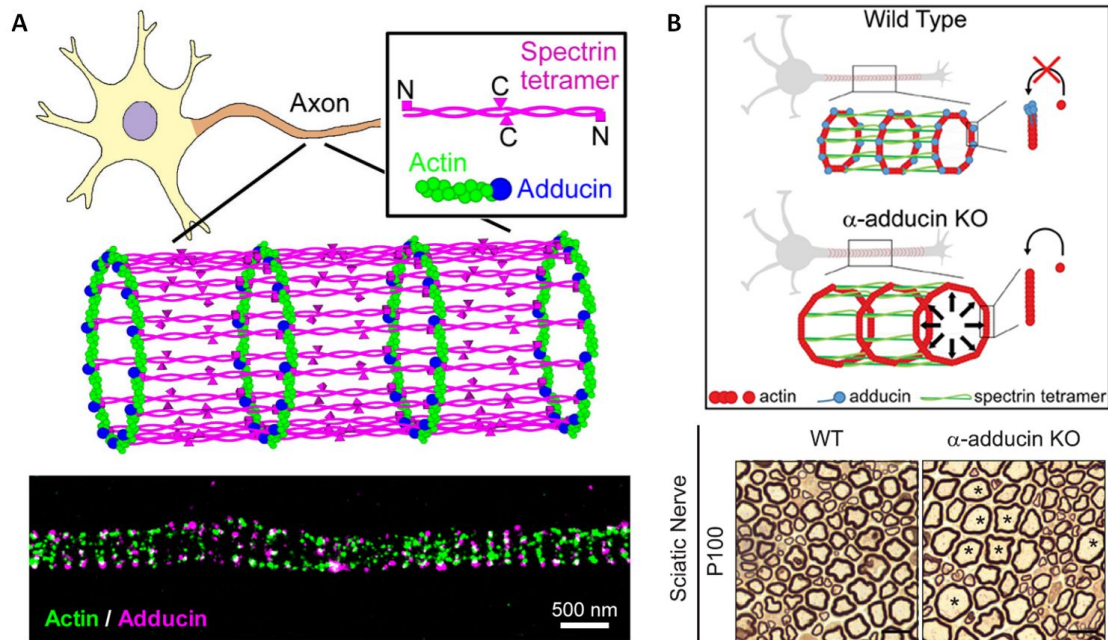


Figure 1.12 – (A) Scheme representing a model for the cortical cytoskeleton in axons, actin rings, accompanied by a two-color STORM image of actin (green) and adducin (magenta), the components of these actin rings [21]. (B) Scheme illustrating the effect of α -adducin KO on actin rings diameter. Representative semi-thin sections of WT and α -adducin KO sciatic nerves; asterisks (*) highlight axons with enlarged diameter; scale bar: 10 μ m [24].

2.1.3 Microtubule polarity

Another interesting specificity in the cytoskeleton organization of neurons concern the microtubule network, the microtubule associated proteins and their repartition in axons and dendrites.

Microtubules (MTs) are long thin structure about 20-25nm diameter and up to 50 μ m in length. MTs are composed of two subunits, α -tubulin and β -tubulin, forming asymmetric α/β -tubulin dimers, and show an helical structure, as represented in **Figure 1.13**. Microtubules polymerization occurs end to end, with one subunit contacting the other subunit of the next dimer.

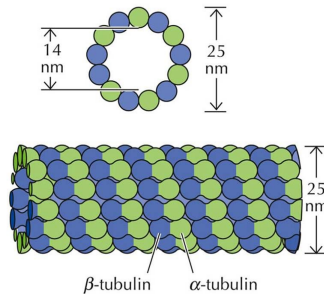


Figure 1.13 – *Microtubules helical structure* [25].

Like actin filaments, they have an intrinsic polarity expressed by a (+) and a (-)-end. At the (+)-end, β -subunits are exposed whereas at the(-)-end, α -subunits are exposed. Microtubules can elongate at both ends, nevertheless it is significantly faster at the (+)-end. Most importantly, MTs act as railways along which cytoplasmic organelles such as mitochondria are transported.

Microtubules density and average length are constant between axons and dendrites at the early stage of growth (< 1 week of culture) [18, 26, 27] whereas there are differences in the density of microtubules in axons and dendrites in older hippocampal cultures (\sim 3-4 weeks of culture), with a greater density of MTs in axons than in dendrites [28]. Up to one week of culture [18], authors measured the microtubules density as the number of microtubules per micrometer of process width and found similar densities of 8.6 ± 2.8 microtubules/ μ m for axons and of 7.1 ± 2.9 microtubules/ μ m for dendrites. Baas et al. [27] reported that MTs length varies from 0.24 to 17.95 μ m for a dendrite and from 0.05 to 40.14 μ m for an axon, with an average of about 4 μ m for both. Increasing the length of a neuronal branch is therefore implemented through abutted MTs rather than from the elongation of existing MTs.

The polarity orientation of microtubules is uniform, with (+)-ends directed away from the cell body and toward the growth cone, until about 2 days in culture for both axons and dendrites. This polarity orientation remains uniform for axons during later stages of development, whereas there is a transition from uniform to nonuniform polarity in dendrites. This transition begins at 4-5 days *in vitro* (DIV) and is fully established after 1 week *in vitro* [29, 30]. This polarity will have important consequences on the motion of cell organelles along these different branches.

Another significant difference between axons and dendrites is the repartition of the Microtubules Associated Proteins (MAPs). MAPs are proteins that bind to tubulin subunits, participating in the regulation of microtubules stability. There are mainly two types of MAPs: type I, including MAP1, and type II, including MAP2, MAP4 and Tau. Essentially only MAP2 and Tau are observed in neurons. MAP2 are big MAPs of molecular weights of about 200 kDa [31] whereas Tau are small MAPs (molecular weights in the range 37-46 kDa [32,33]). The spacing between microtubules is then modified depending on the MAP. This is illustrated in **Figure 1.14**.

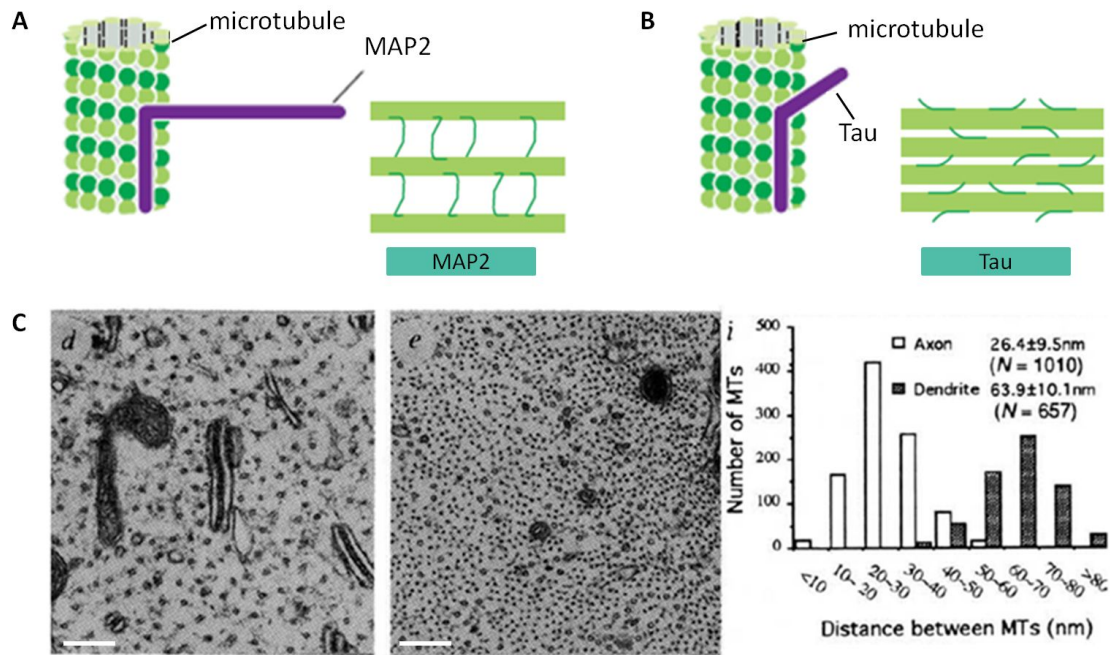


Figure 1.14 – Organization of microtubule bundles by MAPs. (A) MAP2 binds along the microtubule lattice at one of its ends and extends a long projecting arm with a second microtubule-binding domain at the other end. (B) Tau possesses a shorter microtubule cross-linking domain. Adapted from [34]. (C) Cross-section electron micrographs of a Purkinje cell dendrite (d) and a large myelinated axon in the spinal cord (e). (i) Compilation of wall-to-wall distances between nearest adjacent microtubules in Purkinje cell dendrites (d) and spinal cord axons (e). Scale bar 250 nm. Adapted from [35].

The difference in microtubules density between axons and dendrites observed after 1 week in culture could be related to the difference in MAPs, MAP2 being mainly found in dendrites, invading the axon up to the initial segment, and Tau only in axons, as shown in **Figure 1.15**.

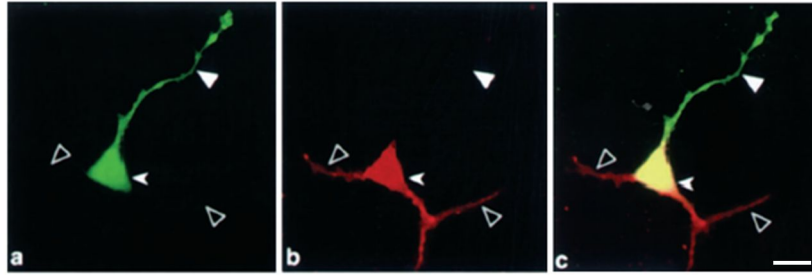


Figure 1.15 – *Confocal image showing MAPs repartition in a neuronally differentiated P19 cell [36]. Left: GFP-Tau protein (green). Middle: MAP2 (red). Right: Merging. Scale bar, 5 μ m.*

The Tau protein, and more specifically the gradient of Tau phosphorylation, is therefore used as an axonal marker [37]. The monoclonal Tau-1 antibody, which recognizes dephosphorylated serine sites [38], is commonly used to identify the axon. The gradient of Tau phosphorylation is visible on the neuron shown in **Figure 1.16**. It has been suggested that Tau may have other roles than promoting microtubules stability and assembly [37]. It could also regulate the bundling and/or spacing of axonal microtubules by its phosphorylation. This idea is supported by two results: Tau is promoting microtubule bundling when overexpressed in several non-neuronal cell types [39–41] and Tau conformation is regulated by phosphorylation, becoming shorter when dephosphorylated and longer and stiffer when phosphorylated [42].

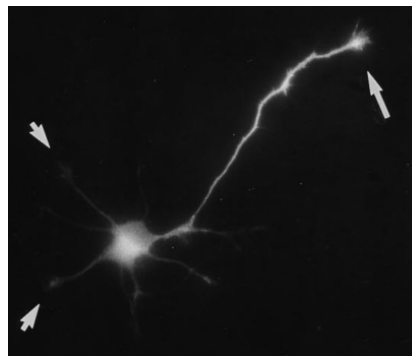


Figure 1.16 – *Tau-1 immunofluorescence is present at high levels in the middle and distal axon (up right arrow) but is barely detectable in minor processes (left arrows) and the proximal axon [37].*

Nonetheless there may be exception in the allocation of MAPs. A study showed that tau seems to be the preferential MAP to control the MTs density in small-caliber axons although other MAPs (MAP1A, MAP2, MAP4) seem to replace it in large-caliber axons [43].

2.2 Axonal size: role and dynamics

2.2.1 The static axon

Studying axons of different calibers and their inner structures is important since the wide variety of axon diameters in the CNS [16, 17] might reflect their function. It was indeed found that the firing frequencies are low for thinner fibers and high for thicker ones, from about 1 to more than 100 Hz [17]. Interestingly an increase in the mitochondrial volume per axonal length scaling with the square of the axon diameter was reported. This would suggest, that the energy capacity would raise with the axon volume, as observed in [44]. Since the axonal diameter is apparently linear with the firing rate, doubling the information rate would imply to quadruple an axon's volume and energy use. Furthermore, abrupt changes in the diameter of axons, but also from axon to soma or dendrites, were observed to provoke propagation failures [45–51]. As thoroughly reviewed by D. Debanne et al [52], many studies showed that an abrupt increase in axon diameter causes a decrease in both velocity and peak amplitude of the action potential, whereas a step decrease in diameter has the opposite local effects on these two parameters [47, 53–59]. Axon caliber seems therefore to be related to the information rate for the delivery of the electrical signals. Similarly, the sharpness of the action potential measured at the soma in mammalian neurons has been recently associated to the relative sizes between the axon and the soma [60] which seems quite conserved in various neuronal types [17].

Besides, the inverse phenomenon can be also observed, i.e. the electrical signal itself seems to have a transient impact on the axonal shape at the time scale of the action potential. This will be further explained in the next section.

2.2.2 The dynamic axon

Mechanical and optical sensitive methods have revealed small changes in the diameter of the axon accompanying the propagation of an action potential. This was for example observed with AFM in mice nerve terminals [61] or with an interferometry method in crayfish giant axon [62]. Correlations between action potentials peaks and associated mechanical deformations are illustrated in **Figure 1.17** for AFM (left) and interferometry (right) studies.

The main finding of these studies is that the axonal surface is moving outward during depolarization and is moving inward during hyperpolarization. These results were mostly obtained on giant axons of molluscs [62–68], or mammals nerves [61, 69] (i.e. bundles of many axons). Let us note that in most cases it was the phase or the optical path length that was recorded instead of the real mechanical deformation. This phenomenon

of axonal transient swelling would need to be confirmed on mammalian isolated neurons. Nevertheless it highlights a possible link between a change of the membrane potential and membrane swelling. This effect was also deduced from indirect measurement methods, as developed below.

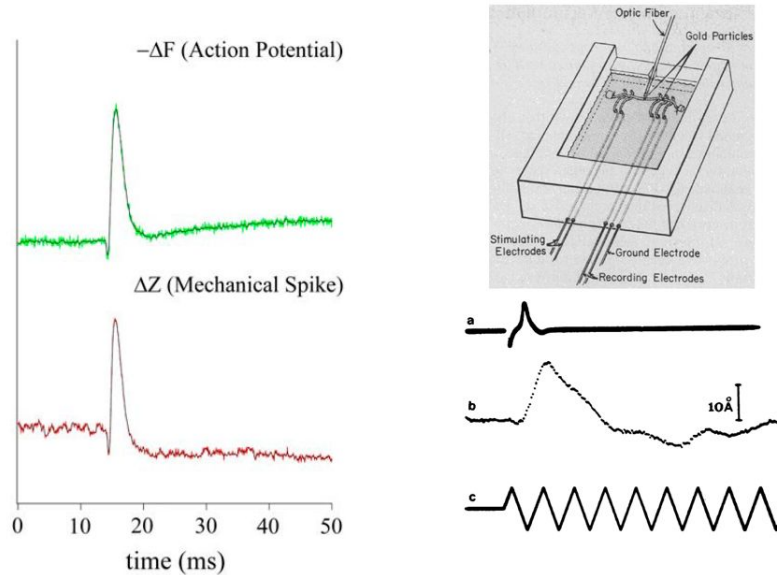


Figure 1.17 – *Neuritic mechanical deformation related to action potentials. **Left:** Comparison of the action potential (ΔF , green trace) and the associated mechanical events measured with AFM (ΔZ , red trace) triggered by a single electrical stimulus ($500 \mu\text{s}$) delivered to the infundibular stalk. The mechanical spike had duration (fullwidth at half-maximum) of 1.6 ms, comparable to that of the action potential. Both traces were sampled at 20 kHz and low-pass filtered at 7 kHz. [61] **Right:** Comparison of the electrical amplitude of the action potential of about 1 mV (a) and the associated mechanical event visualized by an optical technique (b), starting about 250 μsec after stimulation and peaking about 400 μsec later. Experiments were done in a recording chamber showing nerve placement (up) and using a time reference characterized by a 500- μsec period (c) [62].*

At the ionic level, P. Lipton reported that, in cerebral cortical slices, variations in amplitude and duration of the intercellular K ions concentrations cause a cell volume change large enough to drastically reduce the intercellular volumes and so, transiently, increase extracellular molecular and ionic concentrations. Expectedly, this phenomenon would in turn, significantly affect synaptic transmission and spontaneous nervous activity [70].

At the whole brain level probed by NMR imaging, a decrease in the water diffusion coefficient has been observed by D. Bihan in activated regions [71] corresponding to an increase of a so-called "slow" water fraction located near the cell membrane. This might be explained by an increase of the membrane surfaces, i.e. a cell swelling. This swelling

has been indirectly estimated to be about $\approx 4\%$, leading to a few nanometer transient displacement of the axon membrane.

This functional mature state where neurons can interact with each other through electrical and possibly mechanical signals is only the last state in a succession of developmental steps. These steps include neuronal migration, growth and polarization. These processes are different depending on the type of neuron, its final location and function in the brain and can happen in parallel [72]. Some of these mechanisms will be developed in the next section.

2.3 The growing neuron: growth cone and actin waves

The establishment and maintenance of neuronal polarization is crucial for correct nervous system development and function. Whereas growing and polarization steps are well defined *in vitro* (cf **Part 3.1**), at least for specific neuronal types, the same phenomenon *in vivo* is very diverse. Depending on brain region and developmental stage, some neurons inherit their polarity, like vertebrate retinal ganglion cells and retinal bipolar cells [73], whereas others establish it during differentiation, like cortical and hippocampal pyramidal neurons or cerebellar granule neurons [74–76]. Furthermore polarization can occur in parallel to migration. This is illustrated by cortical pyramidal neurons which are generated in the ventricular zone and migrate through the subventricular towards the intermediate zone and, doing so, evolve from a multipolar shape to a bipolar one [74, 77], as illustrated in **Figure 1.18**.

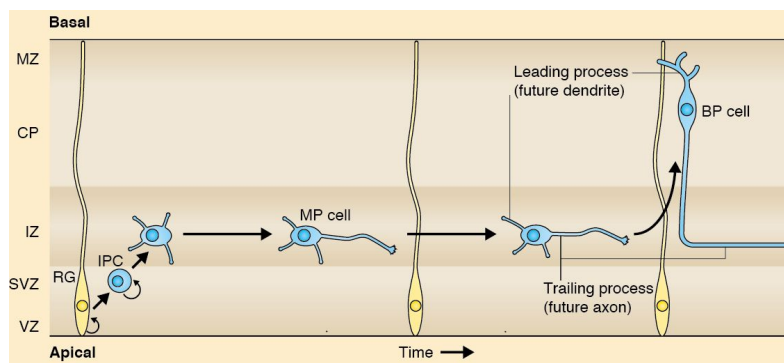


Figure 1.18 – *Cortical neurons, hippocampal neurons and cerebellar granule neurons establishing their polarity. Cortical neurons are generated from radial glia (RG) by asymmetric division in the ventricular zone (VZ). These neurons form multiple minor neurites and migrate through the subventricular zone (SVZ) towards the intermediate zone (IZ). Multipolar (MP) cells extend a trailing process (future axon) and a leading process (future dendrite), and transform into bipolar (BP) cells. BP cells migrate towards the cortical plate (CP) and marginal zone (MZ) [72].*

The migration phenomena involved in the building of the CNS includes the navigation of neurons or neuronal branches over long distances using specific guidance structures. One of these structures is the **growth cone** (or the leading edge in migratory neurons [78]). Its particular architecture will be detailed below. We will also focus on other actin-based structures specific to neurons having strong morphological similarities with growth cones, i.e. **actin waves**. Both of these structures are very active during neuronal growth and correspond to a deformation of the neuronal shaft associated with specific cytoskeleton structures, especially regarding actin.

2.3.1 Growth cone

Growth cones are dynamic, actin-supported extensions facilitating axon growth and guidance by bundling and extending actin filaments into structures known as filopodia and lamellipodia, probing the extracellular matrix (ECM). Many cytoskeletal-associated proteins are present in growth cones to anchor actin filaments and microtubules to each other or to other cytoskeleton components. One example is the myosin II [79], a molecular motor binding with actin (i.e. acto-myosin structures). **Figure 1.19** displays a scheme of a growth cone organized in three domains, each characterized by a specific organization of the cytoskeleton - the peripheral (P) domain, the transitional (T) zone and the central (C) domain [80] - as well as a fluorescence microscope image.

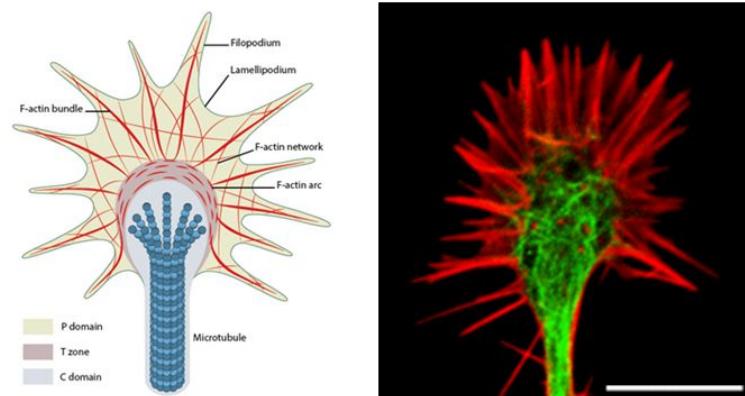


Figure 1.19 – **Left:** Schematic representation of a growth cone with its main cytoskeletal components (actin filaments and microtubules) into the three domains [81]. The **P domain** is primarily composed of unipolar actin filament bundles embedded in a less polar actin network. It contains dynamic lamellipodia and filopodia. Microtubules are also transiently found within this domain. The **T zone** is a thin interface between the P and C domains. The **C domain** is located in the center of the growth cone nearest the axon. It is primarily composed of microtubules and contains numerous organelles and vesicles. **Right:** Fluorescence image of a growth cone. Green: Microtubules. Red: Actin. Scale bar: $10\mu\text{m}$. Adapted from [82].

It has been observed in the particular case of neurons originating from the hippocampus, and more recently in the case of cortical neurons, that growth cone might be reactivated by propagative membrane deformation like growth cones. These structures were named actin waves.

2.3.2 Actin waves

Hippocampal neurons produce propagative, actin-rich membrane deformations in their early stages of growth, named actin waves (AWs) [83, 84]. AWs are physiological events generic for a large set of mammalian neurons, e.g. of hippocampal or cortical origin [85, 86]. AWs observed *in vitro* in a mouse embryo hippocampal neuron expressing lifeAct, a peptide staining F-actin [87], are shown in **Figure 1.20**.

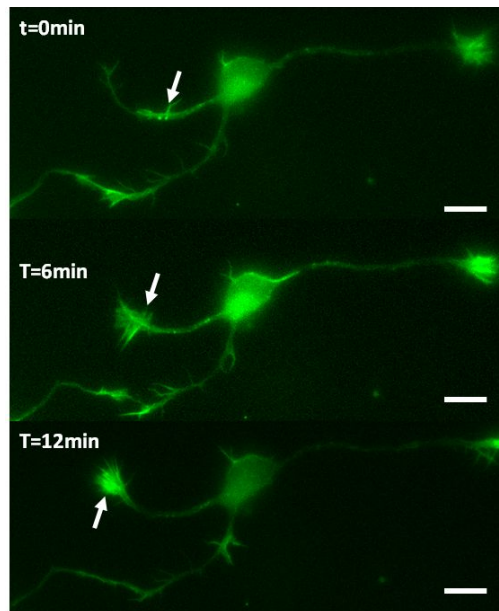


Figure 1.20 – *Actin waves. Fluorescence microscope images showing one actin wave (arrows) propagating on one neurite of a hippocampal neurons coming from a lifeAct mouse embryo. Scale bars: 10 μm .*

The role of these directional structures in neuronal growth and polarization was already underlined in the first occurrences of this phenomena in the literature, about two decades ago [83, 84]. Actin waves are associated with outbursts of neurite growth following the reactivation of the growth cone, and contribute to the fast elongation of the nascent axon. After years of a relative lack of interest for neuronal as compared to non-neuronal actin waves (e.g. actin ruffles [88], circular waves [89]), several in-depth studies published in the recent years have provided new insights into these dynamic structures, although the wave generation mechanism still remains unknown. First, actin waves seem to propagate using directional actin treadmilling that generates mechanical force [85]. Actin polymerization and depolymerization is accompanied by the presence within the wave of

several actin-associated proteins like e.g. Arp3, cofilin, or shootin [86, 90, 91]. Interestingly, the wave of actin polymerization directs microtubule-based transport by triggering an upstream wave of microtubule polymerization [92]. This very recent result is in agreement with previous observations of the presence within waves of microtubule associated proteins like doublecortin (DCX) [93]. These observations are presented in **Figure 1.21**.

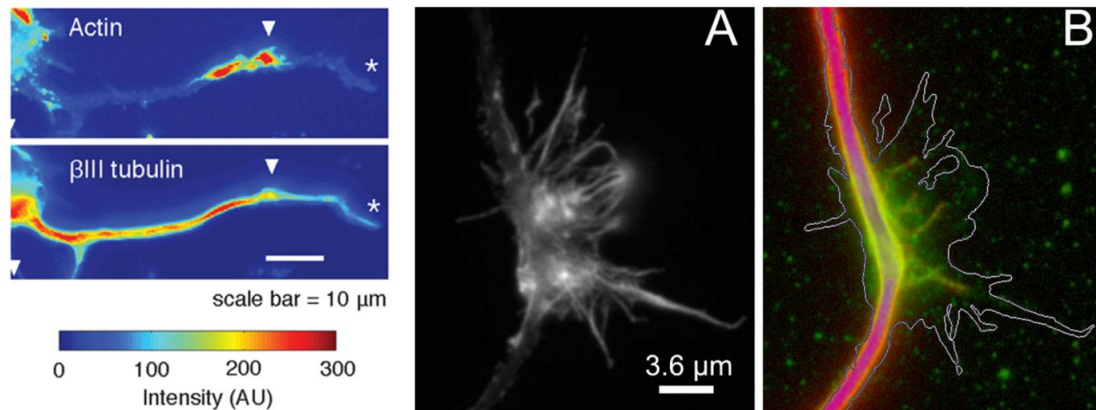


Figure 1.21 – **Left:** Fixed hippocampal neurons stained with phalloidin (actin) and anti- β III tubulin (neuronal microtubules) show enrichment of microtubules in and behind wave. White arrowheads mark actin waves, white asterisks mark neurite tips. Scale bar = $10\mu\text{m}$. [92] **Right:** Splayed microtubules at sites of focal accumulations of DCX along the axon. **Panel A** shows actin filament staining associated with a focal accumulation of DCX. **Panel B** shows an overlay of DCX (green) and microtubule (red) staining in the same region; the white line is an approximate outline of the actin staining. Note that several microtubules splay out from the main microtubule bundle and that these are decorated with DCX. Scale bar = $3.6\mu\text{m}$. [93]

It has been proposed that the coupling between these two main cytoskeleton components, i.e. actin and microtubules, occurs through a transient wave-induced upstream widening of the neurite shaft [92]. This idea is illustrated on the scheme of the **Figure 1.22**.

Still a lot needs to be investigated about actin waves mechanisms, e.g. about their generation, periodicity or velocity. In addition, and although actin waves are associated to a propagative wave of neurite deformation, increasing temporally the local width of the shaft, nothing is known about these local and transient volume changes. These aspects will be studied in **Chapter 4**.

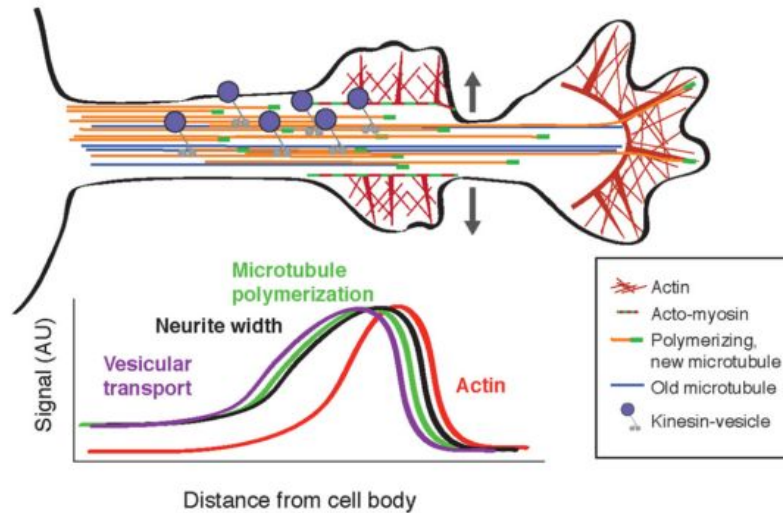


Figure 1.22 – *Model illustrating the co-regulation of actin and microtubules that drive microtubule-based transport. Actin waves cause transient increases in cargo delivery by increasing microtubule polymerization. It is proposed that actin waves aid microtubule polymerization by widening the neurite, allowing more space for microtubules to polymerize within the shaft and leading to an increase in microtubule-based transport. However, the changes are transient and will fade in time. [92]*

After growth and maturation, neurons may experience degeneration as an effect of diseases. Morphological changes are usually accompanying these states.

2.4 The sick axon

Slow changes of neuronal, and more specifically axonal morphologies are observed during brain diseases or trauma, culminating in neuronal death. Cells can disappear by swelling - necrotic death - like for brain trauma, or by shrinking - apoptotic death. The later case occurs in the adult brain as well as in the developing brain. During development, elimination of overproduced neurons or the removal of neuronal branches (a phenomena named pruning) is a physiological process leading to the mature neural circuitry [94]. In the adult brain, neuronal death is observed in acute neuropathologies, some neurodegenerative disorders and in brain aging. Apoptosis is characterized by a reduction in cell volume termed apoptotic volume decrease (AVD) [95]. Degenerative conditions also appear to produce changes in neurons morphology and internal organization before death. One example is the beading effect, which can be artificially induced with an osmotic perturbation [96, 97] as presented in **Figure 1.23**.

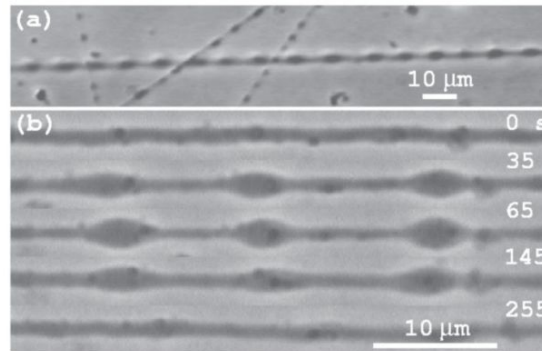


Figure 1.23 – (a) Osmotically induced shape instability in chick-embryo neurons. (b) Image sequence showing the growth and relaxation of the instability in a PC12 neurite. [97]

In this study, the volume change induced by beading is observed to be only transient. The authors propose that the initial swelling phase is mechanically slowed down by microtubules and that the volume recovery is driven by passive diffusion of osmolites [97]. Some neurodegenerative diseases, like Alzheimer's Disease (AD)¹ can provoke spontaneous beading [98]. In **Figure 1.24**, beading in AD can be observed and its link to the presence of β -amyloid protein, the major component of neuritic plaques, is highlighted.

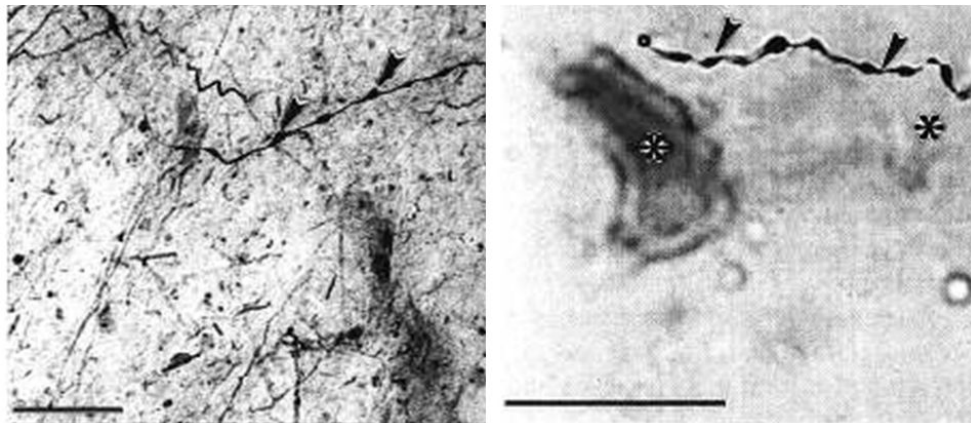


Figure 1.24 – Degenerative similarities between hippocampal neurites in AD brain and in tissue culture. The dystrophic appearance of β -amyloid-associated neurites in vitro (**right**) is quite similar to that in AD brain (**left**). Arrowheads denote degenerating neurites, asterisks indicate deposits of β -amyloid. Scale bars = 25 μ m. [98]

Other morphological consequences derive from AD disease. It was observed that neuronal processes that cross through an β -amyloid deposit are likely to have radically changed morphology [100]. They tend to lose their locally straight morphology and become curved. This phenomenon implies an increase of the axon length between the soma

1. Alzheimer's disease is a neurodegenerative disease that causes progressive and irreversible loss of mental functions, including memory. This is the most common cause of dementia in humans. It was first described by German physician Alois Alzheimer in 1906 [99].

and its multiple targets. It was suggested that it might cause a delay disrupting temporal firing patterns of action potentials. These morphological modifications might be a direct cause of the confusion, mental slowness, and progressive degeneration of cognitive abilities during AD early stages. Another study compared morphometric changes of neurons between asymptomatic Alzheimer's Disease (ASYMAD) and AD patients. They found that, comparing to controls, there is a significant decrease in the neuronal volume in AD, whereas there is a significant increase in ASYMAD [101, 102]. Neuronal hypertrophy, like for neurons of ASYMAD patients, might be associated to resistance to AD. In other studies, looking at the sub-cellular level, it is observed that the Tau protein in AD patients is abnormally hyperphosphorylated and fails to bind to microtubules [103, 104]. This is illustrated in **Figure 1.25**. Interestingly tau phosphorylation, typically related to neuropathological alterations, is reversible during mammalian hibernation [105]. This could represent a model system for this still not well understood regulation of Tau phosphorylation.

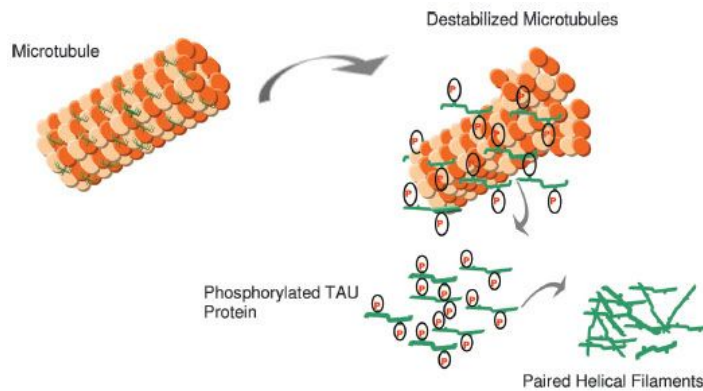


Figure 1.25 – *In AD, there is a reduction in the ability to bind microtubules and promote microtubule assembly. Hyperphosphorylated Tau may contribute to a destabilized microtubule network, impaired axonal transport, and ultimately in neurofibrillary tangle (NFT) formation and neuronal death [106].*

Currently there is no cure for AD which is a major public health problem in developed countries. Still a lot has to be discovered to unravel the causes and mechanisms of this disease. Among other aspects, the study of shape and volume variations would deserve an in depth investigation. Interestingly, cannabinoids, which can trigger dramatic neuronal volume change in acute conditions, are able to block the inflammatory response initiated by amyloid proteotoxicity [107]. Nevertheless it was also shown that the detection of cannabinoids by a type-I cannabinoid receptor can trigger a series of events changing neurons growth and connection [108]. This is illustrated in **Figure 1.26** representing the morphological changes induced by the synthetic cannabinoid receptor agonist WIN on Neuro2A cells, from neurite retraction to cell rounding and transitory blebbing.

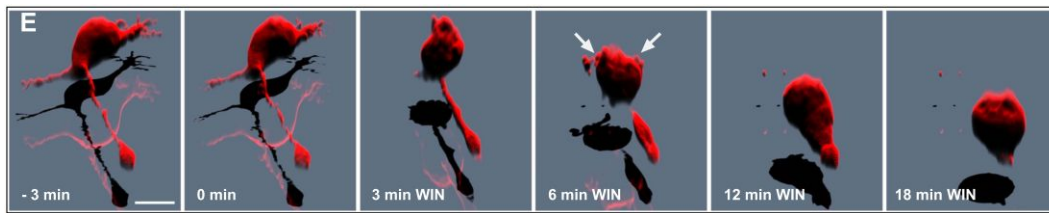


Figure 1.26 – 3D reconstruction of AFM images that shows neurite retraction, cell rounding, and transitory blebbing (arrows) following WIN treatment (100 nM). *n.s* $p > 0.05$; $***p < 0.001$ [108].

All these results show a strong interplay between neuronal morphologies, physiological functions and also physiopathology. To explore the mechanisms linking these different aspects, adapted tools should be chosen. Some of them, illustrating the bottom-up approach that will be the core of this work, will be presented in the next section.

3 Biophysical bottom-up approaches of neuronal shapes



Cortical Columns, Greg Dunn, artist and neuroscientist

"Like the entomologist in pursuit of brightly coloured butterflies, my attention hunted, in the flower garden of the gray matter, cells with delicate and elegant forms, the mysterious butterflies of the soul, the beating of whose wings may some day— who knows— clarify the secrets of mental life".

Ramon y Cajal, 1923

The challenging study of the brain can be performed in many ways. It can be approached through psychology, philosophy, medicine, biology, chemistry and physics. Global approaches concern the study of brain function in living subjects, to decipher the role and functions of the different areas of the brain. This is allowed using tools like Electroencephalogram (EEG), Computerized Axial Tomography (CAT), Magnetic Resonance Imaging (MRI), Positron Emission Tomography (PET) or Functional MRI and methodologies developed by psychologists, physicians... to name a few. When observing which part of the brain is active during a specific task, a lot has already been unraveled about the functional compartmentalization of our decision center. This is illustrated in **Figure 1.27**.

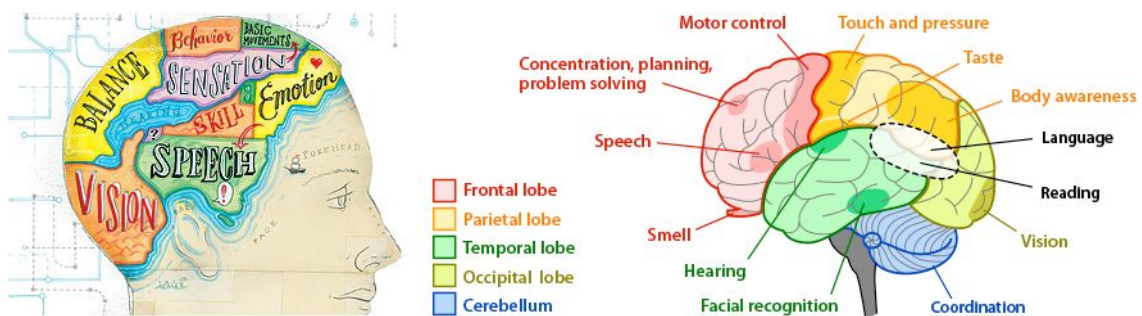


Figure 1.27 – *Brain maps illustrating and showing the establishments of the link between the different zones to the different functions. Illustration for TIME by Leigh Wells and scheme adapted from askabiologist.asu.edu*

On the opposite, the conceptual and experimental approach of the complexity of the brain can be bottom-up, based on the *in vitro* manipulation and understanding of the elementary building blocks of the brain, in particular neurons. Handling cells and building multicellular structures have been the subject of intensive researches for at least two decades, in particular using micropatterns of adhesion and microfluidic technologies. Bottom-up approaches are also particularly suitable for the observation of single cells using various optical techniques. Among these experimental approaches, the ones that will be at the center of my thesis will be detailed in this section, beginning with a presentation of one of the most usual neuronal model in *in vitro* studies.

3.1 Hippocampal and cortical model

Even if the mouse brain shows significant differences in size and structure compared to the human brain, mammals neurons are similar in shape and behaviours. In **Figure 1.28** human and rat or mouse brains are compared.

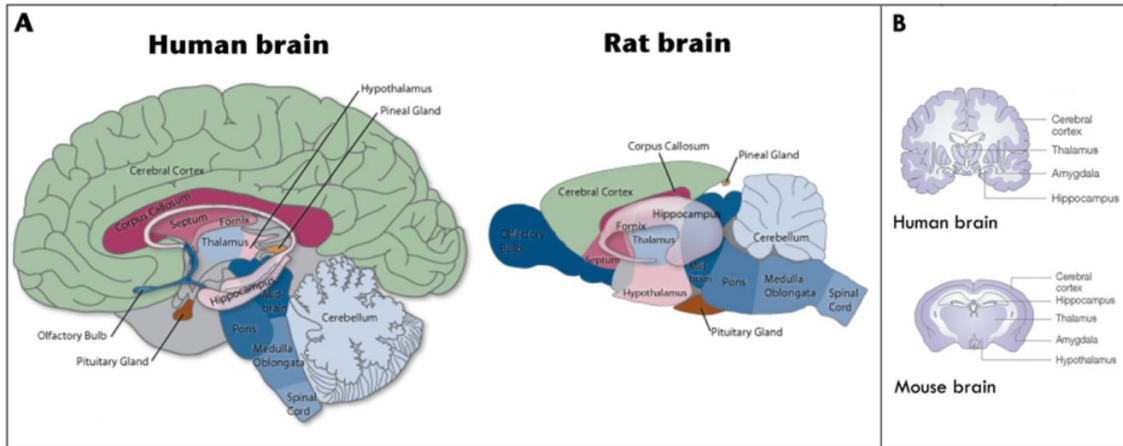


Figure 1.28 – *Left: Longitudinal (A) and transverse (B) sections of human and rat (A) or mouse (B) brains, showing functional similarities although in different proportions. Adapted from [109].*

Hippocampal neurons are highly used in neuroscience as a model system for many reasons. First, the hippocampus is a morphological well defined region in the last embryonic stage (see in **Figure 1.28**) and is therefore relatively easy to dissect. Moreover, this region is composed at roughly 85-90% of pyramidal cells (multipolar neurons), providing a rather homogeneous neuronal population [110]. Besides, its involvement in learning and memory formation is a particular interest in a medical point of view, for example in AD or schizophrenia.

When seeded after dissociation of the hippocampal tissue, they follow *in vitro* specific growth and polarization steps [111] as shown in **Figure 1.29**. First, lamellipodia around the soma are observed (stage 1), followed rapidly by the growth of minor processes in the first 12h after seeding (stage 2). The stage 3 is the axonal outgrowth, or neuronal polarization, which is taking place around 30h after seeding and corresponds to the fast elongation of the neurite that will become the axon. The last two stages are the dendritic outgrowth (stage 4) and the maturation (stage 5) that corresponds to the formation of synapses and the observation of dendritic spines after around 2 weeks in culture

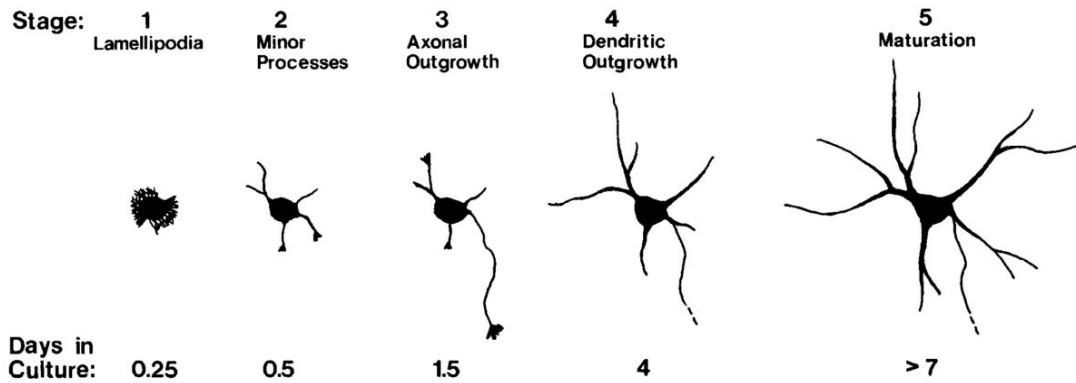


Figure 1.29 – *Stages of development of hippocampal neurons in culture. The approximate times at which cells enter each of the stages is indicated. [111]*

Neurons developing *in vitro* are observed to acquire the phenotypic properties of the corresponding neuronal cell type *in vivo*, e.g. physiological properties of their membranes or their ability to synthesize, release and take up neurotransmitters or to form synapses, as shown in [112] and reviewed in [113] and [114].

3.2 Control of neuronal shapes

The variety of neuronal types, even inside the pyramidal neurons of the hippocampus [115], and the intrinsic variability of morphologies inside a given type is a limitation to the reproducibility of experiments. Generally, to normalize cellular shapes or to spatially organize cell populations are powerful tools to highlight cell responses in well controlled experimental conditions. In that aim, the technology of chemical micropatterning has been developed almost two decades ago [116] and a numerous of biological results have been obtained through this approach [117], mostly at the individual cell level. At a larger scale, microfluidics has proved to be a powerful method to achieve cell compartmentalization through topographical confinement, from bacteria [118] to stem cells [119]. Some examples of these technologies are developed below.

3.2.1 Shaping single cell: micropatterning

The micropatterning of cells, or the application of microelectronic technologies to constrain cell morphologies into well controlled shapes, has grown in popularity in the last decade, from the first paper on cell shape control [120] to the development of a wide variety of cell micropatterning [116, 121, 122], as extensively described in [123]. In few words, it is the expertise to draw micro-drawings of chosen geometries on a substrate, e.g. pre-treated glass coverslips, with adhesive molecules, while other parts of this substrate are repelling. A wide range of shapes can be adopted by cells as illustrated in **Figure 1.30**. Micropatterning recapitulates *in vitro* conditions such as geometry [121], architec-

ture [126], composition [127], mechanisms [128] or dynamics [129] and allow us to study, in a more controlled way, phenomena such as cellular differentiation, migration or polarization, to cite a few.

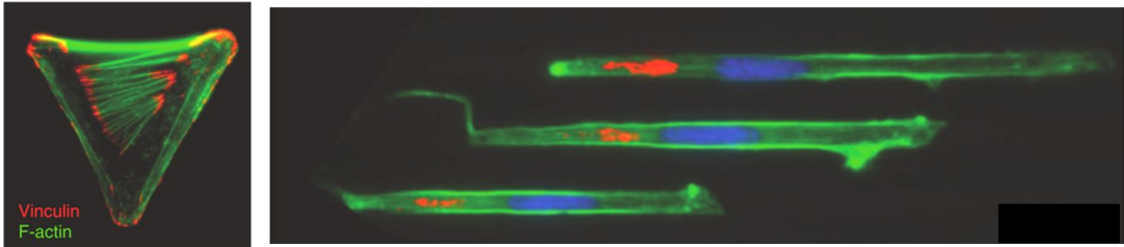


Figure 1.30 – *Examples of micropatterned cells. Left: A "V" shape micropattern with straight edges can promote the assembly of stress fibres. Right: Micropatterning can allow us to mimic cell migration in situ using for example line patterns of different widths. [117, 124, 125]*

This technology was adapted more than one decade ago to constrain neuronal cell bodies and directed the growth of neuronal connection. One of the first extensive study of *in vitro* organized networks was performed by Wyart et al. [112], and one example of the neuronal architecture obtained in this study is displayed in **Figure 1.31**. Big square areas were implemented for the adhesion of cell bodies and 2-4 μ m wide stripes to guide neurite growth. However, the symmetrical design of chemical patterns did not allow to specify the localization of axons, and therefore to implement directional connectivity. This has been the subject of further studies playing with different elements such as discontinuous lines [130, 131]. In the group of Catherine Villard, we demonstrated high control of axo-dendritic polarity by using differential curvatures and cell body constraints [132, 133] or more recently changes in stripe width [134]. This last point will be detailed in **Chapter 2**.

3.2.2 Guiding axons

Due to the extensively branched neuronal morphologies, the association between neurons and microfluidics has proved to be a powerful tool to control the connectivity between neuronal populations. Microfluidics is the use of microfabricated devices, in most of the case made in Polydimethylsiloxane (PDMS) - a biocompatible and transparent silicon-based organic polymer – that include microchannels to control flows at the micro scale. Microfluidics is especially known for the miniaturization of processes to manipulate reduced amount of liquid and reagents within lab on chips devices, and more recently for the possibility to build organ-on-chips by providing controlled cellular microenvironments [135, 136].

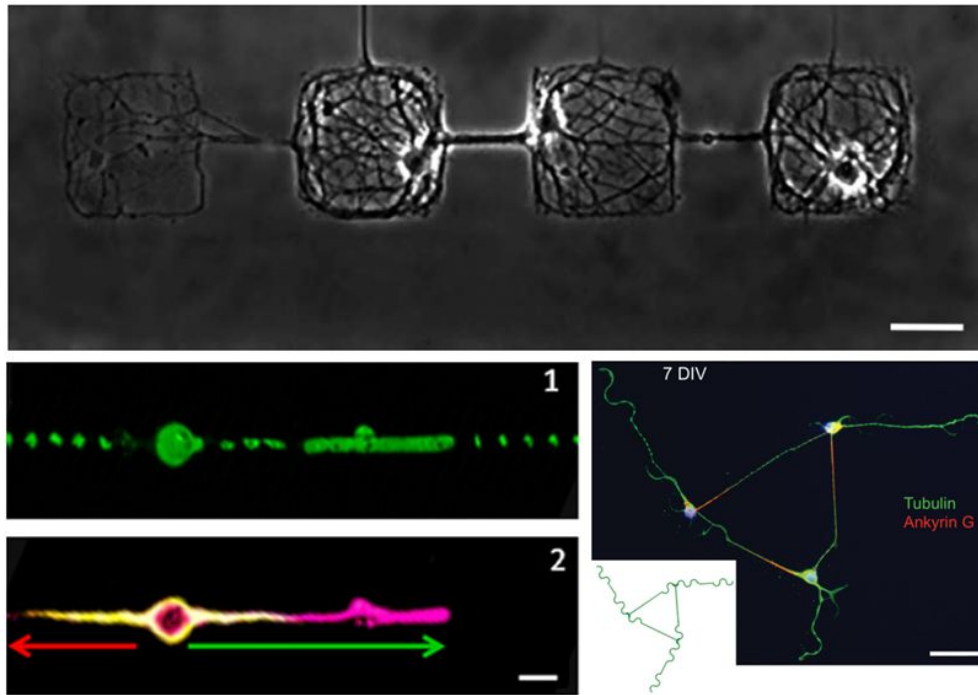


Figure 1.31 – *Micropatterning on neurons. Top: Image of neural networks of controlled architecture in a linear network. Cell bodies of neurons are restricted to squares or disks of $80\ \mu\text{m}$ and neurites to lines ($80\ \mu\text{m}$ length, $2\text{--}4\ \mu\text{m}$ wide). Scale bar: $50\ \mu\text{m}$ [112]. Bottom left: Immunolabeling of neurons at DIV3 with MAP2 (yellow) and Tau-1 (pink) antibody. (1) FITC-PLL showing the pattern composed of discontinuous lines. (2) Neurons adhered onto the nodes and neurites grew out mostly along the pattern, forming bipolar neurons. The MAP2-TAU-1 immunostained neurons were used to determine the length of the neurites grown on the positive side (green arrow) and on the negative side (red arrow) of the gradient. Tau-1 positive neurites are the axons. Scale bar: $10\ \mu\text{m}$ [131]. Bottom right: Triangular looped circuit made of three connected neurons at DIV7. Microtubules (anti-tyrosinated tubulin, green) and axon initial segment (anti-ankyrinG, red) labellings are superimposed on nuclei staining (Hoechst, blue). Note that neurites often cut through the curved lines of the pattern, a feature resulting from neuritic tension during development. Inset: the poly-L-lysine adhesion pattern (in green). Scale bar: $50\ \mu\text{m}$ [133].*

Concerning neurons, PDMS wells were used to seed neuronal populations connected through microfluidic channels acting as guidance structures for axons (usually bundles of axons) connecting the different chambers [137–144]. Following the seminal work of Taylor [137], unidirectional connectivity were implemented using the concept of axon diode, built from tapered channels that promote preferential axonal growth from the larger to the smaller channel opening [138]. More recently, our group has successfully used a mesh of straight and curved microchannels to achieve such unidirectional connectivity [141], as presented in **Figure 1.32**. This technology can also be combined with flow changes [142],

molecular gradients [143] as well as AC electrokinetics forces [144] to guide axons in several ways.

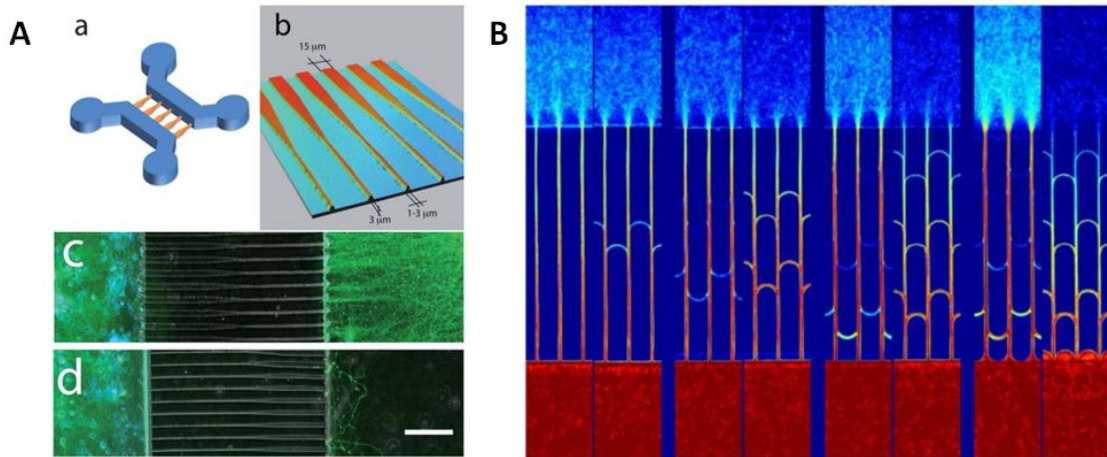


Figure 1.32 – **A:** *In vitro* reconstruction of a neuronal network using "axonal diodes" in microfluidic culture devices. **(a)** Global 3D view of the microfluidic device comprising asymmetrical microchannels **(b)** 3D view of the funnel-shaped micro-channels as observed by white-light optical profiling (WLOP) with an interference microscope. Immunofluorescent images of microfluidic cultures (green: α -tubulin, blue: Hoechst) in which cortical neurons were seeded either on the wide **(c)**, 15 mm) or the narrow **(d)**, 3 mm) side, at a concentration of $45 \cdot 10^6$ cells per ml. Note the lack of labeling in the wide chamber when cortical neurons are seeded in the narrow side **(d)**. Scale bar 50 μm [138]. **B:** Direction selectivity of arches, both sides seeded. The image shows the average intensity maps of axons in the different designs (log scale). This original architecture promotes unidirectional axonal guidance by selectively rerouting with arches axons growing in the unwanted direction. Experiment realized after 8 DIV [141].

3.3 Measuring cell shapes: toward 3D imaging

To look at the morphological changes of neurites in 3D would be of great interest to add more knowledge about relations between morphologies and functions throughout neuronal life, both in physiological and pathological conditions.

Cell volume can be defined as the sum of the cell dry part - the different organelles, lipidic membranes and all kinds of insoluble organic molecules like the proteins of the cytoskeleton - and its liquid part - mainly cytoplasmic. Volume changes accompany phenomena such as cell division [145, 146], cell death [147, 148] and seem to go along with growth and polarization mechanisms in nerve cells (cf **Part 2**). To look at total volume and dry mass separately is interesting since they do not evolve necessarily in concert [145].

Considering the micrometer size of cells and possible nanometric variations, accurate methods have to be chosen.

To measure volume in a simple way, conventional light microscopy can be used, but it is possible mainly on suspended cells [149]. In this specific case, the evaluation of the volume could be indeed easily deduced from the cell diameter considering that floating cells display spherical shapes. Z-stacks with confocal microscopy are also commonly used [150, 151], but the 3D reconstruction implies repeated exposures to excitation light and is therefore time consuming and not suitable for experiments over long time periods. Moreover, the accuracy is limited by the depth of focus at best, which is around 0.8 microns for highest NA objectives. The z-stack steps may thus not be sufficient for the observation of neurites. To achieve better resolution, scanning probe microscopy such as Atomic Force Microscopy (AFM) could be used [61, 152–154]. With AFM we can obtain a very high spatial resolution but it is a contact scanning method, difficult to implement with living cells in their liquid environment and not compatible to follow the dynamical changes of a high number cells with time. Another scanning probe microscopy is the scanning ion conductance microscopy (SICM) [155], but it requires sophisticated and dedicated equipment and is also too slow to follow dynamical changes. Other precise techniques exist but are limited to cells in suspension, such as the coulter counter which is a high throughput technique based on impedance, giving volume independently of cell shape [156–158], or the suspended microchannel resonator which gives cell mass, density and volume [146, 159].

To study neuronal processes, which are submicrometric objects in mammals, suitable methods should be found. Nowadays, the changes of neurites volume in response to external stress is still a poorly studied area. Mainly AFM or custom-made interferometric methods were chosen, providing interesting although limited data [61, 153, 154, 160].

We chose for our study to adapt two methods: the Digital Holographic Microscope (DHM), a commercial interferometric method giving us access to the dry mass and possibly to refractive index and volume; and the Fluorescent eXclusion method (FXm), allowing us to measure directly cell volume. Both methods are presented in the following sections.

3.3.1 Digital Holographic Microscope (DHM)

Cells are mostly micrometric transparent objects. To study cells morphology, in particular versus time and with a good and quantitative resolution, required the development of adapted optical microscopy tools and challenging methods. As cells differ only slightly from their surroundings in terms of optical properties, techniques enhancing these tiny

differences were developed, including Phase Contrast (PhC) or Differential Interference Contrast (DIC) which are the most widely used. In contrast to fluorescence techniques that need to modify the cells by introducing fluorophores (using immunostaining or genetic modifications), PhC and DIC allow the visualization of transparent objects by making visible the fine subcellular structural organization without using any staining contrast agents. This is particularly useful to observe neuronal extensions since they are completely invisible when observed with bright field (BF), as shown in **Figure 1.33**.

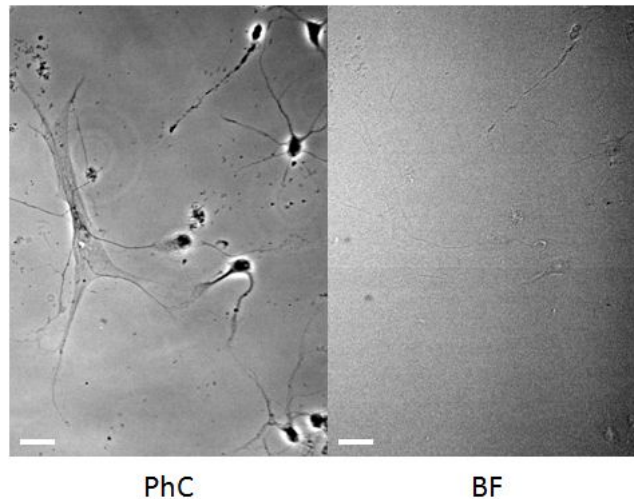


Figure 1.33 – *From left to right: PhC and BF microscope images of the same zone containing fixed neurons and glial cells. Only on the phase image neurons and glial cells details are apparent. Images were taken with a 20X objective. Scale bars: 20 μ m.*

However PhC and DIC do not allow quantitative measurement of phase shift or optical path length (OPL), whereas interference microscopy allows quantitative reconstruction of the OPL. Since the application of quantitative phase measurements with interference microscopy to cell imaging in the fifties [161], few studies have used this method [162]. This is mostly due to the need of sophisticated and delicate optical systems minimizing sources of noise to resolve small phase shifts. Nonetheless, more and more user-friendly systems are developed and are slowly spreading in life science. One of those systems, based on holography techniques developed in 1948 by Gabor [163], is the Digital Holographic Microscope (DHM).

The DHM is a commercial microscope developed by LynceeTec company in EPFL and recently acquired by the Néel Institute. It is basically a Mach-Zehnder interferometer [164]: a laser beam is divided in two using a beam splitter, one is the reference beam whereas the other goes through the sample before interfering with the reference one afterwards. Their interferences create a hologram collected by a CMOS camera and intensity and phase images are further computed. **Figure 1.34** displays the optical paths within the

DHM as well as a comparison between a hologram image and a PhC image on the same sample. In addition to get quantitative phase values, the DHM gets rid of the well-known optical artifacts that suffers PhC microscopy, namely the halo and shading-off effects, which makes the intensity modulation at any pixel not directly proportional to the phase change generated by the corresponding area of the cell.

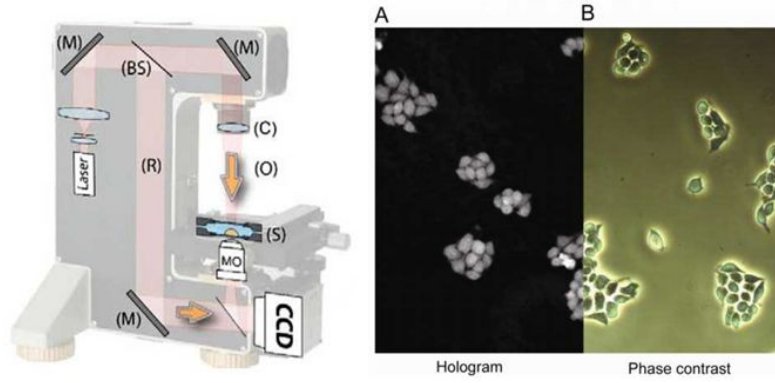


Figure 1.34 – **Left:** Basic configuration for digital holographic microscopy (DHM). A laser diode produces the coherent light ($\lambda=683\text{ nm}$) which is divided by a beam splitter (BS). The specimen (S) is illuminated by one beam through a condenser. The microscope objective (MO) collects the transmitted light and forms the object wave (O) which interferes with a reference beam (R) to produce the hologram recorded by the CMOS camera. The sample is mounted in a chamber used for recording [165]. **Right:** A cell culture captured using digital holographic microscopy (A) and phase contrast microscopy (B). The cells are BN7005-H1D2 mouse fibroblasts which are approximately $20\mu\text{m}$ in diameter. [166]

Theoretically, the phase measured at each pixels, φ_i , is proportional to the OPL, which is the sum of the thickness of the different objects the laser encounters along its path times their refractive indexes. In our system the formula below [164] can be applied:

$$\varphi_i = \frac{2\pi}{\lambda} \text{OPL} = \frac{2\pi}{\lambda} \left[\int_0^{h_i} n_{c,i}(z) dz + n_m(D - h_i) \right] = \frac{2\pi}{\lambda} [(\bar{n}_{c,i} - n_m)h_i + n_m D]$$

where $\lambda = 664.8\text{ nm}$ is the wavelength of a linearly polarized helium-neon laser; $\bar{n}_{c,i} = 1/h_i \int_0^{h_i} n_{c,i}(z) dz$ the intracellular mean refractive index along cellular thickness; n_m the refractive index of the surrounding medium and D its thickness.

Phase measurements can allow us to obtain the dry mass, as described in [167] and detailed in **Chapter 3**. In addition, measuring the cell refractive index (RI) would allow us to obtain the cell volume. This approach is known as the Decoupling Procedure (DP) and will also be detailed in **Chapter 3**.

With the DHM, researchers had been able to measure volume variations of micrometric objects such as erythrocytes (red blood cells (RBC)) [165, 168] as shown in **Figure 1.35**.

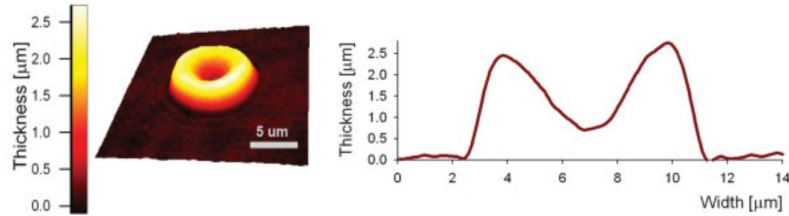


Figure 1.35 – **Left:** Pseudo 3D representation of the cell thickness of an erythrocyte (raw image). **Right:** Thickness profile obtained in central cross-section of the cell. [168]

In the field of neuroscience, issues such as multiple-site optical recording of neuronal activity or noninvasive visualization of dendritic spine dynamics could be studied with this method. This was addressed in [160, 164, 169], where whole cells phase, local RI measurements on soma or RI difference on dendrites were performed, giving some insights into neuronal detailed structure and volume as shown in **Figure 1.36**. Nonetheless data were acquired on a few cells, and focused mainly on the soma or proximal parts of the neurites, stressing the difficulty to image small objects as neurites. Moreover the conversion from phase to volume was performed assuming that the cell body refractive index was the same as the neurite refractive index, which is questionable regarding the very different sub-cellular structure and composition of both compartments.

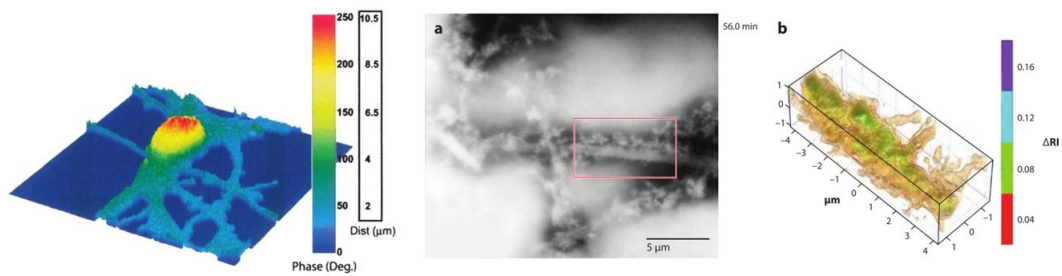


Figure 1.36 – **Left:** Phase map of one neuron, converted to height map with an assumed constant refractive index of 1.375 [164]. **Right:** (a) Superresolved phase image of a dendrite section obtained by synthetic aperture quantitative phase image. (b) 3D representation of the tomographic image of an 8-μm-long section (see inset of panel a). It shows the body of the dendrite section with the details of protruding dendritic spines. Scale is in μm and the color code represents the difference in refractive index (from 0.04 (red) to 0.16 (violet)) between the dendrite and the extracellular medium. [166]

3.3.2 Fluorescence eXclusion method (FXm)

The FXm was first proposed by Gray et al. [170] in 1983 and more recently developed by Verkhovsky and co-workers to study migrating cells [171,172] and Piel and co-workers to study cell mitosis [145]. It is based on the measurement of the fluorescence of the medium surrounding the cell in a chamber of controlled height. The cell is then revealed by excluding the fluorescence and thanks to a calibration object near the cell characterized by a well-known height, the cell height can be easily calculated. The principle of this method is illustrated in **Figure 1.37**. Compared to the use of fluorescence labeling of the cell itself, the use of an external fluorescent medium avoids toxicity issues. Let us note that one of the major drawback of the exclusion method is the possible internalization of the external fluorescent dye, dependant both on the cell type and on the chosen dye.

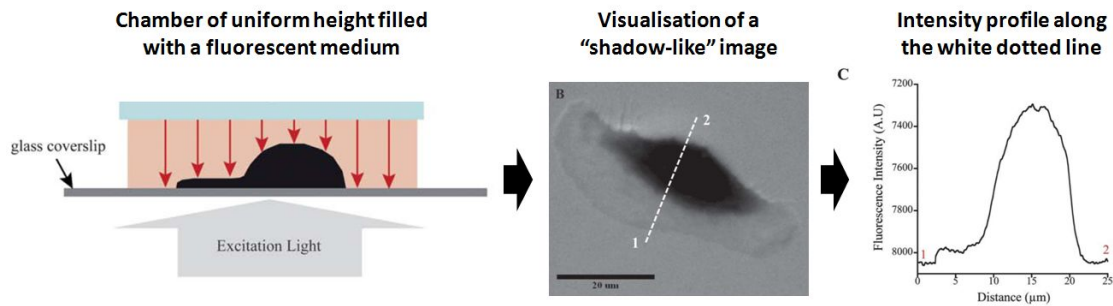


Figure 1.37 – Principle of the fluorescence displacement method for volume measurement. (A) Schematic view of the setup made of a chamber of uniform height containing a migrating cell (not drawn to scale). The chamber is filled with medium containing a fluorescent dye and illuminated with an epifluorescence setup. (B) Fluorescence image of a migrating fish epidermal keratocyte (observed with a 100X lens). This setup generates "shadow-like" images where the decrease in fluorescence intensity is related to the cell height. (C) Fluorescence intensity profile (shown inverted) along the white dotted line in (B), where the lamellipodium (distances between ~ 2.5 and $8\mu\text{m}$) and the cell body (distances between ~ 8 and $23\mu\text{m}$) can be identified. Bar: $20\mu\text{m}$. Adapted from [171].

The linear relationship between the fluorescence intensity and the space filled with the dye is:

$$I_i = \alpha \cdot h_i + I_0$$

with I the measured intensity; h the height of the cell and α the coefficient calculated thanks to the measurement of the calibration object intensity I_0 and of background intensity which is the fluorescence value where there is no object.

FXm, contrarily to interferometric methods, allows a direct visualization of the cell volume without the acquisition of intermediate variables like the optical phase and the

refractive index. All we need is a well characterized reference object. Resolutions down to the submicrometric scale to visualize objects such as lamellipodia, are reachable with optimized measurement chambers and optical parameters. Moreover, real time measurements on long periods allowed the observation of cellular events such as mitosis. These examples are illustrated in **Figure 1.38**. To highlight morphological variations expressed by micrometric neuronal processes, at the static and at the dynamic level, we adapted the FXm technique. This will be at the center of the **Chapter 4**.

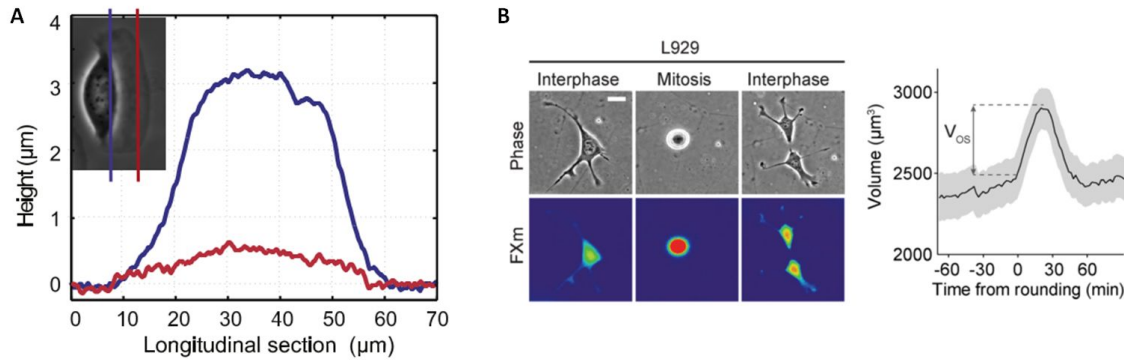


Figure 1.38 – **A:** Lamellipodia height longitudinal profiles taken along the lines shown in the inset [172]. **B:** Phase and FXm images of a L929 cell, and mean volume of fibroblastic L929 cells undergoing mitosis ($n = 38$) [145]

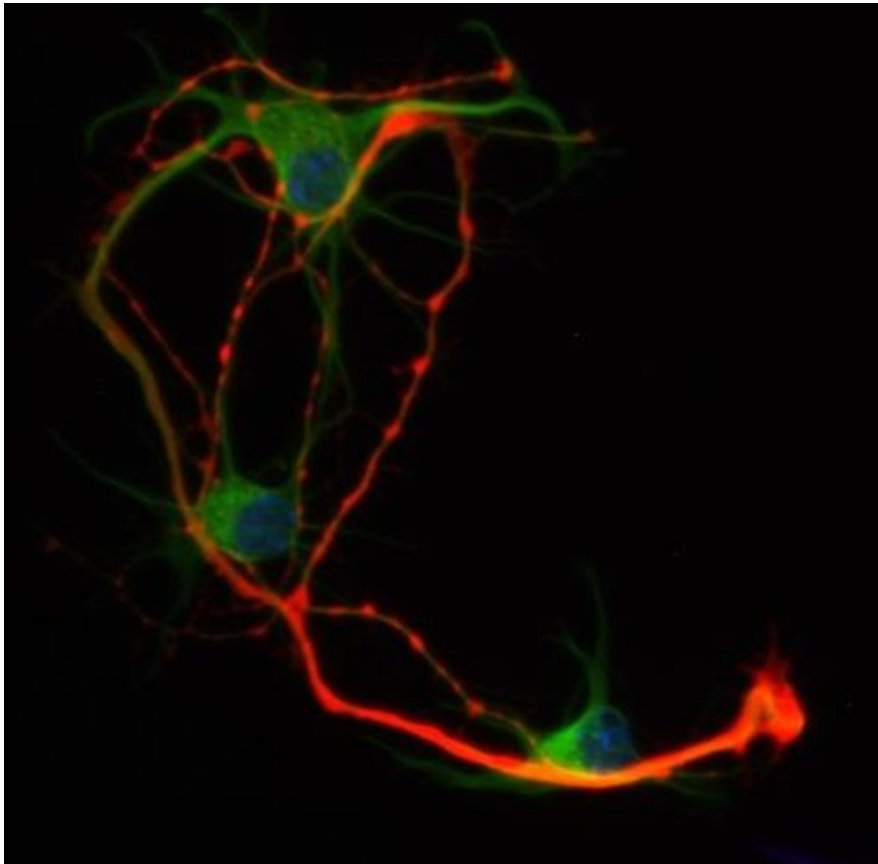
3.4 Context and objective of this thesis

Because both osmolarity regulation and electrical excitability depends on ionic gradients across the plasma membrane, neurons seem more vulnerable to volume changes than most of the cells. All along its life a neuron regulates its morphology, either at the global or the local level. Studying neuronal volume at the resolution of neuronal processes during live experiments would be a great progress, as previous experiments were restricted on soma or on non-mammal (i.e. relatively larger) neuronal processes. Notably it would be interesting to investigate volume changes during neuron growth, e.g. with the actin waves impact, or the polarization, e.g. to investigate further particularities of axons and dendrites. Moreover studying the neuron as a single cell with controlled shapes would be a great system to highlight mechanisms and internal organization as well as volume changes. Shape control and precise volume measurement would open new possibilities in neuropathologies studies, from the observation of mechanisms inducing morphological changes to electrical firing rate disruption or internal atypical reorganization. The biophysical tools developed during this Phd thesis aimed at these goals and results on neuronal growth and polarization were obtained, as presented in the next chapters.

In this thesis, the main problematics I would like to address are:

- How are the different parameters controlling the size of neurites (height, length ..) regulated during neurites growth ? Same question for microtubules density and neurite dry mass.
- Can we control precisely axonal polarization by shaping neurons using micropatterns of adhesion ?
- What is the volume of actin waves, and how this volume evolves during the propagation of the waves ?

CONSTRAINING NEURONAL SHAPE IN 2D



Heart balloon neuron.

C. Braïni and Muireann (high school student), Néel Institute.

1 Introduction

This expertise of neuron shape control in Catherine Villard’s team started in Grenoble, in the Institut Néel, where micro and nanotechnologies are highly employed. Throughout three Ph.D projects [173–175], protocols to apply micropatterning to neurons were improved and optimal designs were produced. In addition, the different institutes where I have conducted my work (i.e. the Néel, Curie and Pierre Gilles de Gennes Institutes) offering slightly different tools, I was led to adapt these protocols to different environments. I will first present these protocols in the next section. Then I will present the results I obtained related to neuronal growth, polarization and the presence and concentration of microtubule associated proteins (MAPs) as a function of neuronal shapes using each time dedicated micropatterns.

2 Methods

2.1 Micropatterning

Different steps are involved in the fabrication of chemical micropatterns on glass substrates. The whole protocol starts with a silanization step followed by photolithography and finally surface functionalization with adhesive molecules. These steps will be detailed below.

2.1.1 Silanization

Silanization of glass coverslips is performed in order to tune the glass surface hydrophobicity, in order to be high enough to prevent cell adhesion, and low enough to facilitate the subsequent step of photoresist spreading.

First, an oxidation step is performed with an O_2 plasma, cleaning the surface and forming free O^- and OH^- radicals and increasing silane binding. The silanisation is conducted right after the plasma. Silanization consists in forming a monolayer of amphiphilic molecules called silanes whose generic formula is $R - (CH_2)_n - Si(X)_3$, where R is a hydrophobic group, X is a hydrolyzable group and n defines the length of the carbon chain tuning the hydrophobicity of the silane.

Experimentally, depending on the equipment, three different silanization methods were used within the project and gave similar results:

Bind-Silane¹: a drop of Bind-Silane is spread on the glass cover slips after washing them with ethanol and dried. Thereafter, cover slips are incubated at room temperature (RT) for a few minutes and then finally wiped.

APTES²: APTES is a silane less sensitive to light and less reactive to humidity than other silanes. It presents the great advantage to be part of an automated vapor-phase set-up at the Néel Institute which can automatically perform plasma step and silanization.

AB 109004³: This silane is deposited on samples using a vapor phase process. About 100 μ l of silane is first put into a little container within the vacuum chamber. This chamber is then pumped for about 20 min before removing samples. This method is the current method used at IPGG.

This three different silanes structure are summarized in **Figure 2.1 A**, while the process steps are summarized in **Figure 2.1 B**.

After this covalent linkage of the silane to the coverslip, samples are ready for the photolithography step.

2.1.2 Photolithography

The objective of this step is to prepare a photoresist stencil on the coverslip in order to protect the areas that have to remain hydrophobic and to select the complementary zones that are intended to be covered by the adhesive molecules later in the process. The most critical part of this process is the design of masks optimized for neuronal cultures. This point will be developed below, followed by a description of the fabrication of the photoresist stencil. Note that all steps are performed within a clean room and protected from natural UV light.

Typical patterns are composed of circles of 15 μ m diameter dedicated to soma adhesion and lines between 2 and 6 μ m to allow neurites growth. The diameter of the circles was optimized as 15 μ m from previous studies within our group. In particular, if the diameter of the circle is bigger, neurites would tend to grow without control within the adhesive spot, limiting the control on the neurites width and number. On the other hand, if the circle is smaller, soma excessive shrinkage would lead to neuronal death. To have a good probability of obtaining isolated neurons, circles are dispatched along connecting lines. Moreover, for the simplest patterns consisting of stripes intercalated or not with disks, a distance of 100 μ m is set between parallel stripes. This value maximizes the number of cells on a coverslip while preventing neurites to cross the non-adhesive gap between lines.

1. 3-methacryloxypropyl-trimethoxysilane: (C₄H₅O₂)-(CH₂)₃-Si(OCH₃)₃, Fischer Scientific
 2. 3-Aminopropyltriethoxysilane: NH₂-(CH₂)₃-Si(OCH₂CH₃)₃, Sigma-aldrich
 3. 3-Methacryloxypropyltrichlorosilane: (C₄H₅O₂)-(CH₂)₃-Si(Cl)₃, Silane AB 109004

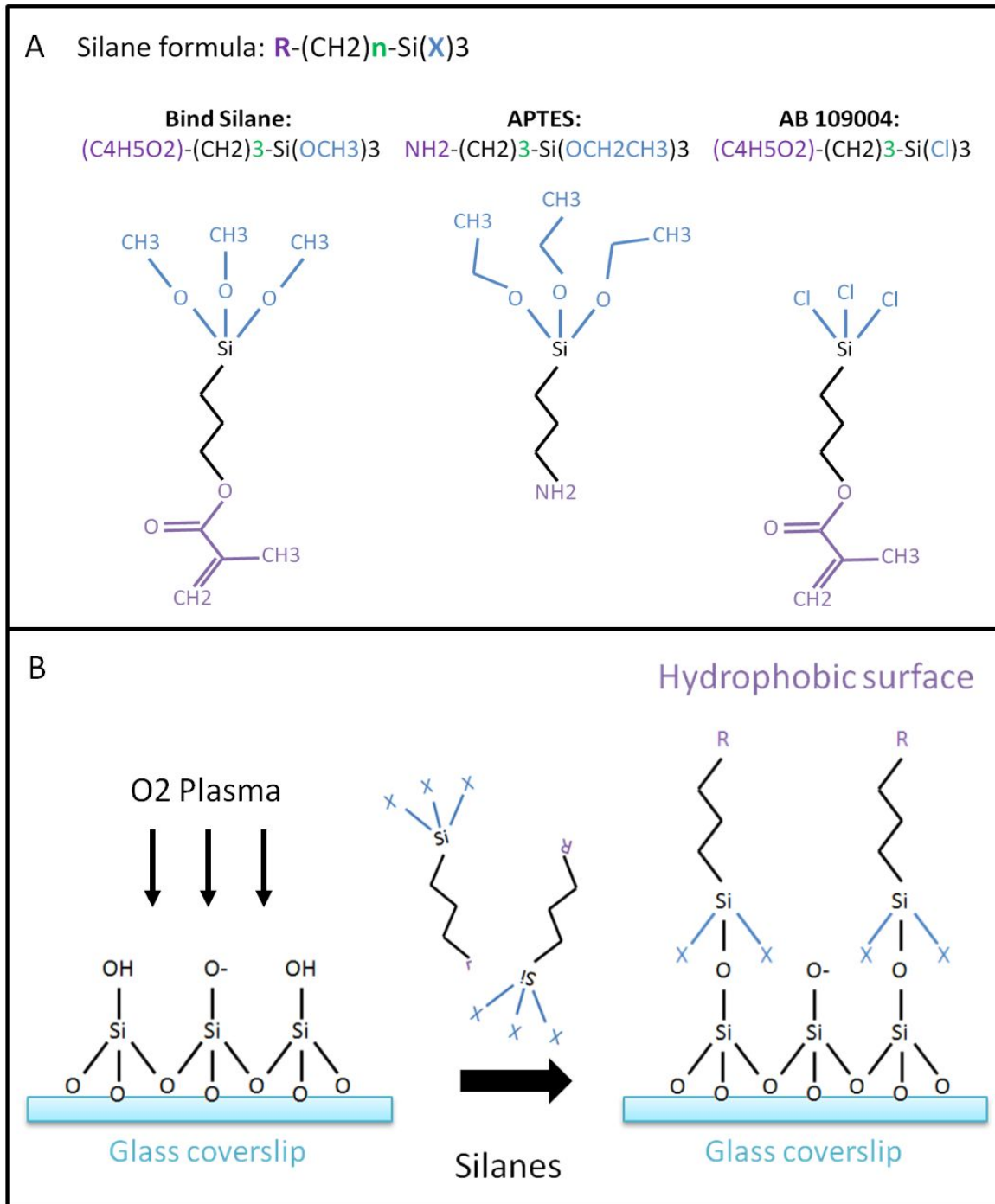


Figure 2.1 – (A) Silane formula and the different silanes used. From left to right: Bind Silane, APTES and AB 109004. Even if hydrophobic (R, purple) and hydrolyzable (X, blue) groups change, the number of CH₂ groups defining the hydrophobicity of the silane remains the same (n=3, green). (B) Steps of silanization. O₂ plasma oxidation, forming free O⁻ and OH⁻ radicals, is followed by silane deposition. A final phase of hydrolysis binds the silane molecules to the glass coverslip.

Patterned areas are systematically surrounded by non-patterned areas allowing neurons to grow unconstrained which has been observed to help patterned neurons to survive. Moreover, when different patterns are designed to coexist on a single glass coverslip, there are dispatched in different sub-zones of different orientations to be able to identify patterns after neuronal seeding. An example of patterns is displayed in **Figure 2.2**.

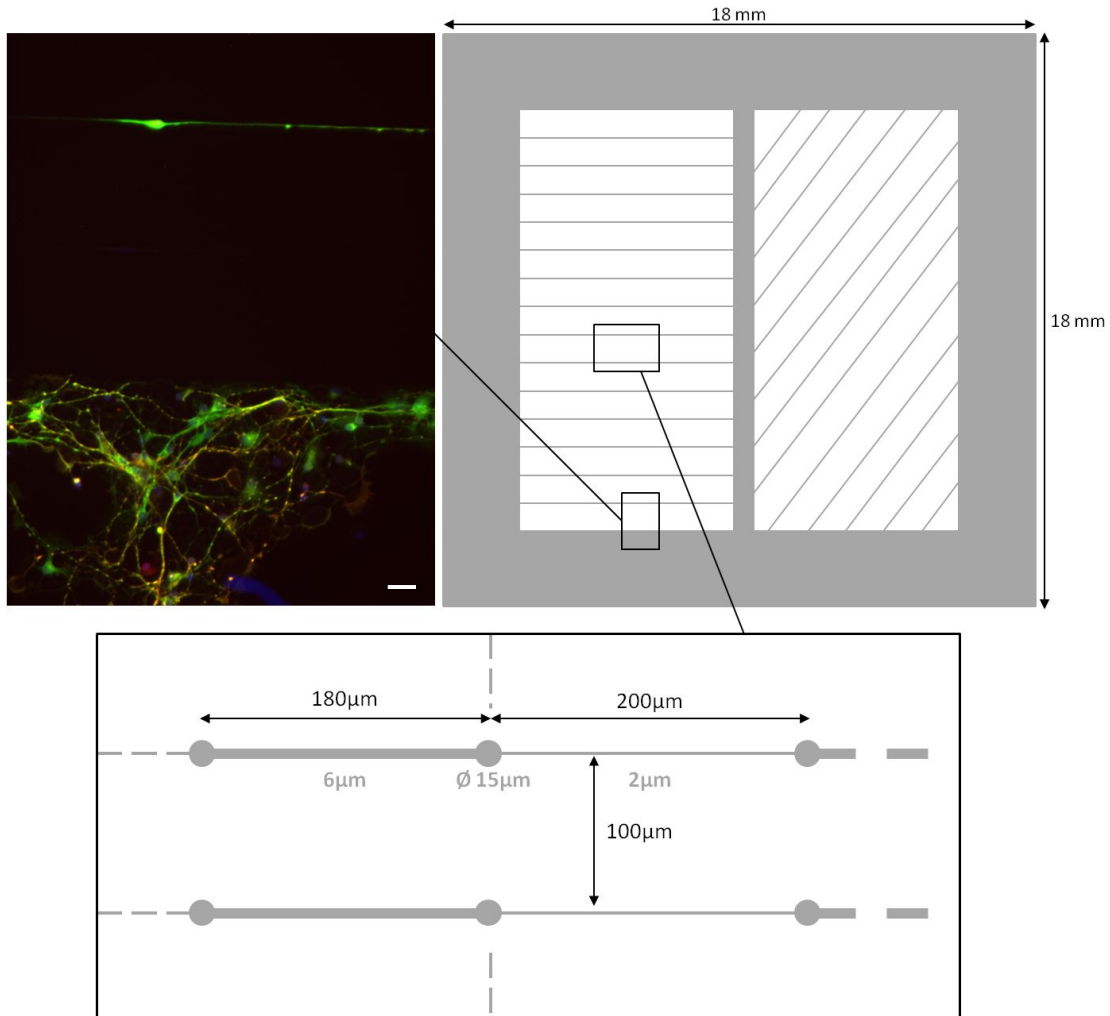


Figure 2.2 – Example of a typical mask design with two subzones of different orientations and non-patterned zones. Grey parts represent adhesive area. Typical dimensions are displayed in the inset. A second inset shows a fluorescence image at the frontier between non-patterned and patterned neurons (left). Scale bar: $20\mu\text{m}$.

The entire pattern is designed to fit into the dimensions of commercial standard coverslips. We used square (18mm and 24mm) and circular coverslips (25mm diameter).

The positive photosensitive resist (S1805 from Shipley) is spincoated on the silanized coverslips with an acceleration of 4000rpm/s and a speed of 4000rpm during 30s, producing a resist layer of $0.5\mu\text{m}$. After annealing it at 115°C during 1min, it is exposed under

UV light through the chosen chrome mask and developed, as summarized in **Figure 2.3**.

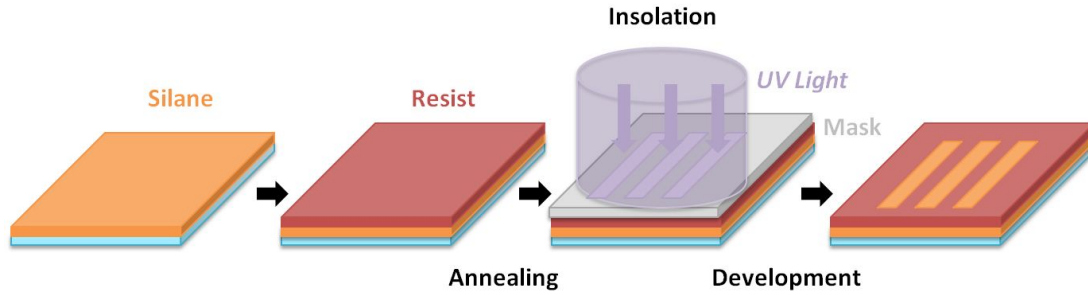


Figure 2.3 – *Steps of the photolithography process.* From left to right: spinning of the photoresist layer and annealing, exposition to ultraviolet (UV) light through a chrome mask, photoresist development to dissolve the exposed regions of the photoresist layer (positive photoresist) followed by a washing step in deionized (DI) water. Light blue: glass coverslip. Orange: silane. Red: photoresist. Grey: chromed regions of the mask.

The UV dose energy E needed for S1805 is about $50\text{-}60 \text{ mJ}\cdot\text{cm}^{-2}$. Exposure time t is calculated after measuring the lamp power P through the equation:

$$t = \frac{E}{P}$$

In the IPGG clean room where exposures are done using a MJB4 mask aligner (Suss Microtec) and a wavelength of 435 nm (G-line), the typical exposure time is 5s.

The exposed areas of the photoresist are then dissolved within a developer. During my Ph.D project, according to location and availability, three different developers were used and worked with a similar effect. Their parameters are summarized in the **Table 2.1**.

Developer name	Dilution and time
Microposit Developer Concentrate (Chimie Tech Services)	1:2 in DI water - during 1min
Megaposit MF-26A (Shipley)	no dilution - during 1min
Microposit 351 Developer (Shipley)	1:5 in DI water - during 50sec

Table 2.1 – *The different developers names and parameters that can be used to develop the S1805 positive photoresist.*

2.1.3 Surface functionalization

In order to adhere cells on the substrate, the photoresist stencil is incubated into an aqueous solution of polycations, in our case Poly-Ornithine (PLO) at a concentration of $80\mu\text{g}/\text{ml}$. After rinsing coverslips in PBS to discard the PLO extra, the resist is removed by immersion in a pure ethanol ultrasonic bath during 1min and 30sec (lift-off). These

coverslips are then rinsed two times with PBS and let in Petri dishes filled with PBS, which will be replaced by the adequate medium before cell seeding. All these steps are summarized in **Figure 2.4**.

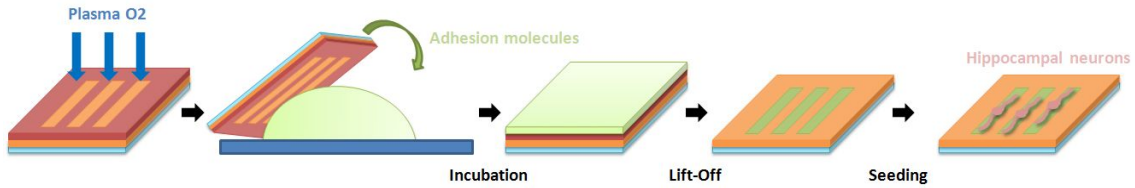


Figure 2.4 – *Surface functionalization with adhesive molecules. From left to right: Surface activation by O₂ plasma. Incubation of the coverslip on a drop of PLO overnight (O/N) at room temperature (RT). Lift-off in a pure ethanol ultrasonic bath in order to remove the photoresist. Seeding of cells which will adhere only on adhesive molecules, adopting the pattern shape.*

2.2 Cell culture

We use primary cells directly extracted from hippocampus of mice embryo of 17 to 19 days in utero (E17-19). One hippocampus usually provides about 0.3 – 0.7 million neurons. Steps of dissection are detailed in **Figure 2.5**.

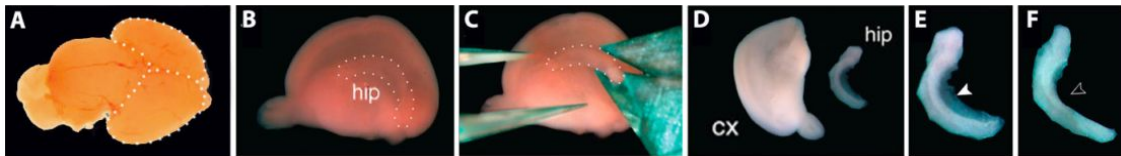


Figure 2.5 – *Dissection of hippocampus and cortex from mouse embryonic brains. A) Fetal mouse brain. Left and right hemispheres of the cerebral cortex are delimited by the dashed white line (external view). B) Right hemisphere (inner view) and the olfactory bulb. Hippocampus ("hip") is delimited by the dashed white line. Meninges surrounding each hemisphere are removed. C) The hippocampus is removed with a microscissor. D) Cortex ("cx") and hippocampus ("hip") are separated. E, F) The fimbriae (arrowhead) on the concave side of the hippocampus are removed (open arrowhead). Adapted from [176].*

After this surgical step, tissues are placed in a falcon tube containing trypsin (0.3ml of trypsin⁴ into 2.7ml of HH medium⁵) during 10 minutes at 37°C in order to initiate a chemical dissociation. Tissues are then rinsed 3 times in HH, to remove and stop trypsin effect, and the mechanical dissociation is done with a micropipette tip in 1mL of plating medium. A few µl of this solution is used to count cells - typically 10µl diluted in 50µl. Usually, to get isolated cells after 1 to 3 days in vitro (DIV), we plate 30 000 cells per glass coverslips for later fixation (2 DIV or 3 DIV) and 40 000 cells per glass coverslips for timelapse experiment beginning at 1 DIV. By optimizing the neuron seeding density for each type of patterns, we in general get a few tens of isolated neurons properly placed (i.e. with the soma placed on the adhesive disks, if present) per coverslip.

Neurons are incubated in a Plating medium, MEMc, during 3 hours after their seeding, then this medium is replaced by a maintenance medium, NBc, containing Neurobasal, more suited for neurons. Interestingly, NBc is characterized by a lower osmolality than MEMc. The composition of these media is detailed in **Table 2.2**. Note that all this work is done in a sterile environment provided by a laminar flow hood and that cells are kept in an incubator with an adapted and controlled environment (37°C, 5% CO₂).

Plating Medium: MEMc [50ml]	Maintenance Medium: NBc [50ml]
Horse Serum (HS): 10% [5ml]	B27 50x: 2% [1ml]
Glutamax 200mM: 1% [500µl]	Glutamax 200mM: 1% [500µl]
Sodium Pyruvate GIBCO 100mM (NaP): 1% [500µl]	Peni-Strept (PS/ATB): 0.05% [25µl]
Penicillin-Streptavidin (PS/ATB): 0.05% [25µl]	Neurobasal (NB): 96.95% [up to 50ml]
Minimum Essential Medium (MEM): 88.95% [up to 50ml]	

Table 2.2 – *Plating and Maintenance media, MEMc and NBc respectively. The "c" stands for "complete", when all the elements to build the medium are added to Minimum Essential Medium (MEM) or Neurobasal (NB) medium respectively. All these components are mixed and filtered.*

A low concentration of antibiotics is added to limit the risks of contamination. The advantage of Penicillin-Streptavidin (PS, Penicillin acting on Gram + bacteria and Streptavidin on Gram – bacteria) is its non-penetration inside mammal cells, but it is instable in cell culture medium. In the later work PS was replaced by gentamicin at 0.2% (100µl in 50ml). Gentamicin is more active and stable and is acting on both Gram + and Gram - bacteria. Experimentally, we observed less contamination with gentamicin and no difference in neurons survival.

4. 2.5%, w/o EDTA

5. HH medium: 44mL DI water, 5ml HBSS (GIBCO Hank's Balanced Salt Solution, Thermo Fisher Scientific), 1ml GIBCO HEPES (1M) (Thermo Fisher Scientific).

2.3 Fixation and immunofluorescence

Neurons on patterns are fixed on a selected day and labeled using immunofluorescence protocol. Immunofluorescence labeling consists in targeting a protein of interest, the antigen, based on specific antibodies.

Two antibodies are used, the primary antibody (AB I) which will target very specifically the protein of interest in the cell, and the secondary antibody (AB II), less specific, which will target the AB I according to species. Both antibodies are obtained in chosen species. The AB II has the particularity to have a fluorochrome attached on it. Though, some antibodies are both fluorescently labeled and specifically targeting a designed protein. In these special cases only a single step of immunostaining is needed.

Experimentally, glass coverslips with neurons are first quickly rinsed with PBS at 37°C, then fixed with paraformaldehyde (PFA) diluted at 4% in PBS, during 15 to 20 min, and finally rinsed three times with PBS. Cells are permeabilized with Triton X100 in order to allow antibodies to access the cytoplasm. To get high antibodies specificity, a blocking step has to be performed using Bovine Serum Albumine (BSA). This two process are done simultaneously by mixing BSA at 2% and Triton at 0.25% in PBS and incubating coverslips with this mix during 15 to 30 min, followed by a rinsing step with PBS. Then antibodies are diluted in a PBS/BSA 2% mix at the optimal dilutions summarized on the table below. Incubation of the primary antibody lasts for 1h at RT, but can also be done overnight (O/N). Incubation of the secondary antibody lasts 45min, with a cover to protect fluorophores from light. Usually a last incubation with Hoechst in order to label the nucleus is done during 5min. Between each incubation step, samples are rinsed two times in a PBS/Triton 0.1% mix during a few minutes. The last rinsing is done first in PBS, then in DI water, before mounting the coverslip using Mowiol Mounting Medium (Sigma) on a glass slide. The different antibodies used are summarized in **Table 2.3**.

Antibody I				
Target molecule	Target localization	Host animal	Dilution	Reference
β III-tubulin	Neurons Microtubules	Mouse	1:300	Millipore MAB1637
$\alpha\beta$ -tubulin	Microtubules	Sheep	1:500	Cytoskeleton ATN02
Monoclonal Tau-1	Tau dephosphorylated serine sites - Axon specific MAP	Mouse	1:1000	Millipore MAB3420
Polyclonal Tau	Tau phosphorylated and non-phosphorylated sites	Rabbit	1:1000	DAKO A0024 ^a
MAP2	Dendrites specific MAP	Rabbit	1:1000	Millipore AB5622
Antibody II				
Target animal	Fluorophore	Host animal	Dilution	Reference
Mouse	Alexa Fluor 488	Goat	1:500	Lifetech A11017
Mouse	Alexa Fluor 647	Goat	1:500	Lifetech A21237
Rabbit	Alexa Fluor 488	Goat	1:500	Lifetech A21206
Rabbit	Alexa Fluor 546	Goat	1:500	Lifetech A11071
Sheep	Alexa Fluor 550	Donkey	1:300	Agrisera AS121983
Sheep	Alexa Fluor 488	Donkey	1:300	Agrisera AS09631
AB - Direct immuno				
Target molecule	Target localization	Fluorophore	Dilution	Reference
Phalloidin	F-Actin	Atto 488	1:300	Sigma 49403
Phalloidin	F-Actin	Alexa Fluor 647	1:300	Invitrogen A2228
DNA (Hoechst)	Nuclei	Blue	1:1000	Sigma 861405

a. Kindly provided by Marie-Laure Parmentier from the Institut de Génomique Fonctionnelle (IGF), Montpellier, France.

Table 2.3 – *First antibodies, secondary antibodies and antibodies for direct immunofluorescence specifications and references.*

3 Growth and polarization

Patterning allows a large flexibility of possible cellular geometries controlling, in the particular case of neurons, e.g. the number of neurites emerging from the soma, their width or curvature. Thanks to such a well controlled system, we addressed some issues regarding neuritic growth and neuronal polarization such as: "Is the total neuronal length before polarization regulated?" or "How can we control the process of neuronal polarization to set the localization of axonal specification?". To gain a control over the axo-dendritic polarity of the network would be an essential condition to build reproducible blocks of computation. Moreover, it would allow us to standardize the positioning of neurons and their different compartments. Especially, this could be a useful tool to test drugs on axons of isolated cells only.

3.1 Contributions

At the beginning of my thesis, issues regarding the dependence of the neurite length according to neurite width as well as the geometrical and deterministic controls of axonal polarization were already addressed and answered from the PhD works of Caterina Tomba and Ghislain Bugnicourt, who pioneered this work (**parts 3.2.2 and 3.3**). Under the supervision of Caterina Tomba and together with Beilun Wu (M2 internship student), I completed this study during my Master's thesis project by studying the influence of the neurites number (**part 3.2.1 and 3.3.1**); In addition, I performed an in-depth investigation of the geometrical control of length and polarization through the design of new patterns (**part 3.4**) in collaboration with Caterina Tomba and Nir Gov, a theoretician from the Weizmann Institute. Furthermore, I investigated at the cytoskeleton response to neurite width changes (**part 4**).

3.2 Neurite length

3.2.1 Dependence on the number of neurites

Using patterns including 15 μ m disks to anchor the soma and different number of stripes, from 2 to 4, of the same width of 2 μ m, we investigated the neurites growth dependence on the number of neurites. After 2 DIV, neurons were fixed and labeled with β III-tubulin and Hoechst. The distribution of the total neuritic length was measured for each isolated neuron. Strikingly we observed a conservation of the mean total neuritic length versus the number of neurites, as shown in **Figure 2.6**.

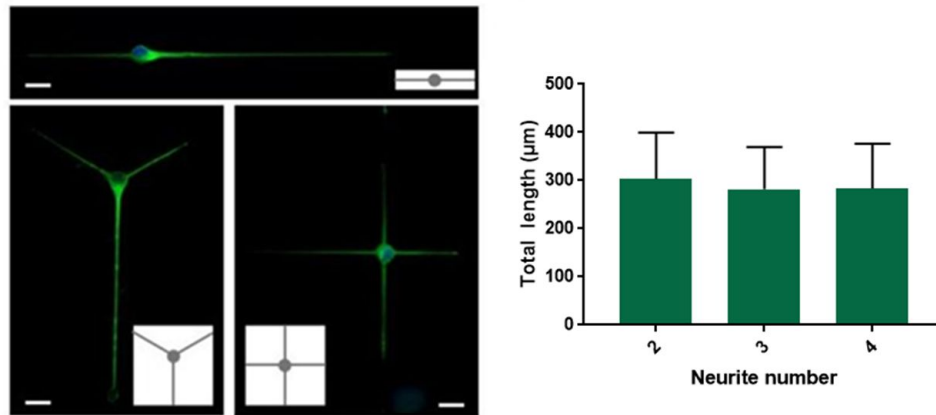


Figure 2.6 – *Neuritic length versus neurite number. Left: fluorescence microscope images showing neurons on the three different patterns. They were fixed at 2 DIV and labeled. Blue: hoechst (nucleus). Green: β III – tubulin (microtubules). Scale bars: $20\mu\text{m}$. Right: Distribution of the total neuritic length. $n(2)=219$ cells; $n(3)=37$ cells; $n(4)=81$ cells.*

3.2.2 Dependence on the neurite width

Interestingly, during the PhD of Caterina Tomba, she observed that the larger are the stripes, the shorter are the neurites (**Figure 2.7**).

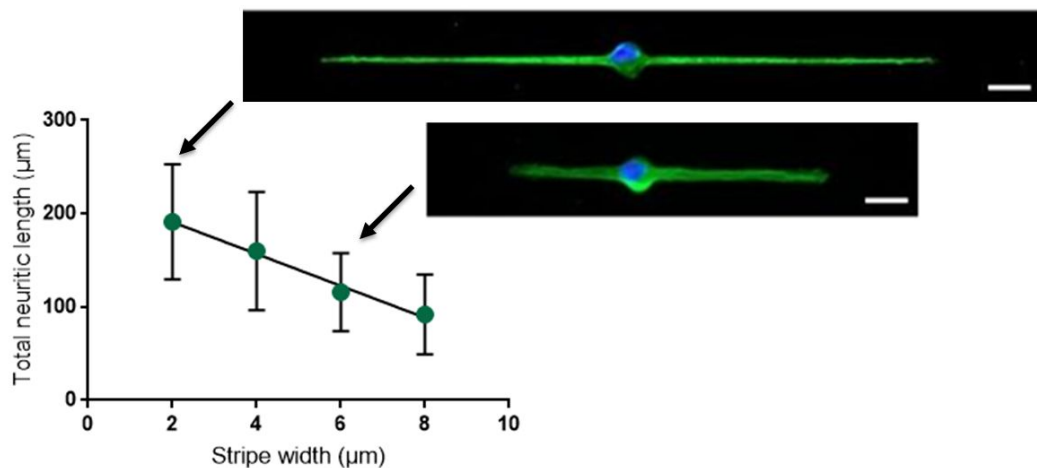


Figure 2.7 – *Total neuritic length versus the stripe width. Linear regression: $y = -17.1x + 225.2$. Fluorescence images represent neurons on 2 and 6 μm wide stripes. Blue: hoechst (nucleus). Green: β III – tubulin (microtubules). Scale bar: $20\mu\text{m}$. Neurons were fixed at 2 DIV. $n(2)=162$ cells; $n(4)=165$ cells; $n(6)=169$ cells; $n(8)=78$ cells; 3 cultures. [175]*

Axons and dendrites having different morphologies (cf **Chapter 1**) it was interesting to study how the neurite geometry influences the overall rate of neuronal polarization and possibly the localization of axonal specification.

3.3 Polarization

3.3.1 Geometrical control of the global polarization rate

Using the same geometries, neurons were fixed at 2 DIV, or 3 DIV to get a higher number of polarized cells. Neurons were then labeled with the monoclonal Tau-1 antibody, to identify the axon, as well as with $\beta III - tubulin$ and hoechst, to visualize microtubules and nuclei respectively. **Figure 2.8** shows the linear decrease of polarization with both neurite number and stripe width. Neurons on thinner stripes or with less neurites polarize faster.

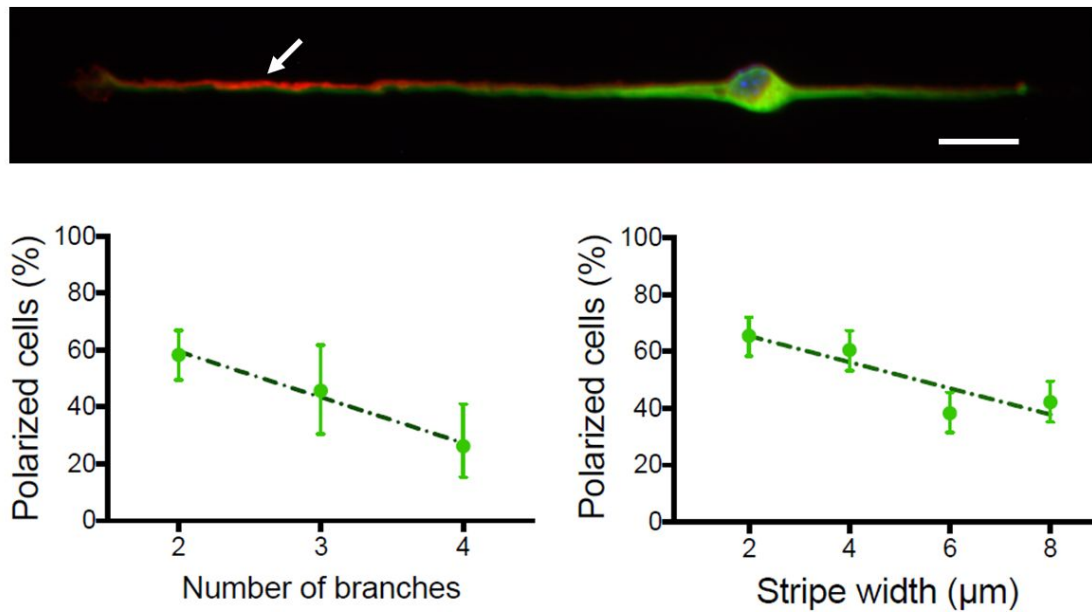


Figure 2.8 – Polarization probability according to the neurite number (left) or the stripe width (right, [175]). More polarized neurons are observed when the number of neurites is lower and when the stripe width is thinner. The polarization probability is decreasing linearly versus both the neurite number and the stripe width. The fluorescence image displays a neuron on a line pattern of $2\mu\text{m}$ width where the Tau-1 gradient can be observed (arrow). Blue: hoechst (nucleus). Green: $\beta III - tubulin$ (microtubules). Red: Tau-1. For the study according to neurites number, cells were fixed at 2 DIV. $n(2)=120$ cells; $n(3)=35$ cells; $n(4)=42$ cells. For the study according to stripe width, cells were fixed at 3 DIV. $n(2)=180$ cells; $n(4)=180$ cells; $n(6)=169$ cells; $n(8)=39$ cells. Error bars denote 95% confidence interval.

3.3.2 Deterministic control of axonal specification on 2:6 pattern

The most striking result from the PhD of Caterina Tomba was the ability to achieve a perfect control of the localization of axonal specification on asymmetric patterns built from 2 and 6 μ m stripes (**Figure 2.8**). Axons were systematically found on the 2 μ m wide stripes, a result in accordance with the observation that the axon is mostly the longest and thinnest neurite (**Chapter 1**).

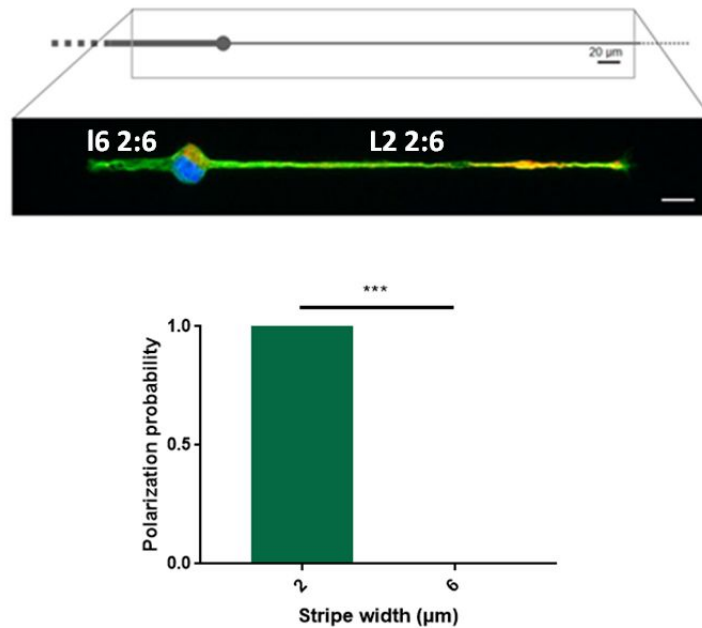


Figure 2.9 – Control of neuronal polarization with the 2:6 asymmetric pattern. 100% of axons were found on the thinner line. Blue: hoechst (nucleus). Green: β III – tubulin (microtubules). Red: Tau-1. Scale bar: 20 μ m. All cells were fixed at DIV3. $n=180$ cells. 3 cultures.

On the basis of this result, we wondered at which distance from the soma do geometrical constraints affect the global polarization rate and the localization of axonal polarization.

3.4 Fine tuning of length and polarization

3.4.1 Exploration of the process of neurite lengthening and competition

To investigate more closely the neurite width dependence of neuronal growth and polarization, new patterns were designed. Their purpose was to establish on which length the width of the proximal part of the neurite close to the soma determines neurite lengthening and axonal polarization. These new patterns were derived from the initial 2:6 motif and were designed by adding short segments of $2\mu\text{m}$ and $6\mu\text{m}$ widths of various lengths on one or the other neurite. These patterns were named 6:62, 2:26, 6:26 and 2:62, with the bold number representing the segments of varying length l (in red in **Figure 2.10**). The length l took the values of 20, 40, 60 and $100\mu\text{m}$ except for 2:62 patterns where l took only the values of $10\mu\text{m}$ and $30\mu\text{m}$.

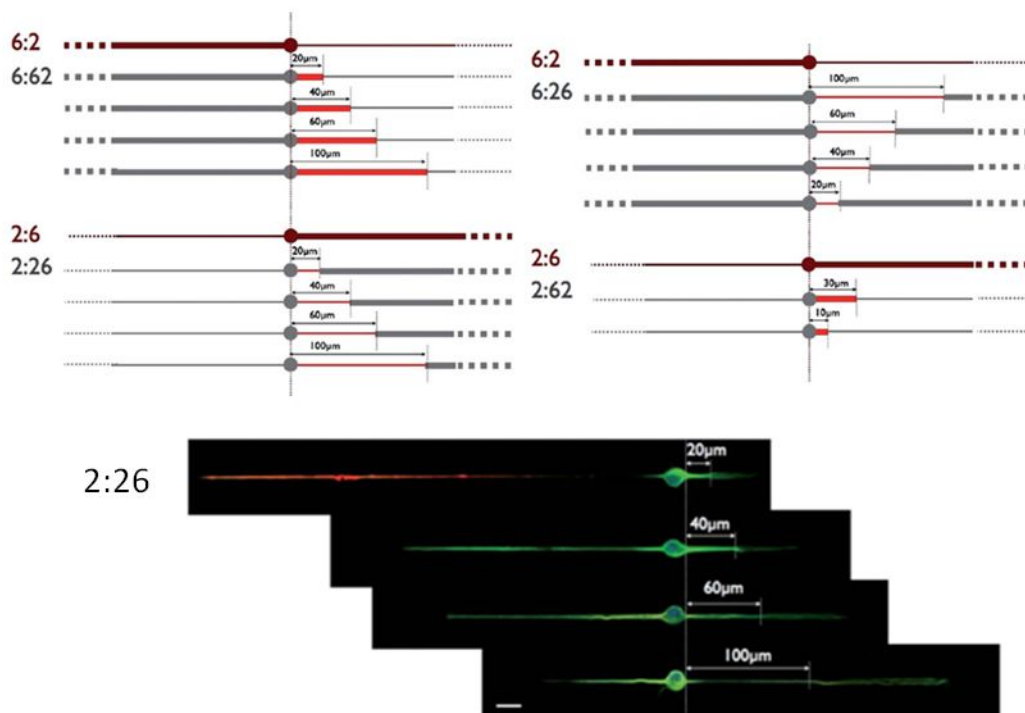


Figure 2.10 – Set of patterns built from 2 and $6\mu\text{m}$ stripes, implementing geometrical changes along neurites. The fluorescence images show neurons on the 2:26 patterns with different $2\mu\text{m}$ segment length (in red on the scheme). Blue: hoechst (nucleus). Green: $\beta\text{III} - \text{tubulin}$ (microtubules). Red: Tau-1. Scale bar: $20\mu\text{m}$. All cells were fixed at DIV3. Scale bar: $20\mu\text{m}$. [177].

Neurons were fixed at 3 DIV. At this early stage of growth, the axonal marker Tau-1 is commonly used to identify the axon. The length of each neurite was measured by the staining of microtubules. The experimental data displayed in **Figure 2.11** show that the geometry of the patterns tunes both the neurite length and the axonal localization.

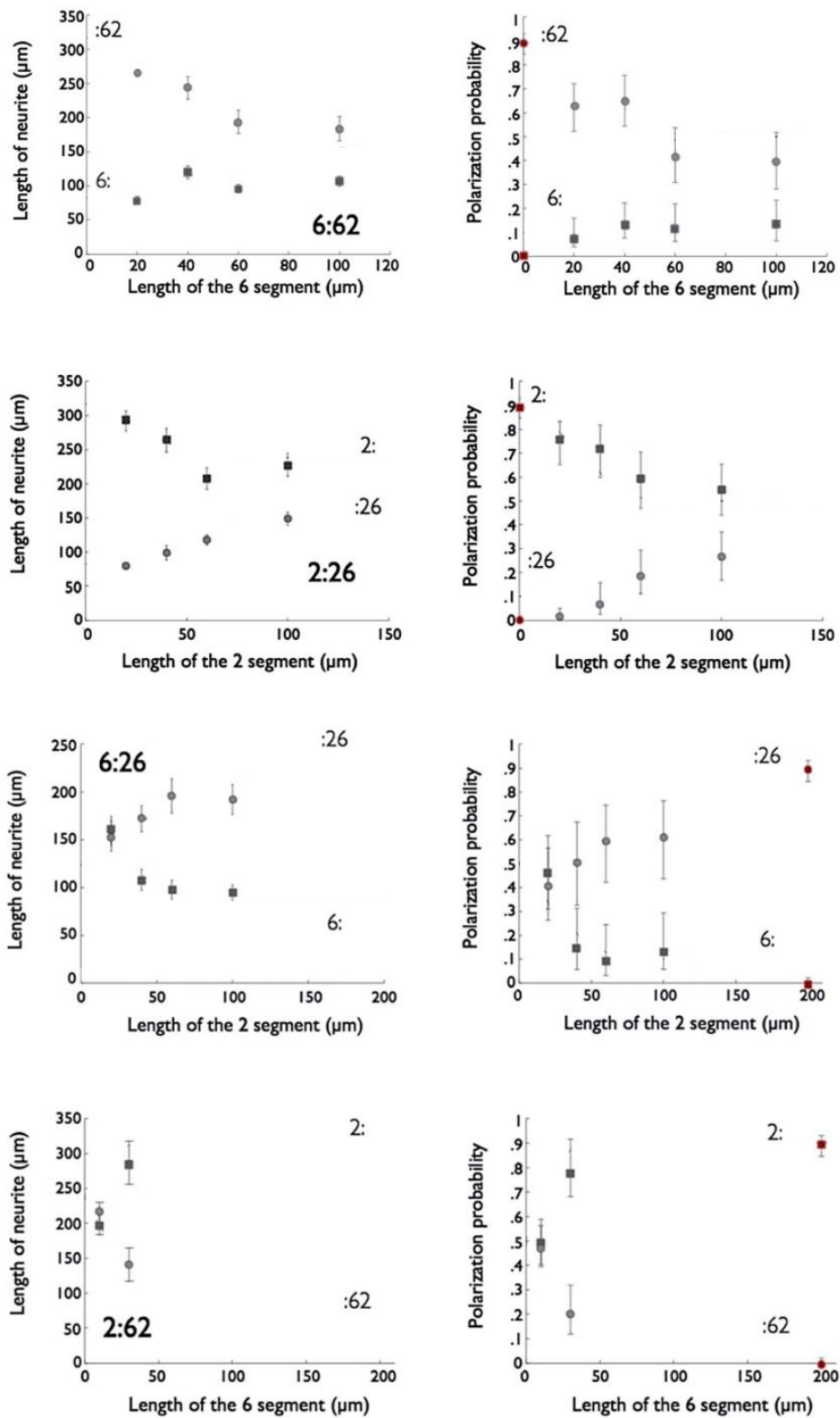


Figure 2.11 – Experimental data of length and polarization obtained from the patterns shown in **Figure 2.10**. $n = 86, 83, 67$ and 61 for the $20, 40, 60$ and $100\mu\text{m}$ length of the $6\mu\text{m}$ proximal stump, respectively (**6:62**). $n = 85, 61, 70$ and 80 (**2:26**) and $n = 37, 28, 32$ and 31 (**6:26**) for the $20, 40, 60$ and $100\mu\text{m}$ length of the $2\mu\text{m}$ proximal stump, respectively. $n = 132$ and 60 for the 10 and $30\mu\text{m}$ length of the $6\mu\text{m}$ proximal stump (**2:62**).

3.4.2 Modeling

3.4.2.1 Ingredients Nir Gov, a theoretician from the Weizmann Institute, has developed during a 3 month sabbatical at the Institut Néel a model of our data using the following ingredients:

1. Following our experimental results (**Figure 2.7**), we consider that growth velocity is controlled by the width of the adhesive stripe on which the neurite is growing (see **Figure 2.7**).
2. The neurites have a certain probability to turn into axons, which signals for the whole cell to polarize. This polarization event seems to depend on the absolute length of the neurite [178, 179]. This hypothesis will introduce the terms L_{pol} , the critical polarization length, and σ_{pol} , the variance of the probability distribution function around this critical length, in the model (see **Figure 2.12**).
3. Following the polarization event the neurite that was "chosen" to become the axon may continue to grow at a different growth velocity $\beta\nu_{tip}$ (with $\beta \geq 1$). The other neurite(s) continues to grow at a reduced growth velocity $\gamma\nu_{tip}$ ($0 \leq \gamma \leq 1$), following the polarization event.

The equations of this model are put in the **Appendix 1**.

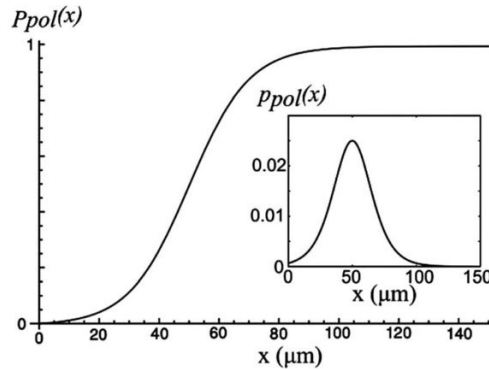


Figure 2.12 – Polarization cumulative probability $P_{pol}(x)$ (**eqn (2.1)**) and the probability distribution function $p_{pol}(x)$ (**eqn (2.2)**) (inset). The parameters used are $L_{pol} = 50 \mu m$ and $\sigma_{pol} = 20 \mu m$.

3.4.2.2 Parameters and Results The model presented above requires a set of parameters, namely the culture duration (T), the elongation rates of neurites constrained by either 2 and 6 μm wide stripes, the multiplicative coefficients controlling the change of these elongation rates after axonal specification (β for the axon and γ for the dendrite), and the characteristic lengths of the probability distribution function L_{pol} and σ_{pol} . The three first parameters are fixed by the experiments, with (i) $T = 72$ h (all neurons were fixed and analyzed after 3 days of culture) and (ii) $\nu_6 = 2 \mu m \cdot h^{-1}$ and $\nu_2 = 4 \mu m \cdot h^{-1}$, as roughly indicated from the data presented in **Figure 2.7**, showing the evolution of the

total neurite length for cells grown on symmetric $x : x$ patterns ($x = 2, 4$ and $6 \mu\text{m}$).

Fitting our model to the experimental data while keeping within the available constraints the values of the different parameters, we were able to obtain the values of L_{pol} , σ_{pol} , γ and β .

The length of neurite and the polarization probability obtained from this model for neurons grown on the 6:62 patterns are displayed in **Figure 2.13** (for more results see [177]). Interestingly experimental data tend to follow the theoretical model, e.g. after a certain length of about $50\mu\text{m}$, neuronal polarization seems to be established in both branches. Even if not perfectly fitting the experiment (this will be discussed in detail below), this model gives us new insights into the axonal polarization phenomenon and new parameters for the building of novel micropatterns for a more precise control of the global polarization rate and axonal localization.

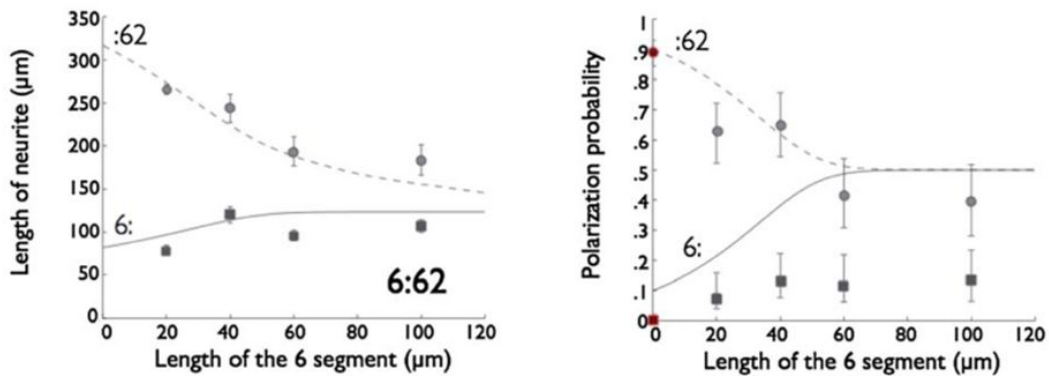


Figure 2.13 – *Neuritic lengths and polarization probability versus lengths of proximal segments for the 6:62 pattern. A) Neurite lengths. B) Polarization probabilities. All results after three days of growth. Symbols denote the experimental data and lines the result of the model calculation: Circles (dashed line) along the :62 neurite and squares (solid line) along the 6: branch). The red symbols correspond to the 2:6 pattern. The parameters used in this calculation are: $T = 72\text{hrs}$, $v_6 = 2\mu\text{m/hr}$, $v_2 = 4\mu\text{m/hr}$, $\beta = 1.2$, $\gamma = 0.4$, $L_{pol} = 50\mu\text{m}$, $\sigma_{pol} = 20\mu\text{m}$ [177]*

3.5 Discussion

The discrepancies observed between experiments and theory in the model developed in [177] concern mainly the polarization data: the model predicts higher probabilities of polarization than computed from experimental data. For example, looking at the nearly 600 cells observed on both the 2:26 and 6:62 patterns, 30% did not show any Tau-1 gradi-

ent and thus were not counted as polarized although we would expect 100% of polarization from the model. One reason for this might be that cells did not have time to differentiate. We decided to control the polarization of the cells previously observed by looking at their morphologies, i.e. their asymmetry in length. Indeed, polarized cells present an asymmetry characterized by the presence of one long axon and a shorter dendrite. In [?], Banker et al. claimed that if one process was $>10\mu\text{m}$ longer than the others, it invariably became the axon. Are cells showing a Tau-1 gradients presenting this asymmetry? Are there cells, among the ones who do not show this gradient, that display this asymmetry and that could be thus added to the current data? To select morphologically polarized cells, we chose as "asymmetric cells", cells having one neurite with a length 2 times longer or more than the other one. Giving $L1$ the length of one neurite and $L2$ the length of the other one, the asymmetry length factor was defined as :

$$\alpha = \frac{|L1 - L2|}{L1 + L2}.$$

We chose $L1 > 2L2$ and therefore $\alpha > 0.33$ as a criterion to identify polarized cells. Among the 70% of cells presenting a Tau-1 gradient, 82% present this asymmetry. As expected, length asymmetry seems to be a fairly robust morphological proof of polarization. Furthermore and most importantly, by including in the results the neurons that did not displayed a Tau-1 gradient but were characterized by an asymmetry length factor $\alpha > 0.33$, new experimental data seem to get closer to the model, as shown for the 6:62 pattern in **Figure 2.14**.

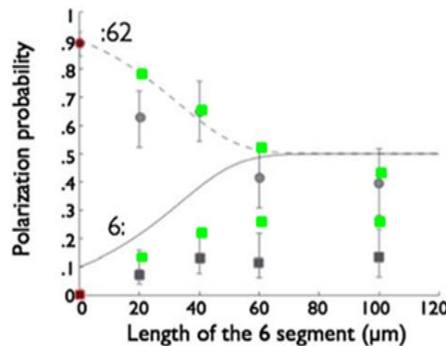


Figure 2.14 – *Neuritic polarization probability versus lengths of the $6\mu\text{m}$ wide proximal segments for the 6:62 pattern. Green points show data including neurons with the asymmetry length factor $\alpha > 0.33$, i.e. presenting a notable asymmetry between neurites. $n=297$ cells fixed at 3 DIV.*

Moreover, although this first model integrates experimental observations, it remains purely descriptive. We will therefore seek in the future for a mechanistic basis of the observed dependence of neurite growth velocities as a function of neurite geometries.

4 Cytoskeleton response to geometrical constrains at the neurite level

In the previous section, we have investigated the influence of the geometry of neurons on their growth and polarization. During my PhD, I became interested into how the neurite spreading on different stripe widths may affect the local neurite cytoskeleton density. In particular, I focused on the microtubule density.

4.1 Microtubules (MTs)

It was recently reported that actin waves trigger a local neurite enlargement and that this increase of the neurite width was accompanied by a polymerization of microtubules (which in turns direct Kinesin-based transport and create bursts of neurite extension [92]). Is this relationship between the neurite width and microtubules polymerization associated only to the presence of actin waves or is this a more general phenomenon? To answer this question, we seeded neurons on patterns in order to obtain 2 and 6 μm wide neurites as well as 2 to 6 μm transitions along a given neurite. Two types of patterns were therefore used: the asymmetric 6:2 patterns and the 2626 patterns presenting successive 2 and 6 μm segments of different lengths (30 or 70 μm). These patterns are presented in **Figure 2.15**.

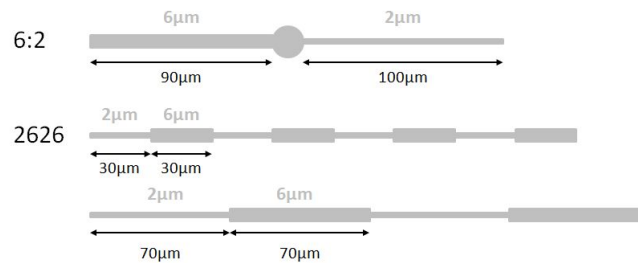


Figure 2.15 – 6:2 and 2626 patterns.

Neurons were fixed at 3 DIV and stained with β III-tubulin (microtubules) and Hoechst (nucleus). Data of 2626 and 6:2 patterns were pooled since they were not significantly different ($p=0.95$ between 2626 and 6:2 values obtained on 2 μm wide stripes and $p=0.33$ for data obtained on 6 μm wide stripes, Student's t-test). In this study we have not sought to distinguish between axons and dendrites, since at this early stage of development the density of microtubules should be similar between both [18, 26].

Analyses were done with ImageJ using the Gels tool. It allowed us to obtain the mean intensity profile (cross section) on different zones of the same length. The mean fluorescence integral was calculated for each zone while removing 15% of the intensity at the base of the profiles peak to get rid of fluorescence artifacts. These ROIs therefore probe

the total microtubules fluorescence intensity over the entire neurite width. The methodology used is summarized in **Figure 2.16**, as well as global results on the variation of the mean fluorescence intensities versus the mean neuritic width.

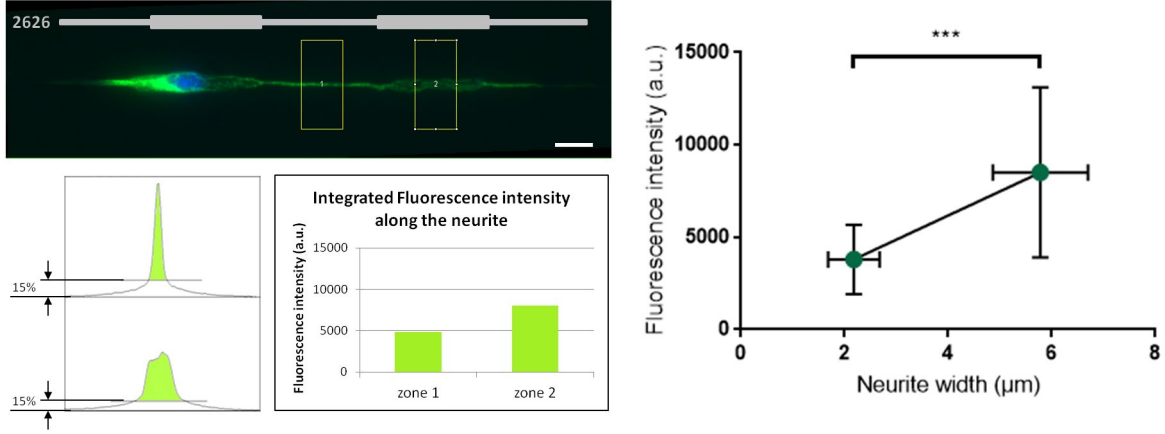


Figure 2.16 – Analysis of the microtubule fluorescence intensity according to the width of the neurite. **Left:** The fluorescence image shows a neuron grown on a 2626 pattern. The length of the 2 and 6 μm segments is 30 μm. Green: β -III-tubulin (microtubules). Blue: hoechst (nucleus). Scale bar: 10 μm. The yellow squares show the ImageJ Gels tool selections, giving the mean profiles and the fluorescence intensity values presented below. **Right:** Mean microtubules fluorescence intensity integral versus neuritic width. The intensity is increasing linearly with the neuritic width ($y = 1306x + 953.2$), with a higher variability on the wider pattern. Data on the 2 μm wide stripes and on the 6 μm wide stripes were significantly different ($p=7.3 \cdot 10^{-9}$ (***) test student). $n=21$ cells; $m=73$ profiles. DIV3.

This graph shows that when a neurite is wider, the total microtubules fluorescence intensity is higher. More microtubules are polymerized on larger neurites. We then calculated the mean MT density ratio r between 6 and 2 stripes

$$r = \frac{d_6}{d_2} = \frac{I_6/w_6}{I_2/w_2}$$

with d_m the mean densities, I_m the mean fluorescence intensities and w_m the mean widths, we obtain $r = 0.88$. When the stripe increases by a factor 3, the microtubules fluorescence intensity increases roughly by the same factor. The density of microtubules is therefore mainly conserved when varying the neurite width. Still we observed a higher variability of the intensity values on wider patterns, as illustrated in **Figure 2.17**. Nevertheless the fact that more microtubules are nucleated when the neurite is larger is here confirmed in a static configuration.

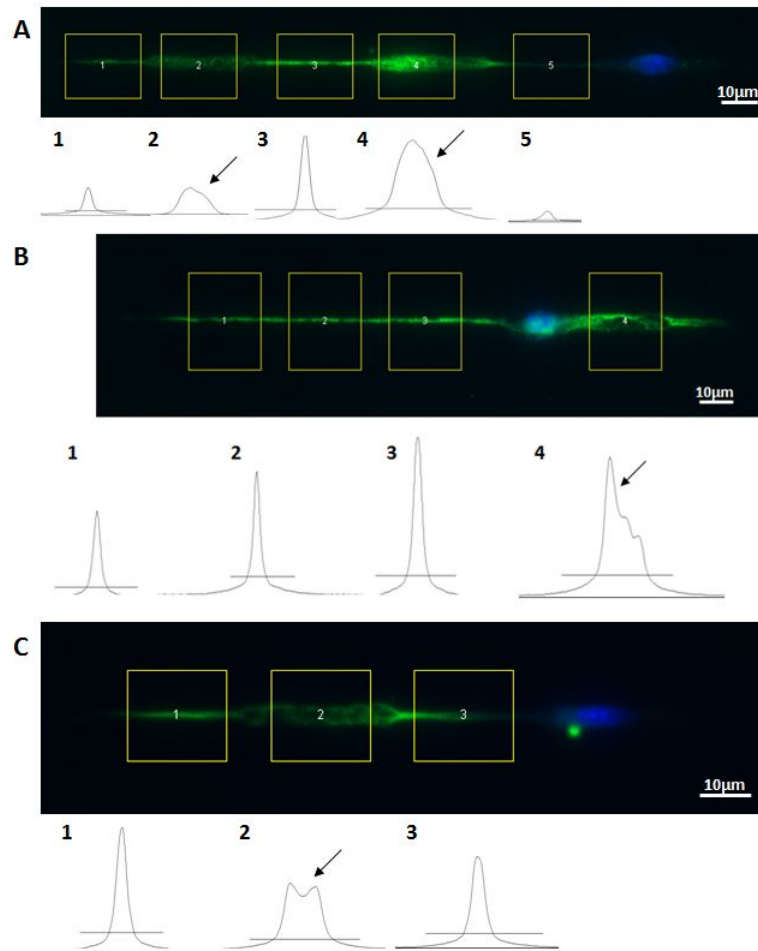


Figure 2.17 – Fluorescence images representing the typically observed behaviour of neurite spreading on large patterns. Neurons were seeded on 2626 and 6-2 patterns fixed at 3 DIV. Green: β -III-tubulin (microtubules). Blue: hoechst (nucleus). On these three cells, the general shape of neurites on $2\mu\text{m}$ wide stripes is conserved whereas on the $6\mu\text{m}$ wide stripes it can either have the same pseudo-parabolic shape as on the $2\mu\text{m}$ wide stripes, but larger (A), or it can be irregular, with more microtubules on one edge (B) or on both edges and a decrease of the tubulin intensity in the middle (C).

5 Conclusion and outlooks

5.1 Summary of most important findings

By constraining neuronal shapes using micropatterning, allowing us to specifically select neurites width and/or number, we were able to highlight some mechanisms about the neurites growth and polarization. We found a conservation of the total neurite length versus the number of neurites, and a decrease of this length when the neurite width increase. We used this last result to achieve a finer geometrical control of both length and axonal polarization. Moreover, we gained some insights into the mechanisms of growth

and polarization through modeling that we confronted to our experimental data. To go further, we looked at the density of microtubules induced by the changes of neurite width at the sub-cellular level. We found that the cell was adjusting its density locally.

5.2 Outlooks

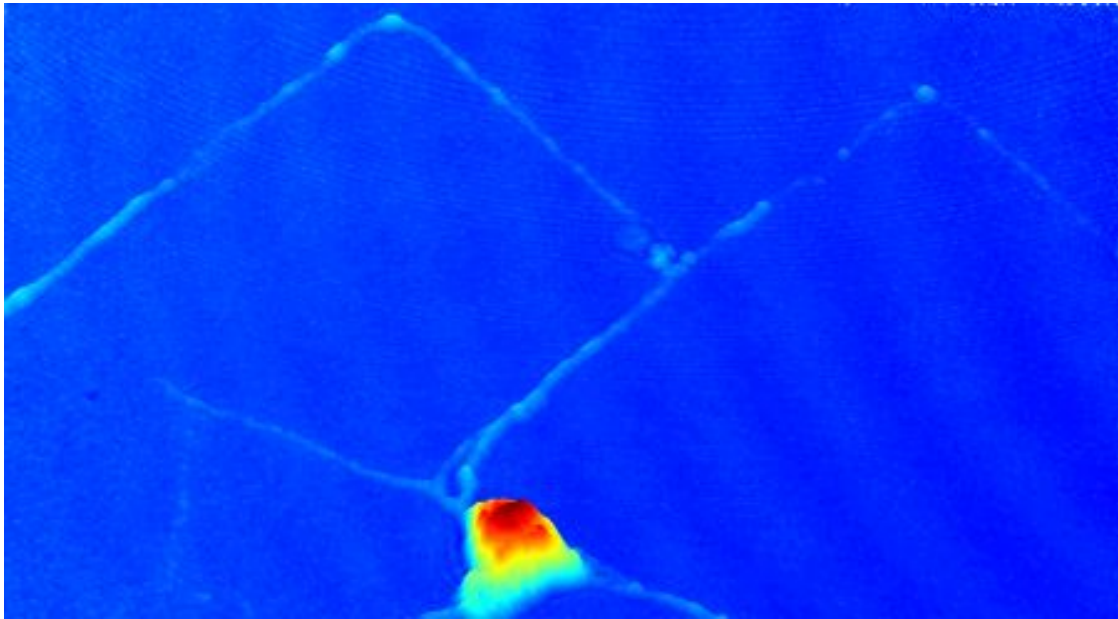
Several questions remain. At the cellular level, they concern for example the mechanistic base of our theoretical model. In the future, we will analyze the role of the adhesive geometry in the production of actin waves, which have been associated to neurite growth and polarization in past studies.

At the molecular level, our study opened several questions: "Is the MAP Tau still present when the neurite enlarges or is it replaced by another MAP?", "Does this have a link with the microtubule polymerisation increase on large neurite ?", or "Is it only the phosphorylation of Tau which is impacted?". We already have some insights for the first question. We labeled, after 3 DIV, patterned neurons of varying widths with MAP2 and polyclonal Tau⁶. Only neurons presenting a notable asymmetry, with the same criterion as previously, were analyzed. We observed around 20 neurons and for 100% of them, the repartition of MAP2 vs Tau polyclonal was not impaired by enlarging the neurite.

This local increase in microtubules polymerization also raised our interest about possible local changes of the cell local mass and/or volume in response to the geometrical characteristics of micropatterns. Moreover, the conservation or not of neuritic length, depending on the neurites number, width or polarization, raised our interest about the evolution of the cell total mass and/or volume in response to micropatterns. These issues will be adressed in the next chapters, concerning the cell mass in **Chapter 3** and concerning the cell volume in **Chapter 4**.

6. Polyclonal Tau labels all sites, i.e. phosphorylated or not, of Tau proteins

MASS MEASUREMENT WITH DIGITAL HOLOGRAPHIC MICROSCOPE (DHM)



Grenoble's neuronal mountains.
C. Braïni, Néel Institute.

1 Introduction

The Digital Holographic Microscope (DHM) is a good compromise between a sophisticated interferometric measurement method and a user-friendly system. We thus selected this microscope to look at the variation of the phase introduced by neuronal cells, including dendrites and axons, grown on micropatterns. In a second step, we deduced from the phase values the neurite dry mass, and eventually the neuritic volume. The DHM is located in the Biofab platform of the Néel Institute. During my PhD, I performed measurement on fixed cells and focused on the ways to improve the resolution of the phase signals by implementing custom-made hardware and dedicated image analysis routines. Moreover, the use of the DHM required for convenience some evolutions in the microfabrication steps, as detailed in the Methods section.

2 Contributions

For this study, I prepared the samples, including microfabrication and cell culture steps, and performed the phase measurement with the DHM. I also wrote a custom-made Matlab program to perform the analysis. Hardware improvements were done in collaboration with Anne Gerardin and Grégory Garde from the mechanical facility of the Néel Institute as well as with the help of Eric Nicolau and Francis Saiag from the mechanical facility of the Curie Institute and the advices of Jean-Luc Mocellin from the electronic departement of the Néel Institute. I performed osmolality measurements first in Oriade clinical laboratory, in Grenoble, which kindly welcomed us, and later at the Curie Institute. Ellipsometry measurements were conducted by David Eon from Institut Néel. Refractometry were performed with the help of Aline Le Roy from IBS (Institut de Biologie Structurale, Grenoble) and with the help of Olivier Thouvenin from Institut Langevin, Paris.

3 Methods

3.1 Microfabrication

A 63x oil objective was used in our measurements to resolve small objects as neurites. Under this magnification and because of the oil, screening the coverslip to select neurons of interest was challenging. Therefore neurons were first identified with a phase contrast microscope, followed by observations with the DHM for higher magnification and interferometric imaging. We had then to find a solution to track down these neurons. In that aim, we chose to etch at the surface of the coverslip numbers and letters next to each adhesive plot dedicated to soma adhesion as well as crosses to identify patterns shape changes,

as illustrated in **Figure 3.1**. This was done through the design of a specific mask and using the same photolithography steps as described in **Chapter 2** (resist spin-coating, UV exposition and development). We used Reactive Ion Etching (RIE, PLASSYS, Nanofab, Néel Institute) under a low pressure of CHF₃ to etch the glass outside of the photoresist stencil. This step takes about 16 minutes to reach an etched depth of about 100 nm. The remaining photoresist was then removed in an ultrasonic ethanol bath and a new photoresist layer was spin-coated. An alignment step, using specific alignment motifs, was then performed to ensure that the adhesive patterns were correctly positioned near etched labels. The patterns used in this chapter are the 2:2, 2-2, 6,6, 6-6 and 2:6 patterns, as summarized in **Figure 3.2**.

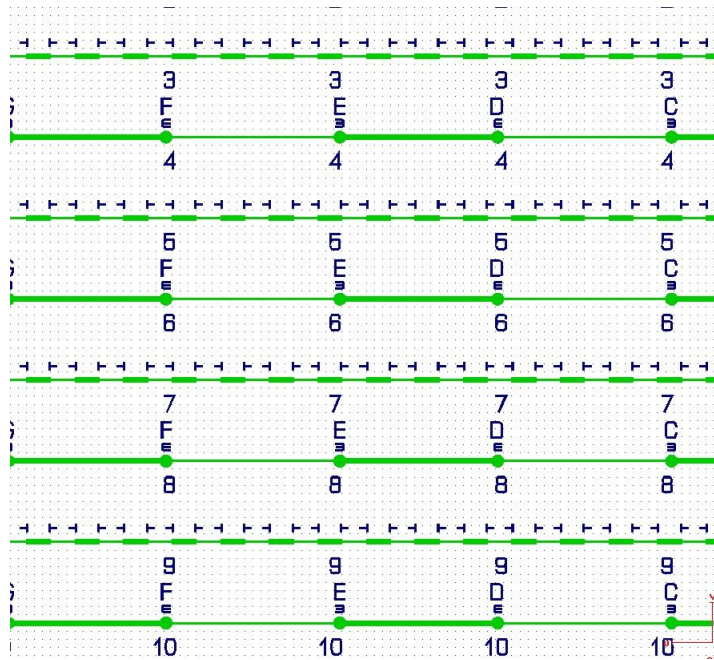


Figure 3.1 – *Superimposition of the two different types of patterns successively implemented on coverslips dedicated to DHM imaging. Dark blue: etched labels at the surface of the glass coverslip). Green: adhesive patterns. Each neuron is associated with numbers and letters. The \in sign indicated the location of the adhesive plot, when implemented, with its central bar pointing toward the position of the 2 μm wide stripe.*

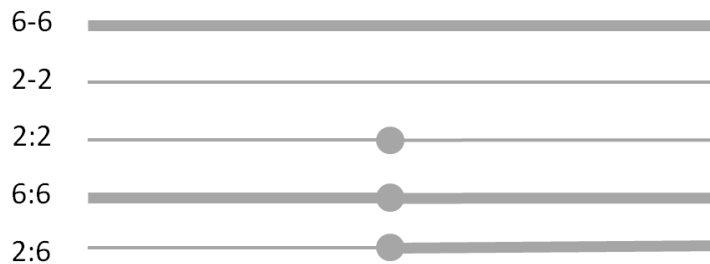


Figure 3.2 – *Patterns used for phase measurements with the DHM.*

3.2 Cell culture

Hippocampal neurons from mice embryo are extracted and seeded at a concentration of 30 000 cells per coverslip in the same way as described in **Chapter 2**. After 2 or 3 DIV neurons are fixed in 4% PFA and kept in PBS buffer. Glass coverslips are mounted inside magnetic holders (Chamlide chambers), in the way that the coverslip becomes the bottom of the imaging chamber, allowing it to be in direct contact with the oil drop of the 63x objective.

3.3 Phase measurement

The interferences measured by the DHM come from the encounter of two monochromatic waves coming from the same source, i.e. a linearly polarized laser diode ($\lambda = 664.8$ nm). One of them constitutes the reference beam, whereas the other one pass through the sample, i.e. a cell culture dish filled with medium and cells. The later one is then delayed by the encountered objects of various refractive indexes, creating a phase shift with the former one. This phase shift creates an intensity modulation of the interference pattern, collected by a CCD camera (**Figure 3.3**), that can be further retrieved by calculation.

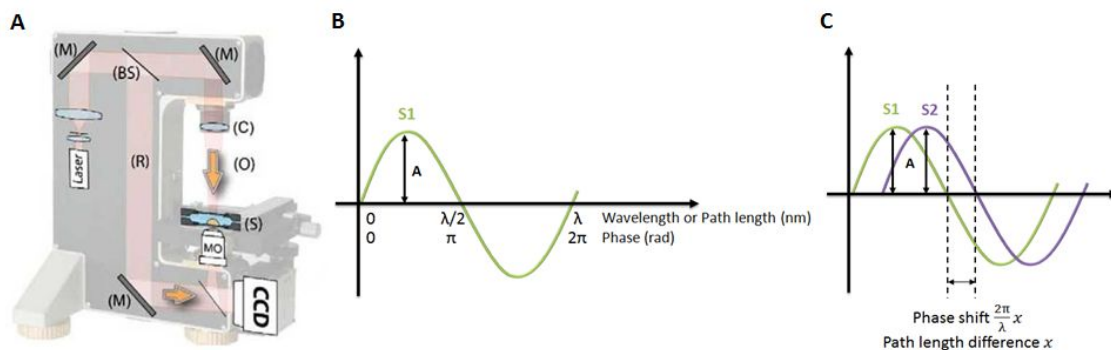


Figure 3.3 – (A) Basic configuration of the digital holographic microscope (DHM). A laser diode produces the coherent light ($\lambda=683$ nm) which is divided by a beam splitter (BS). The specimen (S) is illuminated by one of these beams through a condenser. The microscope objective (MO) collects the transmitted light and forms the object wave (O) which interferes with the reference beam (R) to produce the hologram recorded by the CMOS camera [165]. (B) A typical wave from a source S1 and (C) its interference with a source S2, coming from a common monochromatic source and having the same amplitude A.

The phase delay, i.e. the time corresponding to the phase shift divided by $\omega = \frac{2\pi c}{\lambda}$ (c being the speed of the light), induced by objects of various refractive indexes can also be described by the Optical Path Length (OPL). The OPL is the distance that light would

have traveled in air to arrive at the same time. It is thus the sum of the thickness of the different objects the laser encounters along its path times their refractive indexes. The phase at each pixel $\varphi(x, y)$ is related to the OPL through the formula:

$$\varphi(x, y) = \frac{2\pi}{\lambda} \text{OPL} \quad (3.1)$$

which is, by applying the definition of the OPL,

$$\varphi(x, y) = \frac{2\pi}{\lambda} \left[\int_0^{h(x,y)} n_c(x, y, z) dz + n_m(D - h(x, y)) \right] \quad (3.2)$$

equivalent to

$$\varphi(x, y) = \frac{2\pi}{\lambda} [(\bar{n}_c(x, y) - n_m)h(x, y) + n_m D] \quad (3.3)$$

where $\lambda = 664.8nm$ is the wavelength of the linearly polarized laser diode; $\bar{n}_c(x, y) = 1/h(x, y) \int_0^{h(x,y)} n_c(x, y, z) dz$ the intracellular mean refractive index along the cellular thickness $h(x, y)$ at each pixel; n_m the refractive index of the surrounding medium and D its thickness.

A typical raw phase shift image of a neuron on a patterned coverslip is shown in **Figure 3.4**. The commercial software allows us to set a background - or zero - phase shift $\varphi_{background} = 0$ with a manual selection, and gives the 2D matrix of the values for each pixel of the phase shift of the chosen ROI, $\varphi(x, y)$.

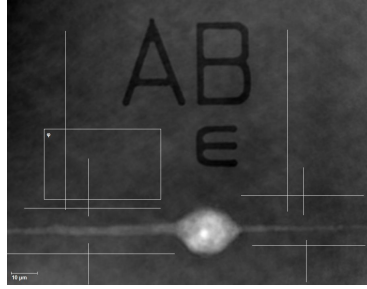


Figure 3.4 – Raw phase shift image of a patterned neuron and background adjustment (lines) and zero phase shift selection (φ) with the commercial software.

With the selection of the background phase as zero

$$\varphi_{background} = n_m D = 0 \quad (3.4)$$

the general equation becomes:

$$\varphi(x, y) = \frac{2\pi}{\lambda} [(\bar{n}_c(x, y) - n_m)h(x, y)] \quad (3.5)$$

The DHM remains a very delicate interferometric instrument, particularly very sensitive to various sources of phase shift other than the one due to the object of interest. Reliable phase shift values measurement therefore required hardware as well as software improvements to assure quantitative measurements with a sufficient resolution to image micron size objects like neurites.

3.4 Experimental improvements for noise reduction

3.4.1 Hardware improvements: "Diver"

The equation (3.5) linking the phase to the cell refractive index and height is only true if everything, except the cell, on the laser path is constant. In other terms, the phase shift between the light passing through the sample and the reference should only be modified by difference of height and refractive index of the cell. If the height of the medium is not constant over time it would introduce an artifact on the measurement. Moreover when moving from one cell to another, a non controlled medium height might introduce systematic errors. To eliminate this non-desirable effects, a "diver" was designed to be mounted on the DHM condenser on one side (technical schemes in **Appendix 2**), and closed on the other side by a glass slide of a well-controlled flatness immersed in the medium. This is illustrated in **Figure 3.5**.

3.4.2 Software improvements: temporal means and background subtraction

To remove the contribution of other external sources of noise that hardware improvements could not remove, we performed noise reduction through image processing. With the commercial software, we performed a temporal average by taking the mean phase from 16 successive images, resulting in a phase stability of 0.007 rad (0.4 degrees). This phase stability is the standard deviation measured between 10 successive data retrieved on the same pixel. Moreover, the process of background removal was performed to minimize the fixed phase pattern noise induced by the coherent noise and to remove possible defects coming from the microscope objective or condenser. This was done by taking, for each cell, a phase blank image of the same size that the phase image with the cell, as close as possible to the cell and in the same condition. This was later subtracted to the cell phase image in the custom Matlab program described in the following section, providing a homogeneous background and allowing some small objects, such as the dendritic little ramification of the neuron presented in **Figure 3.6**, to emerge clearly from the background.

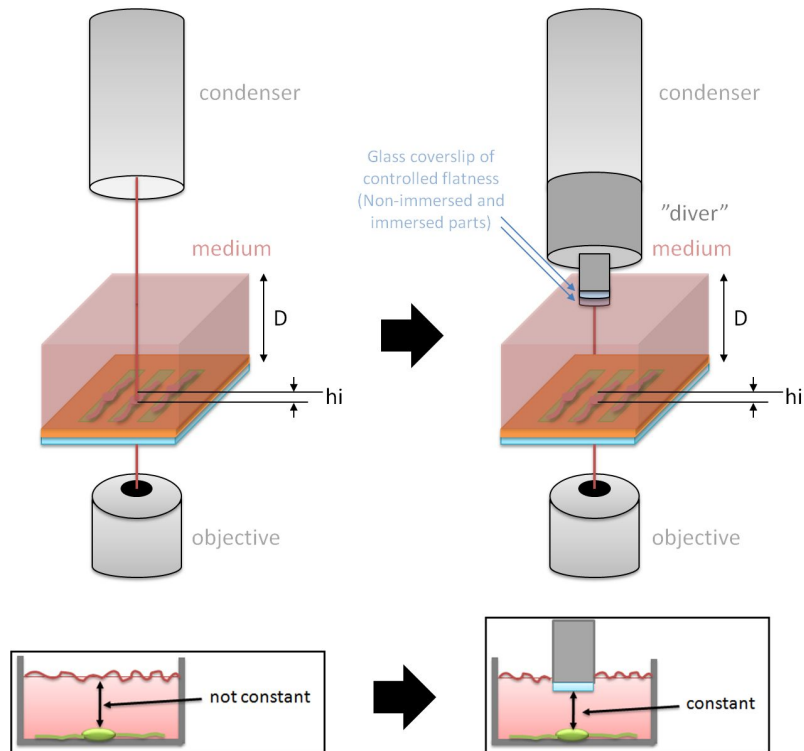


Figure 3.5 – Introduction of a "diver" to the setup.

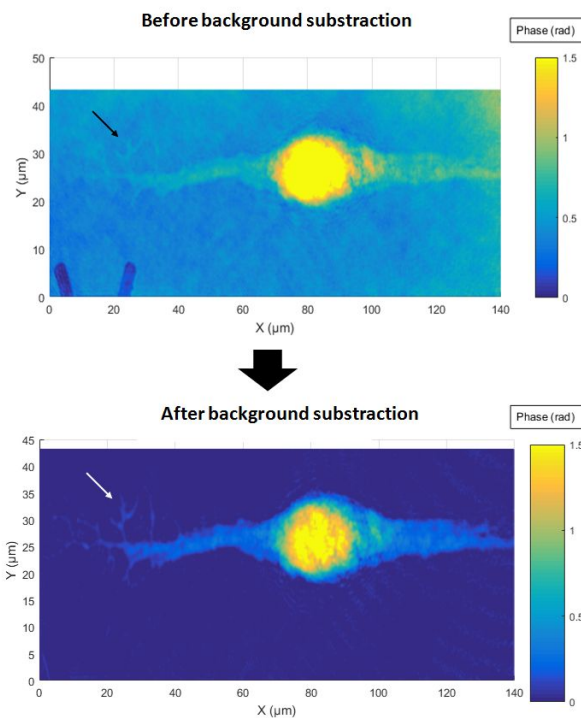


Figure 3.6 – Substraction of the background phase image to the raw phase image (left) in order to get a better phase image (right), with a homogeneus background at zero. Arrows show a zone containing a small object, here dendritic ramifications, getting out of the noise after background subtraction.

3.5 Analysis: custom Matlab program

Analysis of neurites was done with a custom Matlab program. Scripts of this program are presented in **Appendix 3**. Here I will briefly explain, using logic boxes, each main step leading to the outputs.

3.5.1 Neurite selection

First, the data, which take the shape of .txt matrices, are imported and the neurite to analyze is chosen as detailed in **Figure 3.7**.

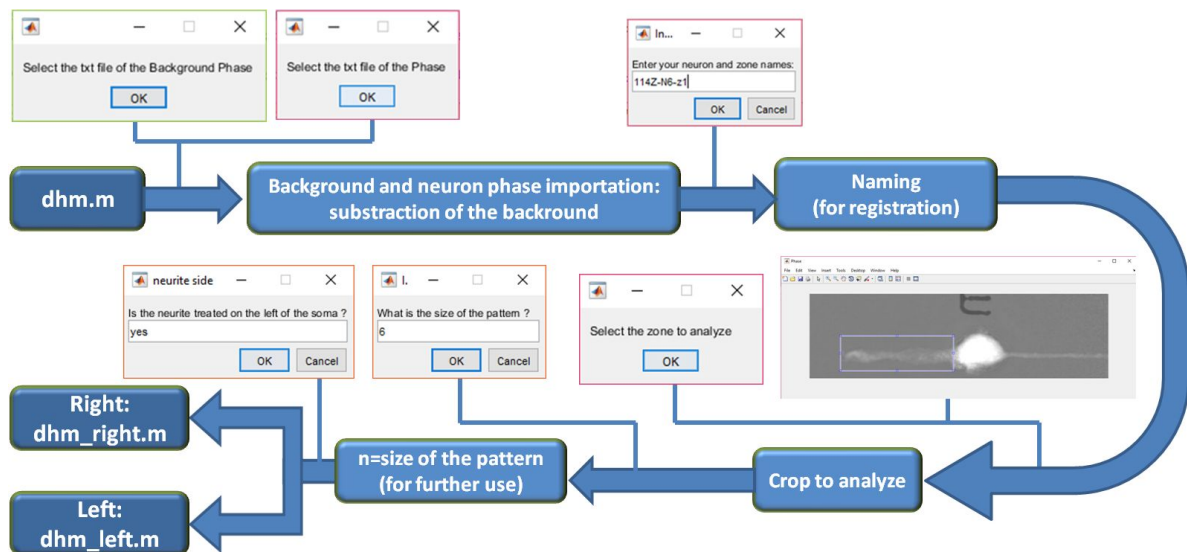


Figure 3.7 – Data importations and neurite selection. The Matlab interface boxes show the windows that the routine displays in order to ask the inputs required for each program step. The Matlab routine names, having the extensions .m, are displayed in dark blue.

3.5.2 Outputs for one neurite zone

After the neurite zone selection, I developed a key routine to integrate the phase over neurite cross sections along the neurite length. These integrations were performed every $5\mu\text{m}$ from a mean profile obtained from the entire length of this $5\mu\text{m}$ long portion.

As outputs, the routine provides an Excel file including: the total value of the length and the "phase volume" ($\text{rad}\cdot\mu\text{m}^2$) as well as mean values of the maximum phase, the width and the phase surface (integral results). These last three parameters are also displayed in columns according to their distance to the soma.

All of these steps are summarized and illustrated in **Figure 3.8**.

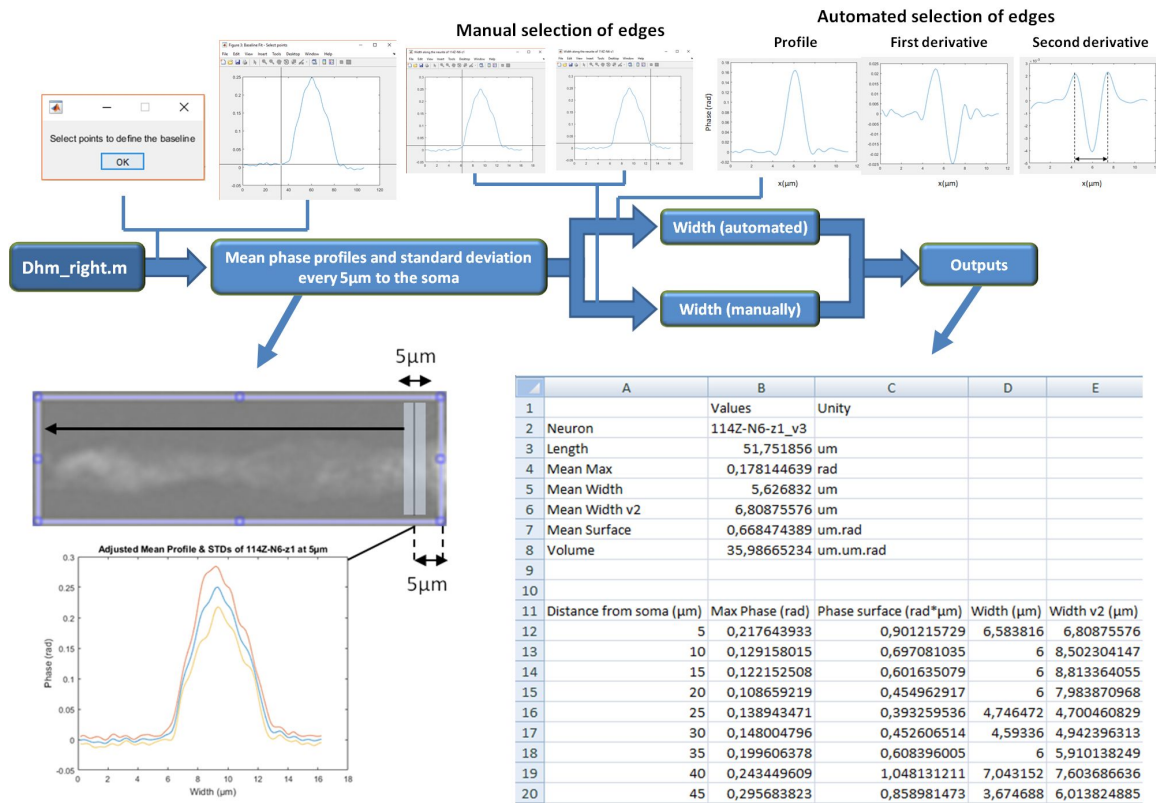


Figure 3.8 – Measurement of the phase integral over neurite cross sections. The Matlab interface proposes a manual choice of the baseline and the limits of the neurite. These limits are also automatically found by taking the distance between the two peaks of the second derivative of each profile (top graphs). The integration of the phase profile is then performed every 5µm from the soma to the neurite tip, on mean profile obtained on neurite lengths of 5µm, as displayed in the scheme in the bottom left. The screenshot of the Excel file shows outputs for one neurite zone. The Matlab routine name, having the extension .m, is displayed in dark blue.

3.5.3 Reconstitution and outputs of a whole neurite

Since we are using a 63x objective, several phase images are often needed to reconstitute a whole neurite. A routine was then written to group different images and sum or take the mean of the outputs. These values are then registered in a new Excel file. This program steps are detailed in **Figure 3.9**. With these phase values we can obtain neurites dry mass through a conversion process detailed in the following section.

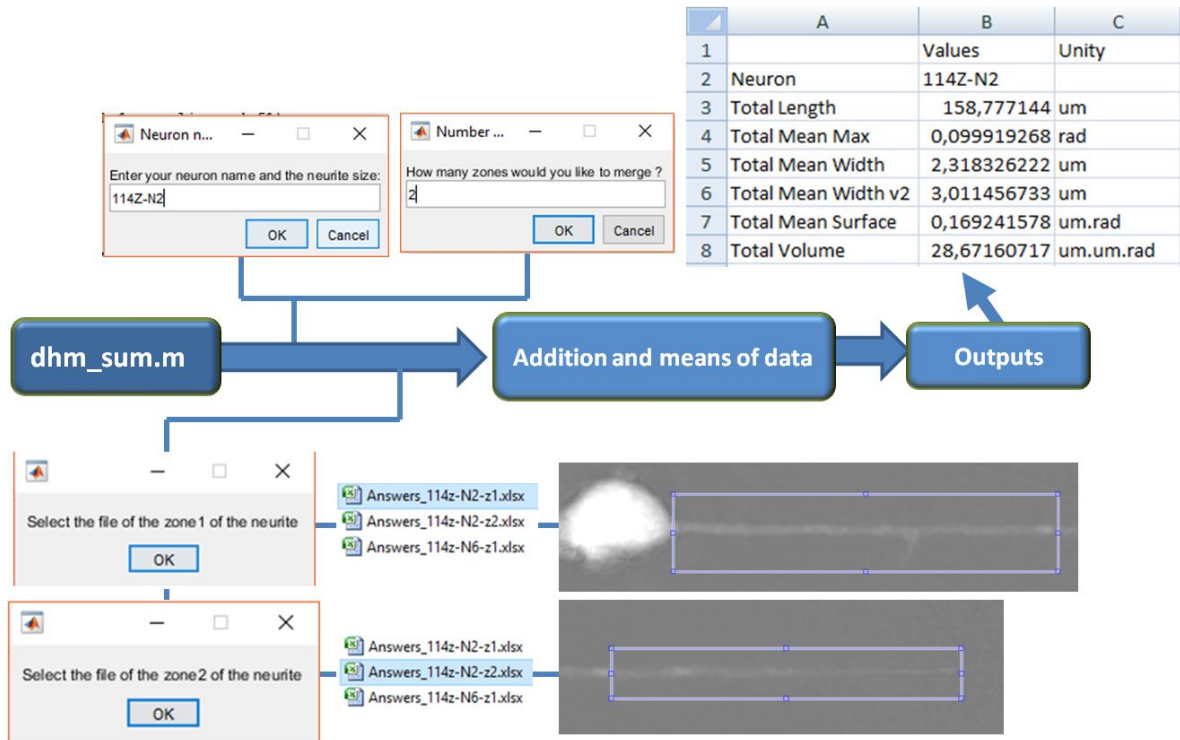


Figure 3.9 – Reconstitution of a whole neurite. The program asks for the different Excel files of each neurite zones to reconstruct the analysis of a whole neurite. This requires to take pictures of the neurite that includes covering regions between the different images. Then, the program writes in a new Excel file the total neurite length and "phase volume" as well as the mean of the maximum phase, the width and the phase surface. An example of the output for one neurite is displayed in the Excel file screenshot. The Matlab routine name, having the extension *.m*, is displayed in dark blue.

4 From phase to dry mass

4.1 From phase and cell dry part RI relationship...

Our starting point will be the equation (3.5) giving the expression of the phase shift produced by a cell of mean intracellular refractive index \bar{n}_c along the cellular thickness h :

$$\varphi = \frac{2\pi}{\lambda}(\bar{n}_c - n_m)h, \quad (3.6)$$

with $\lambda = 664.8nm$ the wavelength of the linearly polarized laser diode, and n_m the refractive index of the surrounding medium; By describing living cells as objects made of a liquid part and a dry part [180], we obtain:

$$\bar{n}_c h = n_l h_l + n_{dry} h_{dry}, \quad (3.7)$$

and

$$n_m h = n_m (h_l + h_{dry}). \quad (3.8)$$

This leads to

$$\varphi = \frac{2\pi}{\lambda} [(n_{dry} - n_m)h_{dry} + (n_l - n_m)h_l], \quad (3.9)$$

where n_l is the RI of the intracellular fluid (a dilute salt solution with a RI very close to water) and n_{dry} the RI of the cells solids, or dry parts, which are constituted by everything making up the cell (proteins, nucleic acids, lipids and so forth) excluding water. In our experiment, the liquid medium surrounding the cells was PBS ($n_m = n_{PBS}$). Note that we measured for PBS a RI close to water as summarized in **Table 3.1**.

Method or origin	Wavelength λ (nm)	Water RI	PBS RI
Refractive Index Detector ¹	664.8	$n_{water} = 1.330 \pm 0.002$	$n_{PBS} = 1.331 \pm 0.002$
Abbe refractometer ²	664.65	$n_{water} = 1.331$	$n_{PBS} = 1.333$
Literature [181]	589	/	$n_{PBS} = 1.334$

Table 3.1 – *Refractive indexes (RI) measurement on water or PBS. 1. Measurement performed with a Optilab T-rEX Refractive Index Detector (Wyatt technology) in IBS (Institut de Biologie Structurale, Grenoble). 2. Measurement performed with an Abbe refractometer in Langevin Institute, Paris.*

Both measured values are in agreement with the literature value, taking into account that the refractive index is inversely proportional to the wavelength.

We then made the approximation that $n_l = n_m$, meaning that we accept here an error on the dry mass due to the possible difference in ionic concentration between the PBS and the intracellular medium. Knowing that the PBS is a dilute salt solution with a RI very close to water, we expect that this error will be negligible³. We then obtain:

$$\varphi(x, y) = \frac{2\pi}{\lambda} (n_{dry}(x, y) - n_m) h_{dry}(x, y) \quad (3.10)$$

This equation shows the relationship between the phase shift detected in the laser path and the dry part of the cell at each pixel.

4.2 ...to dry part RI and cell dry mass relationship

As shown by Barer [182] and Davies and Wilkins [183], the refractive properties of cells exhibit a strong dependence on the total cell proteins concentration. Indeed, most

3. In **Appendix 4**, theoretical and experimental comparisons of measurements with both water and PBS are presented to give an idea of the error between a PBS solution and a non-ionic water solution, which give an first approximation of the error we may have around 7%.

biomolecules exhibit a linear relationship between their refractive index and their concentration. This is illustrated in **Figure 3.10 a**, where RI differences, Δn , between aqueous solutions of several biomolecules and a solution of pure water were plotted as a function of increasing concentration C (in g/l) of these compounds. Interestingly, Δn varies linearly with C , leading to the definition of the specific refractive increment, $\alpha = \frac{dn}{dc}$, relating the refractive index change to the increase in biomolecule mass density. This refractive index increment is similar for many different biomolecules, as shown in **Figure 3.10 b**. Still, variability was observed. In our work we took the value found for whole cells, as in [180, 184].

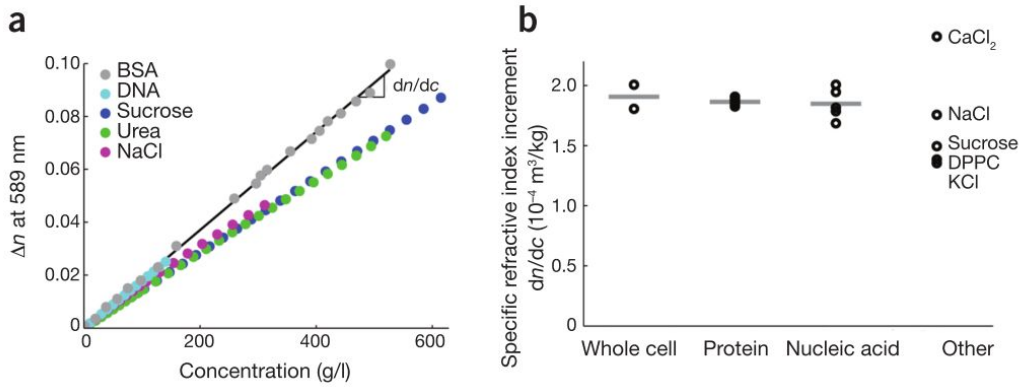


Figure 3.10 – Left: Specific refractive index increment of biomolecules. (a) Changes in refractive index, n , of various biomolecules in solution relative to that of the solvent (water) as a function of biomolecule mass concentration. The slope of this line, dn/dc , is the specific refractive increment used in the determination of the cell dry mass from quantitative phase images. Right: Representative specific refractive index increments of selected biomolecule groups, with the averages of these selected values indicated as horizontal bars. Data are shown for whole-cell average values [180, 184], proteins (multiprotein average [185–188], bovine serum albumin (BSA) [189] and Evans bacteriological peptone [189]), nucleic acids (DNA [190–192] and RNA [193, 194]) and other components (CaCl₂ [195], NaCl [195], KCl [195], sucrose [195] and dipalmitoyl phosphatidylcholine (DPPC), a common phospholipid [196]). [197]

For a whole cell containing dry parts characterized by the RI n_{dry} , the refractive index increment equation is:

$$\alpha = \frac{dn}{dc} = \frac{n_{dry} - n_{water}}{C - C_0}, \quad (3.11)$$

With (by definition) $C_0=0$ and the hypothesis that (see above) that $n_{water} = n_m$, we then get:

$$\alpha = \frac{n_{dry} - n_m}{C}, \text{ or } n_{dry} - n_m = \alpha C \quad (3.12)$$

The equation (3.10) then becomes

$$\varphi(x, y) = \frac{2\pi}{\lambda} \alpha C(x, y) h_{dry}(x, y) \quad (3.13)$$

that we can also write as

$$C(x, y) h_{dry}(x, y) = \frac{\lambda}{2\pi\alpha} \varphi(x, y). \quad (3.14)$$

The integration of this equation over the region of interest leads to the commonly used formula relating the dry mass m and the phase shift distribution:

$$\boxed{m(x, y) = \frac{\lambda}{2\pi\alpha} \int \varphi(x, y) dx dy} \quad (3.15)$$

where $\lambda=664.8\text{nm}$ is the wavelength of the laser, α the specific refractive increment, and $\varphi(x, y)$ the phase at each pixel.

For most biomolecules, particularly those for proteins and nucleic acids involved in the typical cell's dry mass [198], α falls within a very narrow range (**Figure 3.10 b**). It allows a meaningful average value to be used to compute cell dry mass. This average value is typically taken as

$$\boxed{\alpha = 0.180 \mu\text{m}^3 \cdot \text{pg}^{-1}} \quad (3.16)$$

as considered in [182] and [183] and now commonly used as in [197], [199] or by our colleagues in [145].

Thanks to this relationship, we then measured the dry mass evolution in different parts of the neurons, as exposed in the section below.

5 Results

As described in **Chapter 2**, we previously observed that, during early stages of growth, (i) there is a conservation of the total neuritic length independently on the number of neurites but (ii) the neuritic length decreases when the width of the neurites increases (with larger neurites containing more microtubules, approximately maintaining a constant density). Moreover we assessed that (iii) asymmetric patterns promote the axonal polarization on the thinner stripe.

From the above observations, several questions can be raised:

- ◇ How is the cell dry mass locally evolving according to changes in neurites width ?
- ◇ Do shorter and wider neurites grown on increasing stripe widths contain similar total dry mass than neurites grown on thinner stripes?
- ◇ If a neuron extends a long thin neurite on a 2 μm wide stripe and a shorter neurite on a 6 μm wide stripe, how the total dry mass will be shared between both neurites?
- ◇ Does axonal polarization have an effect on dry mass repartition, taking into account the difference in molecular composition between axons and dendrites, as discussed in **Chapter 1**?

I will now present some results associated to these issues, starting with an observation on the evolution of the neurite width as a function of the distance from the soma.

5.1 Neurite tapering

In most neurons, a tapering of the width from the soma to the neurite tip can be observed, as illustrated in **Figure 3.11**. This tapering was previously observed by Banker et al. on non-patterned hippocampal neurons [18], as presented in **Figure 1.10** in **Chapter 1**. It seems thus that this property is robust against the geometrical constraints imposed by patterns of adhesion.

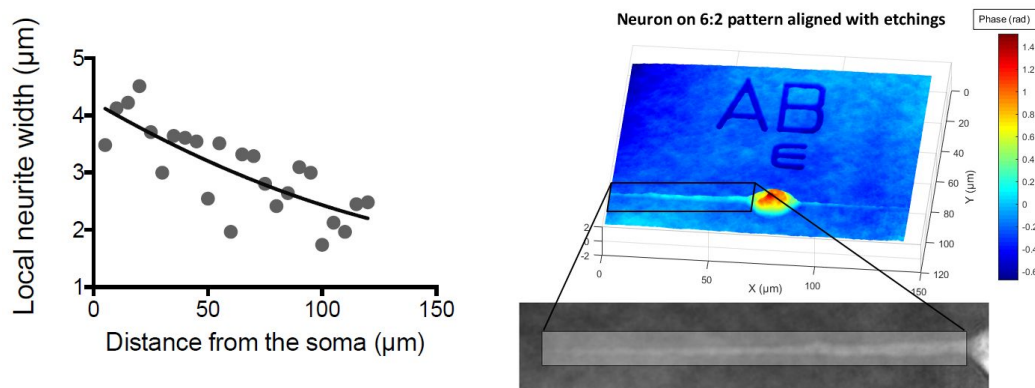


Figure 3.11 – *Neurite width tapering. Local neurite width evolution of the neurite shown on the right, from the soma to the neurite tip.*

Moreover, we have observed that neurites sometimes do not spread over the full stripes width, even in region close to the soma. This is more frequent on wide patterns⁴ where neurites may prefer to shrink down to their spontaneous width on uniformly adhesive substrates and follow the pattern edges. We will take these two effects into account in the analysis of the neurite dry mass data that will be presented below.

4. and very frequent on 8 μm wide stripes, that were not systematically studied for this reason

5.2 Local neurite dry mass as a function of the distance to the soma

To study the tapering effect on the local neurite dry mass, we measured the evolution of the dry mass at different distances from the soma. Note that this local dry mass uses, as explained above, the mean values of the phase integrals computed over portions of 5 μm in length. Therefore we will name this quantity "neurite slices dry mass". Results are displayed in **Figure 3.12** together with the neurite width evolution.

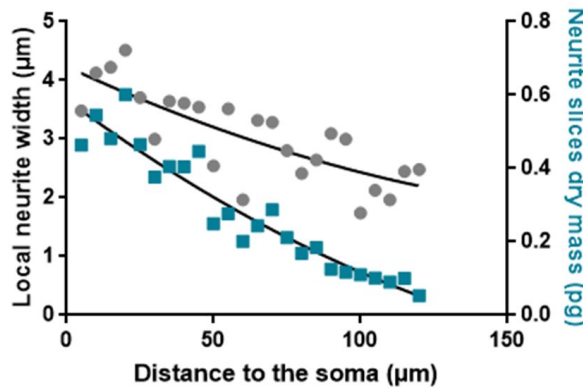


Figure 3.12 – *Neurite width and dry mass tapering.*

On this graph we observe that the local dry mass decreases with the distance to the soma, as does the neurite width (tapering effect). From this preliminary observation, we decided to repeat the same measurement on a high amount of cells grown on different patterns to further investigate the dependence between the imposed and effective neurite width and local dry mass.

5.3 Local neurite dry mass as a function of the neurite width

Based on the observation that neurites do not systematically spread on the entire stripe width, we first focused on the variation of the local dry mass as a function of the effective neuritic width. Neurite slices dry mass was retrieved on neurons grown on 2:2, 2-2, 6:6, 6-6 and 2:6 patterns. Large width values over 6.5 μm corresponding to situations where neurites spread on empty adhesive disks were discarded.

As expected, we observe a general increase of the local neurite dry mass versus the neurite width as shown in **Figure 3.13**. Assuming a linear variation to fit these data, we obtained a line crossing the origin, expressing a proportionality between the local dry mass and the local width. In addition, this graph shows that the dispersion in the dry mass values increase strongly with the neurite width.

The latter observation is even more strengthened by selecting within the above data two ranges of neurite width centered on $2\mu\text{m}$ (range $1.5\text{-}2.5\mu\text{m}$) and $6\mu\text{m}$ (range $5.5\text{-}6.5\mu\text{m}$) corresponding to the widths of the adhesive patterns. We again observed a wider repartition distribution of the local dry mass on larger neurites (**Figure 3.14**).

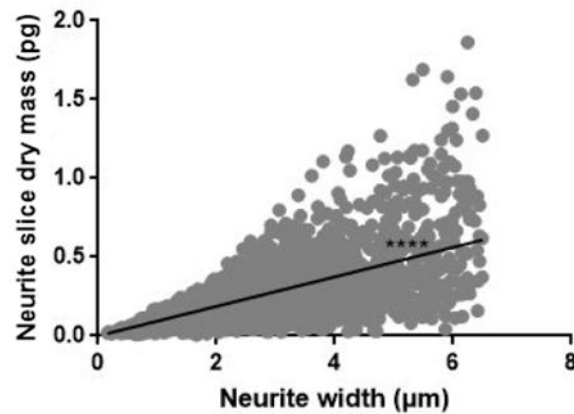


Figure 3.13 – *Neurites slices dry mass distribution versus the neuritic width. The local dry mass increases with the neuritic width with a slope of 0.09363 ± 0.0009418 pg/ μm . $n=2995$ sections, $n=79$ cells (from 2-2, 2:2, 6-6, 6:6 and 2-6 patterns).*

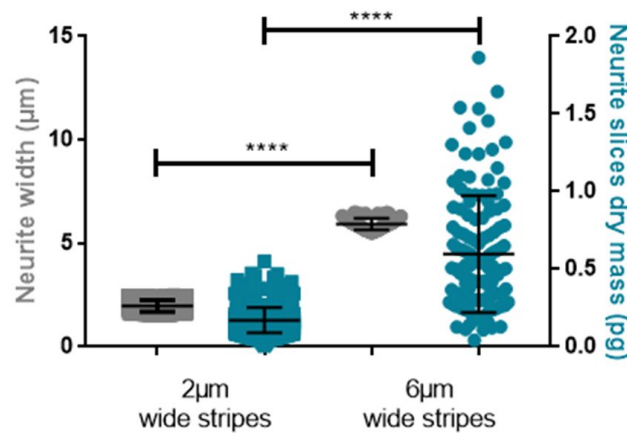


Figure 3.14 – *Distribution of neurite width and neurite dry mass associated to $1\mu\text{m}$ thick longitudinal neurite slices taken within two width ranges: $1.5\text{-}2.5\mu\text{m}$ and $5.5\text{-}6.5\mu\text{m}$. Dry mass per length unit increases with the neuritic width, accompanied by wider data dispersion for larger width. $p<0.0001$ for both parameters with Dunn's multiple comparisons test. $n=79$ cells, $m(2)=383$ sections, $m(6)=238$ sections.*

This phenomenon might be explained by the more diverse shapes that neurites can adopt on larger stripes, as expressed by the phase cross sections displayed in **Figure 3.15**. In these two examples, the neurite phase profiles associated to the $2\mu\text{m}$ wide patterns look

very similar whereas large differences are seen for the larger neurites. Moreover the repartition of mass can be non-uniform, in favor of the edges for example.

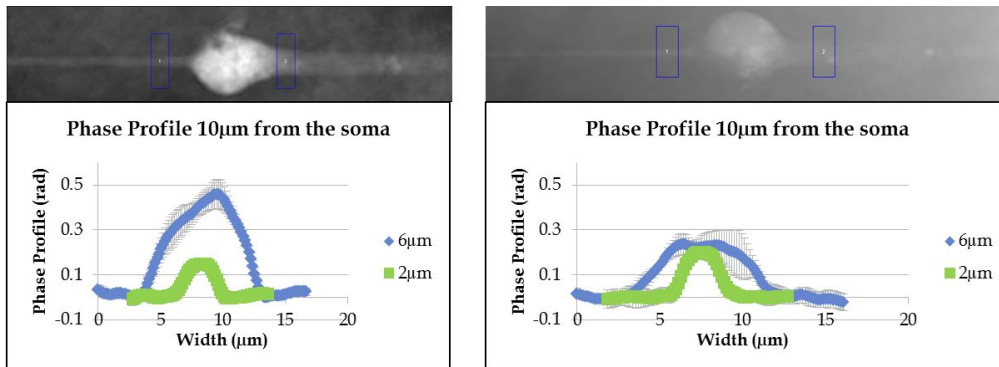


Figure 3.15 – Two phase images of neurons on 2:6 patterns and their neurite profiles taken at 10 μm from the soma. Whereas the profiles are similar for the thinner neurites, the largest ones show a higher variability of shapes.

The linear fit shown in **Figure 3.13** would yield a 0.09363 pg increase per μm of neurite width: a 2 μm wide neurite would thus have in average a dry mass of 0.18726 pg per μm of neuritic length. A 6 μm wide neurite would have then a 3 times higher dry mass (i.e. 0.56178 pg). Assuming that the volume scales with the dry mass, this would suggest that the neurite height should remain constant when increasing the neurite width. The general distribution of the data might even suggest that the dry mass tends to increase faster than linearly with the neurite width.

Following experiments were focused on the dependence of the total neurite dry mass versus the total neurite length. We especially investigated how this total neurite dry mass would evolve during growth and polarization.

5.4 Total neurite dry mass

Thanks to hardware and software improvements, the DHM allowed us to reach whole neurons dry mass measurements, including the neurites parts located far away from the soma and more likely to be lost in noise. We were able to calculate the total neuritic dry mass. Using 2-2, 2:2, 6-6, 6:6 and 2:6 patterns and thanks to the Matlab routine allowing to concatenate and analyze images coming from the successive regions of a given neurite, we studied the total neurite dry mass versus the total neurite length and width.

5.4.1 Influence of the neurite length

From a population of 11 neurons fixed at 2 DIV on 2 μm wide stripes, we first observed that the total neurite dry mass increases linearly with the total neurite length (**Figure 3.16**).

From this linear relation, we computed that the calculated dry mass per unit of length of a $2\mu\text{m}$ wide neurite would be about $0.21\text{ pg}/\mu\text{m}$. Let us note that this value is in agreement with the one that can be deduced from the linear fit of **Figure 3.13** where a $2\mu\text{m}$ wide neurite would have in average a dry mass of $0.19\text{ pg}/\mu\text{m}$ per unit of neuritic length, as discussed above.

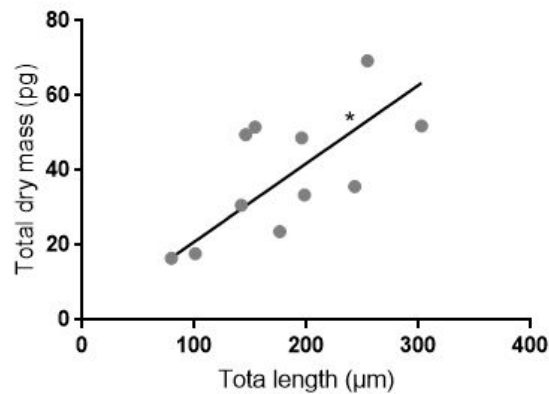


Figure 3.16 – Total dry mass as a function of the total neurite length on $2\mu\text{m}$ wide stripes. The total dry mass is increasing with the total length with a slope of $0.2095 \pm 0.02027\text{ pg}/\mu\text{m}$. $n=11$ cells fixed at 2 DIV.

5.4.2 Influence of the neurite width

We then studied the influence of the neurite width on the total neuritic dry mass. Neurons were fixed at 2 DIV on $2\mu\text{m}$ or $6\mu\text{m}$ wide stripes and the total neurite length as well as the total neurite dry mass were measured. We observed no significant difference in the total neurite dry mass between these two geometrical configurations whereas the total neuritic length decreases when the stripe width increases. This is illustrated in **Figure 3.17**.

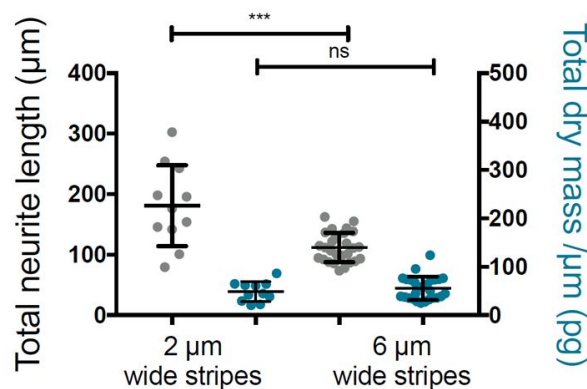


Figure 3.17 – Total neurite length and mass for neurons grown 2 DIV on $2\mu\text{m}$ and $6\mu\text{m}$ wide stripes. A significant difference can be observed between neurite lengths ($p < 0.001$ (***)) but not between neurite dry mass ($p > 0.05$ (ns)). $n(2)=11$ cells, $n(6)=27$ cells.

To further explore if this first indication of the existence of a dry mass homeostasis at the cell level (excluding the soma) might be further validated, we then focused on the length and dry mass distribution at the individual neurite level. In **Figure 3.18**, lengths and dry mass are plotted for the longest and the shortest neurite of the patterned neurons analyzed in **Figure 3.17**.

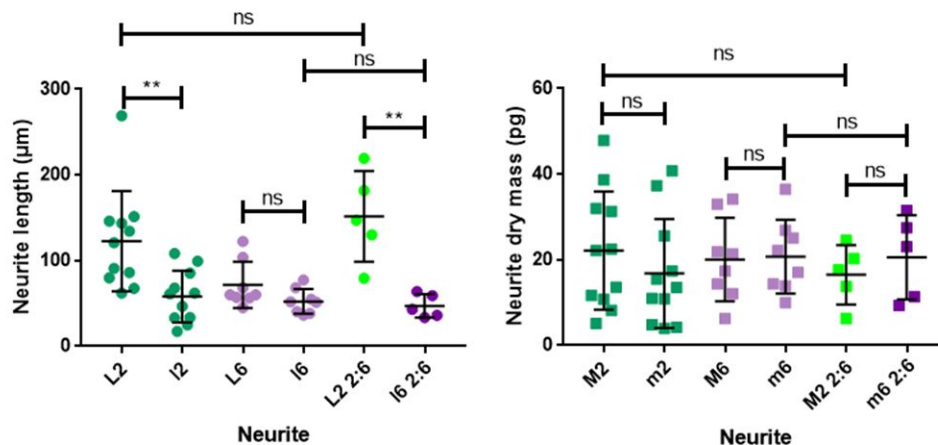


Figure 3.18 – *Neurite length and neurite dry mass for neurons fixed at 2 DIV on 2µm (left) and 6µm (right) wide stripes. L2 and L6 represent the longest neurites on 2 and 6µm wide stripes respectively, whereas l2 and l6 represent the shortest. Significant differences can be observed between the longest and the shortest neurites of neurons on 2µm wide patterns ($p=0.0077$) and on 2:6 patterns ($p=0.0057$). No significance is observed between the different neurites dry mass ($p>0.999$). $n(2)=11$ cells. $n(6)=8$ cells. $n(2:6)=5$ cells.*

For neuron on 2µm wide stripes, L2 and l2 represents the length of the longest and the shortest neurite, respectively. Similarly, lengths for the neurons grown on 6µm wide stripes are labeled as L6 and l6 whereas L2 2:6 and l6 2:6 stand for the 2µm and 6µm neurites of the 2:6 pattern. This notation is kept the same for the dry mass, replacing "L" by "M". For the couple of lengths where a significant difference can be observed, which are (L2-l2) and (L2 2:6-L6 2:6), we obtained a non significant difference between the corresponding total dry masses. This result suggests that cells therefore divide their dry mass equally between their two neurites, independently of the neurites width. Together with the previous result, we suspect a homeostasis in total neuritic dry mass and between the neurites of a given cell, which will have to be confirmed with a larger number of data.

The above study was performed on 2 DIV neurons where most cells did not differentiate an axon. To go further, we studied the evolution of the neuritic dry mass on neurons seeded on 2:6 patterns at different DIV: 2, 3 and 3 and a half DIV to study the effect of axonal polarization. The total neurite lengths and masses for the different pattern widths and culture duration are displayed in **Figure 3.19**.

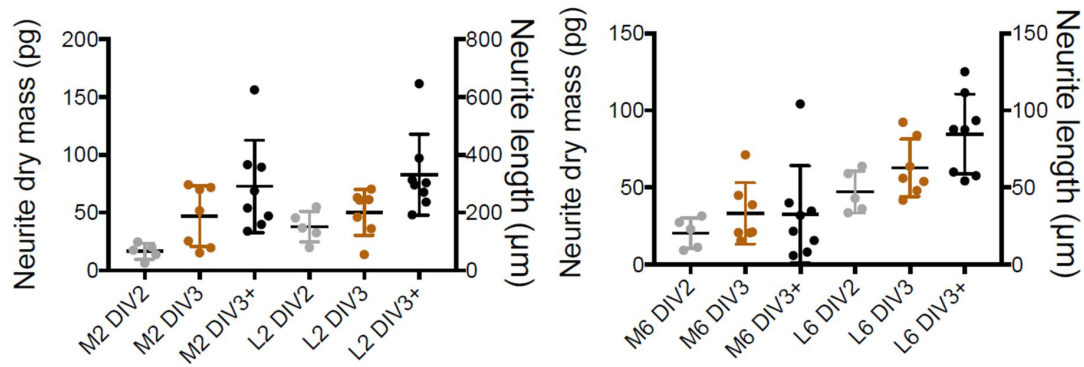


Figure 3.19 – Neurite length and neurite dry mass for neurons on 6:2 patterns fixed at 2, 3 and a little more than 3 (3+) DIV. Using linear fits we have: M6:8.5pg/DIV, L6:24µm/DIV, M2:36.9pg/DIV and L2:116µm/DIV. $n(\text{DIV}2)=5$, $n(\text{DIV}3)=7$, $n(\text{DIV}3+)=8$.

Even if the amount of data is still limited and the variations not always significant, we observed an increase of both length and dry mass. Interestingly, the ratio between the slopes associated to the variations of dry mass and length are very similar for 2 and 6µm wide stripes, underlying again the linear relationship observed in **Figure 3.16**. However, the comparison between the dry mass of 2µm and 6µm wide stripes shows no significant difference before 3.5 DIV (**Figure 3.20**).

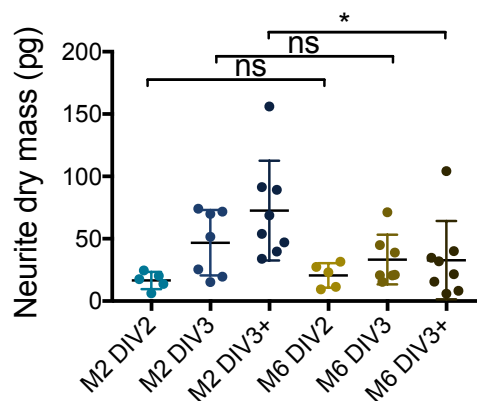


Figure 3.20 – Neurite dry mass for neurons on 6:2 patterns fixed at 2, 3 and a little more than 3 (3+) DIV. $n(\text{DIV}2)=5$, $n(\text{DIV}3)=7$, $n(\text{DIV}3+)=8$. Dry masses at 2 and 3 DIV are not significantly different between the two patterns ($p>0,9999$ Welch's *t*-test) whereas there are significantly different after 3 DIV ($p=0,0418$, Welch's *t*-test).

If confirmed, this would suggest that the process of axonal polarization put an end to the dry mass homeostasis possibly occurring in non-polarized cells. All these trends will have to be confirmed in the future by additional experiments.

6 Accuracy of dry mass measurement with DHM

Previous published studies (as referenced in **Part 4**) directly used the phase shift signal to measure cells dry mass. The DHM was in particular used for similar purpose as ours, i.e. to measure the dry mass production rate and the dry mass surface density of cells (in the case of Rappaz et al., cells were wild-type and mutant fission yeast cells [207]). Following these works, we considered the phase shift signal as the product of the local mean RI of neurons (or of specific sub-cellular neuronal compartments) and thickness. However, we became aware after a first run of experiments that we should consider the birefringence of the cells, as cellular components like microtubules or actin filaments display this optical property.

In the following, we will estimate and discuss the possible errors introduced by not considering the phenomenon of birefringence.

6.1 Phase variation due to birefringence

Contrarily to non birefringent objects, that have a unique refractive index independent of the polarization of the incident beam, a birefringent object has two main axes of different refractive indexes. If the polarization of the incident beam is oriented according to the principal, or ordinary, axis o , the refractive index is n_o . If the polarisation of the incident beam is oriented according to the extraordinary axis e , the refractive index is different and named n_e . For example, the birefringence of microtubules and actin filaments have been observed [203–205]. In that case, the value of the whole cell refractive index could vary depending on the polarization of the incident beam.

A cell containing birefringent components, such as microtubules or actin filaments, should therefore be considered as a birefringent object.

To estimate the error of not considering the existence of ordinary and extraordinary refractive indexes, we compute below the value of the phase obtained for the two extreme cases:

- the polarisation of the incident beam is oriented according to the ordinary axe; The phase shift is then expressed as

$$\Phi_o = \frac{2\pi}{\lambda}(n_o - n_m)h \quad (3.17)$$

- the polarisation of the incident beam is oriented according to the extraordinary

axe, then

$$\Phi_e = \frac{2\pi}{\lambda}(n_e - n_m)h \quad (3.18)$$

with λ the wavelength of the laser beam; n_o the ordinary refractive index of the object; n_e the extraordinary refractive index of the object; n_m the refractive index of the surrounding medium and h the height of the object.

The maximum error on the phase measurement, and thus on the dry mass, can be estimated as

$$e = |\Phi_o - \Phi_e| = \frac{2\pi}{\lambda}|n_o - n_e|h \quad (3.19)$$

and the relative error can be written as

$$e_r = \frac{e}{\Phi} = \frac{|n_o - n_e|}{|\bar{n}_s - n_m|} \quad (3.20)$$

with \bar{n}_s the mean RI of the object, as hypothesized in **Part 3.3**.

To illustrate these equations, let us take the example of microtubules and consider that

- we suppose $\Delta n = |n_e - n_o| \simeq 0.025$, based on the value of the specific birefringence $\Delta n' = \frac{\Delta n}{f}$ measured in [201], with f the volume fraction of the object taken as 1.
- $n_s =$ the tubulin RI measured as 1.512 as a mean RI [201]
- $n_m = 1.33$, considering PBS as the surrounding medium RI,

To neglect birefringence would then give a relative error of 12 %.

6.2 Hypothesis and validations

The birefringence effect implies that refractive index values might be different according to the orientation of the polarized incident beam compared to the orientation of the birefringent object of study. The use of micropatterns, and of straight stripes in particular, should give us a straightforward way to estimate the birefringent properties of neurites. It would suffice to rotate our sample from 0° to 360° , to observe the angular dependence of phase values and finally to deduce from this dependence the ordinary and extraordinary indexes. Such experiments will be performed in the next future.

In a first hypothesis, we took a mean refractive index along the thickness of each pixel of neurites, and a neurite mean refractive index when calculating the neurites total dry mass. Here, the birefringence effect was considered as negligible.

However, birefringence may not be considered if we are only interested into the comparison between e.g. dry mass of neurons grown on $2\mu\text{m}$ and $6\mu\text{m}$ wide stripes, under the condition that we keep the orientation of the neurite identical for both measurements.

This is what we always did, and therefore we are confident in our relative measurements although we have to perform additional experiments to obtain accurate absolute values.

7 Refractive index and cell volume: preliminary results

A change in dry mass is not always correlated with changes in volume, as it was observed for example during cell mitosis in [145] where an increase in volume is not accompanied by an increase in dry mass. Concerning neurons, it was reported that they contain a water part occupying 54% of their total content. This would be relatively unusual, as for other cells such as glial cells the water part occupy between 70 and 90% of their total content. Moreover, the concentration of the dry mass in the total volume seems to vary from a cell compartment to the other: for example the water part of neurons increase to 67% when looking only at their nuclei content [211]. Measuring the real volume of the different neuronal compartments would be needed to complete this study. This would imply to know the RI of each of them. The method presented below is an attempt to retrieve the spatial distribution of RI in neurons and therefore the local cell thickness.

The formula describing the phase shift as a function of the thickness of a cell includes its RI and the RI of the surrounding medium. If the RI of the surrounding medium can be measured directly with dedicated instruments like a refractometer or an ellipsometer, this is not the case for the RI of a neuron. To obtain the cell RI, and therefore to retrieve the height of the cell at each point, our approach was to use the Decoupling Procedure (DP).

7.1 Decoupling Procedure (DP)

The DP principle is the measurement of the phase of a given ROI using two media of different RI. Indeed we would have now two equations instead of one to retrieve two unknown parameters (i.e. the cell height h and local RI \bar{n}_c):

$$\varphi_1 = \frac{2\pi}{\lambda} [(\bar{n}_c - n_1)h] \quad (3.21)$$

and

$$\varphi_2 = \frac{2\pi}{\lambda} [(\bar{n}_c - n_2)h] \quad (3.22)$$

allowing us to calculate \bar{n}_c and h through:

$$\bar{n}_c = \frac{\Delta n \varphi_1}{\varphi_1 - \varphi_2} + n_1 \quad (3.23)$$

and

$$h_{dry} = \frac{\lambda}{2\pi} \frac{\varphi_1 - \varphi_2}{\Delta n} \quad (3.24)$$

with $\Delta n = n_2 - n_1$ and n_1 and n_2 the RI of the two different media.

This technique was developed by Rappaz et al. in [169], who measured the mean phase shift over time during the replacement of one medium by another characterized by a different RI, as displayed in **Figure 3.21**.

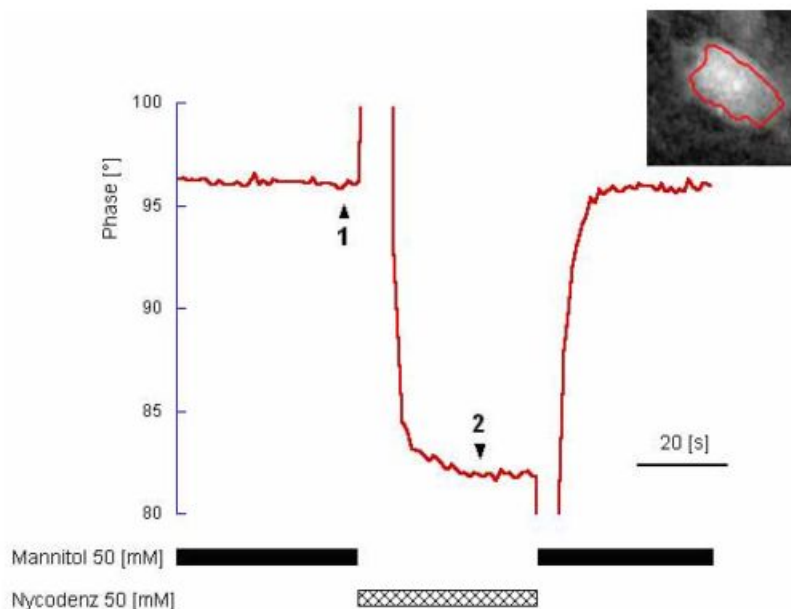


Figure 3.21 – Evolution of the mean phase of a neuron soma over time during the change of two different surrounding media of different RI.

These authors obtained a mean neuron RI of 1.375. This value was computed from the analysis of soma only. As a first hypothesis, they suggest to use this value to calculate the thickness of all neuronal compartments, soma and neurites included. However, this hypothesis is strong and might be irrelevant considering the difference of composition between the different neuronal compartments, in particular between the soma (which contains the nucleus) and the neurites. Following the work of Rappaz et al., we built a system to measure the RI of neuronal processes and prepared suitable medium of different RI.

7.2 Medium preparation and characterization

As described in [169], we prepared medium considering several guidelines considering that we would aim at measuring living neurons. By default, we took the following constraints to prepare our medium : to contain all the element of neurons survival for the purpose of live imaging; to have the same osmolality; to have enough different RI values. Below the two media preparation protocols and RI measurements are detailed.

7.2.1 Medium

The media prepared were exactly the same except for one sugar which was Mannitol is one medium and Nycodenz in the other one. The **Table 3.2** details their composition.

HEPES pH 7.4	5.4mM [1.5 mL]
NaCl	130mM [0.754 g]
KCl	5.4mM [0.040 g]
Glucose	10mM [m = 0.18 g]
CaCl ₂	1mM [m = 0.012 g]
MgCl ₂	0.5mM [m = 0.004 g]
BSA	1mg/ml [m = 100mg]
B27	50x [2ml]
Mannitol or Nycodenz	60mM [1.092 g or 4.926 g]
Water	qsp 100mL

Table 3.2 – *Media components. The only difference between the two media used is the use of mannitol or nycodenz sugar. All these components are mixed and filtered.*

7.2.2 Osmolality adjustment

The osmolality of these media were adjusted by adding water until reaching a value similar to the Neurobasal medium, using a freezing point osmometer (Löser Messtechnik).

We measured values around 218 mOsm/kg \pm 2 mOsm/kg for Neurobasal, which we compared with PBS (280 mOsm/kg \pm 2 mOsm/kg), MEM (290 mOsm/kg \pm 2 mOsm/kg) and DMEM (336 mOsm/kg \pm 2 mOsm/kg) media. These values did not change for complete medium, where serum was added. As the low value of osmolality of the Neurobasal seems to be important in neurons maintenance, we thus keep its value when preparing our media.

NaOH was added to adjust the medium pH before the final step of filtration.

7.2.3 Refractive index measurement

Using an ellipsometer (Néel Institute), we measured, at $\lambda = 664.65$ nm, $n_M = 1.333695$ for the medium containing Mannitol and $n_N = 1.33887$ for the one with Nycodenz. The refractive difference was then only $\Delta n = 0.005205$, in agreement with the work of Rappaz et al. [169]. Knowing that working with such a small difference will be challenging, we nevertheless used these medium as a first attempt to retrieve the cell refractive index.

7.3 Custom-made medium replacing system and closed perfusion chamber

To allow a rapid medium change without inducing a displacement of the chamber, we built a custom-made system as well as a closed perfusion chamber.

The custom-made medium replacing system consists in a 3D printed box containing two peristaltic pumps controlled by three switches and one potentiometer. With the switches we were able to fill and empty at the same time or separately the chamber at a rate controlled by the potentiometer. The **Figure 3.22 Left** displays schemes of this system and in **Appendix 5** is detailed the electronic circuitry.

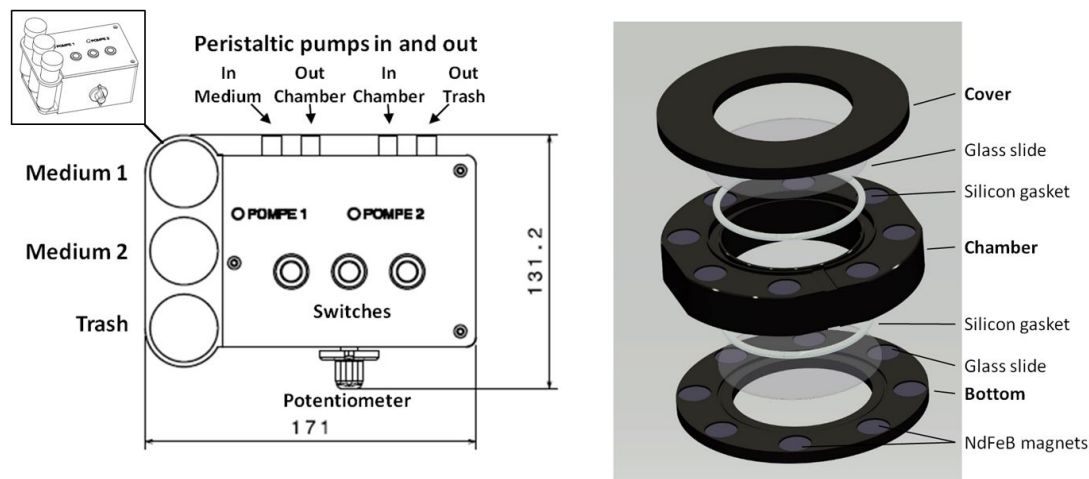


Figure 3.22 – **Left:** Top view of the custom-made medium replacing system schemes. **Inset:** side view. **Right:** Custom-made closed perfusion chamber.

This system was coupled with a custom-made closed perfusion chamber. This chamber was made using the same principle as the magnetic chamber from Chamliide. The glass coverslip on which cells are cultivated closes the bottom part of the chamber. Using a same approach, we designed a chamber with a magnetic closing cover, replacing at the same time the diver function to keep a constant medium thickness, and avoiding air particles to enter into the chamber. This chamber was also designed for further live imaging, providing a close environment to avoid contamination. **Figure 3.22 Right** displays designs of this chamber (without the perfusion tubes that were added later) and technical schemes are available in **Appendix 6**.

7.4 Preliminary result

Despite many improvements of the system stability and resolution and many experimental runs, only one conclusive result was obtained, which is displayed in **Figure 3.23**.

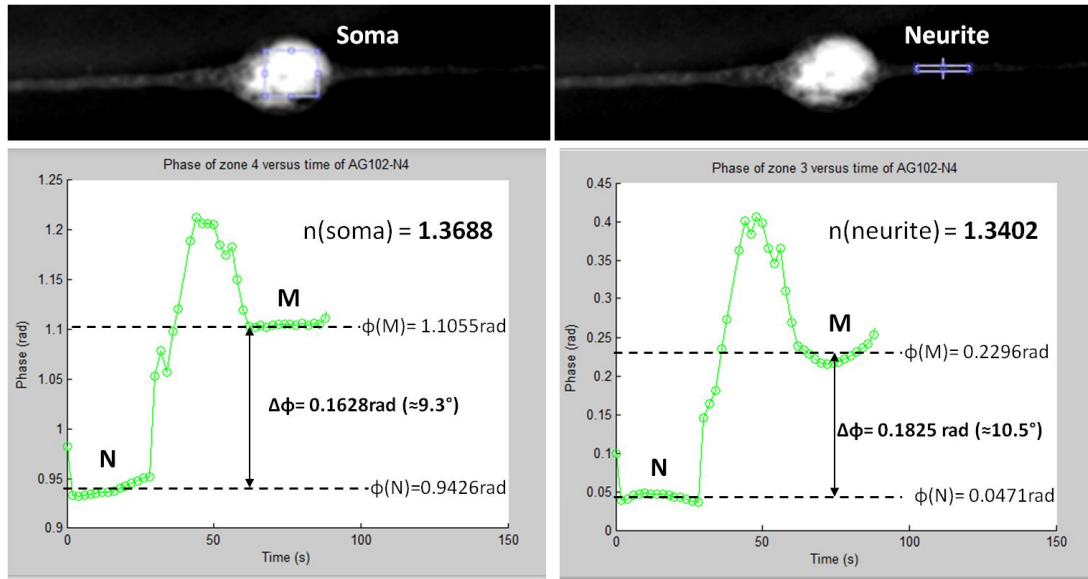


Figure 3.23 – Decoupling procedure on a patterned neuron fixed at DIV3. The upper images show the area selected for the mean phases plotted in the lower graphs showing the mean phase values along the time. We can see different mean phase values for the two different medium containing Mannitol (M), $\varphi_{M \text{ soma}} = 1.1055 \pm 0.005$ and $\varphi_{M \text{ neurite}} = 0.2296 \pm 0.013$, or Nycodenz (N), $\varphi_{N \text{ soma}} = 0.9426 \pm 0.013$ and $\varphi_{N \text{ neurite}} = 0.0471 \pm 0.014$. This gives RI values of 1.37 ± 0.03 for the soma and 1.34 ± 0.07 for the selected neurite part.

This measurement shows a soma RI, $n_{\text{soma}} = 1.37 \pm 0.03$, close to the one measured previously by Rappaz et al. [169], i.e. 1.375. In addition, we found a much lower value for the neurite RI, $n_{\text{neurite}} = 1.34 \pm 0.07$. Nevertheless, the error propagation of errors on phase values doesn't give enough precision on RI. These measurements are then only considered as first glimpses of neuron RI values. The Matlab routine used to plot the phase over time while media were changed is described in **Appendix 3.6**.

Using the the neurite RI instead of the soma RI to convert the neurite phase image into a height map, we observed that one neurite height maps was 5 times higher than the other, which brings the thickness of neurite (eg near the soma) on the order of 1-2 μm . This is illustrated in **Figure 3.24**. However this neurite RI was retrieved on a selected neurite zone. This value may not be constant along the neurite, especially between the part close to the soma and the tip which have different caliber and different internal organizations. The large differences obtained for heights values illustrate the strong dependence of the measured heights on RI values. Accurate measurements would require a knowledge of local RI at each pixel.

This single result is then not sufficient to draw general conclusion and not reliable

looking at the error attached to the phase measurement. Indeed, even with the previously measured phase shift stability of 0.007 rad between successive data retrieved on the same pixel, a lower stability was observed when taking the mean phase on a larger area leading to phase difference errors about 0.02 instead. It would be more reliable to perform this experiment with two media with a more significant RI difference inducing a higher phase difference. Limiting our experiments with fixed cells will open a large range of possibilities for the choice of the medium. Such experiments are planned in the near future.

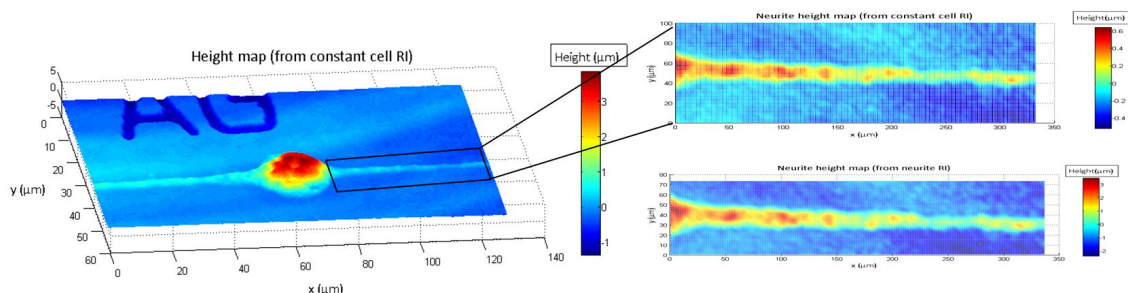


Figure 3.24 – Height maps converted either by using a constant cell RI based on the measured RI of the soma (left), either by using separated RI for soma and neurite (right crops of the neurite).

Moreover, even if, as hypothesized, the RI difference between two neurites is smaller than the RI difference between soma and neurite, we have seen that this small difference in RI induce a significant difference in heights, as shown in **Figure 3.24**. Being able to measure the local RI of neurons is therefore critical.

8 Conclusion and outlooks

8.1 Summary of the most important findings

This study is showing that the DHM provides a great tool to measure the dry mass with a good resolution.

We observed a general increase of the local dry mass per unit of length with the neurite width. Interestingly, we showed before (**Chapter 2 Figure 2.16**) that the microtubules polymerization increases locally of about 2.46 times when the stripe increases by a factor 3. Taking into account the width and material repartition variations, especially on wide stripes, dry mass and microtubules polymerization seem to evolve in concordance.

At the whole cell level, results show interestingly that there may be a homeostasis in the neurite total mass in the early stages of growth and that it might be broken when the axonal polarization takes place. This could be related to the difference in components present in axons and dendrites (cf **Chapter 1**). It would be interesting to study the dry mass density in axons and dendrites of similar widths, after axonal polarization has occurred (at 3 DIV), to observe if the broken homeostasis observed is an effect of the axonal polarization only or if it is also dependent on the neurites widths.

8.2 Outlooks

We observed previously that, on non-polarized neurons grown on symmetric patterns, the total neuritic length decreases by only a factor 1.6 (**Chapter 2, Figure 2.7**) when the stripe width increases by a factor of 3. This would mean that the expected surface of adhesion on larger stripes is not conserved but increased by a factor $3/1.6=1.9$ when increasing the width of the adhesive stripes from 2 to $6\mu\text{m}$. To be coherent with the total dry mass homeostasis that our results suggested, the wider neurite should then be less dense, i.e. showing half of the dry mass density of a neurite grown on a $2\mu\text{m}$ wide stripe, or much thinner. Such conclusions would be in contradiction with what was observed in this chapter and for microtubules (**Chapter 2, Figure 2.16**). One explanation would be to take into account the real neurite width when calculating the neuritic surfaces. Indeed, the total dry mass measurement is here calculated from the computation of the real neurite width along the neurite. For the neurons observed at 2 DIV with the 63x of the DHM, the effective mean width measured on $6\mu\text{m}$ wide stripes, reflecting the tapering effect, is $3.4\mu\text{m} \pm 1.9\mu\text{m}$. On the other hand, the mean width measured on $2\mu\text{m}$ wide stripes is $2.1\mu\text{m} \pm 1.2\mu\text{m}$. We then obtain a width ratio about 1.6 instead of 3. Using this values to calculate the neurite surfaces on the different stripes, we now obtain a conservation of the neuritic surface.

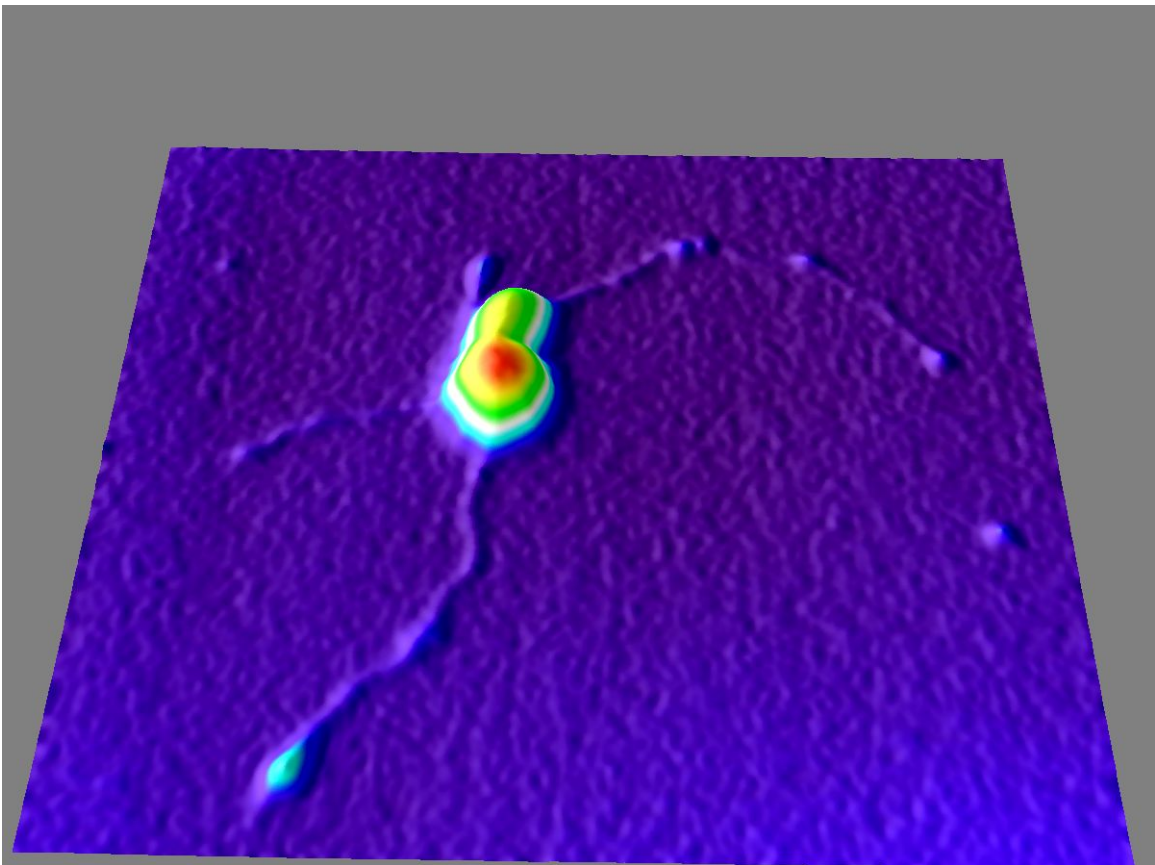
However more data would be needed to confirm this trend regarding the neurite dry mass, which would be now easier to perform with our improved measurement system. In addition, volume measurements would be needed to observe these evolutions considering the whole cell components.

This could be achieved using the DHM if we could retrieve the mean RI values for neurites of different widths, allowing us to deduce the neurites height directly from phase shift measurements. This would be of a great interest since phase shift measurements are now mastered for our system. For that, we would need to perform the DP using two media of larger difference in RI. We are currently looking for such media but these data are not

yet available.

This difficulty led us to adapt another volume measurement technique which was developed at the Curie Institute: the Fluorescent Exclusion method, which is the focus of the next chapter.

VOLUME MEASUREMENT WITH THE FLUORESCENT EXCLUSION METHOD (FXM)



Neuronal constellation.
C. Braïni & A. Mottolese, IPGG, Paris.

1 Introduction

The Fluorescence eXclusion method (FXm) is a novel method to access to cells volume. This technique requires to culture cells into a close biocompatible chamber of known height filled with a fluorescence medium and containing a reference object. The resolution and accuracy of this device depend on its geometrical characteristics as well as on imaging parameters. Some technological choices were thus made to build chambers allowing us to reach a resolution adapted to our objects of interest, i.e. neurons and neurites. The design, and geometrical characterization of the FXm devices and the optical validations of the FXm method are at the center of the three first parts of this chapter. The following sections will describe the suitable cell culture protocol and analysis methods. In the last section, I will finally present preliminary results about neurites static and dynamic volume changes.

2 Contributions

This work was initiated in the Curie Institute with Sylvain Monnier, from Jean-Louis Viovy and then Matthieu Piel's team, who taught me the basics of the FXm method. Molds were designed and fabricated by Ivan Ferrante in collaboration (regarding silicon deep etching) with S. Marasso and F.C. Pirri from Chilab, Politecnico di Torino in Italy. Chips preparation and characterization as well as imaging were performed with the help of Angelo Mottolose, a Master 2 student intern under my supervision. He particularly performed all the profilometer measurements. Optical tests were performed in collaboration with Clotilde Cadart from Matthieu Piel's team, Olivier Thouvenin from Langevin Institute and Benoît Vianay from Cytomorpho Laboratory (Hôpital St Louis, Paris).

3 Chip for neuronal volume measurement

To fabricate measurement chambers, we chose to use PDMS chambers sustained by pillars, as already reported in [145]. Pillars constitute also reference objects of known height used for the conversion from intensity images to height maps. Taking into account the specific micrometric morphologies of neurons, including a cell body relatively big (more than $5\mu\text{m}$) compared to thin and long neurites of micrometric to submicrometric sizes, we chose to work with specific chamber designs.

3.1 Chamber design

Our microfluidic chambers, or chips, consist in a measurement zone of chosen height with sustaining pillars, connected through three other zones of increasing heights to one

inlet and one outlet. These three zones are implemented to avoid fluorescence contamination from the high fluorescence intensity of the inlet and outlet. We chose to build two types of chips: one to measure whole neurons volume, for which measurement chambers contain 10 or 12 μm high pillars; and one to measure only neurites, with a measurement chamber of 3 μm high, blocking the soma at the entry of this zone during the seeding step. A few images of these designs are presented in **Figure 4.1**.

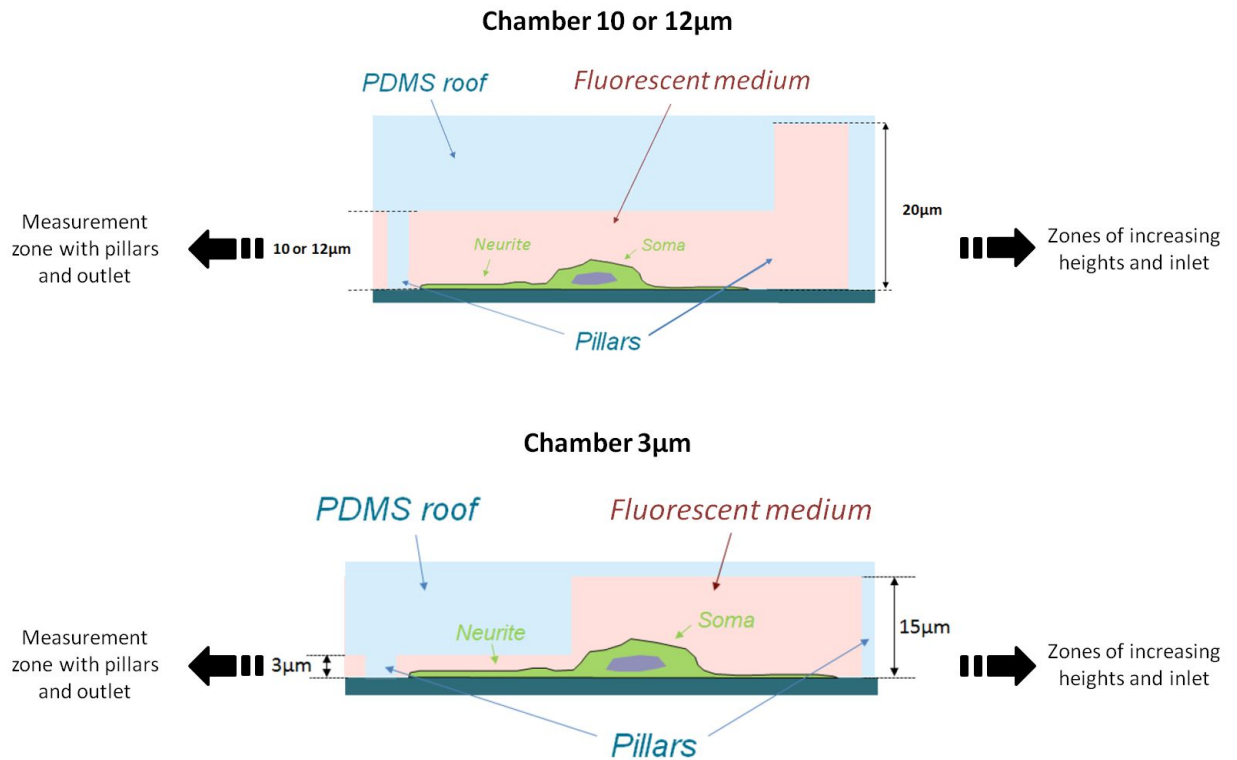


Figure 4.1 – Schematic side views of PDMS chambers adapted to whole neurons (up) or to neurites (down) volume measurement. Chips are made in PDMS (blue) and filled with a fluorescent medium (pink). Only the measurement zone and the last zone between the inlet and the measurement zone are displayed. Pillars are present in these two zones.

3.2 Microfabrication

The effective architecture of the chip for neuronal volume measurement is displayed in **Figure 4.2**. Our first design is shown on the left, including one inlet and one outlet. The right side displays the latest design, where two reservoirs connected to the measurement zone were added. The role of these reservoirs is to improve cells survival. This new design includes also a thinner "neck" between the inlet and the measurement zones. In this case, the width of each intermediate chamber between the inlet and the measurement zone were chosen in order to keep constant the sections encountered by the flow and thus the liquid

flow velocity. This point proved to be important to avoid cell sedimentation next to the inlet.

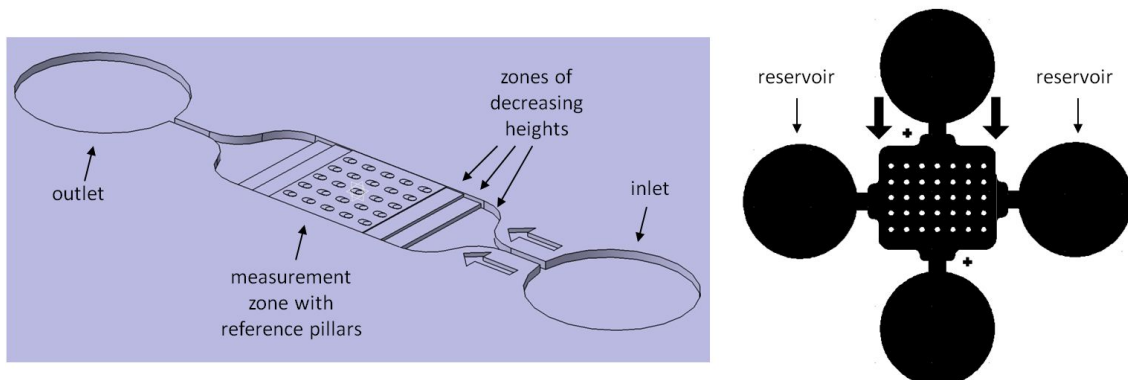


Figure 4.2 – *Designs of the FXm devices. Typical devices include one inlet, one outlet, three zones of intermediate heights and the central measurement zone containing the reference pillars (left). The more recent design (right) includes reservoirs and optimal heights of the intermediate chambers.*

PDMS chips are made by pouring the liquid PDMS into a mold and curing it. Molds are usually created by micro-milling of brass. Traces of the milling machine passage are usually visible on the roof and are replicated to the chip PDMS roof. This induces some roughness which can impact our measurement. We thus chose to use silicon molds using photolithography.

3.2.1 Photolithography

The chip containing four zones of different heights (one measurement zone and three zones of decreasing heights), we designed the four masks displayed in **Figure 4.3**. In order to use the intact silicon surface to mold the roof of the chip, the purpose of the first mask was to etch holes corresponding to the future pillars using Deep Reactive ion etching (DRIE).

After the deep etching step, the wafer is cleaned using successively acetone, pirana etching solution¹ and DI water. Three layers of SU-8 negative resist are then deposited through alignment steps using the last three masks of the **Figure 4.3**.

1. Pirana bath: mixing about 1 part of H_2O_2 and 3 parts of H_2SO_4 .

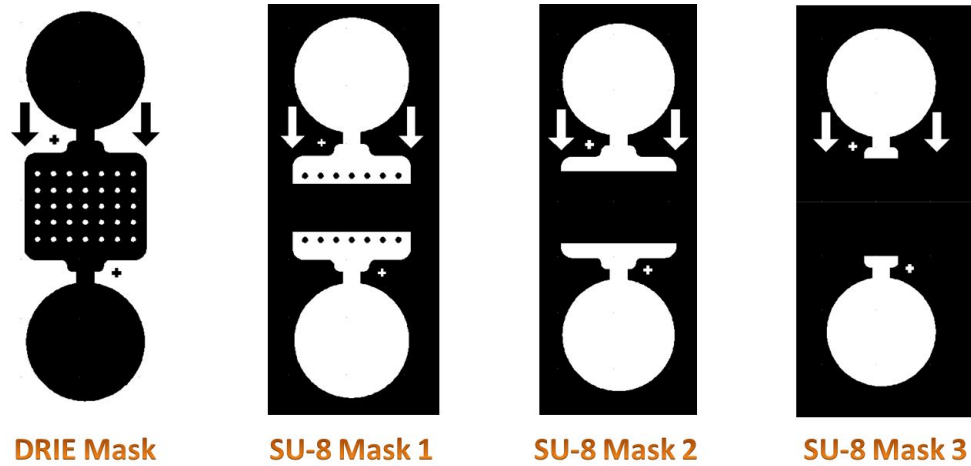


Figure 4.3 – Masks used for the different steps in the chip fabrication.

The different SU-8 types used for each intermediate chambers and the parameters for spincoating, baking, exposure or development steps are detailed in the **Tables 4.1, 4.2 and 4.3**. **Figure 4.4** summarizes the results of the different photolithography steps leading to the final composite Silicon-Su8 mold.

Step	Mask 1: 8 μ m layer	Mask 2: 30 μ m layer	Mask 3: 50 μ m layer
SU-8 type	2007	2025	2050
Spincoating	30s @ 2000rpm	30s @ 3050rpm	30s @ 3250rpm
Soft bake	3min @ 95°C	2min @ 65°C + 6min @ 95°C	3min @ 65°C + 7min @ 95°C
Exposure time	11s	15.5s	17s
Post-exposure bake	4min @ 95°C	1min @ 65°C + 6min @ 95°C	2min @ 65°C + 7min @ 95°C
Development	2min 30s	5min	6min
Hard Bake (optional)	3-5min @ 200°C	3-5min @ 200°C	3-5min @ 200°C

Table 4.1 – Photolithography steps performed to build a device including a central chamber of 12 μ m in height. Heights of the intermediate chambers: 20, 50 and 100 μ m.

Step	Mask 1: 10 μ m layer	Mask 2: 30 μ m layer	Mask 3: 50 μ m layer
SU-8 type	2007	2025	2050
Spincoating	30s @ 1500rpm	30s @ 3050rpm	30s @ 3250rpm
Soft bake	3min @ 95°C	2min @ 65°C + 6min @ 95°C	3min @ 65°C + 7min @ 95°C
Exposure time	12.5s	15.5s	17s
Post-exposure bake	4min @ 95°C	1min @ 65°C + 6min @ 95°C	2min @ 65°C + 7min @ 95°C
Development	2min 30s	5min	6min
Hard Bake (optional)	3-5min @ 200°C	3-5min @ 200°C	3-5min @ 200°C

Table 4.2 – Photolithography steps performed to build a device including a central chamber of 10 μ m in height. Heights of the intermediate chambers: 20, 50 and 100 μ m.

Step	Mask 1: 12 μm layer	Mask 2: 35 μm layer	Mask 3: 50 μm layer
SU-8 type	2015	2025	2050
Spincoating	30s @ 3250rpm	30s @ 2500rpm	30s @ 3250rpm
Soft bake	3min @ 95°C	2min @ 65°C + 5min @ 95°C	3min @ 65°C + 7min @ 95°C
Exposure time	14s	15.7s	17s
Post-exposure bake	4min @ 95°C	1min @ 65°C + 5min @ 95°C	2min @ 65°C + 7min @ 95°C
Development	3min	5min	6min
Hard Bake (optional)	3-5min @ 200°C	3-5min @ 200°C	3-5min @ 200°C

Table 4.3 – *Photolithography steps performed to build a device including a central chamber of 3 μm in height. Heights of the intermediate chambers: 15, 50 and 100 μm .*

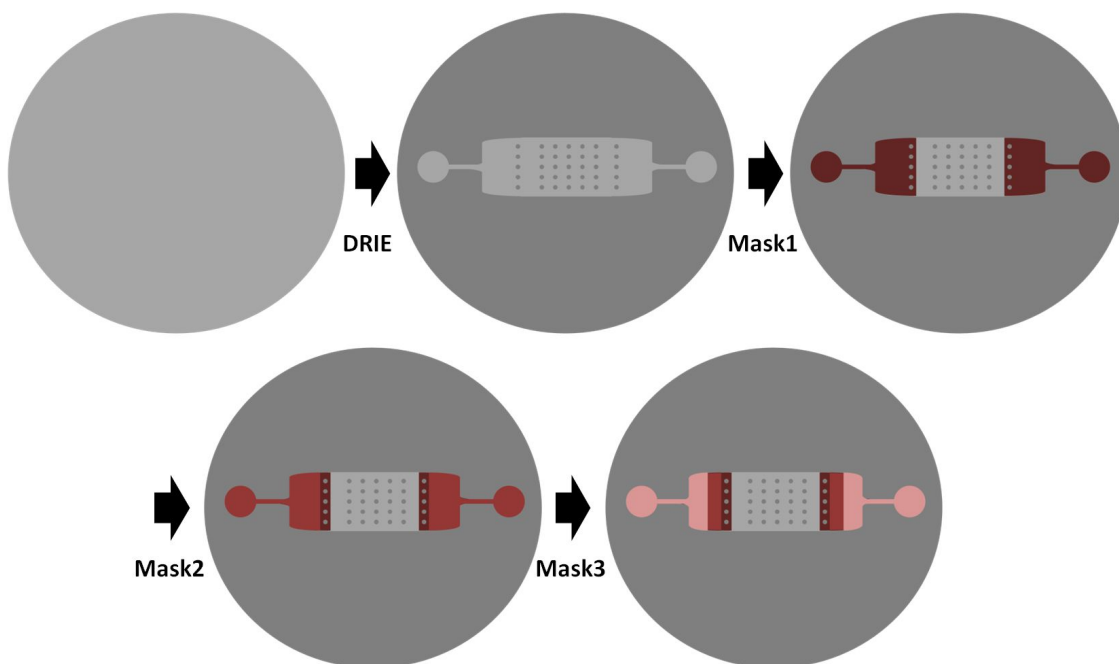


Figure 4.4 – *Photolithography steps. Following arrows: The silicon wafer (light grey) is etched by DRIE (dark grey); three layers of SU-8 negative resist (reds) are spincoated and exposed through Mask1, Mask2 and Mask3. All these steps requires specific alignment using alignment crosses (not shown).*

3.2.2 PDMS molding

First, the molds are silanized to facilitate the demolding of the PDMS. In that aim, about 200 μl of silane² are dispatched as droplets near the silicon master in a ParaFilm-sealed Petri dish. After 20 minutes incubation the silanization reaction has been performed and the master is removed.

2. Trichloro(1H,1H,2H,2H-perfluoro-octyl) silane (Sigma-Aldrich).

The type of PDMS used for this work is Sylgard 184 (Sigma Aldrich). It is mixed with a curing agent, at 1:10, which polymerizes the silicone oil base. This mix is poured into the mold using a syringe to control the chip height that we fixed at 1.5-2mm. Degasing steps are performed under a vacuum cup, before and after pouring the mix into the mold, in order to remove bubbles which could impair the micrometric structures of the chip. To harden the PDMS, the mold is placed in an oven at 67°C for at least 2h. It is finally demolded using steel tools and isopropanol and chips are cut from the PDMS block with a razor blade. Inlets and outlets are punched with a 1.5mm puncher, and chips are cleaned with isopropanol and air gun to remove remaining PDMS parts or dust. The chip is now ready for bonding on a glass coverslip. This bonding step requires to expose both the PDMS chip and the glass coverslip to an oxygen plasma during 30 seconds. We usually stick chips on FluoroDish, which are plastic Petri dish with a glass bottom, convenient for time-lapse imaging. All these steps are summarized in **Figure 4.5** together with the previous photolithography steps.

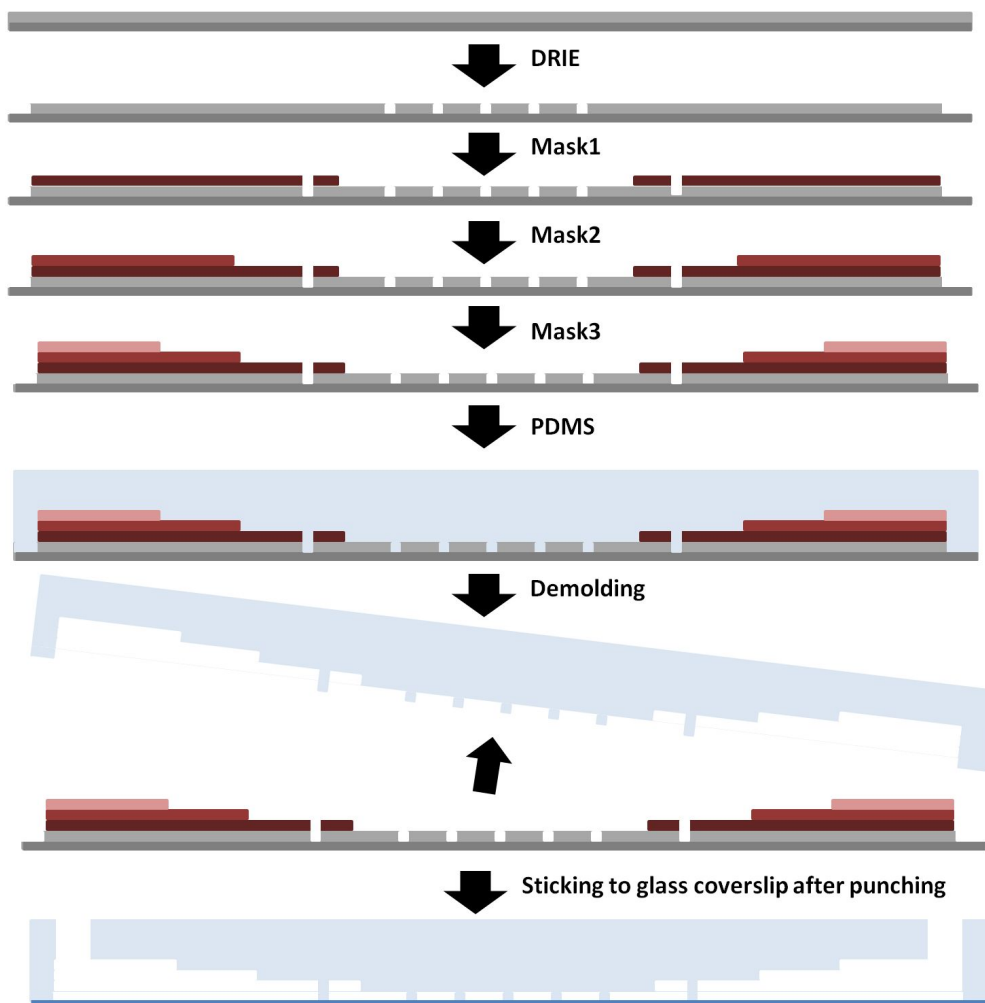


Figure 4.5 – Side view of the different photolithography steps, followed by PDMS pouring, demolding and sticking to the glass coverslip.

4 Characterization

An accurate knowledge of the dimensions and geometrical characteristics (in particular surface roughness and flatness) of the chip is critical for FXm. These characterization are presented below.

4.1 Pillars height

PDMS pillars in the measurement chambers are used as references to obtain the volume of cells. Values of pillars height must thus be measured in a precise way. Optical and mechanical profilometer measurements were performed on the three different types of FXm devices (i.e. including 3, 10 or 12 μ m in height central chambers) and on the two types of general design per central chamber (D1 standing for the first chip design and D2 standing for new design with the thin "neck"). For each case, 21 pillars were measured. The distribution of their heights are detailed in **Figure 4.6**. Their mean values will be used for all the following intensity-to-height conversions performed in these chambers.

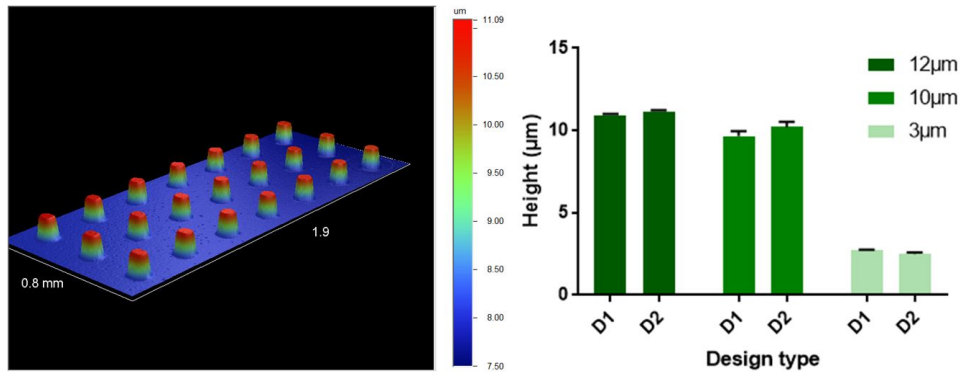


Figure 4.6 – *Left: 3D visualization of the pillars in the measurement zone of the 3 μ m high chamber. Right: Profilometer measurements of pillars height for the 3, 10 and 12 μ m high molds. Mean values: 12-D1: 10.95 \pm 0.05 μ m; 12-D2: 11.16 \pm 0.07 μ m; 10-D1: 9.67 \pm 0.28 μ m; 10-D2: 10.21 \pm 0.32 μ m; 3-D1: 2.74 \pm 0.02 μ m; 3-D2: 2.50 \pm 0.09 μ m.*

4.2 Roof roughness

We made the choice of silicon molds instead of brass molds in order to decrease the roughness of the chips roof. We therefore measured using optical profilometer the arithmetic average roughness R_a of several PDMS chips through the formula

$$R_a = \frac{1}{L} \cdot \int_0^L |Z(x)| dx \quad (4.1)$$

where L is the length of the selected zone and Z the height. 3D profilometer images of pillars found in the measurement zone of each type of chamber, including a double-height

PDMS pillar obtained from a brass mold, are presented in **Figure 4.7**.

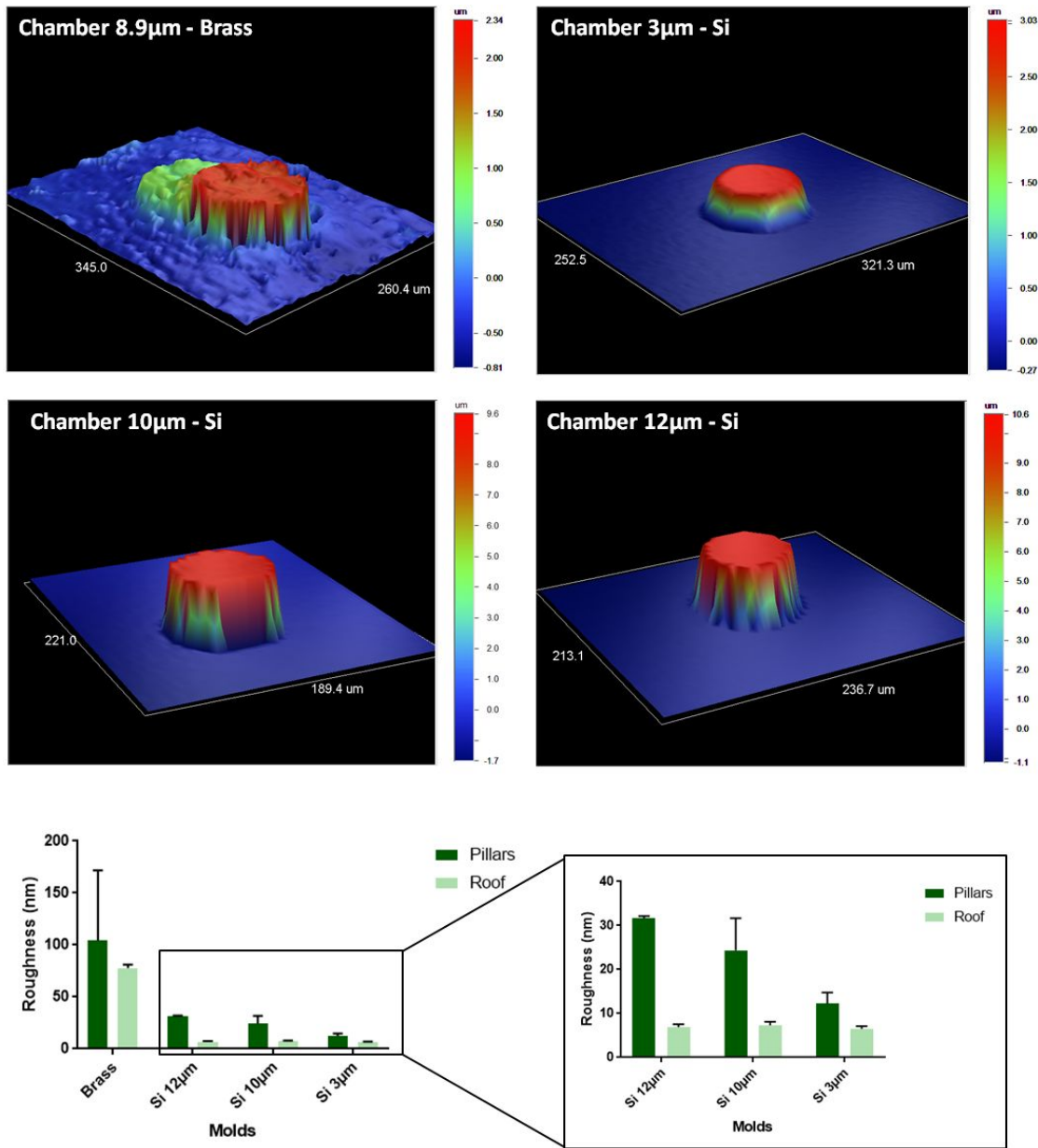


Figure 4.7 – Comparison of the PDMS roof roughness between brass molds and silicon molds with central chambers of different heights. The images display 3D representations of one PDMS pillar per type of chip. The roughness of the roof and of the top of the pillars was measured on 3 zones for each mold on areas of $180 \times 180 \mu\text{m}^2$. The graphs display mean and standard deviation values. The roughness on the brass mold (brass pillars: $104.28 \pm 67.47 \text{ nm}$; brass roof: $77.96 \pm 3.08 \text{ nm}$) is about 3 times higher than the roughness on the etched silicon parts (Si pillars: $31.67 \pm 0.47 \text{ nm}$, $24.37 \pm 7.32 \text{ nm}$ and $12.2 \pm 2.57 \text{ nm}$, for the 12, 10 and $3 \mu\text{m}$ high chambers respectively), which is itself 3 times higher than the roughness of the pure silicon (Si roof: $6.93 \pm 0.65 \text{ nm}$, $7.32 \pm 0.78 \text{ nm}$ and $6.51 \pm 0.61 \text{ nm}$, for the 12, 10 and $3 \mu\text{m}$ high chambers respectively).

4.3 Roof flatness

PDMS is a soft material and the distance between pillars, in our case $275\mu\text{m}$, is quite large in order to keep the highest possible adhesive surface for cells. The flatness of the roof is thus an important issue for the FXm method. We addressed it using ImageJ to draw profiles on chips filled with a fluorescent medium. **Figure 4.8 (A)** shows that the roof between two pillars remains flat.

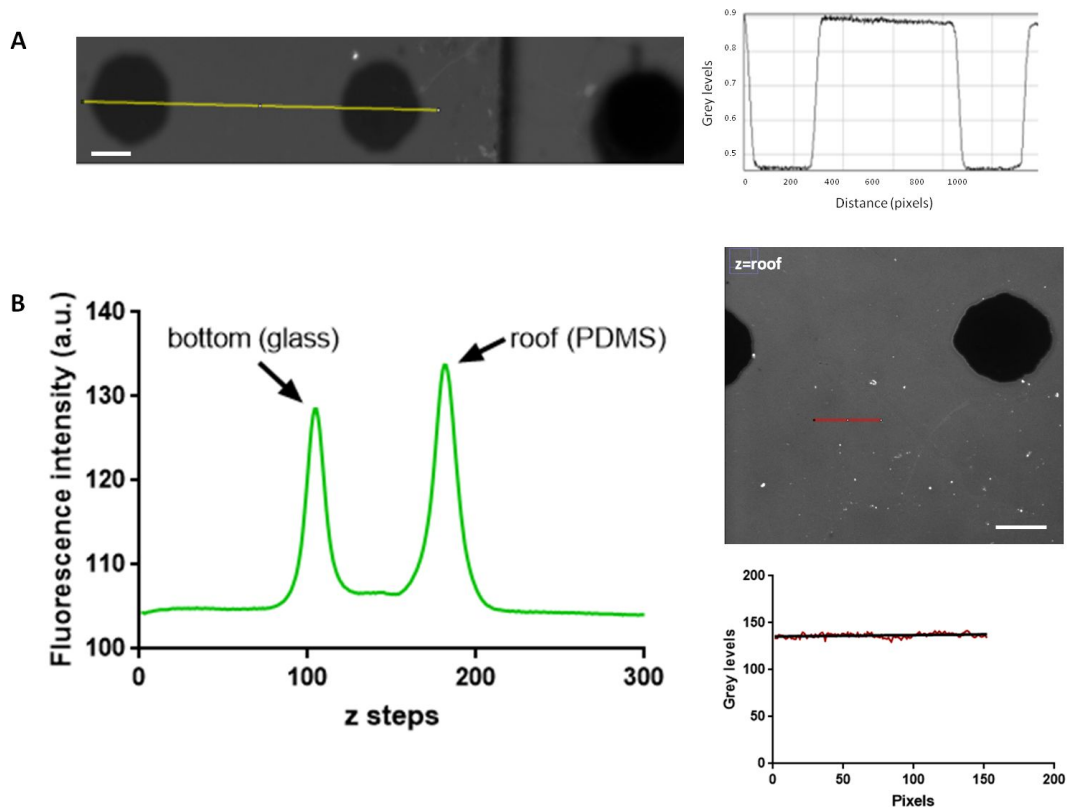


Figure 4.8 – (A) Fluorescence image of the transitions between the last zone of decreasing height (pillar on the right) and the measurement zone (2 pillars on the left) of a $3\mu\text{m}$ high chamber filled with a fluorescence medium. The cross section shows the linear repartition of the fluorescence between pillars. Scale bar: $50\mu\text{m}$. (B) Left: Spinning disk z-stack on a chamber coated with PLL-FITC and filled with PBS. The fluorescent PLL is present on the glass bottom part of the chip as well as on the PDMS roof upper part of the chip. The two peaks represent the positions of the bottom and of the roof of the chip (arrows). The peak observed for PDMS is higher in amplitude, suggesting that the PLL adsorbance is higher on the PDMS than on the glass. The cartography (line profile) of the image taken at the z-position corresponding to the PDMS roof, represented by the red line on the fluorescence image, is another evidence of its flatness (see the graph displaying the grey levels associated values, linear fit of nearly null slope 0.01463 ± 0.004208 grey level/pixel). Z-stack steps: $0.1\mu\text{m}$. Objective: 20x NA 0.75. Scale bar: $50\mu\text{m}$.

To highlight this flatness with a different approach, we coated, in a second experiment, the bottom glass coverslip and the PDMS roof with a fluorescent solution, PLL-FITC³. This was performed by incubating this solution into the chip at a concentration of 10 μ g/ml during 1h. The chip was then rinsed 3 times with PBS to wash the free fluorescent molecules in solution. Using a spinning disk to perform a z-stack⁴ we observed two peaks: one for the glass bottom, one for the PDMS roof. We confirmed the roof flatness by drawing profiles at the precise z position of the roof (**Figure 4.8 (B)**).

4.4 Control of the fluorescence contamination

The control of the fluorescence intensity pollution is important since measurements of volume are made using a reference value for the roof fluorescence intensity. If this value is not constant it can impair our measurement.

As explained previously, we implemented in our chip intermediate zones of decreasing height between the inlet and the measurement zone with the aim to avoid any fluorescence pollution into the measurement zone. To check if our designs match our initial goal, we draw fluorescent profiles crossing the different zones. We observed a constant intensity in each zone, ruling out the existence of a fluorescent pollution (**Figure 4.9**. Note that such a pollution was observed in former chips were the length of these intermediate zones were only 25 μ m (**Figure 4.10**).

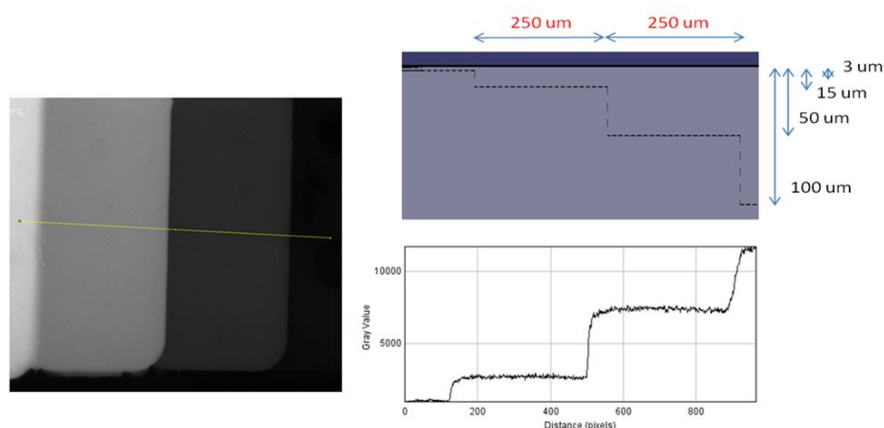


Figure 4.9 – *Absence of fluorescence pollution. The fluorescence image shows a 3 μ m high chip filled with a fluorescence medium. The upper right scheme represents the heights and lengths of the different parts of the device. The graphs displays the grey levels values of the profile drawn on the fluorescence image. The lengths of the zones of decreasing heights before the measurement zone are long enough (250 μ m) and no fluorescent contamination is observed. Scale bars: 100 μ m.*

3. PLL-FITC: Poly-L-Lysine fluorescent, emitting at 488nm (green).

4. Spinning disk set-up: Leica DMi8, Yokogawa CSU-X disk, Andor ILE laser, Nanoscan Z controller.

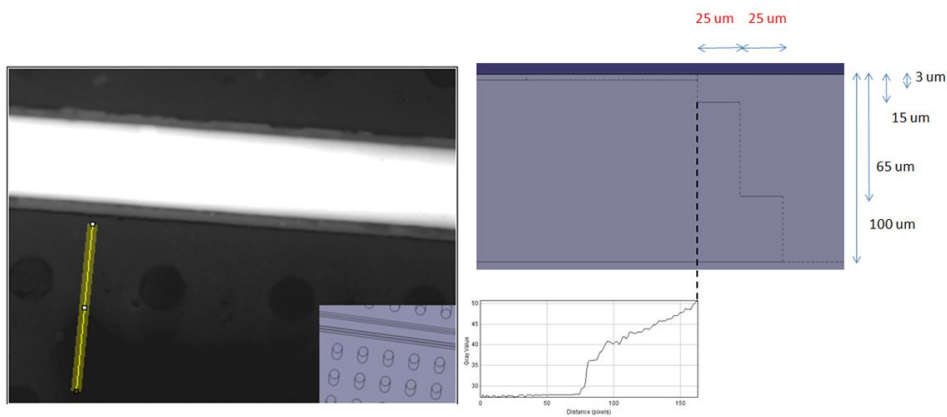


Figure 4.10 – *Fluorescence pollution. The fluorescence image show a chip filled with a fluorescence medium. The inset represents the design of the chip. The upper right scheme represents the heights and lengths of the different zones. The graphs displays the grey levels values of the profile drawn on the fluorescence image. Because of the short width of the central bright zone (25 μ m) the fluorescence of this higher chamber is contaminating the measurement chambers on each side. Scale bars: 100 μ m.*

The quality of the FXm approach depends on many other methodological choices than those associated to the chip designs. Optical constraints and the choice we made accordingly are detailed in the following section.

5 From fluorescence intensity to height

The FXm is a sensitive method and careful choices should be made concerning the optical setup. I will first assess the validity of the linear conversion from fluorescence intensity to height, then I will discuss our analysis methods and precautions we took about chambers and objectives choices.

5.1 Conversion law

The FXm method is based on the ability to convert a fluorescence intensity into an height value using a reference object in the field of view.

Figure 4.11 shows a typical intensity map we can obtain in one of our 12 μ m high chamber where neurons were seeded with a fluorescent medium. Expectedly, the intensity goes to the minimum intensity at the pillar level, whereas the soma gives an intermediate fluorescent signal. We can observe a small decrease of the fluorescent intensity at the neurite level, which indicates that the study of the neurite morphologies will be possible in our devices. To be confident that the fluorescent intensity scales with the size of the objects, we performed the following experiments using as references different objects of known height.

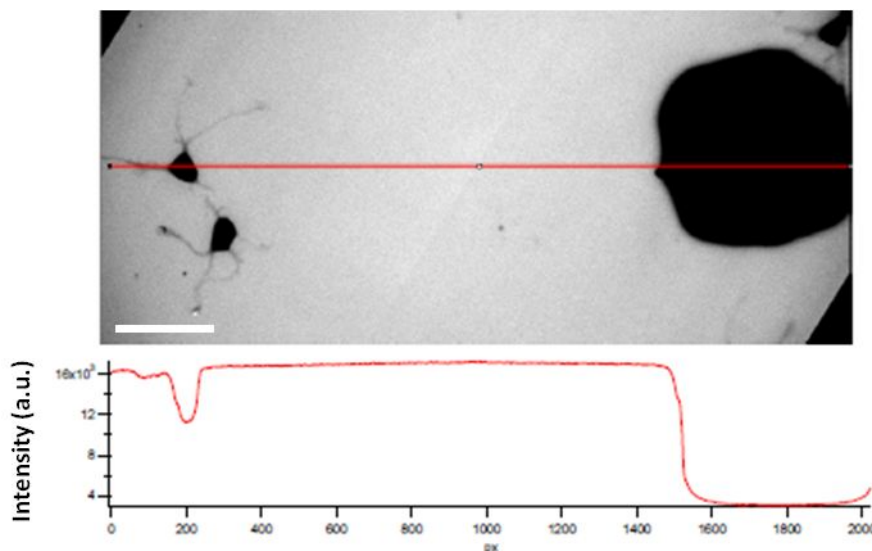


Figure 4.11 – *The fluorescence image represents a part of the measurement zone of a chamber 12 μ m filled with a fluorescent medium. Neurons and one reference pillar are imaged. The profile displays the variation of intensity of the different objects (pillar, soma, neurite). Objective: 20x NA 0.75. Microscope: Leica DMI8. Camera: Hamamatsu ORCA Flash 4.0 V2. Scale bar: 50 μ m.*

Using a PDMS chip filled with a fluorescent medium, we measured the mean intensity values of a pillar of three different micrometric heights⁵ (**Figure 4.12 A**). The fluorescence intensity to height conversion was observed to follow a linear variation. In a second experiment, we confirmed the linearity of the intensity to height conversion using sub-micrometric structures etched on a glass coverslip⁶ (**Figure 4.12 B**). These experiments show that pillars with only one height are sufficient to get the linearity factor needed for conversion.

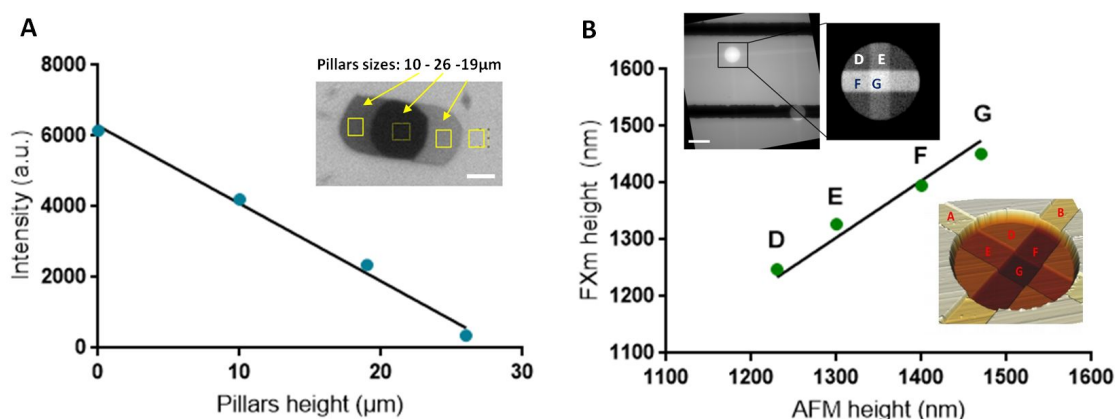


Figure 4.12 – **(A)** Experimental validation of the linear relationship between fluorescence intensity and pillars of different heights. Measurements were made in a 26 μm high PDMS chamber, with pillars with 3 different heights in the measurement zones: 10, 19 and 26 μm . The inset represents one pillar surrounding by a fluorescent medium, with the yellow areas displaying the zones where were calculated mean intensities displayed in the graph. Objective: 40x NA 0.8. **(B)** Experimental validation of the method on sub-micrometric objects. A fluorescent medium was introduced between the etched glass coverslip and another glass coverslip positioned on 0.5 μm high resist stripes used as spacers. Insets display fluorescence (Objective: 20x NA 0.4. Scale bar: 100 μm .) and AFM images showing the structures of different heights (A to G letters). Taken the photoresist spacers as height references, we were able to measure the height of different zones (D to G) with the FXm. These results were compared to the AFM measured heights. The linear fit (1.003 ± 0.007942) displayed on the graph shows the good correlation between the two measurements. Microscope: Leica DMi8. Camera: Hamamatsu ORCA Flash 4.0 V2.

5. The chip used for this experiment was provided by Matthieu Piel's team.

6. The etched glass coverslip used for this experiment was provided by Benoît Vianay, together with AFM measurements of each zone of this coverslip

5.2 Choice of objectives

Whereas high NA are better for a high lateral resolution, their depth of field (DOF) is smaller compared to low NA objectives (**Figure 4.13**). Since neurites are very thin structures, we chose to keep a good enough lateral resolution and thus to work with higher NA. To assess the role of DOF in the precision of our measurements, we observed the same cell in a chamber of $12\mu\text{m}$ high with four different objectives of different NA: 20x with a NA of 0.4, 20x with a NA of 0.7, 40x with a NA of 0.65 and 40x with a NA of 0.8. These combinations have respectively a DOF of about 4.0, 1.3, 1.5 and $1.0\mu\text{m}$ ⁷. These observations were performed at different z positions around the focus (**Figure 4.14**).

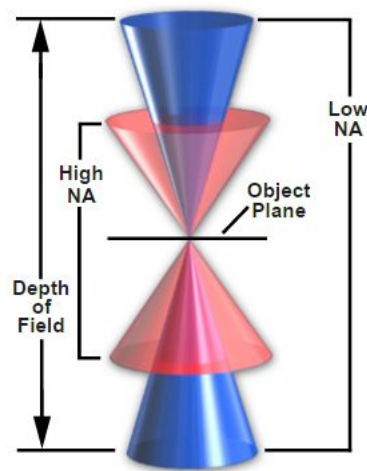


Figure 4.13 – *Depth of Field Ranges. Adapted from MicroscopyU is Nikon’s educational website.*

Depending on both magnitude and NA, we found different linear slopes between intensity and the height. We used these slope to convert into volume values the same area around the cell. Interestingly at the focus the volume values are quite similar for the different objectives. For high NA, and thus lower DOF, the measured volume value differs rapidly from reality with the distance to focus. This result might express the existence of a light pollution from regions of the fluorescent medium that are not immediately above the object of interest but close to it when the height of the object is higher than the DOF of the objective. Depending on the measurement conditions, this pollution can be high enough to impair the value of the volume we retrieve by drawing a contour even much larger than the object itself. To avoid such drawbacks of the FXm, our strategy will be to stay at the focus and to verify that our object’s height is compatible with the DOF.

7. The DOF value is here taken as $\text{DOF} \simeq \frac{\lambda n}{(NA)^2}$, with $\lambda = 647\text{nm}$, the wavelength of illuminating light, and $n=1.000$, the refractive index of the medium between the coverslip and the objective front lens element.

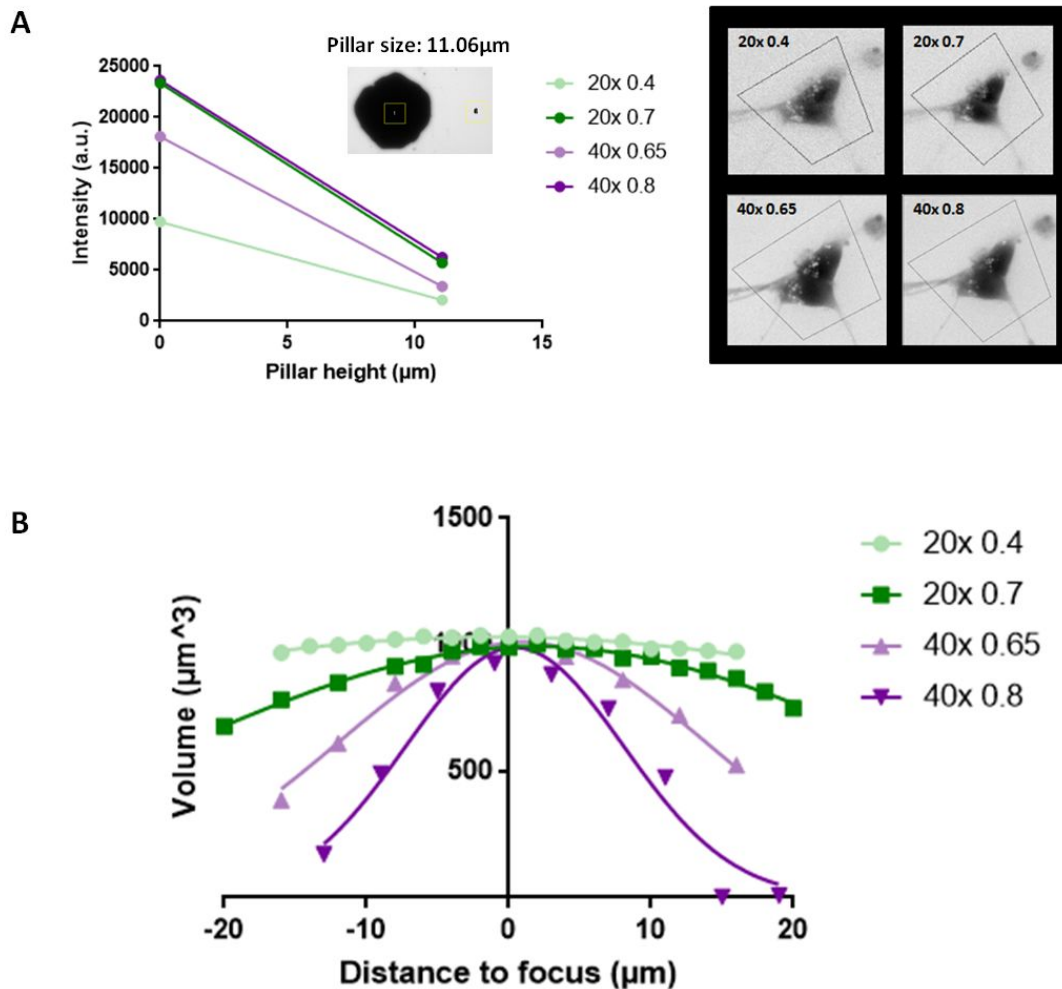


Figure 4.14 – Comparison of volume measurements on the same cell with different objectives of different magnifications and numerical apertures. (A) Intensities of background and pillars of a 12µm high chamber used to get the intensity-to-height conversion factor (left) to convert the fluorescent images (right) into height maps. (B) Volume of areas around the cell showed in (A) calculated with the FXm. Fluorescent pictures were taken at different distances from the focus. For higher NA, when the measurement is done out of focus, less intensity signal is collected. The calculated volume values are thus getting away from reality rapidly with the distance to focus. Objectives: 20x NA 0.4, 20x NA 0.7, 40x NA 0.65, 40x NA 0.8. Microscope: Leica DMI8. Camera: Hamamatsu ORCA Flash 4.0 V2. Fluorescent medium emitting at 488nm (green).

The validation of the volume measurement on the chamber of 12µm in height with the 40x of NA 0.8, which was the chosen objective to study neurons, validates thus measurements on lower chambers of 3 and 10µm height.

5.3 Measuring volumes and heights

From the previous discussion about light pollution from fluorescent regions not immediately above the object of interest, it is not straightforward that the FXm will provide the exact height of a given object at each pixel. The accuracy of the measurement depends in particular of the height of the object of interest compared to the depth of field defined by the numerical aperture (NA) of the objective. We have seen that working at focus minimizes the error on the volume if integrating the fluorescence intensity within a region larger than the object of interest. Nevertheless, the phenomenon of light pollution might locally affect the converted height value at a given pixel, especially if this pixel is located at the edge of the object. We have therefore performed experiments with a reference object whose volume and height on each point is known, as described below.

5.3.1 Volume

We produced a reference object characterized by a height similar to those of neurites (**Figure 4.15**). This object is a $1.18 \pm 0.02\mu\text{m}$ ⁸ high and $10\mu\text{m}$ wide S1805 resist stripe made by photolithography⁹ on a glass coverslip. After sticking a chip on this coverslip and filled it with a fluorescent medium, we calculated the volume of the whole stripe as well as the volume of some small areas of the stripe with the FXm. As expected FXm and geometric volumes values are similar.

5.3.2 Height

We then extracted intensity profiles, perpendicularly to the stripe, and converted them into height profiles. These profiles were taken with a width of 10 pixels, which is about $1\mu\text{m}$ of stripe length, to get rid of some background noise and to be sure to collect a representative number of pixels of such a profile at this position. For three different positions on the stripe, we obtained a height of $1.16 \pm 0.03\mu\text{m}$ (**Figure 4.15**). This validates height measurements at the local level.

Nevertheless this is especially true since this object is flat. However neurons are not expected to be flat objects. We thus chose not to measure the height at each pixel but to perform analysis as described below.

8. Measurements performed on 8 zones with a profilometer.

9. See **Chapter 2** for S1805 photolithography steps parameters.

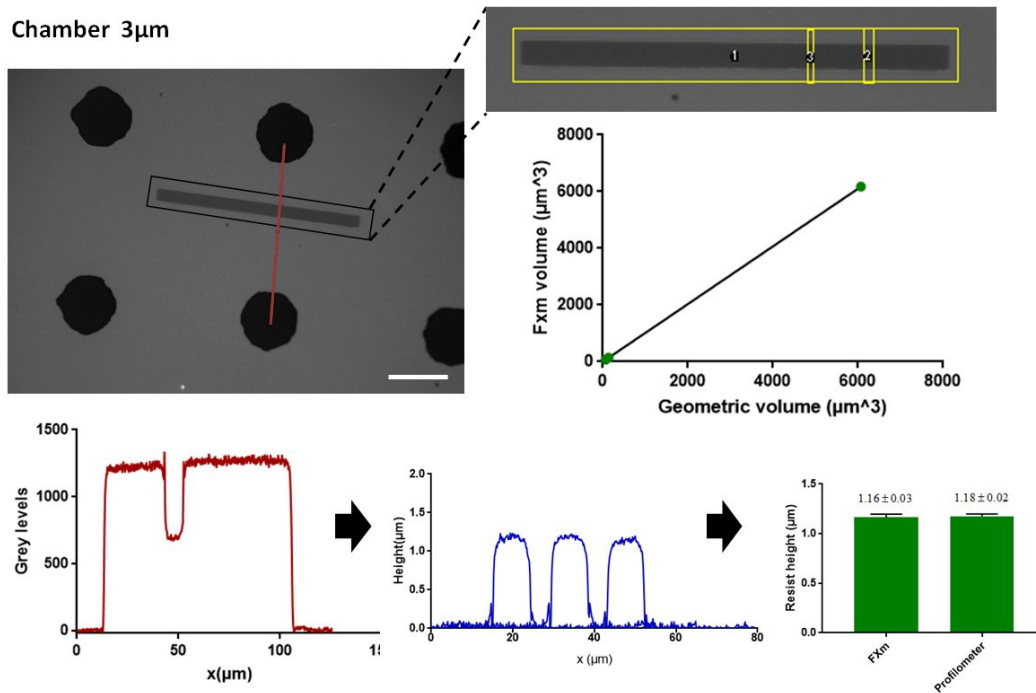


Figure 4.15 – Validation of volume and height measurements. The fluorescence image shows a resist stripe surrounding by pillars of $3\mu\text{m}$ high in a PDMS chamber filled with a fluorescent medium (emitting at 488nm (green)). The volume of the areas in yellow in the upper image were calculated with the FXm and compared with the geometrical values. The linear fit presented here shows that, as expected, similar values were obtained. The red line on the fluorescence image corresponds to the grey level profile on the graph below. These profiles were taken with a width of 10 pixels. Three profiles were extracted and converted into height profiles, as presented in blue in the second graph. Average height values calculated with FXm, $1.16 \pm 0.03\mu\text{m}$, are similar to the height values measured with a profilometer ($1.18 \pm 0.02\mu\text{m}$). Scale bar: $100\mu\text{m}$. Objective: $20\times$ NA 0.7. Microscope: Leica DMI8. Camera: Hamamatsu ORCA Flash 4.0 V2.

5.3.3 Static analysis

As illustrated in **Figure 4.15**, height profiles are extracted from cross sections defined by a width of 10 pixels (about $1\mu\text{m}$) of neuritic length. Pillars and background intensities values are then used for the intensity-to-height conversion and an integration over the height profiles is performed to obtain the volume per μm of neurite length, which we will name "volume of neurite slice". This process is illustrated in **Figure 4.15** and the Matlab routine is described in **Appendix 7**. This Matlab routine allows us to select the baseline and perform a tilt correction, if necessary. The neurite width is manually defined.

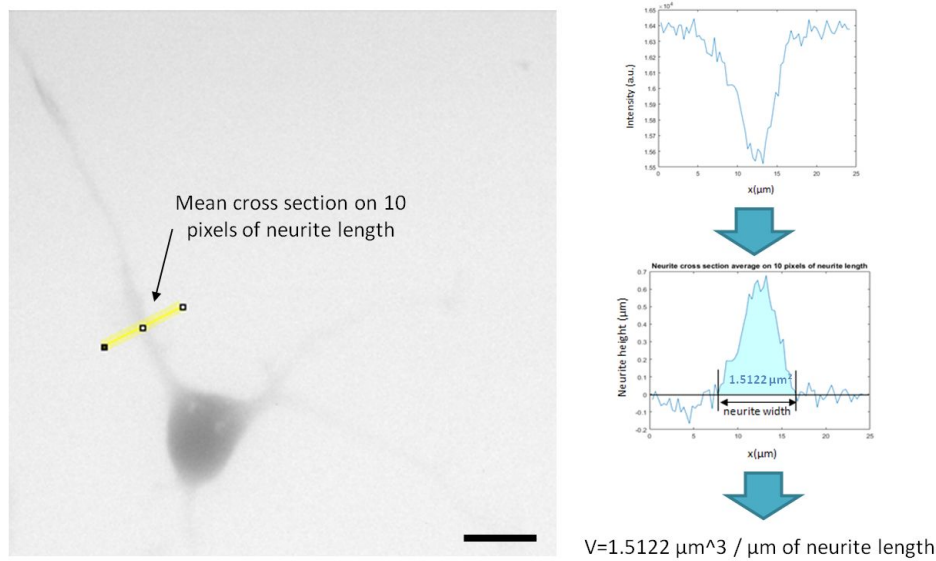


Figure 4.16 – Extraction of values of volume per μm of neurite length named neurite slice volume. Mean cross sections on 10 pixels (i.e. $1\mu\text{m}$) of neurite length are drawn with imageJ. The intensity profile is converted to a height profile using a linear conversion law obtained from the fluorescence intensities values of pillars and background. The integration limits are manually chosen and give the neurite width. Scale bar: $10\mu\text{m}$. Microscope: Leica DMI8. Camera: Hamamatsu ORCA Flash 4.0 V2.

5.3.4 Dynamic analysis

The analysis of time-lapse experiments was performed using ImageJ. We first mounted the time-lapse images as a stack. The area of interest was selected for the first image and the ROI manager tool was used to obtain integrated intensities for all stacks. To obtain the volume over time of each selected area, the linear height-intensity conversion was performed as previously described.

5.3.5 Remarks about the use of chambers of different heights

As observed in [171], using thicker chambers can result in a deterioration of the signal-to-noise ratio of the measurement. To overcome this deterioration, changes in exposure times are required, to keep the background fluorescence intensity within the dynamic range of the camera. To control this effect on our chambers, we used the same system described in **Figure 4.15** (resist stripe in a chamber filled with a fluorescent medium) in the three chambers of different height. We took images at the same exposure time in order to compare the contrast of the measured object over the background noise. Using ImageJ, we extracted intensity profiles on the different chips roof and looked at the standard deviation of these data. This gave us the average intensity noise of each chamber. Converting the intensity data into heights we obtained the average height noise. The contrast of the

object over the background noise is then deduced by dividing the resist height value to these values. For the highest chamber of 10 and 12 μm , the signal is between 10 et 20 times higher than the noise whereas for the chamber of 3 μm it is about 30 times higher (Figure 4.17). This difference shows that, at a same exposure time, the signal is slightly better in a lowest chamber.

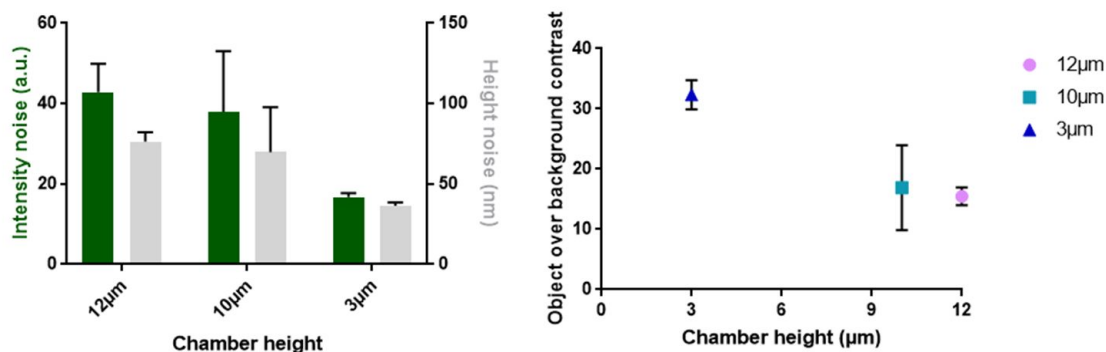


Figure 4.17 – Noise quantification in the chamber of different heights. Left: Intensity and deduced height noise values calculated with the standard deviation of intensity profiles of the roof of the different chips. Right: Signal (resist height of 1.18 μm) over the height noise ratio. The signal for the 3 μm chamber is 32.34 times higher than the noise whereas it is 16.92 times higher for the 10 μm high chamber and 15.47 for the 12 μm high chamber. Objective: 20x NA 0.7. Microscope: Leica DMI8. Camera: Hamamatsu ORCA Flash 4.0 V2.

6 Cell culture

The culture of neurons inside the FXm devices obeys to the same principles described in the previous chapters, e.g. an adhesive coating and suitable medium. However, seeding and growing neurons into close and Low-ceilinged chambers impose specific constraints and protocols. The following section describe how we adapted our methodologies of hippocampal neuron culture to FXm devices.

6.1 Surface fonctionnalization

The surface functionalization of the chip is performed in the 30 minutes following its sticking to the glass coverslip to be sure to beneficiate of the activated and hydrophilic surface provided by the oxygen plasma. As for glass coverslips used in **Chapter 2 and 3**, we are using polyOrnithine (PLO) diluted in PBS. The concentration of 80 $\mu\text{g}/\text{ml}$ has shown to allow a acceptable survival rate of neurons into chips, nevertheless we also used concentrations of 100 or 200 $\mu\text{g}/\text{ml}$ as a few experiments shown an improvement

of neuron survival under these conditions. PLO is injected inside the chip and the petri dishes containing the chip are filled with PBS and sealed with ParaFilm to avoid drying. After an overnight incubation step (minimum 5h), the chip is rinsed few times with PBS in order to eliminate the fraction of non-adsorbed PLO. Plating medium MEMc is then injected into and outside the chip. The MEMc composition is similar to the one described in **Chapter 2**, except for the Horse Serum (HS) quantity that we increased to 20% instead of 10% to improve cells survival. Chips are kept in the incubator until cells seeding.

6.2 Seeding

We used hippocampal neurons extracted from mice embryo in the same way as described in **Chapter 2**. Then, after dissociation, a centrifugation step is added. We centrifuge at 1000rpm during a couple of seconds, in order to get cells at the bottom of the tubes and keep cellular debris in suspension. The supernatant is removed, therefore discarding cellular debris, and cells are resuspended at a concentration of 10 million/ml of MEMc. We finally inject about 2 to 10 μ l of this solution into chips in several steps. This quantity depends on the number of neurons present in the measurement chamber after each injection. In general, about 3 μ l through both inlet and outlet of the 10 and 12 μ m high chambers and 1 to 2 μ l into each reservoir (when present) is sufficient. Since cells don't have a physical barrier to stop them in the highest chambers, compared to the 3 μ m high chamber, the flux may need to be adjusted using micropipettes and medium additions. In the case of the 3 μ m high chamber, about 6 μ l is generally injected through the inlet and 3 μ l through each reservoir. After seeding, chips are kept in the incubator, at 37°C and 5% CO₂.

6.3 Imaging medium

After 1 DIV, the medium is replaced with a Neurobasal-conditioned (NBcC) medium. Basically, NBcC was made by letting NBc in contact with a confluent layer of glial cells for 1 to 3 days in 100mm petri dishes. NBcC is expected to mimick the presence of glial cells in the chip, and improve neurons survival. The protocol is described in **Appendix 8**. Transparent neurobasal is also used to prepare this medium in order to not interfere with the fluorescent dye added for fluorescence imaging. We chose 10kD Dextran, with either an excitation wavelength of 647nm (emission in red) or of 488nm (emission in green). In some case GFP-LifeAct mice were used, required an observation with the 488nm excitation wavelength. In this case we had to use the 647nm Dextran to discriminate between the actin and the exclusion fluorescence signals. The Dextran dyes were diluted in the transparent NBcC at a concentration of 1mg/ml.

7 Results

The FXm allowed us to obtain data on the local neurites volume, i.e. looking at the tapering effect from height and volume values. Coupling the FXm with time-lapse observations enabled dynamical observations of neuritic volume. We focused our attention on the dynamical propagative structures observed during the early stages of neuronal growth, i.e. the actin waves already introduced in **Chapter 1**. To the best of our knowledge, the volume changes induced by actin waves along the neurite shaft have never been studied. Lastly, I will present preliminary results on patterned neurons.

7.1 Neurite tapering

As reported by Banker et al. on non-patterned hippocampal neurons [18] (**Chapter 1 Figure 1.10**) a neurite tapering is observed away from the soma. In **Chapter 3**, we confirmed this effect on patterned neurons and we observed that it was accompanied by a decrease of the dry mass.

Extracting cross sections of 10 pixels of neuritic length (about $1\mu\text{m}$) along the neurite we observed that this local volume per μm of neuritic length, that we named neurite slice volumes, is also decreasing with the distance to soma (**Figure 4.18**) suggesting that the dry mass correlates with the neurite width.

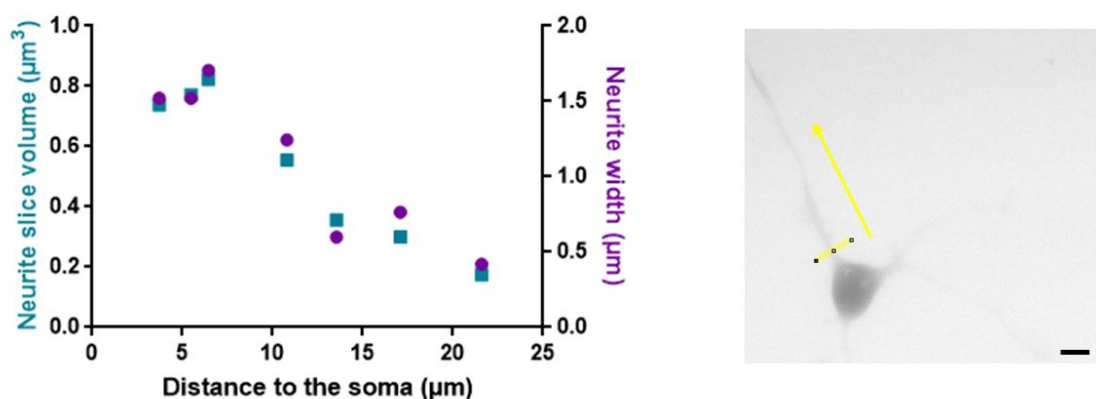


Figure 4.18 – *Neurite local volume and width taperings observed in a $12\mu\text{m}$ high chamber filled with NbcC-647nm-Dextran. Scale bar: $10\mu\text{m}$. Objective: $40\times$ NA 0.8.*

From this preliminary observation, we chose to repeat the same measurement on many cells to further investigate the dependence between the neurite width, local dry mass and volume.

7.2 Neurites slices volume and dry mass as function of the width: toward neurite RI ?

As expected from the above result, we observed a general increase of the local neurite volume versus the neurite width as shown in **Figure 4.19 Left**. Assuming a linear variation to fit these data, we obtained a line crossing the origin, expressing a proportionality between the local volume and the local width. The slope of this linear fit suggests a constant neuritic height of about $0.4 \mu\text{m}$. Nevertheless, a quadratic fit would give a completely different evolution. Data from neurites of higher width would be needed to confirm, or infirm, this tendency. Here neurons were not constrained using micropatterns, their spontaneous width range is then concentrated around $1 \mu\text{m}$ and data from larger neurites could not be obtained. Coupling the FXm with micropatterning could allow us to obtain data for higher neurites width.

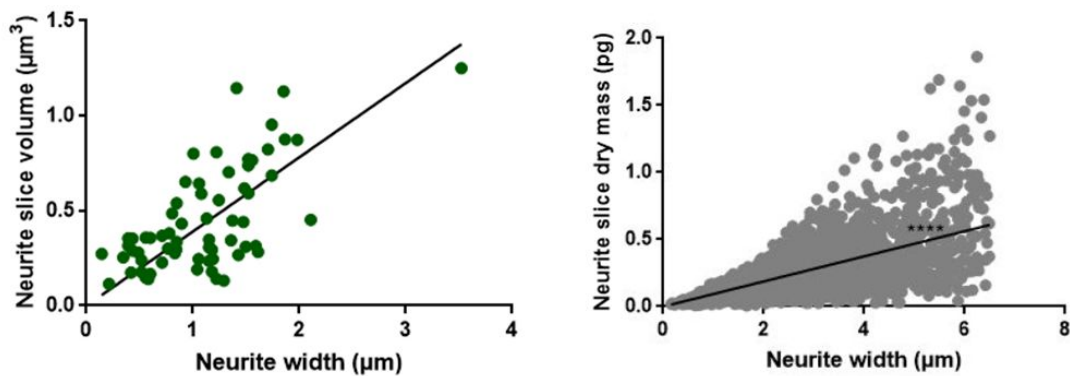


Figure 4.19 – **Left:** Neurites slice volume increasing linearly with the neurite width (slope: $y = 0.3908 \pm 0.02057 \mu\text{m}^3 / \mu\text{m}$). $n=4$ cells in Chamber $12 \mu\text{m}$. $n=4$ cells in Chamber $3 \mu\text{m}$. $n=65$ profiles. 2 cultures. DIV 1. Objective: $40\times$ NA 0.8. **Right:** Neurite slice dry mass distribution versus the neuritic width obtained with the DHM. The local dry mass increases with the neuritic width with a slope of $0.09363 \pm 0.0009418 \text{ pg}/\mu\text{m}$. $n=79$ cells (from 2-2, 2:2, 6-6, 6:6 and 2-6 patterns), $n=2995$ sections. These two linear fit would give a mean neurite RI of $\bar{n}_{neurite} = 1.376$.

The similarity of linear increases of neurite slices volume and neurite slices dry mass (**Figure 4.19**) could offer an alternative way to the decoupling procedure for the obtention of cells RI. The different compartments of neurons RI might then be obtained in a robust way if coupling phase and volume measurements, i.e. coupling DHM observations and FXm. This point is the subject of ongoing discussion with Olivier Thouvenin from the Langevin Institute.

7.3 Actin waves

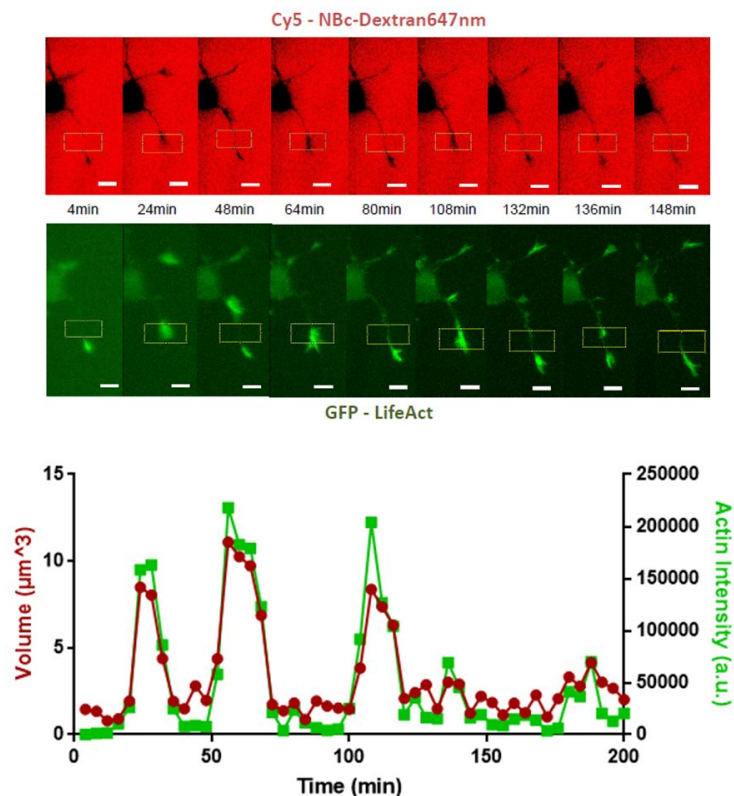
Actin waves (AWs) are one of the identified mechanisms participating in neuronal growth (cf **part 2.3.2** of **Chapter 1**). At DIV1, it was assessed that AWs contribute for 90% of neurite growth [92]. The question of how the properties of AWs might be influenced by the geometrical characteristics of neurites remains however to be explored, as well as how the propagation of actin waves transiently modifies the geometry (i.e. width and height) of the neurite shaft. I will present below preliminary results on the volume of actin waves.

7.3.1 Neuritic volume changes with AWs motion

To follow precisely the morphology of actin waves (AWs), we used hippocampal neurons from GFP-LifeAct mice embryo, which are genetically modified to expressed GFP associated with actin.

AWs were observed in $12\mu\text{m}$ high chambers from images taken every 4 minutes from two fluorescent channels: red (NbcC-647nm-Dextran) for fluorescent exclusion data and green (LifeAct) for actin, enabling the localization of actin waves. **Figure 4.20** illustrates the strong correlation between the neurite local volume changes and the propagation of AWs. **Figure 4.21** shows the proportionality between volume and actin concentration.

Figure 4.20 – *Volume changes related to actin waves motion. Fluorescence images show the evolution of volume and actin intensity on a neuron at selected times. Green: actin. Red: NbcC-647nm-Dextran. LifeAct neurons were observed every 4min from DIV1 to DIV2. The graph displays the volume and actin intensity signal of the neurite zone selected on the time lapse images versus time. It shows that AWs increase substantially the neurite volume. Chamber: $12\mu\text{m}$. Scale bar: $10\mu\text{m}$. Objective: 40x NA 0.8.*



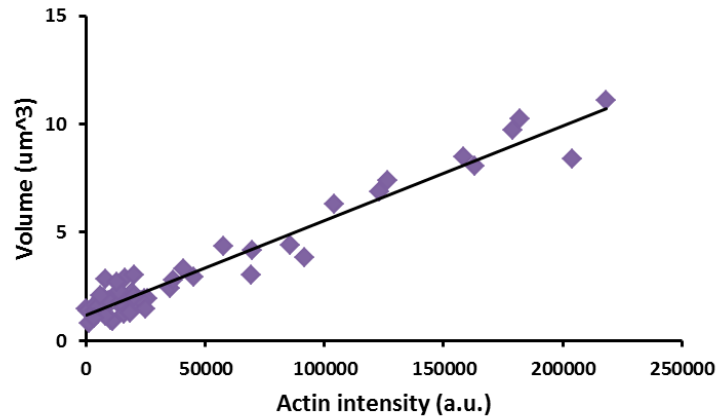


Figure 4.21 – Volume vs actin intensity of the neurites selected zones shown in **Figure 4.20**. The linear fit, $y = 4.10^{-5}x + 1.1763$, illustrates the proportionality between neurite volume and actin concentration.

7.3.2 AWs and neurite enlargement

Looking at the local neurite volume and at neuritic width changes, we also observed a neurite enlargement correlated with AWs motion, in accordance with observations made in [92] (**Figure 4.22**).

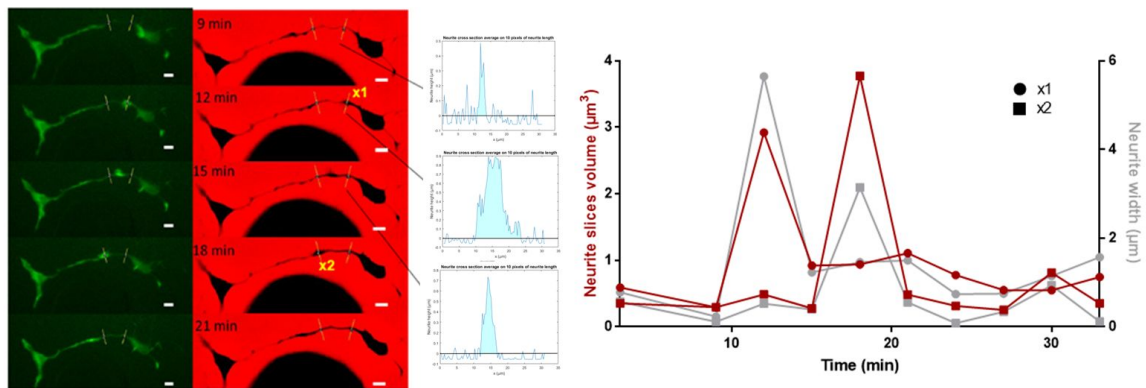


Figure 4.22 – Volume changes related to neurite enlargement during actin waves motion. Fluorescence images show, at the actin and at the volume level, the motion of 2 AWs of a neuron (right cell) connected to a glial cell (left cell). Green: actin. Red NBcC-647nm-Dextran647. x1 and x2 cross sections were drawn to observe the local increase of neurite volume and width, as highlighted in the insets. The graph displays the volume and actin intensity signal versus time of these two zones. It shows that AWs increase in a non negligible way the neurite volume. LifeAct neurons were observed every 4min at DIV1. Chamber: 12 μ m. Scale bar: 10 μ m. Objective: 40x NA 0.8.

7.3.3 AWs intrinsic volume

To assess the AWs volume over time, i.e. during their propagation from the soma to the neurite tip, we used the green fluorescence channel to select precisely the AW shape, that we further used to calculate the AW exact volume from the red fluorescence images. **Figure 4.23** displays the results obtained for several AWs observed on two neurites. This preliminary result shows that AWs volume is decreasing when traveling along the neurite. This very interesting result might suggest that waves loose a part of their content during their journey from the soma to the tip. An alternative explanation would consider the effect of neurite tapering, and assess that the volume of AWs scales with the local size of neurites. To explore this issue, we might use neurites of controlled geometries, observing for example the evolution of the volume of an AW before and after a change of width imposed by micropatterns.

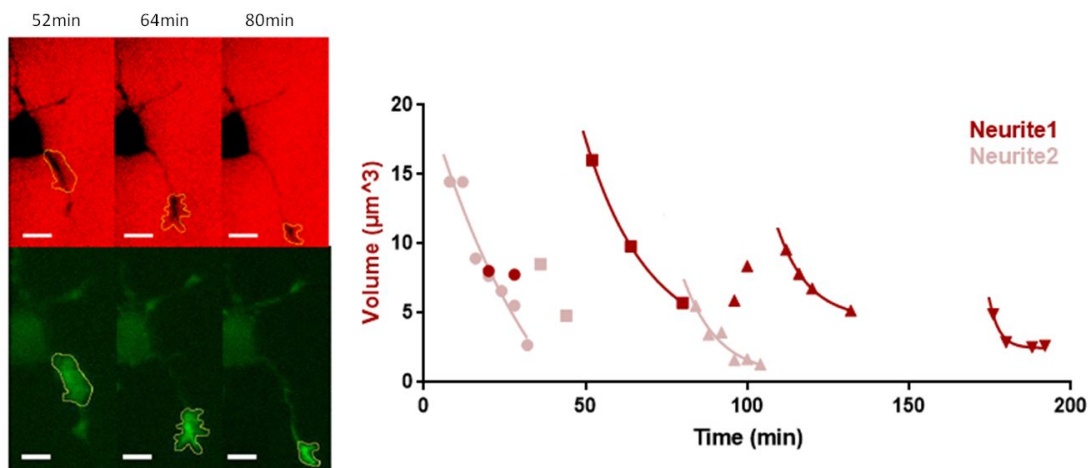


Figure 4.23 – Actin waves volume. Fluorescence images show the selection of one actin wave shape at different times thanks to actin imaging. Green: actin. Red: NBcC-647nm-Dextran. LifeAct neurons were observed every 4min from DIV1 to DIV2. The graph displays actin waves volume evolution versus the time of 4 AWs for one neurite (Neurite 1) and 3 AWs for another neurite (Neurite2). It shows that actin waves volume seems to decrease when traveling along the neurite. Chamber: 12μm. Scale bar: 10μm. Objective: 40x NA 0.8.

In order to extract some mechanisms about AWs volume relation to neuritic width and growth velocity, it would be of a great interest to repeat these observations on neurons of constrained shapes. The following section gives some preliminary results on this question.

7.4 Coupling FXm and micropatterning

7.4.1 Methods

Patterned glass coverslips were prepared in the same way as in **Chapter 2**. To stick the PDMS chip on glass coverslips, no oxygen plasma was applied on the glass coverslip to protect the patterns. We choose the best pattern geometry to observe neurite width changes, i.e. 2626 patterns (**Figure 4.24**). Since the mask used was not designed for FXm chips shape and that an alignment step between the glass coverslip and the PDMS chip is currently not fully mastered, we did not succeed to define the position of patterned and non-patterned neurons in the chamber. In preliminary experiments, we however managed to position patterned neurons within the measurement chamber. However, these constraints imply that only few neurons were located in this zone and their survival was problematic. We are now working on improvements to couple micropatterning and FXm. Nevertheless measurements on one patterned neuron were quite promising as illustrated below.



Figure 4.24 – Pattern 2626. Alternation of 2 and 6 μm wide stripes of 30 μm length.

7.4.2 Neurite local volume on a patterned neuron

A neuron grown on a 2626 pattern in a 10 μm high chamber filled with a NbcC-647nm-Dextran was observed. **Figure 4.25** displays the height map of this neuron obtained using the usual procedure of intensity-to-height conversion.

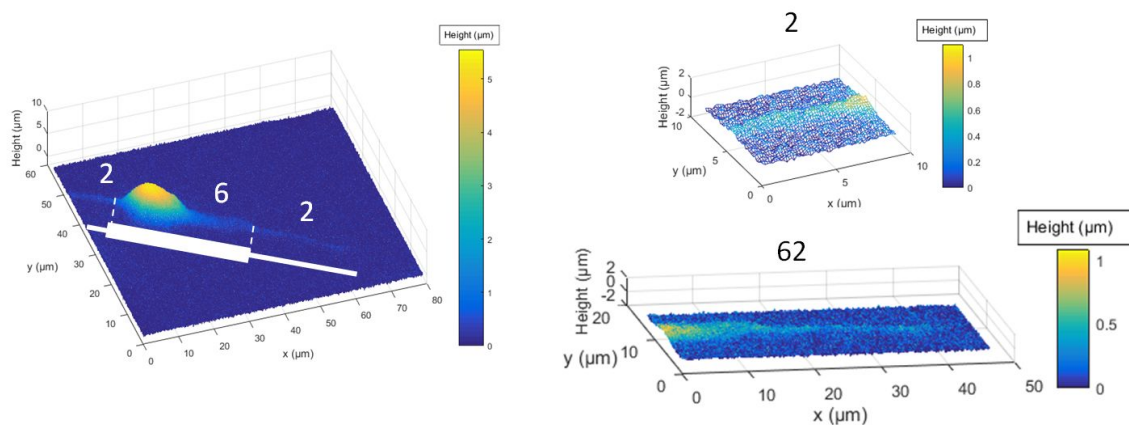


Figure 4.25 – 3D height maps of a neuron at 1 DIV on a 2626 pattern. The white lines display the pattern. Measurement made in a 10 μm high chamber filled with NbcC-647nm-Dextran. Objective: 40x NA 0.8.

By extracting cross sections as previously, we could observe the difference in heights and widths between the different pattern zones (**Figure 4.26**). Interestingly, we observe that neurite heights are around $0.4\mu\text{m}$, as observed before on non-patterned neurons (**Figure 4.19**).

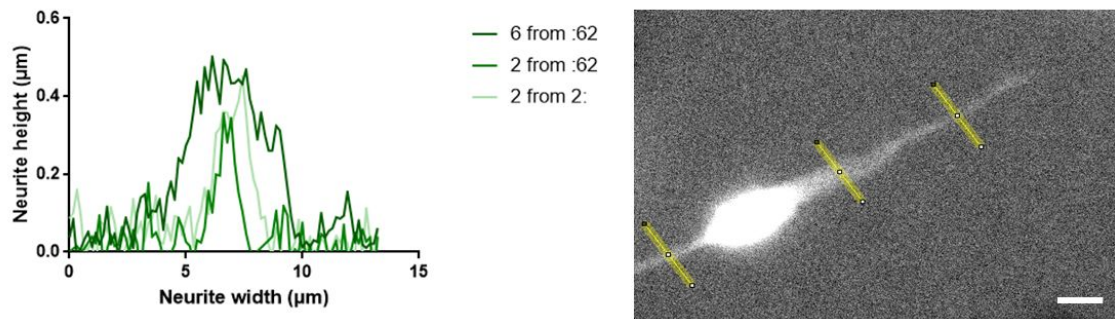


Figure 4.26 – Cross sections of the neurites on the two stripe widths of 2 and $6\mu\text{m}$. Distances to soma: $7\mu\text{m}$ for the two profiles drawn near the soma and $26\mu\text{m}$ for the further one. Scale bar: $10\mu\text{m}$. Objective: $40\times$ NA 0.8.

As done for non-patterned neurons, we then studied the evolution of the local neurite volume versus the neurite width. Interestingly, we observed a linear evolution that matches very well with the linear evolution observed on non-patterned neurons (**Figure 4.27**). As expected, we now can obtain data coming from larger neurite.

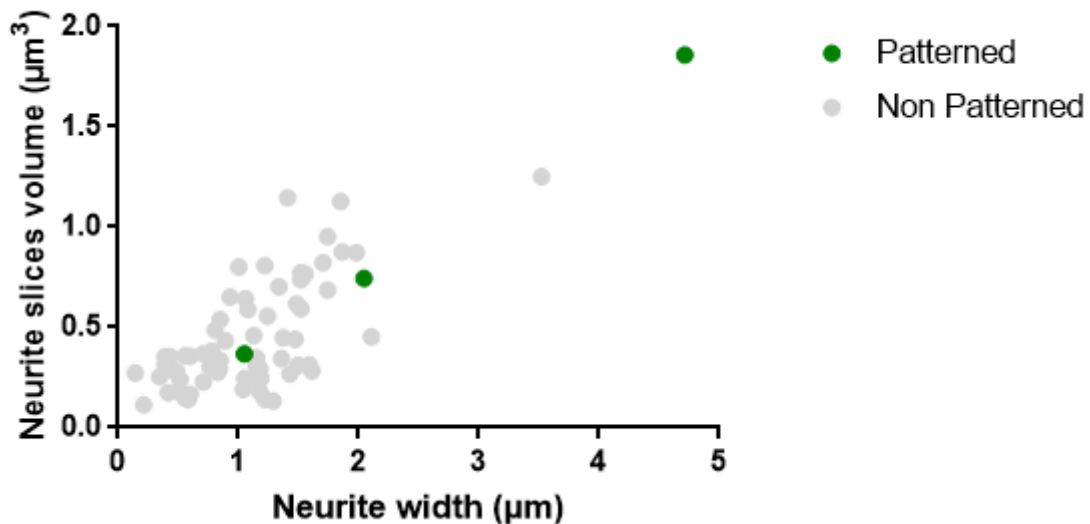


Figure 4.27 – Local volume of neurites on stripes of controlled widths. The local volume of the neurites on patterns is increasing linearly with the neurite width (green) in the same way as neurites with no constraints (grey).

8 Conclusion and prospects

8.1 Main findings

The use of silicon molds proved to be efficient to reach high resolution volume measurement.

We assessed that the changes in neuritic local volume seem to follow a similar variation as a function of the neurite width than microtubules and dry mass evolutions (**Chapter 2 and 3**). This linear variation is implying a constant height of about $0.4\mu\text{m}$ for neurite grown *in vitro*, undependently of their widths. This result has still to be confirmed with data coming from neurites of higher width. Nevertheless, if confirmed, it would raise the question of the mechanism of height regulation for neurites grown *in vitro* on 2D substrates. This would also question the mechanism of height regulations *in vivo*, although neurites in the environment of the brain form adhesions in 3D and display cylinder shapes. For instance, the diameter of hippocampal axons is about $0.8\mu\text{m}$ *in vivo* (cf **Figure 1.10**). Interestingly, this value is twice the maximal height of neurites which adhere on flat surfaces.

In addition, we confirmed that AWs induce a transient enlargement of neurite as well as an increase of neurite local volume. Interestingly, AWs seem to lose volume when traveling along the neurite.

8.2 Outlooks

Coupling phase and FXm measurements would allow to retrieve RI, in particular of neurites. This will be further explored in collaboration with Olivier Thouvenin from the Langevin Institute.

Coupling micropatterning and FXm would also be of a great interest to measure the dependence of the neurite volume on the neuritic width, to confirm, or infirm, the constant height of neurites *in vitro*, as well as to observe AWs in a control morphological conditions.

Technologically, this will require a challenging alignment step between the adhesive patterns and the microfluidic chip.

A last issue, that we did not discussed in this chapter, is the possible effect of the constraints applied by the chambers height to the cells. In addition to the fact that chambers

height is selecting neurons according to their size, we also observed that axons seem to prefer to grow toward the lowest chamber compared to higher zones. This could have interesting effects for neurons type selection or guidance.

Lastly, we observed that the fluorescence medium was slowly internalized by neurons and travelled within vesicles from the neurites tip to the cell body. After a while, these vesicles are all concentrated in the cell body and are no longer able to interfere with our measurements. Nevertheless we are currently looking for another fluorescent medium that would not present this drawback.

GENERAL CONCLUSION

From the different approaches developed during my PhD project, I got an ensemble of results associated with the control and the measurements of neuronal morphologies. I showed that the length and the axo-dendritic polarity of isolated neurons on micropatterns could be defined from a control over their neurite widths. I also highlighted the existence of an homeostasis of the total neuritic length when varying the number of branches. Moreover, I raised the issue of a possible homeostasis of the total neuritic dry mass before axonal polarization. Locally I assessed that the quantity of microtubules as well as the dry mass and the volume of neurites increase with the neurite width, i.e. the neurite height seems to be regulated by the cell. Finally, I focused on the propagative structures named actin waves and showed preliminary results regarding their volume loss during their journey from the soma to the tip.

All of this work was achieved through the design and development of various biophysical tools to investigate neuronal shapes. These different approaches have arisen through the different locations and environment where this project took place and that shaped this research:

- At the NanoFab facility of the Neel Institute, I had access to technological tools coming from the field of microelectronic, including the in-house fabrication of masks, photoresist stencils and etched coverslips. This allowed me to implement new ideas very quickly. Playing with micropatterns shapes, we highlighted some mechanisms about neuronal growth, polarization and cytoskeleton organization.

- From the Digital Holographic Microscope (DHM) acquired at the Neel Institute, and with the support of the Neel Institute and the Curie Institute mechanical facilities, I was able to perform phase imaging of neurons. Then, thanks to discussions at the Curie Institute, I became interested into retrieving the neurites dry mass and got some preliminary results on that topic.

- Lastly, again by joining the team of Jean-Louis Viovy at the Curie Institute and by working in the new Institut Pierre Gilles de Gennes microfluidic research center, I developed the FXm technique for neuronal volume measurement and was able to achieve first

observations of neurite height, local volume, including the dynamical changes induced by the motion of actin waves.

Now that these different tools and set-ups are well characterized and optimized, the different outlooks presented at the end of chapters 1 to 3 will be reachable. During the next months, I will in particular focus on:

- ◇ Acquiring enough statistics on the total dry mass as well as total neuritic volumes on patterned neurons
- ◇ Studying the volume of actin waves on patterned neurons, in particular to follow the evolution of this volume when the neurite width varies abruptly
- ◇ Retrieving the RI of the different neuronal compartments

These goals will be achieved in the great biophysics environment provided by the IPGG and the neighboring institutes.

This leads me to a more personal conclusion where I would like to highlight what I learned by working at the interface of different fields and especially by sharing my research with a non-scientific public.

Working at the interface of biology and physics has proved to bring a lot to my subject. Working at the interface between fields is especially needed in our century, where science became highly specialized and fragmented. Without interactions with colleagues from very different fields, I could not have achieved this work.

But not only scientific colleagues can bring to us ideas and technologies. Describing our science to a non-scientific public has also proved to be of a great interest to me. To simplify our project and adapt its presentation in order that everyone can understand it, brought me many new interesting ideas from an unexpected point of view. I am therefore particularly interested in sharing science with a large public. During my PhD, I participate to different projects, from my investment in the creation of the "Parcours Biophysique" for the Néel Institute Science festival and scientific journalism courses provided by the doctoral school of Grenoble to my implication in different events at the ESPGG (Espace Pierre Gilles de Gennes) scientific mediation center (Science festival, Nuit des Chercheurs, Un chercheur et moi).

I would say that an important part of a PhD life is not only to learn techniques and to spend time at the bench or to analyze data but it is also to learn how to share science and how to build new research projects by being ready to always learn new things. Therefore, I wish that all the other PhD students can have the same great experience as me.

RÉSUMÉ DE LA THÈSE EN FRANÇAIS

Ce résumé a pour but de donner au public non anglophone un aperçu semi-détaillé de la thèse. L'introduction et la conclusion générale sont traduites, ainsi que les conclusions principales de chaque chapitre et le début du **Chapitre 1**. Quant au reste, des résumés succincts sont fournis, avec des références aux figures du manuscrit.

1 Introduction générale

Le cerveau reste la plus complexe et extraordinaire des machines dans l'univers connu. Ses briques élémentaires, les neurones, sont nombreux (120 milliards) et montrent une grande diversité de formes et de fonctions.

Durant mon projet de thèse, j'ai étudié les formes neuronales à travers l'utilisation de différentes approches biophysiques. (i) Avec le micropatterning pour contraindre les formes cellulaires, j'ai exploré des questions comme la polarisation axo-dendritique. (ii) En utilisant une méthode d'interférométrie, j'ai étudié la répartition de la masse sèche dans les différents compartiments neuronaux. (iii) Finalement, j'ai effectué des mesures de volume et de hauteur pour avoir une idée de l'évolution des formes neuronales en 3D.

Dans le **Chapitre 1**, j'introduis en premier lieu les différents éléments de ma thèse en me concentrant sur les acteurs des formes neuronales. J'introduis ensuite les trois techniques que j'ai développées: le micropatterning, la Microscopie Holographique Digitale (DHM) et la méthode d'exclusion de Fluorescence (FXm). Le développement de ces outils biophysiques ainsi que les résultats obtenus sur les formes neuronales, en particulier concernant la croissance et la polarisation neuronale, sont détaillés dans les **Chapitres 2, 3 et 4**.

Mon projet de thèse a aussi été mené dans un contexte unique. J'ai commencé ma thèse dans un environnement de physique fondamentale à l'Institut Néel à Grenoble, avant de déménager à l'Institut Curie à Paris, au début de ma seconde année de thèse, pour finalement m'installer, comme toute l'équipe de Jean-Louis Viovy, à l'Institut Pierre Gilles de Gennes (IPGG) pour ma troisième et dernière année. Ces différents environnements scientifiques, et en particulier la possibilité d'intégrer les outils microfluidiques dans mes

recherches à partir de la deuxième année, ont fortement contribué au contenu final de cette thèse.

1.1 Une brève histoire du cerveau

1.1.1 Du coeur au cerveau

Le coeur fut associé aux origines de l'activité mentale pendant des millénaires et ce dans différentes cultures. Cette approche peut être illustrée par la théorie coeur-esprit [1] du philosophe grec Aristotle (384-322 av. J.-C), par la tradition en Egypte Ancienne (3100-332 av. J.-C) d'extraire et de se débarrasser du cerveau durant le processus de momification, tout en préservant précautionneusement le coeur [2], et par la croyance hindouiste d'une âme de la taille d'un atome située dans le coeur, développée dans le Bhagavad-Gita (V^e au IInd siècle av. J.-C) [3], qui ne sont que quelques exemples parmi d'autres. Cette théorie n'est pas tellement surprenante sachant que le coeur est l'organe le plus représentatif de notre activité mentale, l'exprimant d'une façon perceptible tout le long de notre vie. Cela a mené à l'utilisation, jusqu'à aujourd'hui, d'expressions comme "Un coeur brisé" à la place d'"un cerveau brisé". Néanmoins, petit à petit, à travers les siècles, les connaissances ont beaucoup évolué. Notamment à la Renaissance, lorsque la prohibition de l'Eglise de disséquer des corps humains tombe, les anatomistes ont alors été capable d'établir un lien entre l'activité mentale et le cerveau. Ils ont pu mettre en évidence des connections entre le cerveau et les autres organes en révélant la présence de nerfs, comme illustré par le dessin de Leonard de Vinci (1452 - 1519) présenté en **Figure 1.1**. De nos jours, il est intéressant de remarquer que la suprématie du cerveau est à nouveau contestée avec l'arrivée dans la partie d'un nouveau joueur, le microbiote intestinal. De récentes études ont reconnus son rôle dans la détermination du comportement et de la cognition [4]. L'organisation centrale de l'activité mentale établie autour du cerveau seul est alors challengée. Cependant, le cerveau reste la machine la plus complexe et extraordinaire de l'univers connu et est toujours considéré comme l'organe majoritairement impliqué dans le contrôle de chacune de nos actions, pensées, sentiments, rendant possible l'existence de notre monde intérieur (i.e. développant notre imagination), ainsi que notre perception de la réalité et la possibilité d'interagir avec le monde extérieur, par exemple en développant l'empathie. Il nous permet de ressentir la joie, la douleur ou l'amour et d'une façon remarquable nous donne la conscience ainsi que l'expérience (ou l'illusion..) du libre arbitre. Comment la conscience est née de cette machine biologique est l'une des questions les plus difficiles à laquelle les scientifiques de différents domaines, utilisant différentes et spécifiques approches et techniques, essaient de répondre. Cependant, ils semblent tous s'accorder sur le fait qu'elle provienne d'un objet, certes toujours compliqué, mais défini: un réseau de cellules nerveuses communiquant entre elles à travers des centaines de trillions d'interconnections se trouvant principalement dans **le cerveau**.

La fin de cette partie décrit les deux types de cellules nerveuses: les neurones et les cellules gliales. En particulier, la lumière est faite sur les neurones, qui sont considérés comme les unités fondamentales du système nerveux de part leur excitabilité. Leur grande diversité morphologique est alors décrite (**Figure 1.3**), illustrant la complexité de ces réseaux neuronaux. Néanmoins une forme générique existe tout de même et est présentée en dernière partie (**Figure 1.5**), où l'on apprend que le neurone a trois parties principales: le corps cellulaire, ou soma, et deux types de prolongements appelés neurites: les dendrites, qui reçoivent l'information électrique d'autres neurones, et l'axone, unique, qui envoie l'information aux neurones suivants. Cette information se propage sous la forme d'un signal électrique appelé potentiel d'action (**Figure 1.6**).

1.2 Compartiments neuronaux: formes et fonctions

Le neurone assure ses fonctions grâce à sa forme particulière. Dans cette partie, les différences de formes et de structures entre les différents compartiments du neurone ou bien entre des neurones de différentes zones sont mises en évidence.

1.2.1 Axone et dendrites

Ces différences peuvent être au niveau cellulaire, comme des différences de taille entre axones (**Figures 1.8 & 1.9**) ou entre axones et dendrites (**Figure 1.10**), ou, elles peuvent être au niveau sub-cellulaire, notamment au niveau du cytosquelette de la cellule composé principalement d'actine et de microtubules. Il est alors décrit que l'actine s'organise sous forme d'anneaux, que ce soit dans les axones ou les dendrites (**Figure 1.12**), mais que les microtubules ont des orientations différentes dans ces deux types de prolongements. L'organisation de ces deux structures peut alors jouer un rôle dans le contrôle des diamètres des neurites, par exemple en lien avec les MAPs (Protéines Associées aux Microtubules) concernant les microtubules (**Figure 1.14**), qui sont des protéines liant les microtubules, et qui, de part de leur différence de répartition entre axones et dendrites, sont communément observées pour reconnaître l'un ou l'autre (**Figure 1.15 et 1.16**).

1.2.2 Calibres axonaux: rôles et dynamiques

Le lien entre formes et fonctions neuronales s'observe par exemple lorsque l'on mesure les potentiels d'action de neurones présentant des axones de différents calibres. On observe alors que plus l'axone est gros, plus les fréquences de décharge sont importantes. On observe également des arrêts de propagation de signaux lors de brusques changements

de forme. Nous avons qualifié cet effet de "statique", car dépendant de caractéristique statique des axones. Néanmoins il existe aussi un effet "dynamique", observé durant la propagation de potentiels d'action le long des axones. Les passages de potentiel d'action ont pu être associés à des changements locaux de diamètre axonal (**Figure 1.17**). Ces observations sont seulement préliminaires et ont été effectuées principalement par AFM sur des nerfs de souris et par interférométrie sur des axones géants d'écrevisse.

1.2.3 Le neurone grandissant: cône de croissance et vagues d'actine

Ces formes neuronales spécifiques se développent durant leur croissance, à des vitesses différentes selon le type neuronal et pouvant inclure des étapes de migration (**Figure 1.18**). Une structure jouant un rôle dans le guidage des neurones est le cône de croissance. Celui-ci est présenté en **Figure 1.19**. Une autre structure ressemblant au cône de croissance et jouant un rôle dans la croissance des neurones est la vague d'actine (**Figure 1.20**). Les vagues d'actine se propagent à partir des corps cellulaires vers le bout des neurites pendant les premiers stades de croissance et sont supposées jouer un rôle important dans la croissance des neurones. Elles ne sont pas encore très étudiées, mais il a tout de même déjà été mis en évidence par exemple que le passage d'une vague provoque une vague de polymérisation des microtubules (**Figure 1.21**).

1.2.4 Le neurone malade

Après leur croissance et leur maturation, les neurones peuvent faire l'expérience de dégénération causées par des maladies. Ces dégénération sont souvent accompagnées de changements morphologiques et les observer et les comprendre pourrait apporter beaucoup dans la lutte contre les maladies neurodégénératives. Quelques exemples sont illustrés ici, comme l'effet "beading" (perlage) observé en **Figure 1.23** ou dans le cas de la maladie d'Alzheimer (**Figure 1.24**) ou des changements de formes induits par du cannabinoïde synthétique.

1.3 Approches biophysiques "bottom-up" des formes neuronales

Cette partie présente l'approche et les outils utilisés durant cette thèse. Le terme "bottom-up", terme emprunté entre autres au monde des nanotechnologies et signifiant une approche "ascendante", est notamment choisi pour illustrer notre approche qui consiste à partir des briques élémentaires de notre cerveau, les neurones, pour remonter pas à pas à l'organe entier.

En premier lieu, les modèles hippocampaux et corticaux habituellement utilisés en neuroscience sont décrits. Les neurones hippocampaux utilisés dans cette thèse sont extraits d'embryons de souris et leur développement *in vitro* est bien connu et est décrit en **Figure 1.29**. Pour notre approche "bottom-up", nous avons choisi le micropatterning pour isoler et contrôler les formes neuronales. L'historique de cette technique est alors décrit, notamment son utilisation préalable sur les neurones (**Figure 1.31**). Pour compléter l'état de l'art sur le contrôle des formes neuronales, une description des puces microfluidiques en PDMS communément utilisées pour guider les faisceaux d'axones *in vitro* s'ensuit (**Figure 1.32**). La dernière partie se concentre sur la description de deux systèmes que nous avons choisi pour mesurer les formes neuronales en 3D: le Microscope Holographique Digital (DHM), qui nous permet de mesurer quantitativement le signal de phase et de remonter à la masse sèche de la cellule, et la méthode d'exclusion de Fluorescence (FXm) qui nous permet, en chambre fermée remplie d'un milieu fluorescent, de mesurer le volume et la hauteur de notre cellule par une simple conversion intensité de fluorescence - hauteur à l'aide d'un objet référent présent dans le champ de mesure.

1.4 Contexte et objectifs de la thèse

Comme la régulation de l'osmolarité et l'excitabilité électrique dépendent de gradients ioniques à travers la membrane plasmique, les neurones semblent plus vulnérables à des changements de volume que la plupart des cellules. Tout au long de sa vie un neurone régule sa morphologie, autant à l'échelle globale qu'à l'échelle locale. Pouvoir étudier le volume neuronal à la résolution des prolongements neuronaux pendant des expériences en temps réel serait un réel progrès, sachant que les précédentes études étaient restreintes au soma ou à des prolongements neuronaux ne provenant pas de mammifères (i.e. relativement plus gros). En particulier, cela serait intéressant d'étudier les changements de volume pendant la croissance neuronale, e.g. avec l'impact des vagues d'actine, ou pendant la polarisation, e.g. pour étudier en détail les particularités des axones et des dendrites. De plus, étudier le neurone en tant que cellule isolée et de forme contrôlée serait un système intéressant pour mettre en évidence certains mécanismes, l'organisation interne ainsi que les changements de volume du neurone. Le contrôle des formes et une mesure précise du volume ouvrirait la porte à de nouvelles possibilités dans les études de neuropathologies, de l'observation de mécanismes induisant des changements morphologiques à l'étude des perturbations dans la fréquence de décharge ou d'une réorganisation interne atypique. Les outils biophysiques développés durant ce projet de thèse ont pour but ces différentes applications et des résultats sur la croissance et la polarisation neuronale ont été obtenus et sont présentés dans les chapitres suivants.

Dans cette thèse, les principales problématiques que je voulais adresser sont:

- Comment sont régulés les différents paramètres contrôlant la taille des neurites (hauteur, longueur..) durant la croissance des neurites ? Même question pour la densité de microtubules et la masse sèche.
- Pouvons-nous contrôler précisément la polarisation axonale en contrôlant la forme des neurones à l'aide des micropatterns adhésifs ?
- Quel est le volume des vagues d'actine and comment ce volume évolue durant la propagation des vagues ?

2 Contrainte des formes neuronales en 2D

2.1 Résumé

Dans ce chapitre, la technique de micropatterning permettant de contrôler la forme des neurones *in vitro* sur des lamelles de verre est décrite. Celle-ci comporte une étape de silanisation (**Figure 2.1**), pour rendre la surface assez hydrophobe pour éviter que les cellules ne s'étalent sur certaines zones et assez hydrophile pour que la résine photosensible nécessaire dans l'étape suivante puisse s'étaler ; puis une étape de photolithographie à travers un masque préalablement dessiné et contenant les formes voulues (**Figure 2.2 & 2.3**) ; ensuite une fonctionnalisation de la surface est faite grâce à l'utilisation d'un poly-cation comme molécules d'adhésion, où les cellules, chargées négativement, viendront préférentiellement adhérer (**Figure 2.4**). Enfin les étapes de culture cellulaire, de la préparation des milieux à la dissection des hippocampes d'embryons de souris (**Figure 2.5**) et aux marquages d'immunofluorescence sont décrites.

La **partie 3** présente les résultats obtenus sur l'observation et le contrôle de la croissance et de la polarisation axonale. La **partie 4** quant à elle présente les résultats sur la réponse du cytosquelette des neurites, en particulier les microtubules, aux contraintes géométriques.

2.2 Conclusions principales

En contraignant les formes neuronales grâce au micropatterning, nous permettant de sélectionner spécifiquement la largeur et/ou le nombre de neurites, il nous a été possible de mettre en évidence certains mécanismes de la croissance et de la polarisation neuritique.

Nous avons trouvé une conservation de la longueur neuritique totale indépendamment du nombre de neurites, et une décroissance de cette longueur quand la largeur du neurite augmente. Nous avons utilisé ce dernier résultat pour atteindre un contrôle géométrique précis de la longueur neuritique ainsi que de la polarisation axonale. De plus, nous avons acquis de nouvelles idées concernant les mécanismes de croissance et de polarisation à travers une modélisation que nous avons confronté à nos données expérimentales. Pour aller plus loin, nous avons regardé la densité de microtubules en réponse à des changements de largeur neuritique à l'échelle sub-cellulaire. Nous avons trouvé que la cellule ajuste sa densité localement.

3 Mesure de masse sèche avec le Microscope Holographique Digital (DHM)

3.1 Résumé

Dans ce chapitre, les techniques de microfabrication, notamment une partie sur l'ajout de gravures pour identifier les neurones sur les lamelles (**Figure 3.1**), de culture cellulaire et de mesure de la phase par interférométrie grâce au microscope holographique digital sont premièrement décrites. Les améliorations expérimentales pour amoindrir le bruit lors des mesures sont ensuite détaillées, au niveau "hardware" (amélioration de l'installation directement par l'ajout d'un instrument appelé "plongeur" - **Figure 3.5**) et au niveau "software" (amélioration de la prise de mesure et du traitement avec le logiciel par un moyennage temporel et une soustraction de fond vide - **Figure 3.6**). Le programme d'analyse "fait maison" et adapté aux analyses des neurites est ensuite présenté. La **partie 4** démontre alors la conversion du signal de phase en mesure de masse sèche.

La **partie 5** présente les résultats de mesure de masse sèche sur des neurones cultivés *in vitro* sur des lignes de 2 ou 6 μm de large, au niveau local et au niveau des neurites entiers. La **partie 6** présente une étude préliminaire de mesures de l'indice de réfraction et du volume de la cellule grâce à la procédure de découplage qui permet d'obtenir ces paramètres par des mesures de phase simultanées dans des milieux d'indice différents mais de pression osmotique similaire.

3.2 Conclusions principales

Cette étude montre que le Microscope Holographique Digital (DHM) est un outil adéquat pour mesurer la masse sèche avec une bonne résolution.

Nous avons observé une augmentation générale de la masse sèche locale par unité de longueur avec la largeur neuritique. Ceci est intéressant, car nous avons montré précédemment (**Chapitre 2 Figure 2.16**) que la polymérisation des microtubules augmente localement, d'environ 2.46 fois, quand la largeur du pattern augmente d'un facteur 3. En prenant en compte les variations de la largeur et de la répartition du matériel de la cellule, en particulier sur des patterns larges, la masse sèche et la polymérisation des microtubules semblent évoluer de concert.

Au niveau de la cellule, les résultats montrent de façon intéressante qu'il semble y avoir une homéostasie dans la masse neuritique totale dans les premiers stades de croissance et que celle-ci pourrait être brisée avec la polarisation axonale. Cela pourrait être lié à la différence entre les composants présents dans les axones et les dendrites (cf **Chapitre 1**). Cela serait alors intéressant d'étudier la densité de masse sèche dans des axones et des dendrites de largeurs similaires, après polarisation (3 DIV), pour observer si la brisure de l'homéostasie observée est seulement un effet de la polarisation axonale ou si elle est aussi dépendante des largeurs neuritiques.

4 Mesure de volume avec la Méthode d'eXclusion de Fluorescence

4.1 Résumé

Dans ce chapitre, le design de la puce microfluidique en PDMS et les étapes de sa fabrication sont premièrement présentés. Cette puce est notamment constituée d'une zone de mesure où des piliers supportent une chambre de hauteur contrôlée. Ces hauteurs ont été définies à $3\mu\text{m}$ pour l'étude des axones seuls et 10 et $12\mu\text{m}$ pour l'étude des neurones entiers (**Figure 4.1**). La **partie 4** présente la caractérisation de la chambre nécessaire à la validité des mesures. La hauteur des piliers (**Figure 4.6**), la rugosité du plafond (**Figure 4.7**) ainsi que le contrôle d'un plafond plat entre piliers (**Figure 4.8**) et d'une non contamination de la fluorescence entre l'inlet et la zone de mesure (**Figure 4.9 & 4.10**) sont alors présentés. La **partie 5** présente la méthode d'eXclusion de Fluorescence (FXm) permettant de convertir un signal d'intensité de fluorescence en hauteur grâce à la présence dans le champ de mesure d'un objet de hauteur connue précisément (en l'occurrence les piliers). L'utilisation de moule en silicone nous permet d'assurer la possibilité de mesurer de petits objets tels que les neurites dont on peut observer le signal de fluorescence (**Figure 4.11**) et la mesure de hauteur par exclusion de fluorescence a été validé pour des objets submicrométriques comme présenté en **Figure 4.12**. Le choix des objectifs est ensuite discuté et testé puis les mesures de volume et de hauteur sont alors validées

par la mesure d'un objet de dimension connues (**Figure 4.15**). La technique d'analyse est ensuite décrite, suivie par la **partie 6** décrivant les étapes de culture cellulaire et notamment l'étape de mise en culture dans les puces microfluidiques et les milieux de culture choisis.

La **partie 7** décrit les résultats de mesures de volume, au niveau local et statique de neurites non-patternés puis en dynamique en suivant le volume de vagues d'actine sur des neurones également non-patternés. Ces mesures de volume de vagues d'actine sont en particulier corrélées à des mesures d'intensité de fluorescence de l'actine possibles grâce à l'utilisation de souris LifeAct permettant d'observer l'actine en vert. Cette partie se finit sur des résultats préliminaires sur le couplage micropatterning - mesure de volume.

4.2 Conclusions principales

L'utilisation de moules en silicone s'est avérée efficace pour atteindre de hautes résolutions dans les mesures de volume.

Nous avons estimé que les changements de volume neuritique local semblent suivre une variation similaire en fonction des largeurs neuritiques que les microtubules et la masse sèche (**Chapitres 2 et 3**). Cette variation linéaire signifie une hauteur constante d'environ $0.4\mu\text{m}$ pour des neurites cultivés *in vitro*, indépendamment de leur largeur. Ce résultat doit encore être confirmé avec des données provenant de neurites de largeur plus grande. Néanmoins, si confirmé, cela soulèverait la question du mécanisme de régulation de la hauteur de neurites cultivés *in vitro* sur des substrats 2D. Cela soulèverait également la question d'un mécanisme de régulation de hauteur *in vivo*, bien que les neurites dans le cerveau forment des adhésions en 3D et déploient des formes cylindriques. De plus, le diamètre d'axones hippocampaux a été mesuré autour de $0.8\mu\text{m}$ *in vivo* (cf **Chapitre 1 Figure 1.10**). Cela est intéressant car cette valeur est le double de la valeur maximale de la hauteur des neurites adhérant sur des surfaces planes.

En outre, nous avons confirmé que les vagues d'actine provoquent un élargissement transitoire du neurite ainsi qu'une augmentation locale du volume neuritique. Curieusement, les vagues d'actine semblent perdre du volume lors de leur voyage le long du neurite.

5 Conclusion générale

Par les différentes approches développées durant mon projet de thèse, j'ai obtenu un ensemble de résultats associés au contrôle et aux mesures des morphologies neuronales. J'ai montré que la longueur et la polarité axo-dendritique de neurones isolés sur des micropatterns peuvent être définies par un contrôle sur les largeurs des neurites. J'ai aussi mis en évidence l'existence d'une homéostasie de la longueur neuritique totale lorsque le nombre de neurites varie. De plus, j'ai soulevé la question d'une possible homéostasie de la masse sèche totale avant et après la polarisation axonale. Localement, j'ai montré que la quantité de microtubules ainsi que la masse sèche et le volume des neurites augmentent avec la largeur des neurites, i.e. que la hauteur neuritique semble être régulée par la cellule. Finalement, je me suis concentrée sur des structures propagatives appelées vagues d'actine et j'ai obtenu des résultats préliminaires concernant leur perte de volume pendant leur voyage entre le soma et le bout des neurites.

Tout ce travail a été réalisé avec le design et le développement de plusieurs outils biophysiques afin d'étudier les formes neuronales. Ces différentes approches se sont construites au fil des différents lieux et environnements où ce projet a pris place et qui ont modelé cette recherche:

- A la plateforme Nanofab de l'Institut Néel, j'ai eu accès aux outils technologiques provenant du monde de la microélectronique, incluant la fabrication sur place de masques, la présence d'un grand nombre de photorésines et la possibilité de graver les lamelles de verre. Cela m'a permis de mettre en place de nouvelles idées très rapidement. En jouant avec les formes des micropatterns, nous avons mis en évidence certains mécanismes de la croissance, de la polarisation et de l'organisation du cytosquelette des neurones.
- Avec le Microscope Holographique Digital (DHM), acquis par l'Institut Néel, et avec le support des ateliers mécaniques de l'Institut Néel et de l'Institut Curie, j'ai pu effectuer des images de phase des neurones. Puis, grâce à des discussions à l'Institut Curie, je me suis intéressée à l'obtention de la masse sèche des neurites et j'ai obtenu des résultats préliminaires sur ce sujet.
- Finalement, par mon intégration à l'équipe de Jean-Louis Viovy à l'Institut Curie et par le travail prenant place dans le nouveau centre de recherche sur la microfluidique qu'est l'Institut Pierre Gilles de Gennes, j'ai développé la méthode d'exclusion de fluorescence pour la mesure du volume neuronal et j'ai pu obtenir des premières observations de la hauteur neuritique et du volume local, incluant

les changements dynamiques provoqués par le mouvement des vagues d'actine.

Maintenant que ces différents outils et installations sont bien caractérisés et optimisés, les différentes perspectives présentées aux fins des chapitres 1 à 3 (version originale) sont atteignables. Durant les prochains mois, je vais particulièrement me concentrer sur:

- ◇ Acquérir assez de statistiques sur la masse sèche totale ainsi que sur le volume neuritique total sur des neurones patternés
- ◇ Etudier le volume des vagues d'actine sur des neurones patternés, en particulier suivre l'évolution de ce volume lorsque les largeurs neuritiques varient abruptement
- ◇ Obtenir l'indice de réfraction de différents compartiments neuronaux

Ces objectifs seront atteints dans l'environnement biophysique de l'IPGG et des instituts voisins.

Cela m'amène à une conclusion plus personnelle où j'aimerais mettre en valeur ce que j'ai appris en travaillant à l'interface de différents domaines et en particulier en partageant mes recherches avec un public non scientifique.

Travailler à l'interface de la biologie et de la physique a apporté beaucoup à mon sujet. Travailler à l'interface entre les domaines est en particulier nécessaire dans notre siècle, où la science est devenue de plus en plus fragmentée. Sans les interactions avec mes collègues de différents domaines, je n'aurais pas pu achever ce travail.

Mais ce n'est pas que le dialogue avec des collègues scientifiques qui peut nous apporter des idées et des technologies. Décrire notre recherche à un public non-scientifique m'a aussi semblé d'un grand intérêt. Simplifier notre projet et adapter sa présentation pour que tout le monde puisse le comprendre m'a apporté beaucoup de nouvelles idées intéressantes d'un point de vue inattendu. Je suis alors particulièrement intéressée dans le partage des sciences avec un large public. Durant ma thèse, j'ai participé à différents projets, de mon investissement à la création du Parcours Biophysique pour la Fête de la Science de l'Institut Néel et des cours de journalisme scientifique procurés par l'école doctorale de Grenoble à mon implication dans différents événements de l'espace de médiation scientifique ESPGG (Espace Pierre Gilles de Gennes) comme la Fête de la Science, la Nuit des Chercheurs ou Un chercheur et moi.

J'aimerais dire qu'une part importante de la vie de doctorant n'est pas seulement dans l'apprentissage de techniques et dans la consécration de son temps à la paillasse ou à l'analyse des données, mais qu'elle est aussi d'apprendre comment partager la science et comment construire de nouveaux projets de recherche en étant prêt à toujours apprendre de nouvelles choses. Pour ces raisons, je souhaite que tous les autres doctorants puissent avoir une expérience aussi intéressante que la mienne.

APPENDICES

1 Appendix 1: Model calculation of neurites length and polarization

To turn these assumptions into a calculation of the mean neurite length on the patterns shown in **Figure 2.10**, we need to assume some probability density function that describes the probability for the neurite to undergo polarization, as a function of its length. Based on the notion of a critical length for this transition [178, 179], we consider the following simple step-like cumulative probability to polarize

$$P_{pol}(x) = \frac{1}{2} \left(1 + \tanh \left[\frac{x - L_{pol}}{\sigma_{pol}} \right] \right) \quad (7.1)$$

$$\Rightarrow p_{pol}(x) = \frac{dP_{pol}(x)}{dx} = \frac{1}{2\sigma_{pol}} \operatorname{sech} \left[\frac{x - L_{pol}}{\sigma_{pol}} \right]^2 \quad (7.2)$$

where L_{pol} is the critical polarization length and σ_{pol} gives the variance of the probability distribution function around this critical length, as shown in **Figure 7.1**.

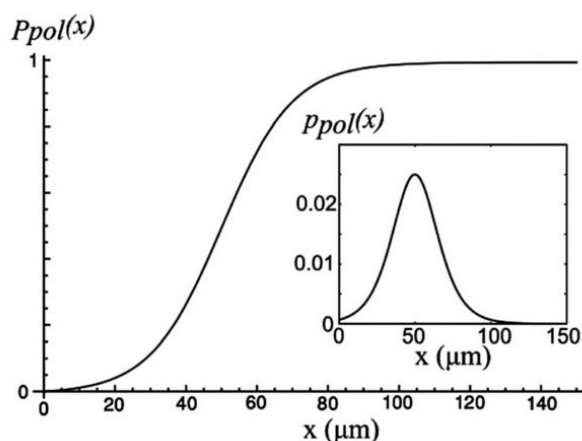


Figure 7.1 – Polarization cumulative probability $P_{pol}(x)$ (eqn (2.1)) and the probability distribution function $p_{pol}(x)$ (eqn (2.2)) (inset). The parameters used are $L_{pol} = 50 \mu\text{m}$ and $\sigma_{pol} = 20 \mu\text{m}$.

We then divide the calculation into two cases, for the case of polarization along the right neurite and along the left neurite. We now demonstrate the calculations that result from our model for the x:xy patterns (shown in **Figure 2.10**). A similar calculation follows along the same lines for the y:xy patterns. For polarization along the right neurite, the length of the right neurite is given by the following

$$L_{R,R} = \begin{cases} x_{pol} + (T - t_{pol,1})\beta\nu_y, & [x_{pol} > l] \\ l + (T - t_l)\beta\nu_y, & [x_{pol} < l, T > t_l] \\ l + (T - t_{pol,2})\beta\nu_x, & [x_{pol} < l, T < t_l] \end{cases} \quad (7.3)$$

where l is the length of the x -segment on the right side, x_{pol} is the location of the polarization event on the right neurite, T is the time at which the observation is performed and $\nu_{x,y}$ are the tip velocities on the respective widths. The different times are defined as

$$t_{pol,1} = \frac{l}{\nu_x} + \frac{x_{pol} - l}{\nu_y} \quad (7.4)$$

$$t_{pol,2} = \frac{x_{pol}}{\nu_x} \quad (7.5)$$

$$t_l = t_{pol,2} + \frac{l - x_{pol}}{\beta\nu_x} \quad (7.6)$$

The maximal value of x_{pol} for the right neurite is

$$x_{pol,max,R} = \begin{cases} l + (T - (l/\nu_x))\nu_y, & [T > (l/\nu_x)] \\ T\nu_x, & [T < (l/\nu_x)] \end{cases} \quad (7.7)$$

Over the possible range of x_{pol} we need to integrate the lengths in **eqn (2.3)** multiplied by the probability that the right neurite polarizes at position x_{pol} , which is given by $p_{pol}(x)$ (eqn (2)). In addition we need to multiply by the probability that the competing neurite has not already polarized itself by this time. This probability is given by the cumulative probability up to the position of the tip on the left neurite $x_{pol,L}$, corresponding to x_{pol} on the right neurite

$$p_{nopol,L}(x_{pol}) = 1 - \int_0^{x_{pol,L}} p_{pol}(x)dx = 1 - \frac{1}{2} \left(\tanh \left[\frac{L_{pol}}{\sigma_{pol}} \right] - \tanh \left[\frac{L_{pol} - t_{pol}\nu_x}{\sigma_{pol}} \right] \right) \quad (7.8)$$

where t_{pol} stands for $t_{pol,1}$ and $t_{pol,2}$ given in **eqn (2.4) and (2.5)** respectively, and $x_{pol,L} = t_{pol}\nu_x$.

The final mean length that we get is

$$\langle L_{R,R} \rangle = \int_0^{x_{pol,max,R}} L_{R,R} p_{pol}(x_{pol}) p_{nopol,L}(x_{pol}) dx_{pol} \quad (7.9)$$

where the overall probability for polarization of the right neurite is given by

$$P_R = \int_0^{x_{pol,max,R}} p_{pol}(x_{pol})p_{nopol,L}(x_{pol})dx_{pol} \quad (7.10)$$

For completeness, the overall probability for polarization of the left neurite is given by

$$P_L = \int_0^{x_{pol,max,L}} p_{pol}(x_{pol})p_{nopol,R}(x_{pol})dx_{pol} \quad (7.11)$$

where: $x_{pol,max,L} = T\nu_x$, and

$$p_{nopol,R}(x_{pol}) = 1 - \int_0^{x_{pol,R}} p_{pol}(x)dx = \begin{cases} 1 - \frac{1}{2} \left(\tanh \left[\frac{L_{pol}}{\sigma_{pol}} \right] - \tanh \left[\frac{L_{pol} - x_{pol}}{\sigma_{pol}} \right] \right), & [l > x_{pol}] \\ 1 - \frac{1}{2} \left(\tanh \left[\frac{L_{pol}}{\sigma_{pol}} \right] - \tanh \left[\frac{L_{pol} - (l + (x_{pol} - l)\nu_y/\nu_x)}{\sigma_{pol}} \right] \right), & [l < x_{pol}] \end{cases} \quad (7.12)$$

In a similar manner we calculate the length of the left neurite when the right one is polarized ($\langle L_{L,R} \rangle$) and the lengths for the case of polarization on the left neurite (i.e. $\langle L_{L,L} \rangle$ and $\langle L_{R,L} \rangle$). In order to get the total mean length along each side, we also need to consider the lengths of the neurites when no side has polarized. For the x:xy these lengths are given by

$$L_{L,0} = T\nu_x p_{nopol} \quad (7.13)$$

and

$$L_{R,0} = \begin{cases} (l + (T - (l/\nu_x))\nu_y)p_{nopol}, & [T > (l/\nu_x)] \\ T\nu_x p_{nopol}, & [T < (l/\nu_x)] \end{cases} \quad (7.14)$$

where the probability for no polarization is given by $p_{nopol} = 1 - P_R - P_L$, where P_R is given in **eqn (10)**.

Summing up the lengths on each neurite from all the possible polarization outcomes gives the final mean lengths: $L_L = L_{L,0} + \langle L_{L,R} \rangle + \langle L_{L,L} \rangle$ and $L_R = L_{R,0} + \langle L_{R,R} \rangle + \langle L_{R,L} \rangle$.

2 Appendix 2: "Diver" design and technical scheme

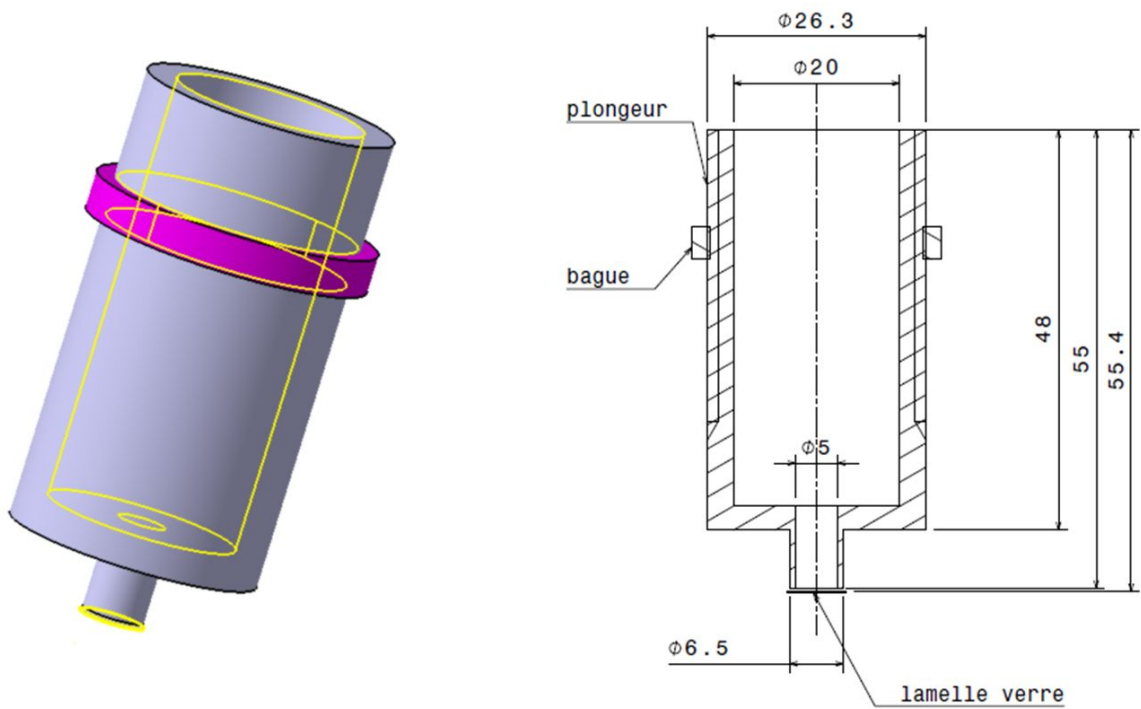


Figure 7.2 – Design and technical scheme of the "diver". Anne Gerardin, Institut Néel, Grenoble.

3 Appendix 3: Matlab program for Phase analysis

3.1 Main program: dhm5201601.m

```

goAgain = true;
while goAgain

%% Look for the Background Phase txt file
message = sprintf('Select the txt file of the Background Phase');
uiwait(msgbox(message));
[filename0,pathname0] = uigetfile('*.txt','Select the Txt-file');

%% Import the .txt file of the background phase in a matrix
name = [pathname0 filename0];
importfiledhm(name);
Phase0 = data;
clearvars data name;

%% Look for the Phase txt file
message = sprintf('Select the txt file of the Phase');
uiwait(msgbox(message));
[filename,pathname] = uigetfile('*.txt','Select the Txt-file');
mkdir(pathname, '\results');

%% Import the .txt file in a matrix
name = [pathname filename];
importfiledhm(name);
Phase=data;
Phase1 = data;
Phase = Phase1 - Phase0;

%% Clear temporary variables
clearvars data textdata;

%% Manual crop on the neuron phase image to selection a neurite zone
prompt = {'Enter your neuron and zone names: '};
dlg_title = 'Input crop';
num_lines = 1;
def = {'AC104-N2-z1'};
answer = inputdlg(prompt,dlg_title,num_lines,def);
message = sprintf('Select the zone to analyze');
uiwait(msgbox(message));
figure('Name','Phase','NumberTitle','off')
[crop rect]=imcrop(Phase,[-1 1]);
zone1=crop;

    s1 = size(zone1);
    x1=1:s1(1);
    x1_um=x1*0.153112;
    x2=1:s1(2);
    x2_um=x2*0.153112;

promptb = {'What is the size of the pattern ?'};
dlg_titleb = 'Input crop';
num_lines = 1;
defb = {'2'};
patt = inputdlg(promptb,dlg_titleb,num_lines,defb);
pattern_size=str2num(patt{1});

figure('Name',answer{1},'NumberTitle','off')
imshow(zone1,[-1 1])
title(answer{1})
hgexport(gcf, strcat(pathname, '\results\',answer{1},'.tiff'), hgexport('factorystyle'), 'Format', 'tiff');

prompt2 = {'Is the neurite treated on the left of the soma ?'};
dlg_title2 = 'neurite side';
num_lines = 1;
def = {'no'};
side = inputdlg(prompt2,dlg_title2,num_lines,def);
a=side{1};
b='yes';
tf = strcmp(a,b)
if (tf == 1)
    dhm_left5
else
    dhm_right5
end

%%Cleaning the workspace and request for doing a new study or not
clear;
close all;
res = input('Would you like to have more fun and to study a new zone :) ', 's');
goAgain = isequal(upper(res), 'YES');
end

```

3.2 Routine to analyze neurite on the right of the soma: dhwright5.m

```

%% Mean profile every 5µm on 2µm each side
i=0;
j=0;
l=s1(2)-50;
while j < l
    i=i+5;
    j=floor(i/0.153112);
    mean_profile=zone1(:,j);
    for k=1:16
        mean_profile=mean_profile+zone1(:,j-k)+zone1(:,j+k)
    end
    mean_profile=mean_profile/33;
    mean_prof(:,i)=mean_profile;
%Standard Deviation
    m=j-13;
    n=j+13;
    for o=m:n
        p=o-m+1;
        Sd(:,p)=zone1(:,o);
    end
    standard_dev(:,i)=std(transpose(Sd));
end
smp=size(mean_prof);
for i=5:5:smp(2)
    i2=i-1/5*4;
    mean_prof5(:,i2)=mean_prof(:,i);
    standard_dev5(:,i2)=standard_dev(:,i);
end

%Adjustment every 5µm
smp2=size(mean_prof5)
message = sprintf('Select points to define the baseline');
uiwait(msgbox(message));
for i=1:smp2(2)
    [ycorr,yfit] = bf(mean_prof5(:,i));
    coupe_reaj(:,i)=ycorr;
end

%Graphs
ETmax=coupe_reaj+standard_dev5;
ETmin=coupe_reaj-standard_dev5;
for i=1:smp2(2)
    i3=i*5;
    figure('Name',strcat(['Adjusted Mean Profile & STDs of ', answer{1}, '_at_',
    ', num2str(i3), 'µm']), 'NumberTitle', 'off')
    plot(x1_um,coupe_reaj(:,i),x1_um,ETmax(:,i),x1_um,ETmin(:,i));
    title(strcat(['Adjusted Mean Profile & STDs of ', answer{1}, '_at_',
    ', num2str(i3), 'µm']))
    xlabel('Width (µm)')
    ylabel('Phase (rad)')
    hgexport(gcf,
    strcat(pathname, '\results\', 'Adjusted_Mean_Profile_and_STDs_of_', answer{1}, '_at_', num2str(i3), 'µm
    '.tiff'), hgexport('factorystyle'), 'Format', 'tiff');
    saveas(gcf,
    strcat(pathname, '\results\', 'Adjusted_Mean_Profile_and_STDs_of_', answer{1}, '_at_', num2str(i3), 'µm
    '.fig'), 'fig');
end

%% Maximal Phase Value every 5µm and Mean
x5_um=x2(:,1:smp2(2))*5;
for i=1:smp2(2)
    mean_max_mean_profile(:,i)=max(coupe_reaj(:,i));
end
figure('Name',strcat(['Max. phase along the neurite of ', answer{1}], 'NumberTitle', 'off')
hold on
scatter(x5_um,mean_max_mean_profile,'g')
plot(x5_um,mean_max_mean_profile,'g')
hold off
title(strcat(['Max. phase along the neurite of ', answer{1}]))
xlabel('Distance from the soma (µm)')
ylabel('Max. phase (rad)')

```

```

hgexport(gcf, strcat(pathname, '\results\', 'Max_phase_along_the_neurite_of_', answer{1}, '.tiff'),
hgexport('factorystyle', 'Format', 'tiff');
saveas(gcf,
strcat(pathname, '\results\', 'Max_phase_along_the_neurite_of_', answer{1}, '.fig'), 'fig');

mean_max=sum(mean_max_mean_profile(:, :), 2)/smp2(2)

%% Width every 5 µm
for i=1:smp2(2)

D=diff(coupe_reaj(:, i));
D1=[D;0];
D12=smooth(D1);
D13=smooth(D12);
D14=smooth(D13);
D2=smooth(D14);
D3=diff(D2);
D4=[D3;0];
D5=smooth(D4);
D6=smooth(D5);

[pks, locs] = findpeaks(D6);

P1=(pks>0.0015);
P2 = sum(P1(:, :), 1);
if P2 == 2

k=size(pks);
k1=k(1);
for n=1:k
    if pks(n)>0.0015
        w(n)=locs(n);
    else w(n)=0;
    end
end
mean_width=abs(sum(w)-2*max(w));
mean_width_mean_profile(:, i)=mean_width*0.153112;
else
    mean_width_mean_profile(:, i)=pattern_size;
end
end
tot_mean_width=sum(mean_width_mean_profile(:, :), 2)/smp2(2)

%Graphs
figure('Name',strcat(['Width along the neurite of ', answer{1}]),'NumberTitle','off')
hold on
scatter(x5_um,mean_width_mean_profile,'r');
plot(x5_um,mean_width_mean_profile,'r');
hold off
title(strcat(['Width along the neurite of ', answer{1}]))
xlabel('Distance from the soma (µm)')
ylabel('Width (µm)')
hgexport(gcf, strcat(pathname, '\results\', 'Width_along_the_neurite_of_', answer{1}, '.tiff'),
hgexport('factorystyle', 'Format', 'tiff');
saveas(gcf, strcat(pathname, '\results\', 'Width_along_the_neurite_of_', answer{1}, '.fig'), 'fig');

%% Phase surface along the neurite
for i=1:smp2(2)

plot(x1_um, coupe_reaj(:, i));
fprintf(['\n Now select baseline points to fit by positioning cursor', ...
        '\n   and selecting points with mouse button or key press.', ...
        '\n Press Enter key when done.\n'])

[a,b] = ginput; %a contient les deux coordonnees x voulues
sx1=size(x1_um);
width_v2(i)=a(2)-a(1);
for j=1:sx1(2)
    if (x1_um(j)>a(1)) & (x1_um(j)<a(2))

```

```

        small_coupe(j,i)=coupe_reaj(j,i);
    else small_coupe(j,i)=0;
    end
end
end

d1=size(small_coupe)
for r=1:d1(2)
    if small_coupe(:,1)==0
        small_coupe(:,1)=[]
    end
end
end
dt=transpose(small_coupe);
d2=size(dt)

for r=1:d2(2)
    if dt(:,1)==0
        dt(:,1)=[]
    end
end
end
small_coupe=transpose(dt);
d3=size(small_coupe)
xlb=xl_um(:,1:d3(1))
for i=1:smp2(2)
    surf_moy(:,i)=trapz(xlb,small_coupe(:,i));
end

mean_width_v2=sum(width_v2(:,:),2)/smp2(2)

figure('Name',strcat(['Width v2 along the neurite of ', answer{1}]),'NumberTitle','off')
hold on
scatter(x5_um,width_v2,'r');
plot(x5_um,width_v2,'r');
hold off
title(strcat(['Width v2 along the neurite of ', answer{1}]))
xlabel('Distance from the soma ( $\mu\text{m}$ )')
ylabel('Width v2 ( $\mu\text{m}$ )')
hgexport(gcf, strcat(pathname, '\results\', 'Widthv2_along_the_neurite_of_', answer{1}, '.tiff'),
hgexport('factorystyle', 'Format', 'tiff');
saveas(gcf, strcat(pathname, '\results\', 'Widthv2_along_the_neurite_of_', answer{1}, '.fig'), 'fig');

figure('Name',strcat(['Phase surface along the neurite of ', answer{1}]),'NumberTitle','off')
hold on
scatter(x5_um,surf_moy);
plot(x5_um,surf_moy);
hold off
title(strcat(['Phase surface along the neurite of ', answer{1}]))
xlabel('Distance from the soma ( $\mu\text{m}$ )')
ylabel('Phase surface ( $\mu\text{m}\cdot\text{rad}$ )')
hgexport(gcf,
strcat(pathname, '\results\', 'Phase_surface_along_the_neurite_of_', answer{1}, '.tiff'),
hgexport('factorystyle', 'Format', 'tiff');
saveas(gcf,
strcat(pathname, '\results\', 'Phase_surface_along_the_neurite_of_', answer{1}, '.fig'), 'fig');

mean_phase_surf=sum(surf_moy(:,:),2)/smp2(2)

%% Mean volume (using the surface of the mean profile and the length of the zone)
%% Integral calculated by the trapeze method
long_tot_um=s1(2)*0.153112

%cas 1 : proche soma et i=1
vol_moy(:,1)=surf_moy(:,1)*7.5;
%cas 2 : i=2:n-1
smp3=smp2(2)-1;
for i=2:smp3
    vol_moy(:,i)=surf_moy(:,i)*5;
end
%cas 3 : i=n + fin

```

```

vol_moy(:,smp2(2))=surf_moy(:,smp2(2))*(long_tot_um - (smp2(2)*5-2.5));
%vol total
vol_moy_tot=sum(vol_moy(:,:),2)

%%Registration of the obtained data

X={' ' ; 'Neuron' ; 'Length' ; 'Mean Max' ; 'Mean Width' ; 'Mean Width v2' ; 'Mean Surface' ;
'Volume'};
Y={'Values' ; answer{1} ; long_tot_um ; mean_max ; tot_mean_width; mean_width_v2 ;
mean_phase_surf ; vol_moy_tot};
Z={'Unity' ; ' ' ; 'um' ; 'rad' ; 'um' ; 'um' ; 'um.rad' ; 'um.um.rad'};

Answers = [X Y Z];
filename1 = strcat(pathname,'results',filesep,'Answers_', answer{1},'.xlsx');
xlswrite(filename1,Answers)
%xlwwrite(filename1,Answers)

%javaaddpath(['\Users\Celine/Documents/Matlab/analyses_fin_2/poi_library' filesep 'poi-3.8-
20120326.jar']);

Z0={'Distance from soma (µm)'};
xlswrite(filename1,Z0,1,'A11')
x2t=transpose(x5_um);
xlswrite(filename1,x2t,1,'A12')
Z1={'Max Phase (rad)'};
xlswrite(filename1,Z1,1,'B11')
max_radt=transpose(mean_max_mean_profile);
xlswrite(filename1,max_radt,1,'B12')
Z2={'Phase surface (rad*µm)'};
xlswrite(filename1,Z2,1,'C11')
integt=transpose(surf_moy);
xlswrite(filename1,integt,1,'C12')
Z3={'Width (µm)'};
xlswrite(filename1,Z3,1,'D11')
width_omt=transpose(mean_width_mean_profile);
xlswrite(filename1,width_omt,1,'D12')
Z4={'Width v2 (µm)'};
xlswrite(filename1,Z4,1,'E11')
width_v2_omt=transpose(width_v2);
xlswrite(filename1,width_v2_omt,1,'E12')

fid=fopen(strcat(pathname,'results',filesep,'all_data_',answer{1},'.txt'),'a+');
fprintf(fid,'%6s %6s %6s %6s\r\n','Distance from soma (µm)', 'MaxPhase (rad)', 'Phase surface (rad*µm)', '
Width (µm)');
A=[x5_um;mean_max_mean_profile;surf_moy;mean_width_mean_profile];
fprintf(fid,'%6f %6f %6f %6f\r\n',A);
fclose(fid);

```

3.3 Routine to analyze neurite on the left of the soma: dhmleft5.m

```

%% Mean profile every 5µm on 2.4µm (16pixels) each side
i=floor(s1(2)*0.153112);
j=floor(i/0.153112);
while j > 50
    i=i-5;
    j=floor(i/0.153112);
    mean_profile=zone1(:,j);
    for k=1:16
        mean_profile=mean_profile+zone1(:,j-k)+zone1(:,j+k)
    end
    mean_profile=mean_profile/33;
    i1=floor(s1(2)*0.153112-i);
    mean_prof(:,i1)=mean_profile;
%Standard Deviation
m=j-13;
n=j+13;
for o=m:n
    p=o-m+1;
    Sd(:,p)=zone1(:,o);
end
standard_dev(:,i1)=std(transpose(Sd));
end
smp=size(mean_prof);
for i=5:5:smp(2)
    i2=i-i/5*4;
    mean_prof5(:,i2)=mean_prof(:,i);
    standard_dev5(:,i2)=standard_dev(:,i);
end

%Adjustment every 5µm
smp2=size(mean_prof5)
message = sprintf('Select points to define the baseline');
uiwait(msgbox(message));
for i=1:smp2(2)
    [ycorr,yfit] = bf(mean_prof5(:,i));
    coupe_reaj(:,i)=ycorr;
end

%Graphs
ETmax=coupe_reaj+standard_dev5;
ETmin=coupe_reaj-standard_dev5;
for i=1:smp2(2)
    i3=i*5;
    figure('Name',strcat(['Adjusted Mean Profile & STDs of ', answer{1}, ' ', 'at ', '
',num2str(i3), 'µm']), 'NumberTitle','off')
    plot(x1_um,coupe_reaj(:,i),x1_um,ETmax(:,i),x1_um,ETmin(:,i));
    title(strcat(['Adjusted Mean Profile & STDs of ', answer{1}, ' ', 'at ', ' ', num2str(i3), 'µm']))
    xlabel('Width (µm)')
    ylabel('Phase (rad)')
    hgexport(gcf,
    strcat(pathname, '\results\', 'Adjusted_Mean_Profile_and_STDs_of_', answer{1}, '_at_', num2str(i3), 'µm'
    '.tiff'), hgexport('factorystyle'), 'Format', 'tiff');
    saveas(gcf,
    strcat(pathname, '\results\', 'Adjusted_Mean_Profile_and_STDs_of_', answer{1}, '_at_', num2str(i3), 'µm'
    '.fig'), 'fig');
end

%% Maximal Phase Value every 5µm and Mean
x5_um=x2(:,1:smp2(2))*5;
%21
for i=1:smp2(2)
    mean_max_mean_profile(:,i)=max(coupe_reaj(:,i));
end
figure('Name',strcat(['Max. phase along the neurite of ', answer{1}]),'NumberTitle','off')
hold on
scatter(x5_um,mean_max_mean_profile,'g')

```

```

plot(x5_um,mean_max_mean_profile,'g')
hold off
title(strcat(['Max. phase along the neurite of ', answer{1}]))
xlabel('Distance from the soma ( $\mu\text{m}$ )')
ylabel('Max. phase (rad)')
hgexport(gcf, strcat(pathname, '\results\', 'Max_phase_along_the_neurite_of_', answer{1}, '.tiff'),
hgexport('factorystyle'), 'Format', 'tiff');
saveas(gcf, strcat(pathname, '\results\', 'Max_phase_along_the_neurite_of_', answer{1}, '.fig'), 'fig');

mean_max=sum(mean_max_mean_profile(:, :), 2)/smp2(2)

%% Width every 5  $\mu\text{m}$ 
for i=1:smp2(2)

D=diff(coupe_reaj(:, i));
D1=[D;0];
D12=smooth(D1);
D13=smooth(D12);
D14=smooth(D13);
D2=smooth(D14);
D3=diff(D2);
D4=[D3;0];
D5=smooth(D4);
D6=smooth(D5);

[pks,locs] = findpeaks(D6);

P1=(pks>0.0015);
P2 = sum(P1(:, :), 1);
if P2 == 2

k=size(pks);
k1=k(1);
for n=1:k
    if pks(n)>0.0015
        w(n)=locs(n);
    else w(n)=0;
    end
end
mean_width=abs(sum(w)-2*max(w));
mean_width_mean_profile(:, i)=mean_width*0.153112;
else
    mean_width_mean_profile(:, i)=pattern_size;
end
end
tot_mean_width=sum(mean_width_mean_profile(:, :), 2)/smp2(2)

%Graphs
figure('Name',strcat(['Width along the neurite of ', answer{1}]),'NumberTitle','off')
hold on
scatter(x5_um,mean_width_mean_profile,'r');
plot(x5_um,mean_width_mean_profile,'r');
hold off
title(strcat(['Width along the neurite of ', answer{1}]))
xlabel('Distance from the soma ( $\mu\text{m}$ )')
ylabel('Width ( $\mu\text{m}$ )')
hgexport(gcf, strcat(pathname, '\results\', 'Width_along_the_neurite_of_', answer{1}, '.tiff'),
hgexport('factorystyle'), 'Format', 'tiff');
saveas(gcf, strcat(pathname, '\results\', 'Width_along_the_neurite_of_', answer{1}, '.fig'), 'fig');

%% Phase surface along the neurite
% for i=1:smp2(2)
% surf_moy(:, i)=trapz(x1_um,coupe_reaj(:, i));
% end

for i=1:smp2(2)

plot(x1_um,coupe_reaj(:, i));

```

```

fprintf(['\n Now select baseline points to fit by positioning cursor',...
        '\n   and selecting points with mouse button or key press.',...
        '\n Press Enter key when done.\n'])

[a,b] = ginput; %a contient les deux coordonnees x voulues
    sx1=size(x1_um);
    width_v2(i)=a(2)-a(1);
for j=1:sx1(2)
if (x1_um(j)>a(1)) & (x1_um(j)<a(2))
    small_coupe(j,i)=coupe_reaj(j,i);
else small_coupe(j,i)=0;
end
end

end

d1=size(small_coupe)
for r=1:d1(2)
    if small_coupe(:,1)==0
        small_coupe(:,1)=[]
    end
end
dt=transpose(small_coupe);
d2=size(dt)
for r=1:d2(2)
    if dt(:,1)==0
        dt(:,1)=[]
    end
end
small_coupe=transpose(dt);
d3=size(small_coupe)
x1b=x1_um(:,1:d3(1))
for i=1:smp2(2)
surf_moy(:,i)=trapz(x1b,small_coupe(:,i));
end

mean_width_v2=sum(width_v2(:,:),2)/smp2(2)

figure('Name',strcat(['Width v2 along the neurite of ', answer{1}]),'NumberTitle','off')
hold on
scatter(x5_um,width_v2,'r');
plot(x5_um,width_v2,'r');
hold off
title(strcat(['Width v2 along the neurite of ', answer{1}]))
xlabel('Distance from the soma ( $\mu\text{m}$ )')
ylabel('Width v2 ( $\mu\text{m}$ )')
hgexport(gcf, strcat(pathname, '\results\', 'Widthv2_along_the_neurite_of_', answer{1}, '.tiff'),
hgexport('factorystyle'), 'Format', 'tiff');
saveas(gcf, strcat(pathname, '\results\', 'Widthv2_along_the_neurite_of_', answer{1}, '.fig'), 'fig');

figure('Name',strcat(['Phase surface along the neurite of ', answer{1}]),'NumberTitle','off')
hold on
scatter(x5_um,surf_moy);
plot(x5_um,surf_moy);
hold off
title(strcat(['Phase surface along the neurite of ', answer{1}]))
xlabel('Distance from the soma ( $\mu\text{m}$ )')
ylabel('Phase surface ( $\mu\text{m}\cdot\text{rad}$ )')
hgexport(gcf, strcat(pathname, '\results\', 'Phase_surface_along_the_neurite_of_', answer{1}, '.tiff'),
hgexport('factorystyle'), 'Format', 'tiff');
saveas(gcf,
strcat(pathname, '\results\', 'Phase_surface_along_the_neurite_of_', answer{1}, '.fig'), 'fig');

mean_phase_surf=sum(surf_moy(:,:),2)/smp2(2)

%% Mean volume (using the surface of the mean profile and the length of the zone)
%% Integral calculated by the trapeze method
long_tot_um=s1(2)*0.153112

%cas 1 : proche soma et i=1

```

```

vol_moy(:,1)=surf_moy(:,1)*7.5;
%cas 2 : i=2:n-1
smp3=smp2(2)-1;
for i=2:smp3
vol_moy(:,i)=surf_moy(:,i)*5;
end
%cas 3 : i=n + fin
vol_moy(:,smp2(2))=surf_moy(:,smp2(2))*(long_tot_um - (smp2(2)*5-2.5));
%vol total
vol_moy_tot=sum(vol_moy(:,:),2)

%%Registration of the obtained data

X={' ' ; 'Neuron' ; 'Length' ; 'Mean Max' ; 'Mean Width' ; 'Mean Width v2' ; 'Mean Surface' ;
'Volume'};
Y={'Values' ; answer{1} ; long_tot_um ; mean_max ; tot_mean_width; mean_width_v2 ; mean_phase_surf ;
vol_moy_tot};
Z={'Unity' ; ' ' ; 'um' ; 'rad' ; 'um'; 'um' ; 'um.rad' ; 'um.um.rad'};

Answers = [X Y Z];
filename1 = strcat(pathname,'results',filesep,'Answers_', answer{1},'.xlsx');
xlswrite(filename1,Answers)
%xlwrite(filename1,Answers)

%javaaddpath(['\Users\Celine/Documents/Matlab/analyses_fin_2/poi_library' filesep 'poi-3.8-
20120326.jar']);

Z0={'Distance from soma ( $\mu\text{m}$ )'};
xlswrite(filename1,Z0,1,'A11')
x2t=transpose(x5_um);
xlswrite(filename1,x2t,1,'A12')
Z1={'Max Phase (rad)'};
xlswrite(filename1,Z1,1,'B11')
max_radt=transpose(mean_max_mean_profile);
xlswrite(filename1,max_radt,1,'B12')
Z2={'Phase surface (rad* $\mu\text{m}$ )'};
xlswrite(filename1,Z2,1,'C11')
integt=transpose(surf_moy);
xlswrite(filename1,integt,1,'C12')
Z3={'Width ( $\mu\text{m}$ )'};
xlswrite(filename1,Z3,1,'D11')
width_omt=transpose(mean_width_mean_profile);
xlswrite(filename1,width_omt,1,'D12')
Z4={'Width v2 ( $\mu\text{m}$ )'};
xlswrite(filename1,Z4,1,'E11')
width_v2_omt=transpose(width_v2);
xlswrite(filename1,width_v2_omt,1,'E12')

fid=fopen(strcat(pathname,'results',filesep,'all_data_', answer{1},'.txt'),'a+');
fprintf(fid,'%6s %6s %6s %6s\r\n','Distance from soma ( $\mu\text{m}$ )','Max Phase (rad)','Phase surface (rad* $\mu\text{m}$ )','Wi
dth ( $\mu\text{m}$ )');
A=[x5_um;mean_max_mean_profile;surf_moy;mean_width_mean_profile];
fprintf(fid,'%6f %6f %6f %6f\r\n',A);
fclose(fid);

```

3.4 Routine to sum results from the different parts of a neurite: dhm-sum5.m

```

prompt1 = {'Enter your neuron name and the neurite size: '};
dlg_title1 = 'Neuron name';
num_lines = 1;
def1 = {'AC104-N2'};
res1 = inputdlg(prompt1,dlg_title1,num_lines,def1);

prompt = {'How many zones would you like to merge ?'};
dlg_title = 'Number of zones';
num_lines = 1;
def = {'4'};
res = inputdlg(prompt,dlg_title,num_lines,def);
n=str2num(res{1});

total_length=0;
tot_max=0;
tot_width=0;
tot_width_v2=0;
tot_surf=0;
total_volume=0;

message = sprintf(strcat('Select the file of the zone ',num2str(1),' of the neurite (placement in the folder)'));
uiwait(msgbox(message));
[filename1,pathname1] = uigetfile('*.xlsx','Select the xlsx-file');

for i=1:n

message = sprintf(strcat('Select the file of the zone ',num2str(i),' of the neurite'));
uiwait(msgbox(message));
[filename{i},pathname{i}] = uigetfile(strcat(pathname1,'*.xlsx'),'Select the xlsx-file');

%Total Length
l{i}=xlsread(strcat(pathname{i},filename{i}),1,'B3');
total_length=l{i}+total_length;
%Total Mean Max
max{i}=xlsread(strcat(pathname{i},filename{i}),1,'B4');
tot_max=max{i}+tot_max;
%Total Mean Width
width{i}=xlsread(strcat(pathname{i},filename{i}),1,'B5');
tot_width=width{i}+tot_width;
%Total Mean Width v2
width_v2{i}=xlsread(strcat(pathname{i},filename{i}),1,'B6');
tot_width_v2=width_v2{i}+tot_width_v2;
%Total Mean Surface
surf{i}=xlsread(strcat(pathname{i},filename{i}),1,'B7');
tot_surf=surf{i}+tot_surf;
%Total Volume
volume{i}=xlsread(strcat(pathname{i},filename{i}),1,'B8');
total_volume=volume{i}+total_volume;
end

%Results
total_length
tot_mean_max=tot_max/n
tot_mean_width=tot_width/n
tot_mean_width_v2=tot_width_v2/n
tot_mean_surface=tot_surf/n
total_volume

%%Registration of the obtained data
X={' ' ; 'Neuron' ; 'Total Length' ; 'Total Mean Max' ; 'Total Mean Width' ; 'Total Mean Width v2' ; 'Total Mean Surface' ; 'Total Volume'};
Y={'Values' ; res1{1} ; total_length ; tot_mean_max ; tot_mean_width ; tot_mean_width_v2 ; tot_mean_surface ; total_volume};
Z={'Unity' ; ' ' ; 'um' ; 'rad' ; 'um' ; 'um' ; 'um.rad' ; 'um.um.rad'};

Answers = [X Y Z];
filename = strcat(pathname{1},'Merging_', res1{1},'.xlsx');
xlswrite(filename,Answers)
clear

```

3.5 Routine to calculate the mean values for a group of neurons:

moyenne.m

```

message = sprintf('Before beginning : create a file "Mean_6-2.xlsx" in the
directory containing all neurons data');
    uiwait(msgbox(message));

prompt1 = {'Enter the pattern: '};
    dlg_title1 = 'Pattern';
    num_lines = 1;
    def1 = {'2-6um'};
    res1 = inputdlg(prompt1,dlg_title1,num_lines,def1);

prompt = {'How many zones would you like to average ?'};
    dlg_title = 'Number of zones';
    num_lines = 1;
    def = {'10'};
    res = inputdlg(prompt,dlg_title,num_lines,def);
    n=str2num(res{1});

message = sprintf('Select the output file in the main directory');
    uiwait(msgbox(message));
[filename,pathname] = uigetfile('*.xlsx','Select the xlsx-file');

    for i=1:n
message = sprintf(strcat('Select the file of values close to the soma for the
N2 of the neuron ',num2str(i)));
        uiwait(msgbox(message));
[filename_cs2{i},pathname_cs2{i}] =
uigetfile(strcat(pathname,'*.xlsx'),'Select the xlsx-file');

message = sprintf(strcat('Select the file of all values for the N2 of the
neuron ',num2str(i)));
        uiwait(msgbox(message));
[filename_all2{i},pathname_all2{i}] =
uigetfile(strcat(pathname,'*.xlsx'),'Select the xlsx-file');

message = sprintf(strcat('Select the file of values close to the soma for the
N6 of the neuron ',num2str(i)));
        uiwait(msgbox(message));
[filename_cs6{i},pathname_cs6{i}] =
uigetfile(strcat(pathname,'*.xlsx'),'Select the xlsx-file');

message = sprintf(strcat('Select the file of all values for the N6 of the
neuron ',num2str(i)));
        uiwait(msgbox(message));
[filename_all6{i},pathname_all6{i}] =
uigetfile(strcat(pathname,'*.xlsx'),'Select the xlsx-file');

message = sprintf(strcat('Select the file of the ratio close to the soma of
the neuron ',num2str(i)));
        uiwait(msgbox(message));
[filename_ratio_cs{i},pathname_ratio_cs{i}] =
uigetfile(strcat(pathname,'*.xlsx'),'Select the xlsx-file');

message = sprintf(strcat('Select the file of the total ratio of the neuron
',num2str(i)));

```

```
        uiwait(msgbox(message));
[filename_ratio_all{i},pathname_ratio_all{i}] =
uigetfile(strcat(pathname, '*.xlsx'), 'Select the xlsx-file');

%%Close to the soma
%N2
%Length
l_cs2{i}=xlsread(strcat(pathname_cs2{i},filename_cs2{i}),1, 'B3');
%Max
max_cs2{i}=xlsread(strcat(pathname_cs2{i},filename_cs2{i}),1, 'B4');
%Width
width_cs2{i}=xlsread(strcat(pathname_cs2{i},filename_cs2{i}),1, 'B5');
%Surface
surf_cs2{i}=xlsread(strcat(pathname_cs2{i},filename_cs2{i}),1, 'B6');
%Volume
volume_cs2{i}=xlsread(strcat(pathname_cs2{i},filename_cs2{i}),1, 'B7');

%N6
%Length
l_cs6{i}=xlsread(strcat(pathname_cs6{i},filename_cs6{i}),1, 'B3');
%Max
max_cs6{i}=xlsread(strcat(pathname_cs6{i},filename_cs6{i}),1, 'B4');
%Width
width_cs6{i}=xlsread(strcat(pathname_cs6{i},filename_cs6{i}),1, 'B5');
%Surface
surf_cs6{i}=xlsread(strcat(pathname_cs6{i},filename_cs6{i}),1, 'B6');
%Volume
volume_cs6{i}=xlsread(strcat(pathname_cs6{i},filename_cs6{i}),1, 'B7');

%Ratio
%Pattern
patt_ratio_cs{i}=xlsread(strcat(pathname_ratio_cs{i},filename_ratio_cs{i}),1, '
B2');
%Length
l_ratio_cs{i}=xlsread(strcat(pathname_ratio_cs{i},filename_ratio_cs{i}),1, 'B3'
);
%Max
max_ratio_cs{i}=xlsread(strcat(pathname_ratio_cs{i},filename_ratio_cs{i}),1, 'B
4');
%Width
width_ratio_cs{i}=xlsread(strcat(pathname_ratio_cs{i},filename_ratio_cs{i}),1,
'B5');
%Surface
surf_ratio_cs{i}=xlsread(strcat(pathname_ratio_cs{i},filename_ratio_cs{i}),1, '
B6');
%Volume
volume_ratio_cs{i}=xlsread(strcat(pathname_ratio_cs{i},filename_ratio_cs{i}),1
, 'B7');

%%All neurite
%N2
%Length
l_all2{i}=xlsread(strcat(pathname_all2{i},filename_all2{i}),1, 'B3');
%Max
```

```

max_all2{i}=xlsread(strcat(pathname_all2{i},filename_all2{i}),1,'B4');
%Width
width_all2{i}=xlsread(strcat(pathname_all2{i},filename_all2{i}),1,'B5');
%Surface
surf_all2{i}=xlsread(strcat(pathname_all2{i},filename_all2{i}),1,'B6');
%Volume
volume_all2{i}=xlsread(strcat(pathname_all2{i},filename_all2{i}),1,'B7');

%N6
%Length
l_all6{i}=xlsread(strcat(pathname_all6{i},filename_all6{i}),1,'B3');
%Max
max_all6{i}=xlsread(strcat(pathname_all6{i},filename_all6{i}),1,'B4');
%Width
width_all6{i}=xlsread(strcat(pathname_all6{i},filename_all6{i}),1,'B5');
%Surface
surf_all6{i}=xlsread(strcat(pathname_all6{i},filename_all6{i}),1,'B6');
%Volume
volume_all6{i}=xlsread(strcat(pathname_all6{i},filename_all6{i}),1,'B7');

%Ratio
%Pattern
patt_ratio_all{i}=xlsread(strcat(pathname_ratio_all{i},filename_ratio_all{i}),
1,'B2');
%Length
l_ratio_all{i}=xlsread(strcat(pathname_ratio_all{i},filename_ratio_all{i}),1,'
B3');
%Max
max_ratio_all{i}=xlsread(strcat(pathname_ratio_all{i},filename_ratio_all{i}),1
,'B4');
%Width
width_ratio_all{i}=xlsread(strcat(pathname_ratio_all{i},filename_ratio_all{i})
,1,'B5');
%Surface
surf_ratio_all{i}=xlsread(strcat(pathname_ratio_all{i},filename_ratio_all{i}),
1,'B6');
%Volume
volume_ratio_all{i}=xlsread(strcat(pathname_ratio_all{i},filename_ratio_all{i}
),1,'B7');
    end

%%Results
%Close to the soma
%N2
l_cs2=cell2mat(l_cs2);
    mean_length_cs2=sum(l_cs2,2)/n;
    std_length_cs2=std(l_cs2);
max_cs2=cell2mat(max_cs2);
    mean_max_cs2=sum(max_cs2,2)/n;
    std_max_cs2=std(max_cs2);
width_cs2=cell2mat(width_cs2);
    mean_width_cs2=sum(width_cs2,2)/n;
    std_width_cs2=std(width_cs2);
surf_cs2=cell2mat(surf_cs2);
    mean_surf_cs2=sum(surf_cs2,2)/n;
    std_surf_cs2=std(surf_cs2);

```

```
volume_cs2=cell2mat(volume_cs2);
    mean_volume_cs2=sum(volume_cs2,2)/n;
    std_volume_cs2=std(volume_cs2);
%N6
l_cs6=cell2mat(l_cs6);
    mean_length_cs6=sum(l_cs6,2)/n;
    std_length_cs6=std(l_cs6);
max_cs6=cell2mat(max_cs6);
    mean_max_cs6=sum(max_cs6,2)/n;
    std_max_cs6=std(max_cs6);
width_cs6=cell2mat(width_cs6);
    mean_width_cs6=sum(width_cs6,2)/n;
    std_width_cs6=std(width_cs6);
surf_cs6=cell2mat(surf_cs6);
    mean_surf_cs6=sum(surf_cs6,2)/n;
    std_surf_cs6=std(surf_cs6);
volume_cs6=cell2mat(volume_cs6);
    mean_volume_cs6=sum(volume_cs6,2)/n;
    std_volume_cs6=std(volume_cs6);
%Ratio
patt_ratio_cs=cell2mat(patt_ratio_cs);
mean_patt_ratio_cs=sum(patt_ratio_cs,2)/n;
l_ratio_cs=cell2mat(l_ratio_cs);
    mean_length_ratio_cs=sum(l_ratio_cs,2)/n;
    std_length_ratio_cs=std(l_ratio_cs);
max_ratio_cs=cell2mat(max_ratio_cs);
    mean_max_ratio_cs=sum(max_ratio_cs,2)/n;
    std_max_ratio_cs=std(max_ratio_cs);
width_ratio_cs=cell2mat(width_ratio_cs);
    mean_width_ratio_cs=sum(width_ratio_cs,2)/n;
    std_width_ratio_cs=std(width_ratio_cs);
surf_ratio_cs=cell2mat(surf_ratio_cs);
    mean_surf_ratio_cs=sum(surf_ratio_cs,2)/n;
    std_surf_ratio_cs=std(surf_ratio_cs);
volume_ratio_cs=cell2mat(volume_ratio_cs);
    mean_volume_ratio_cs=sum(volume_ratio_cs,2)/n;
    std_volume_ratio_cs=std(volume_ratio_cs);

%All Neurite
%N2
l_all2=cell2mat(l_all2);
    mean_length_all2=sum(l_all2,2)/n;
    std_length_all2=std(l_all2);
max_all2=cell2mat(max_all2);
    mean_max_all2=sum(max_all2,2)/n;
    std_max_all2=std(max_all2);
width_all2=cell2mat(width_all2);
    mean_width_all2=sum(width_all2,2)/n;
    std_width_all2=std(width_all2);
surf_all2=cell2mat(surf_all2);
    mean_surf_all2=sum(surf_all2,2)/n;
    std_surf_all2=std(surf_all2);
volume_all2=cell2mat(volume_all2);
    mean_volume_all2=sum(volume_all2,2)/n;
    std_volume_all2=std(volume_all2);
%N6
l_all6=cell2mat(l_all6);
```

```

    mean_length_all6=sum(l_all6,2)/n;
    std_length_all6=std(l_all6);
max_all6=cell2mat(max_all6);
    mean_max_all6=sum(max_cs6,2)/n;
    std_max_all6=std(max_all6);
width_all6=cell2mat(width_all6);
    mean_width_all6=sum(width_all6,2)/n;
    std_width_all6=std(width_all6);
surf_all6=cell2mat(surf_all6);
    mean_surf_all6=sum(surf_all6,2)/n;
    std_surf_all6=std(surf_all6);
volume_all6=cell2mat(volume_all6);
    mean_volume_all6=sum(volume_all6,2)/n;
    std_volume_all6=std(volume_all6);
%Ratio
patt_ratio_all=cell2mat(patt_ratio_all);
mean_patt_ratio_all=sum(patt_ratio_all,2)/n;
l_ratio_all=cell2mat(l_ratio_all);
    mean_length_ratio_all=sum(l_ratio_all,2)/n;
    std_length_ratio_all=std(l_ratio_all);
max_ratio_all=cell2mat(max_ratio_all);
    mean_max_ratio_all=sum(max_ratio_all,2)/n;
    std_max_ratio_all=std(max_ratio_all);
width_ratio_all=cell2mat(width_ratio_all);
    mean_width_ratio_all=sum(width_ratio_all,2)/n;
    std_width_ratio_all=std(width_ratio_all);
surf_ratio_all=cell2mat(surf_ratio_all);
    mean_surf_ratio_all=sum(surf_ratio_all,2)/n;
    std_surf_ratio_all=std(surf_ratio_all);
volume_ratio_all=cell2mat(volume_ratio_all);
    mean_volume_ratio_all=sum(volume_ratio_all,2)/n;
    std_volume_ratio_all=std(volume_ratio_all);

%%Registration of the obtained data
filename=strcat(pathname,filename);
%Close to soma N2
X1={'Pattern' ;'CLOSE TO THE SOMA' ; 'Mean Length' ; 'Mean Max' ; 'Mean
Width' ; 'Mean Surface' ; 'Mean Volume' ; 'Cell Number'};
X2={res1{1} ; 'Mean Values' ; mean_length_cs2 ; mean_max_cs2 ; mean_width_cs2 ;
mean_surf_cs2 ; mean_volume_cs2 ; res{1}};
X3={'N2' ; 'Standard Deviation' ; std_length_cs2 ; std_max_cs2 ;
std_width_cs2 ; std_surf_cs2 ; std_volume_cs2;''};
X4={'' ; 'Unity' ; 'um' ; 'rad' ; 'um' ; 'um.rad' ; 'um.um.rad' ; ''};
xlswrite(filename,X1,1,'A1')
xlswrite(filename,X2,1,'B1')
xlswrite(filename,X3,1,'C1')
xlswrite(filename,X4,1,'D1')

%Close to soma N6
X5={'Pattern' ;'CLOSE TO THE SOMA' ; 'Mean Length' ; 'Mean Max' ; 'Mean
Width' ; 'Mean Surface' ; 'Mean Volume' ; 'Cell Number'};
X6={res1{1} ; 'Mean Values' ; mean_length_cs6 ; mean_max_cs6 ; mean_width_cs6 ;
mean_surf_cs6 ; mean_volume_cs6 ; res{1}};
X7={'N6' ; 'Standard Deviation' ; std_length_cs6 ; std_max_cs6 ;
std_width_cs6 ; std_surf_cs6 ; std_volume_cs6;''};
X8={'' ; 'Unity' ; 'um' ; 'rad' ; 'um' ; 'um.rad' ; 'um.um.rad' ; ''};
xlswrite(filename,X5,1,'A10')

```

```
xlswrite(filename,X6,1,'B10')
xlswrite(filename,X7,1,'C10')
xlswrite(filename,X8,1,'D10')

%All neurite N2
X9={'Pattern' ; 'ALL NEURITE' ; 'Mean Length' ; 'Mean Max' ; 'Mean Width' ;
'Mean Surface' ; 'Mean Volume' ; 'Cell Number'};
X10={res1{1} ; 'Mean Values' ; mean_length_all2 ; mean_max_all2 ;
mean_width_all2 ; mean_surf_all2 ; mean_volume_all2 ; res{1}};
X11={'N2' ; 'Standard Deviation' ; std_length_all2 ; std_max_all2 ;
std_width_all2 ; std_surf_all2 ; std_volume_all2;''};
X12={' ' ; 'Unity' ; 'um' ; 'rad' ; 'um' ; 'um.rad' ; 'um.um.rad' ; ''};
xlswrite(filename,X9,1,'A19')
xlswrite(filename,X10,1,'B19')
xlswrite(filename,X11,1,'C19')
xlswrite(filename,X12,1,'D19')

%All neurite N6
X13={'Pattern' ; 'ALL NEURITE' ; 'Mean Length' ; 'Mean Max' ; 'Mean Width' ;
'Mean Surface' ; 'Mean Volume' ; 'Cell Number'};
X14={res1{1} ; 'Mean Values' ; mean_length_all6 ; mean_max_all6 ;
mean_width_all6 ; mean_surf_all6 ; mean_volume_all6 ; res{1}};
X15={'N6' ; 'Standard Deviation' ; std_length_all6 ; std_max_all6 ;
std_width_all6 ; std_surf_all6 ; std_volume_all6;''};
X16={' ' ; 'Unity' ; 'um' ; 'rad' ; 'um' ; 'um.rad' ; 'um.um.rad' ; ''};
xlswrite(filename,X13,1,'A28')
xlswrite(filename,X14,1,'B28')
xlswrite(filename,X15,1,'C28')
xlswrite(filename,X16,1,'D28')

%Close to soma ratio
X17={'CLOSE TO THE SOMA' ; 'Pattern ratio' ; 'Mean Length ratio' ; 'Mean Max
ratio' ; 'Mean Width ratio' ; 'Mean Surface ratio' ; 'Mean Volume ratio' ;
'Cell Number'};
X18={'Mean Values' ; mean_patt_ratio_cs ; mean_length_ratio_cs ;
mean_max_ratio_cs ; mean_width_ratio_cs ; mean_surf_ratio_cs ;
mean_volume_ratio_cs ; res{1}};
X19={'Standard Deviation' ; '' ; std_length_ratio_cs ; std_max_ratio_cs ;
std_width_ratio_cs ; std_surf_ratio_cs ; std_volume_ratio_cs;''};
xlswrite(filename,X17,1,'A37')
xlswrite(filename,X18,1,'B37')
xlswrite(filename,X19,1,'C37')

%All neurite ratio
X20={'ALL NEURITE' ; 'Pattern ratio' ; 'Mean Length ratio' ; 'Mean Max ratio' ;
'Mean Width ratio' ; 'Mean Surface ratio' ; 'Mean Volume ratio' ; 'Cell
Number'};
X21={'Mean Values' ; mean_patt_ratio_all ; mean_length_ratio_all ;
mean_max_ratio_all ; mean_width_ratio_all ; mean_surf_ratio_all ;
mean_volume_ratio_all ; res{1}};
X22={'Standard Deviation' ; '' ; std_length_ratio_all ; std_max_ratio_all ;
std_width_ratio_all ; std_surf_ratio_all ; std_volume_ratio_all;''};
xlswrite(filename,X20,1,'A46')
xlswrite(filename,X21,1,'B46')
xlswrite(filename,X22,1,'C46')
```

3.6 Decoupling procedure routine

```

prompt1 = {'Enter your neuron name and the neurite size: '};
dlg_title1 = 'Neuron name';
num_lines = 1;
def1 = {'AG102-N4'};
res1 = inputdlg(prompt1,dlg_title1,num_lines,def1);

prompt = {'How many zones would you like to compare ?'};
dlg_title = 'Number of zones';
num_lines = 1;
def = {'72'};
res = inputdlg(prompt,dlg_title,num_lines,def);
n=str2num(res{1});

message = sprintf('Select the txt file of the PhaseM_zero');
uiwait(msgbox(message));
[filenameb,pathnameb] = uigetfile('*.txt','Select the Txt-file');
name = [pathnameb filenameb];
importfiledhm(name);
PhaseM_zero = data;
clearvars data textdata name;

message = sprintf('Select the txt file of the PhaseN_zero ');
uiwait(msgbox(message));
[filenamec,pathnamec] = uigetfile('*.txt','Select the Txt-file');
name = [pathnamec filenamec];
importfiledhm(name);
PhaseN_zero = data;
clearvars data textdata name;

message = sprintf(strcat('Select the txt file of the zone ',num2str(1),' of
the neurite (placement in the folder)'));
uiwait(msgbox(message));
[filename1,pathname1] = uigetfile('*.txt','Select the Txt-file');
name = [pathname1 filename1];
importfiledhm(name);
Ph = data;
Phase = Ph-PhaseN_zero;
clearvars data textdata name;

message = sprintf('Select the zone 1 to analyze');
uiwait(msgbox(message));
figure('Name','Phase','NumberTitle','off')
[crop1 rect1]=imcrop(Phase);

message = sprintf('Select the zone 2 to analyze');
uiwait(msgbox(message));
figure('Name','Phase','NumberTitle','off')
[crop2 rect2]=imcrop(Phase);

message = sprintf('Select the zone 3 to analyze');
uiwait(msgbox(message));
figure('Name','Phase','NumberTitle','off')
[crop3 rect3]=imcrop(Phase);

message = sprintf('Select the zone 4 for the soma to analyze');
uiwait(msgbox(message));
figure('Name','Phase','NumberTitle','off')
[crop4 rect4]=imcrop(Phase);

```

```
meanPh1(1)=mean(mean(crop1));
meanPh2(1)=mean(mean(crop2));
meanPh3(1)=mean(mean(crop3));
meanPh4(1)=mean(mean(crop4));
clearvars crop1 crop2 crop3 crop4 Phase Ph;

cd(pathname1)
A=ls;
n2=n+2;
for k=3:n2
    filename{k}=A(k,:);
    name = [pathname1 filename{k}];
    importfiledhm(name);
    k=k-2;
    Ph{k} = data;
clearvars data textdata name;
end

t=0;
time(1)=0;
m=21;

for i=2:m
    Phase{i}=Ph{i}-PhaseN_zero;
clearvars data textdata name;
[crop1 rect]=imcrop(Phase{i},rect1);
[crop2 rect]=imcrop(Phase{i},rect2);
[crop3 rect]=imcrop(Phase{i},rect3);
[crop4 rect]=imcrop(Phase{i},rect4);
meanPh1(i)=mean(mean(crop1));
meanPh2(i)=mean(mean(crop2));
meanPh3(i)=mean(mean(crop3));
meanPh4(i)=mean(mean(crop4));
t=t+2;
time(i)=t;
clearvars crop1 crop2 crop3 crop4;
end

for i=m:n
    Phase{i}=Ph{i}-PhaseM_zero;
clearvars data textdata name;
[crop1 rect]=imcrop(Phase{i},rect1);
[crop2 rect]=imcrop(Phase{i},rect2);
[crop3 rect]=imcrop(Phase{i},rect3);
[crop4 rect]=imcrop(Phase{i},rect4);
meanPh1(i)=mean(mean(crop1));
meanPh2(i)=mean(mean(crop2));
meanPh3(i)=mean(mean(crop3));
meanPh4(i)=mean(mean(crop4));
t=t+2;
time(i)=t;
clearvars crop1 crop2 crop3 crop4;
end

figure('Name',strcat(['Phase of zone 1 versus time of ',
res1{1}]),'NumberTitle','off')
hold on
scatter(time,meanPh1,'g');
plot(time,meanPh1,'g');
hold off
title(strcat(['Phase of zone 1 versus time of ', res1{1}]))
xlabel('Time (s)')
ylabel('Phase (rad)')
```

```

%hgexport(gcf,
strcat(pathname,'\results\','Widthv2_along_the_neurite_of_',answer{1},'.tiff'),
hgexport('factorystyle'),'Format','tiff');
%saveas(gcf,
strcat(pathname,'\results\','Widthv2_along_the_neurite_of_',answer{1},'.fig'),
'fig');

figure('Name',strcat(['Phase of zone 2 versus time of ',
res1{1}]),'NumberTitle','off')
hold on
scatter(time,meanPh2,'g');
plot(time,meanPh2,'g');
hold off
title(strcat(['Phase of zone 2 versus time of ', res1{1}]))
xlabel('Time (s)')
ylabel('Phase (rad)')
%hgexport(gcf,
strcat(pathname,'\results\','Widthv2_along_the_neurite_of_',answer{1},'.tiff'),
hgexport('factorystyle'),'Format','tiff');
%saveas(gcf,
strcat(pathname,'\results\','Widthv2_along_the_neurite_of_',answer{1},'.fig'),
'fig');

figure('Name',strcat(['Phase of zone 3 versus time of ',
res1{1}]),'NumberTitle','off')
hold on
scatter(time,meanPh3,'g');
plot(time,meanPh3,'g');
hold off
title(strcat(['Phase of zone 3 versus time of ', res1{1}]))
xlabel('Time (s)')
ylabel('Phase (rad)')
%hgexport(gcf,
strcat(pathname,'\results\','Widthv2_along_the_neurite_of_',answer{1},'.tiff'),
hgexport('factorystyle'),'Format','tiff');
%saveas(gcf,
strcat(pathname,'\results\','Widthv2_along_the_neurite_of_',answer{1},'.fig'),
'fig');

figure('Name',strcat(['Phase of zone 4 versus time of ',
res1{1}]),'NumberTitle','off')
hold on
scatter(time,meanPh4,'g');
plot(time,meanPh4,'g');
hold off
title(strcat(['Phase of zone 4 versus time of ', res1{1}]))
xlabel('Time (s)')
ylabel('Phase (rad)')
%hgexport(gcf,
strcat(pathname,'\results\','Widthv2_along_the_neurite_of_',answer{1},'.tiff'),
hgexport('factorystyle'),'Format','tiff');
%saveas(gcf,
strcat(pathname,'\results\','Widthv2_along_the_neurite_of_',answer{1},'.fig'),
'fig');

dn=0.005175;
nm=1.333695;

%zone1
%N
for i=1:15
phase1_1(i)=meanPh1(i);
end

```

```
moyenne1_1=mean(phase1_1)
%M
for i=30:43;
    j=i-29;
    phase2_1(j)=meanPh1(i);
end
moyenne2_1=mean(phase2_1)
%M-N
DeltaPhi_1=moyenne2_1-moyenne1_1
RI_1=moyenne2_1*dn/DeltaPhi_1+nm

%zone2
for i=1:15;
    phase1_2(i)=meanPh2(i);
end
moyenne1_2=mean(phase1_2)

for i=30:43;
    j=i-29;
    phase2_2(j)=meanPh2(i);
end
moyenne2_2=mean(phase2_2)

DeltaPhi_2=moyenne2_2-moyenne1_2
RI_2=moyenne2_2*dn/DeltaPhi_2+nm

%zone3
for i=1:15;
    phase1_3(i)=meanPh3(i);
end
moyenne1_3=mean(phase1_3)

for i=30:43;
    j=i-29;
    phase2_3(j)=meanPh3(i);
end
moyenne2_3=mean(phase2_3)

DeltaPhi_3=moyenne2_3-moyenne1_3
RI_3=moyenne2_3*dn/DeltaPhi_3+nm

%zone4
for i=1:15;
    phase1_4(i)=meanPh4(i);
end
moyenne1_4=mean(phase1_4)

for i=30:43;
    j=i-29;
    phase2_4(j)=meanPh4(i);
end
moyenne2_4=mean(phase2_4)

DeltaPhi_4=moyenne2_4-moyenne1_4
RI_4=moyenne2_4*dn/DeltaPhi_4+nm
```

3.7 Subsidiary routines used

3.7.1 Importe file routine: importfiledhm.m

```
function importfile(fileToRead1)
%IMPORTFILE(FILETOREAD1)
% Imports data from the specified file
% FILETOREAD1: file to read

% Auto-generated by MATLAB on 10-Nov-2015 10:30:41

DELIMITER = ' ';
%DELIMITER = {'\t',' '};
HEADERLINES = 4;

% Import the file
newData1 = importdata(fileToRead1, DELIMITER, HEADERLINES);

% Create new variables in the base workspace from those fields.
vars = fieldnames(newData1);
for i = 1:length(vars)
    assignin('base', vars{i}, newData1.(vars{i}));
end
```

3.7.2 Baseline adjustment routine: bf.m created by Mirko Hrovat

```

function [ycorr,yfit] = bf(y,varargin)
% Baseline Fit each column in "x".
% Syntax: [ycorr,yfit] = bf(y,pts,avgpts,method,confirm);
%   ycorr = bf(y);   ycorr = bf(y,method);   ycorr = bf(y,avgpts);
%   ycorr = bf(y,pts);   ycorr = bf(y,pts,avgpts);
% A baseline fit is interpolated from selected points and then applied to the
data.
%   "y" is a vector or array.
%       If an array, the baseline fit is performed for each column of data
(dim 1).
% Arguments following "y" may be in any order.
%   "pts" is vector specifying the indices of the points for a baseline fit.
%       If not specified then a plot is displayed and the user is instructed
to
%       interactively select points for the baseline fit.
%       End points are always automatically included for interactive "pts"
selection,
%       and do not need to explicitly selected. It is recommended that the end
points
%       be included in any list of "pts".
%       It is not necessary to order or sort "pts" before use.
%   "avgpts" determines the width in points for the calculation of the mean
y(x)
%       value, where x is a selected point in "pts". (Default = 3).
%       This can be helpful for noisy data.
%   "method" controls the algorithm applied for the baseline fit. The routine
uses
%       Matlab's interp1 command. "method" must be one of the methods
supported by
%       interp1. (Default is 'spline').
%   "confirm", if specified as the string 'confirm', will allow the user to
see the
%       result and to confirm it is acceptable. If not the user can reslect
"pts".
%   "ycorr" is the baseline corrected data in the same format as "y".
%   "yfit" is a vector or array with the interpolated baseline fit.
%
% Examples:
%   [y,yfit] = bf(y,'confirm','linear');
%       "y" will be plotted and the user is instructed to select points for
the fit.
%       A baseline will be linearly interpolated from the selected points and
will be
%       plotted together with "y". The user is prompted as to whether to redo
the
%       baseline selection. Upon completion, the corrected data "y" and the
fitted
%       baseline "yfit" are output.
%   ycorr = bf(y,5);
%       "y" is plotted and the user is instructed to select points for the fit.
%       The baseline fit is based on the mean value of "y" over 5 points
centered on
%       the selected points. Cubic spline interpolation is used for the
baseline fit.
%       The corrected data "ycorr" is output.
%   ycorr = bf(y,[5,10,15,30,35,40],'pchip');

```

```

%      Points with the specified indices are used to calculate a baseline fit
using
%      the piecewise cubic Hermite interpolation method. No data is plotted.
%      The baseline fit is based on the mean value of "y" over 3 points
centered on
%      the selected points. The corrected data "ycorr" is output.
%
% See Also:   interp1, spline, ginput

% Copyright 2009 Mirtech, Inc.
% Created by   Mirko Hrovat   08/01/2009   contact:mhrovat@email.com

def_method = 'spline';
def_avgpts = 3;

method = [];
avgpts = [];
pts = [];
confirm = false;
for n = 2:nargin,
    f = varargin{n-1};
    if ischar(f),
        if strcmpi(f,'confirm'),
            confirm = true;
        else
            method = f;
        end
    elseif isnumeric(f) && numel(f) == 1,
        avgpts = f;
    elseif isnumeric(f) && numel(f) > 1,
        pts = f;
    elseif isempty(f),
        continue
    else
        error (' Invalid input argument!')
    end
end
if isempty(method),      method = def_method;          end
if isempty(avgpts),     avgpts = def_avgpts;          end
dimy = size(y);
lst = dimy(1);
newdimy = [dimy(1),prod(dimy(2:end))];
y = reshape(y,newdimy);
x = 1:lst;
if isempty(pts),
    interactive = true;
else
    interactive = false;
end
if interactive || confirm,
    bffig = figure;
else
    bffig = 0;
end
ok = false;
while ~ok,

```

```

if interactive,
    plot(x,real(y(:,1)))
    set(bffig, 'Name', 'Baseline Fit - Select points')
    fprintf(['\n Now select baseline points to fit by positioning
cursor, ', ...
        '\n   and selecting points with mouse button or key press.', ...
        '\n Press Enter key when done.\n'])
    [a,b] = ginput;           %#ok
    pts = round(a. ');
end
pts = sort(pts);
pts(diff(pts)==0) = [];      % delete duplicate points
if pts(1)~=1, pts = [1,pts]; end %#ok
if pts(end)~=lst, pts = [pts,lst]; end %#ok
npts = numel(pts);
pss = zeros(npts,2);
pss(:,1) = pts - floor(avgpts/2);
pss(:,2) = pss(:,1) + avgpts;
pss(pss < 1) = 1;
pss(pss > lst) = lst;
yavg = zeros([npts,newdimy(2)]);
for n = 1:npts,
    yavg(n,:) = mean(y(pss(n,1):pss(n,2),:),1);
end
yfit = interp1(pts,yavg,x,method);
if size(yfit,1) ==1,
    yfit = shiftdim(yfit,1); % make yfit a column if it is a row vector
end
if confirm,
    interactive = true;
    figure(bffig)
    plot(x,real(y(:,1)), 'b',x,real(yfit(:,1)), 'r',pts,real(yavg(:,1)), 'ob')
    set(bffig, 'Name', 'Baseline Fit - Verify baseline')
    answer = input(' Do you to redo fit and reselect baseline points?[N]
', 's');
    if isempty(answer), answer = 'n'; end
    if strcmpi(answer, 'y'),
        ok = false;
    else
        ok = true;
    end
else
    ok = true;
end
end
if any(findobj('Type','figure')==bffig),
    close(bffig), % close figure if it exists
end
ycorr = y - yfit;
ycorr = reshape(ycorr,dimy);
yfit = reshape(yfit,dimy);

```

4 Appendix 4: Theoretical and experimental comparisons between water and PBS phase measurements

4.1 Theoretically

In **Chapter 3, Part 4**, we measured a maximum refractive indexes difference between water and PBS of $\Delta n = 0.003$. The specific refractive increment α was measured as $0.18 \mu\text{m}^3 \cdot \text{pg}^{-1}$ for whole cells in water. Nevertheless we chose to make our measurements in PBS, which is an ionic solution.

Supposing $\Phi_{PBS} = \Phi_m$ the measured phase and $\Phi_{Water} = \Phi_t$ the theoretical phase we should have measured. The phase difference is then

$$\Delta\Phi = \Phi_t - \Phi_m = \frac{2\pi}{\lambda} \Delta n h \quad (7.15)$$

The phase difference is then linearly dependant to the object height as shown in **Figure 7.3**.

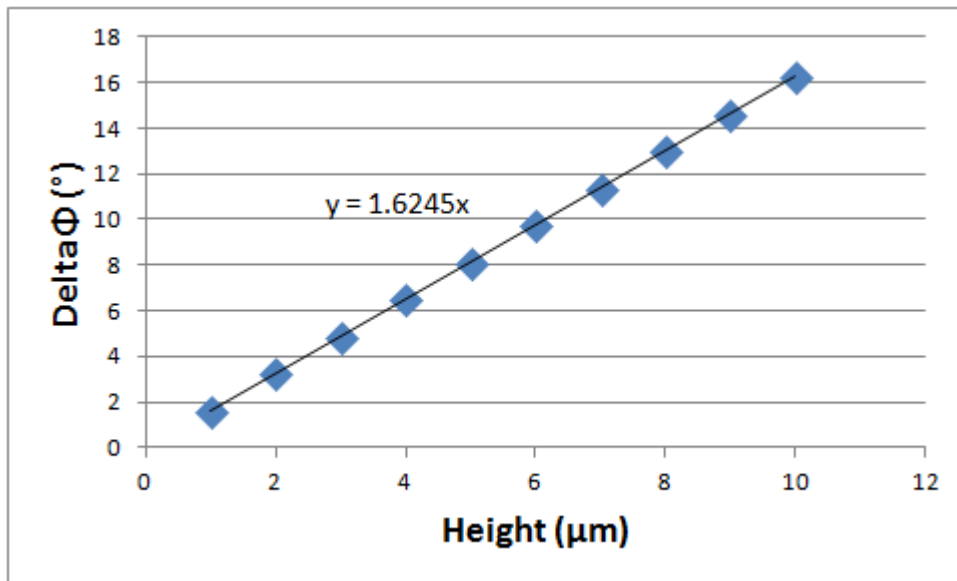


Figure 7.3 – The phase difference between water and PBS $\Delta\Phi$ as a function of the object height.

4.2 Experimentally

Experimentally, we performed a timelapse using the DHM to measure the phase map of a neuron while changing the surrounding medium from water to PBS. Mean phases values were then calculated for each time point for four different zones on the neuron. Results are presented in **Figure 7.4**. Here we can observe that the phase difference is quite low for neurites (below 3°) but is increasing a lot for the soma (about 6°).

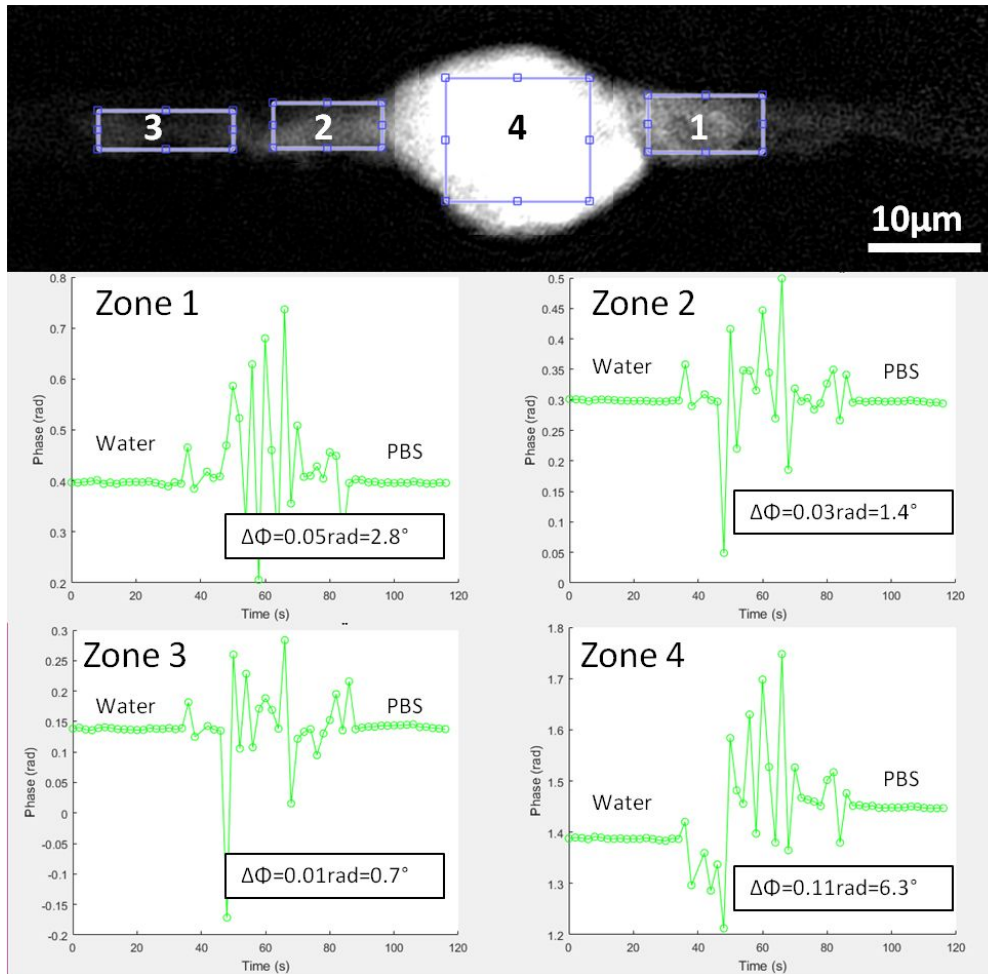
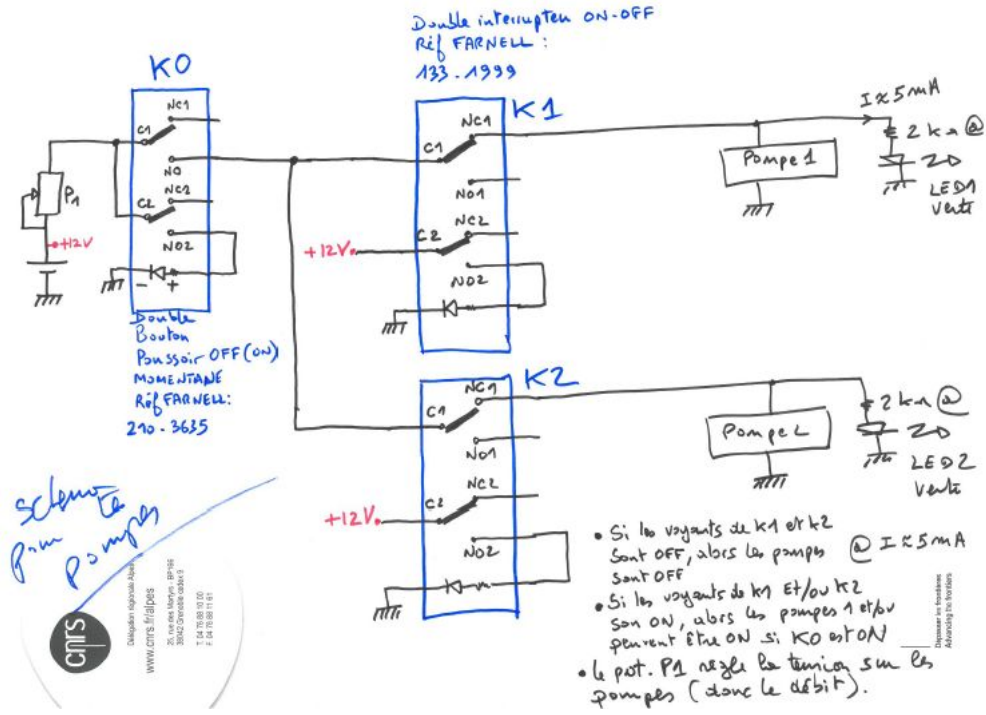


Figure 7.4 – Phase measurement on several zones of a neurone while changing the surrounding medium from water to PBS.

4.3 Error estimation

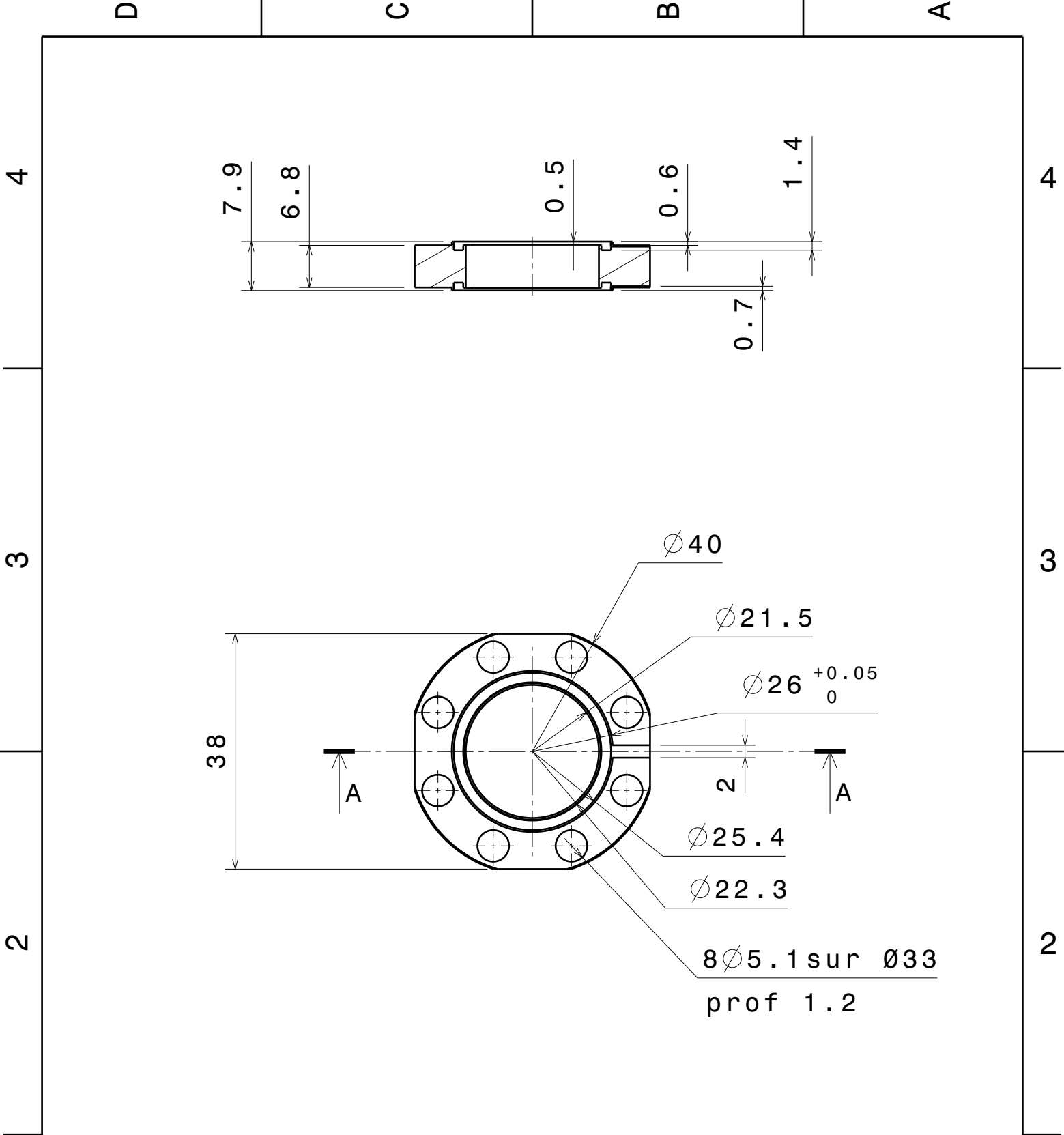
Both theoretical and experimental observations show that the phase difference between water and PBS increases with the object height. Nevertheless, calculating the percentage of this phase difference to the phase value measured in PBS, we found similar values for each zones around 7%.

5 Appendix 5: Electronic circuitry for the custom-made medium replacing system



6 Appendix 6: Technical schemes of the custom-made closed perfusion chamber

The next two pages display the technical schemes of the custom-made closed perfusion chamber.

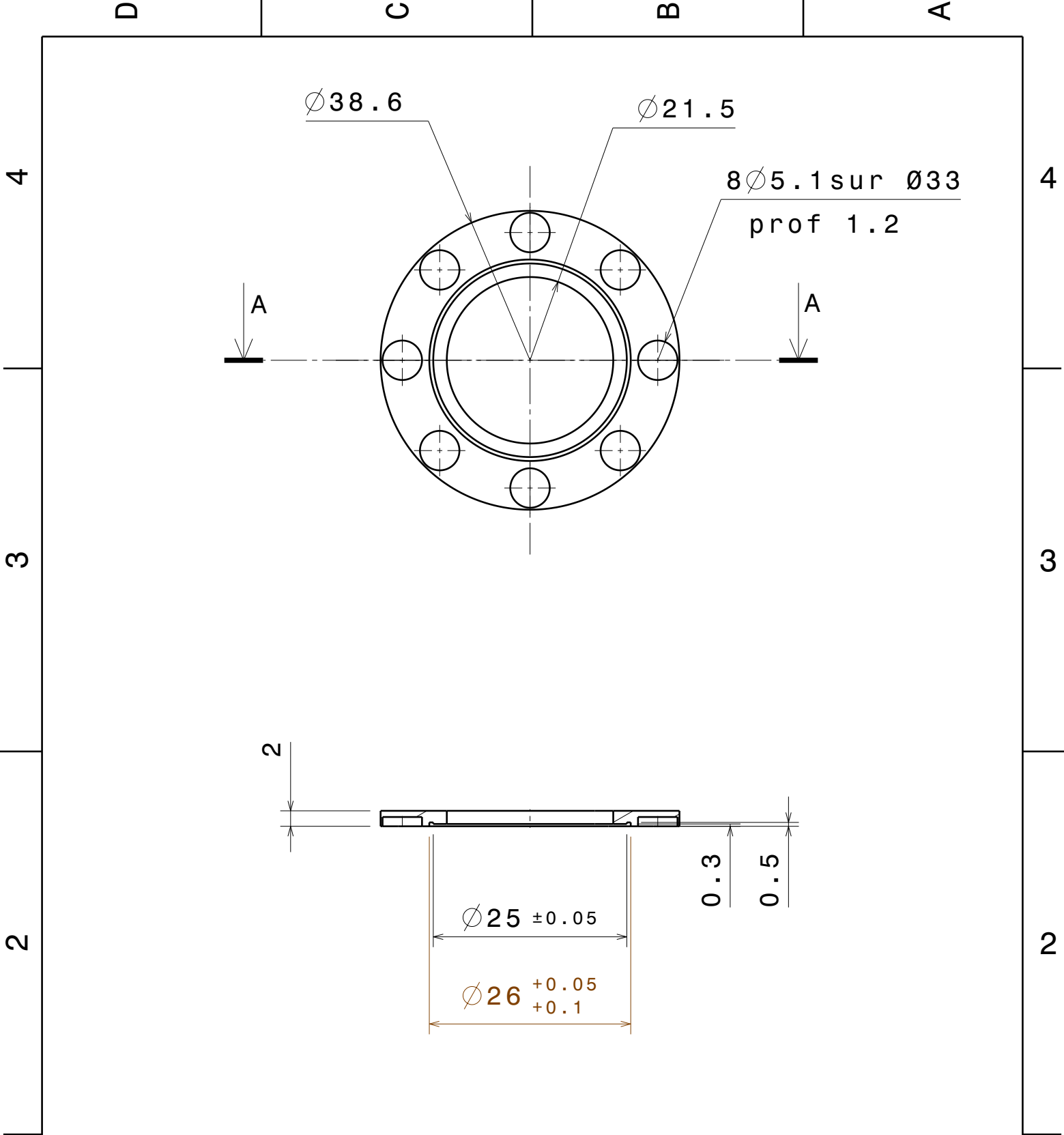


Dessiné par Gregory Garde DATE: 02/02/2016		corps chambre n2		Modifié le:	
Téléphone 04 76 88 12 23		CHAMBRE NEURONALE N2		date	
Courrier électronique gregory.garde@neel.cnrs.fr				date	
Format A4				date	
Echelle 1.5				date	
Institut NEEL-MCBT		Tolérances générales: ISO 2768-mK		Rugosité générale: Ra 3.2	
Dessin n° XXXXXX		Matière: lexan 920-701 polycarbonate noir		Nombre 1	
Institut NEEL-MCBT, Bat E, 25 Avenue des Martyrs, BP 166, 38042 Grenoble Cedex - Fax: 04 56 38 70 87					

4
3
2
1

4
3
2
1

D A



Dessiné par Gregory Garde DATE: 02/02/2016		couvercle n2		Modifié le:	
Téléphone 04 76 88 12 23		CHAMBRE NEURONALE N2		date	
Courrier électronique gregory.garde@neel.cnrs.fr				date	
Format A4				date	
				date	
				date	
Echelle 1.5		Dessin n° XXXXXX		Matière: lexan 920-701 polycarbonate noir	
		Nombre 2		date	
		Institut NEEL-MCBT, Bat E, 25 Avenue des Martyrs, BP 166, 38042 Grenoble Cedex - Fax: 04 56 38 70 87		date	

4
3
2
1

4
3
2
1

7 Appendix 7: Matlab program for FXm analysis

```
prof=VarName1;
s=size(prof)
message = sprintf('Select points to define the baseline');
uiwait(msgbox(message));
for i=1:s(2)
[ycorr,yfit] = bf(prof(:,i));
prof2(:,i)=ycorr;
end

s1 = size(prof2);
x1=1:s1(1);
%x1_um=x1*0.16125;
x1_um=x1*0.3225;

alpha=-0.0009;
beta=14.379;
height_prof=prof2*alpha+beta;

message = sprintf('Select points to define the baseline');
uiwait(msgbox(message));
for i=1:s(2)
[ycorr,yfit] = bf(height_prof(:,i));
height_prof2(:,i)=ycorr;
end

plot(x1_um,height_prof2);
fprintf(['\n Now select baseline points to fit by positioning cursor',...
        '\n   and selecting points with mouse button or key press.',...
        '\n Press Enter key when done.\n'])

[c,d] = ginput; %a contient les deux coordonnees x voulues
width=c(2)-c(1)
height_prof3=height_prof2;

    for j=1:s1(1)
    if (x1_um(j)>c(1)) & (x1_um(j)<c(2))
        height_prof3(j)=height_prof3(j);
    else height_prof3(j)=0;
    end
    end

vol=trapz(x1_um,height_prof3)
maxh=max(height_prof3)

plot(x1_um,height_prof2)
xlabel('x (µm)')
ylabel('Neurite height (µm)')
title('Neurite cross section average on 10 pixels of neurite length')
```

8 Appendix 8: Conditioned medium

After extracting and dissociating cortex from hippocampal mice embryo, cells coming from one hemisphere are seeded in B100 (10cm diameter) Petri dishes coated with 15µg/ml of PLO. The medium used is DMEMc which composition is described in the Table 7.1. This medium is changed at 1, 3 and 8 DIV. This medium is then changed once a week. When glial cells occupy all the Petri dish area (at 10-12 DIV generally), DMEMc is replaced by NBc with AraC2 which is killing microglia. After one to three days, the NBc is removed and stocked in Falcon tubes, after adding AraC2 a second time and filtering at 0.22µm. This medium is then stocked in Falcon tubes as NBcC, with the "C" standing for "Conditioned".

DMEMc [50ml]
Fetal bovine serum (FBS): 10% [5ml]
Sodium Pyruvate GIBCO 100mM (NaP): 1% [500µl]
Penicillin-Streptavidin (PS/ATB): 0.1% [50µl]
Dulbecco's Modified Eagle's medium (DMEM): 88.9% [up to 50ml]

Table 7.1 – *Maintenance media for glial cells, DMEMc. The "c" stands for "complete", when all the elements to build the medium are added to Dulbecco's Modified Eagle's medium (DMEM). All these components are mixed and filtered.*

BIBLIOGRAPHY

- [1] Stephen F. Mason, *A History of the Sciences*, Macmillan General Reference, 1962 (ISBN 978-0020934004)
- [2] Françoise Dunand , Roger Lichtenberg, *Les momies. Un voyage dans l'éternité*, Collection *Découvertes Gallimard (n°118)*, Série *Archéologie*, Gallimard, 1991
- [3] A. C. Bhaktivedanta Swami Prabhupada, *Bhagavad-Gita As It Is*, Macmillan Publishers, 1968.
- [4] Jane A Foster, Mark Lyte, Emeran Meyer, and John F Cryan, Gut Microbiota and Brain Function: An Evolving Field in Neuroscience, *International Journal of Neuropsychopharmacology*, (2016) 19(5): 1–7
- [5] Santiago Ramón y Cajal, The structure and connexions of neurons, *December 12, 1906, Nobel Lecture*.
- [6] Lopez-Munoz F, Boya J, Alamo C., 2006, Neuron theory, the cornerstone of neuroscience, on the centenary of the Nobel Prize award to Santiago Ramon y Cajal, *Brain Res Bull*, 70:391-405.
- [7] Suzana Herculano-Houzel, The human brain in numbers: a linearly scaled-up primate brain, *Frontiers in Human Neuroscience*, November 2009 - Volume 3 - Article 31
- [8] <http://www.virtualflybrain.org/>
- [9] Diana Kwon & Liz Tormes, The Brainbow Connection, *Scientific American Mind* 26, 52 - 55 (2015), doi:10.1038/scientificamericanmind1115-52
- [10] Marco Piccolino, Luigi Galvani and animal electricity: two centuries after the foundation of electrophysiology, *TINS Vol. 20, No. 10*, 1997
- [11] Mary Wollstonecraft (Godwin) Shelley, *Frankenstein, or, the Modern Prometheus*, *Author's Introduction of the 1831 edition*, Zorba Press
- [12] Nerves, membrane potential, etc, *April 17 2005, Biology 172 with Olsen at University of Michigan - Ann Arbor*.
- [13] <http://bio1152.nicerweb.com/Locked/media/ch48/axon.html>
- [14] Ulfhake B, Kellerth JO, A quantitative light microscopic study of the dendrites of cat spinal alpha-motoneurons after intracellular staining with horseradish peroxidase, *J Comp Neurol*. 1981 Nov 10;202(4):571-83, DOI: 10.1002/cne.902020409
- [15] D. A. Sholl, *The Organization of the Cerebral Cortex*, Hafner Publishing Company, 1956
- [16] Joana Câmara, Zhen Wang, Cristina Nunes-Fonseca, Hana C. Friedman, Matthew Grove, Diane L. Sherman, Noboru H. Komiyama, Seth G. Grant, Peter J. Brophy, Alan Peterson, and Charles French-Constant, 2008, Integrin-mediated axoglial interactions initiate myelination in the central nervous system, *J. Cell Biol. Vol. 185 No. 4* 699–712

-
- [17] János A. Perge, Jeremy E. Niven, Enrico Mugnaini, Vijay Balasubramanian, Peter Sterling, Why Do Axons Differ in Caliber?, *The Journal of Neuroscience*, January 11, 2012 - 32(2):626–638
- [18] William P. Bartlett and Gary A. Banker, An Electron Microscopic study of the development axons and dendrites by hippocampal neurons in culture, *The Journal of Neuroscience Vol.4, No. 8, pp. 1944-1953, August 1984*
- [19] <http://www.slideshare.net/suknamgoong/structural-basis-of-actin-nucleation>
- [20] Subhojit Roy, Waves, rings, and trails: The scenic landscape of axonal actin, *JCB - Volume 212 - Number 2 - 2016*
- [21] Ke Xu, Guisheng Zhong, Xiaowei Zhuang, Actin, Spectrin, and Associated Proteins Form a Periodic Cytoskeletal Structure in Axons, *Scienceexpress 2012*
- [22] G. Zhong et al., Developmental mechanism of the periodic membrane skeleton in axons, *eLife. 2014; 3: e04581*
- [23] Elisa D’Este, Dirk Kamin, Fabian Göttfert, Ahmed El-Hady, and Stefan W. Hell, STED Nanoscopy Reveals the Ubiquity of Subcortical Cytoskeleton Periodicity in Living Neurons, *Cell Reports 10, 1246–1251, March 3, 2015*
- [24] Leite et al., 2016, The Actin-Binding Protein α -Adducin Is Required for Maintaining Axon Diameter, *Cell Reports 15, 1–9 April 19, 2016*
- [25] Geoffrey M. Cooper, Robert E. Hausman, 2006, The Cell A Molecular Approach, *Fourth Edition, Sinauer Associates, Inc, ISBN-13: 978-0878939640*
- [26] Jeffrey S. Deitch and Gary A. Banker, An Electron Microscopic Analysis of Hippocampal Neurons Developing in Culture: Early Stage 1s in the Emergence of Polarity, *The Journal of Neuroscience, October 1993, 13(10): 4301-4315*
- [27] Wenqian Yu and Peter W Baas, Changes in Microtubule Number and Length during Axon Differentiation, *The Journal of Neuroscience, May 1994, 14(5): 2818-2829*
- [28] Bartlett, W. P., and G. A. Banker (1984) An electron microscopic study of the development of axons and dendrites by hippocampal neurons in culture. *II. Synaptic relationships. J. Neurosci. 4: 1954-1965.*
- [29] Peter W. Baas, Jeffrey S. Deitch, Mark M. Black, and Gary A. Banker, Polarity orientation of microtubules in hippocampal neurons: uniformity in the axon and nonuniformity in the dendrite, *Proc. Natl. Acad. Sci. USA, Vol. 85, pp. 8335-8339, November 1988*
- [30] Baas PW, Black MM, Banker GA, Changes in microtubule polarity orientation during the development of hippocampal neurons in culture, *J Cell Biol. 1989 Dec;109(6 Pt 1):3085-94*
- [31] Matus A., Microtubule-associated proteins and neuronal morphogenesis, *J Cell Sci Suppl. 1991;15:61-7.*
- [32] Goedert M, Crowther RA, Garner CC, Molecular characterization of microtubule-associated proteins tau and MAP2, *Trends Neurosci. 1991 May;14(5):193-9.*

-
- [33] N. Hirokawa, S. Hisanaga, and Y. Shiomura, MAP2 is a Component of Crossbridges Between Microtubules and Neurofilaments in the Neuronal Cytoskeleton: Quick-Freeze, Deep-Etch Immunoelectron Microscopy and Reconstitution Studies, *The Journal of Neuroscience*, August 1988, B(8): 2769-2779
- [34] <http://reasonandscience.heavenforum.org/t2096-the-astonishing-language-written-on-microtubules-amazing-evidence-of->
- [35] Chen J, Kanai Y, Cowan NJ, Hirokawa N, Projection domains of MAP2 and tau determine spacings between microtubules in dendrites and axons, *Nature*. 1992 Dec 17;360(6405):674-7.
- [36] Stella Aronov, Gonzalo Aranda, Leah Behar, and Irith Ginzburg, Axonal Tau mRNA Localization Coincides with Tau Protein in Living Neuronal Cells and Depends on Axonal Targeting Signal, *The Journal of Neuroscience*, September 1, 2001, 21(17):6577–6587
- [37] James W. Mandell, and Gary A. Banker, A Spatial Gradient of Tau Protein Phosphorylation in Nascent Axons, *The Journal of Neuroscience*, September 15, 1996, 16(18):5727–5740
- [38] G. I. Szendrei, V. M.-Y. Lee, Dr. L. Otvos Jr., Recognition of the minimal epitope of monoclonal antibody Tau-1 depends upon the presence of a phosphate group but not its location, *Journal of Neuroscience Research* 34:243-249 (1993)
- [39] Kanai Y, Takemura R, Oshima T, Mori H, Ihara Y, Yanagisawa M, Masaki T, Hirokawa N (1989) Expression of multiple tau isoforms and microtubule bundle formation in fibroblasts transfected with a single tau cDNA. *J Cell Biol* 109:1173–1184.
- [40] Baas PW, Pienkowski TP, Kosik KS (1991) Processes induced by tau expression in Sf9 cells have an axon-like microtubule organization. *J Cell Biol* 115:1333–1344.
- [41] Knops J, Kosik KS, Lee G, Pardee JD, Cohen GL, McConlogue L (1991), Overexpression of tau in a nonneuronal cell induces long cellular processes. *J Cell Biol* 114:725–733.
- [42] Hagestedt T, Lichtenberg B, Wille H, Mandelkow EM, Mandelkow E (1989), Tau protein becomes long and stiff upon phosphorylation: correlation between paracrystalline structure and degree of phosphorylation. *J Cell Biol* 109:1643–1651.
- [43] A. Harada, K. Oguchi, S. Okabe, J. Kuno, S. Terada, T. Ohshima, R. Sato-Yoshitake, Y. Takei, T. Noda, N. Hirokawa, Altered microtubule organization in small-calibre axons of mice lacking tau protein, *Nature*, Vol. 369, 9 June 1994
- [44] Perge JA, Koch K, Miller R, Sterling P, Balasubramanian V, 2009, How the optic nerve allocates space, energy capacity, and information, *J Neurosci* 29:7917–7928
- [45] Yau KW. Receptive fields, Geometry and conduction block of sensory neurones in the central nervous system of the leech. *J Physiol* 263: 513–538, 1976.
- [46] Bourque CW. Intraterminal recordings from the rat neurohypophysis in vitro. *J Physiol* 421: 247–262, 1990.
- [47] Jackson MB, Zhang SJ. Action potential propagation and propagation block by GABA in rat posterior pituitary nerve terminals. *J Physiol* 483: 597–611, 1995
- [48] Zhang SJ, Jackson MB. GABA-activated chloride channels in secretory nerve endings. *Science* 259: 531–534, 1993.

-
- [49] Antic S, Wuskell JP, Loew L, Zecevic D. Functional profile of the giant metacerebral neuron of *Helix aspersa*: temporal and spatial dynamics of electrical activity in situ. *J Physiol* 527: 55–69, 2000
- [50] Evans CG, Ludwar B, Cropper EC. Mechanoafferent neuron with an inexcitable somatic region: consequences for the regulation of spike propagation and afferent transmission. *J Neurophysiol* 97: 3126–3130, 2007
- [51] Luscher C, Streit J, Quadroni R, Luscher HR. Action potential propagation through embryonic dorsal root ganglion cells in culture. I. Influence of the cell morphology on propagation properties. *J Neurophysiol* 72: 622–633, 1994.
- [52] Dominique Debanne, Emilie Campanac, Andrzej Bialowas, Edmond Carlier, and Gisèle Alcaraz, Axon Physiology, *Physiol Rev* 91: 555–602, 2011; doi:10.1152/physrev.00048.2009
- [53] Goldstein SS, Rall W. Changes of action potential shape and velocity for changing core conductor geometry. *Biophys J* 14: 731–757, 1974.
- [54] Graham B, Redman S. A simulation of action potentials in synaptic boutons during presynaptic inhibition. *J Neurophysiol* 71: 538–549, 1994
- [55] Luscher HR, Shiner JS. Computation of action potential propagation and presynaptic bouton activation in terminal arborizations of different geometries. *Biophys J* 58: 1377–1388, 1990.
- [56] Luscher HR, Shiner JS. Simulation of action potential propagation in complex terminal arborizations. *Biophys J* 58: 1389–1399, 1990.
- [57] Manor Y, Gonczarowski J, Segev I. Propagation of action potentials along complex axonal trees. Model and implementation. *Biophys J* 60: 1411–1423, 1991.
- [58] Manor Y, Koch C, Segev I. Effect of geometrical irregularities on propagation delay in axonal trees. *Biophys J* 60: 1424–1437, 1991.
- [59] Parnas I, Hochstein S, Parnas H. Theoretical analysis of parameters leading to frequency modulation along an inhomogeneous axon. *J Neurophysiol* 39: 909–923, 1976.
- [60] Brette R (2013) Sharpness of Spike Initiation in Neurons Explained by Compartmentalization. *PLoS Comput Biol* 9(12): e1003338. doi:10.1371/journal.pcbi.1003338
- [61] G. H. Kim, P. Kosterin, A. L. Obaid, and B. M. Salzberg, A mechanical spike accompanies the action potential in Mammalian nerve terminals, *Biophysical Journal Volume 92 May 2007* 3122–3129
- [62] BC Hill, ED Schubert, MA Nokes, RP Michelson, Laser interferometer measurement of changes in crayfish axon diameter concurrent with action potential, *Science* 22 Apr 1977: Vol. 196, Issue 4288, pp. 426-428, DOI: 10.1126/science.850785
- [63] K. Iwasa, I. Tasaki, and R.C. Gibbons, 1980, *Science* 210, 338 - 339
- [64] K. Iwasa, I. Tasaki, 1980, *Biochem. Res. Commun.* 95, 1328 - 1331
- [65] I. Tasaki, K. Iwasa, and R. C. Gibbons, 1980, *Jpn. J. Physiol.* 30, 897 - 905
- [66] I. Tasaki, and K. Iwasa, 1982, *Jpn. J. Physiol.* 32, 69 - 81

-
- [67] Taner Akkin, David Landowne, Aarthi Sivaprakasam, Optical Coherence Tomography Phase Measurement of Transient Changes in Squid Giant Axons During Activity, *J Membrane Biol* (2009) 231:35–46
- [68] Jennifer L. Schei, Matthew D. McCluskey, Amanda J. Foust, Xin-Cheng Yao, and David M. Rector, Action potential propagation imaged with high temporal resolution near-infrared video microscopy and polarized light, *NeuroImage* 40 (2008) 1034–1043
- [69] Shin Ae Kim, Kyung Min Byun, Jonghwan Lee, Jung Hoon Kim, Dong-Ghi Albert Kim, Hyoungwon Baac, Michael L. Shuler, and Sung June Kim, Optical measurement of neural activity using surface plasmon resonance, *OPTICS LETTERS / Vol. 33, No. 9 / May 1, 2008*
- [70] P. Lipton, Effects of Membrane Depolarization on Light Scattering By Cerebral Cortical Slices, *J. Physiol.* (1973), 231, pp. 365-383
- [71] D. Le Bihan, The wet mind : water and functional neuroimaging, *Phys. Med. Biol.* 52, R57 (2007).
- [72] Tetsuya Takano, Chundi Xu, Yasuhiro Funahashi, Takashi Namba and Kozo Kaibuchi, Neuronal polarization, *Development* (2015) 142, 2088-2093 doi:10.1242/dev.114454
- [73] Barnes, A. P. and Polleux, F. (2009). Establishment of axon-dendrite polarity in developing neurons. *Annu. Rev. Neurosci.* 32, 347-381. doi:10.1146/annurev.neuro.31.060407.125536
- [74] Noctor, S. C., Martínez-Cerdeño, V., Ivic, L. and Kriegstein, A. R. (2004). Cortical neurons arise in symmetric and asymmetric division zones and migrate through specific phases. *Nat. Neurosci.* 7, 136-144. doi:10.1038/nn1172
- [75] Solecki, D. J., Govek, E.-E., Tomoda, T. and Hatten, M. E. (2006). Neuronal polarity in CNS development. *Genes Dev.* 20, 2639-2647. doi:10.1101/gad.1462506
- [76] Funahashi, Y., Namba, T., Nakamuta, S. and Kaibuchi, K. (2014). Neuronal polarization in vivo: growing in a complex environment. *Curr. Opin. Neurobiol.* 27, 215-223. doi:10.1016/j.conb.2014.04.009
- [77] Miyata, T., Kawaguchi, A., Saito, K., Kawano, M., Muto, T. and Ogawa, M. (2004). Asymmetric production of surface-dividing and non-surface-dividing cortical progenitor cells. *Development* 131, 3133-3145. doi:10.1242/dev.01173
- [78] Yanagida, M., Miyoshi, R., Toyokuni, R., Zhu, Y., and Murakami, F. (2012). Dynamics of the leading process, nucleus, and Golgi apparatus of migrating cortical interneurons in living mouse embryos. *Proceedings of the National Academy of Sciences*, 109(41), 16737-16742.
- [79] Burnette DT, Ji L, Schaefer AW, Medeiros NA, Danuser G, and Forscher P. Myosin II activity facilitates microtubule bundling in the neuronal growth cone neck. *Dev. Cell* 2008; 15(1):163-9. [PMID: 18606149]
- [80] Suter DM, and Forscher P. An emerging link between cytoskeletal dynamics and cell adhesion molecules in growth cone guidance. *Curr. Opin. Neurobiol.* 1998; 8(1):106-16. [PMID: 9568398]
- [81] <https://www.mechanobio.info>

-
- [82] Melanie Knorr, Daniel Koch, Thomas Fuhs, Ulrich Behnc and Josef A. Käs, Stochastic actin dynamics in lamellipodia reveal parameter space for cell type classification, *Soft Matter*, 2011, 7, 3192
- [83] G. Ruthel, G. Banker, (1998), Actin-dependent anterograde movement of growth-cone-like structures along growing hippocampal axons: A novel form of axonal transport?, *Cell Motility and the Cytoskeleton*, 40, 160-173
- [84] G. Ruthel, G. Banker, (1999), Role of moving growth cone-like "wave" structures in the outgrowth of cultured hippocampal axons and dendrites, *Journal of Neurobiology*, 39, 97-106, 1999
- [85] Katsuno et al., *Cell Reports*, 2015, 12, 648
- [86] K.C. Flynn, C.W. Pak, A.E. Shaw, F. Bradke F., and J.R Bamberg, *Dev Neurobiol.*, 2009, 69, 761
- [87] Riedl, J., Crevenna, A. H., Kessenbrock, K., Yu, J. H., Neukirchen, D., Bista, M., ... and Sixt, M. (2008). Lifeact: a versatile marker to visualize F-actin. *Nature methods*, 5(7), 605-607.
- [88] S. Goicoechea, D. Arneman, A. Disanza, R. Garcia-Mata, G. Scita, G. and C.A. Otey, *Journal of cell science*, 2006, 119, 3316.
- [89] E. Bernitt, C.G. Koh, N. Gov, and H.G. Döbereiner, *PloS one*, 2015, 10, e0115857.
- [90] M. Toriyama, et al., *J. Cell Biol.*, 2006, 175, 147.
- [91] M. Toriyama, Y. Sakumura, T. Shimada, S. Ishii, and N. Inagaki, *Mol. Syst. Biol.*, 2010, 6, 589
- [92] Winans et al., *eLife* 2016;5:e12387. DOI: 10.7554/eLife.12387
- [93] I. Tint, D. Jean, P. W. Baas, and M. M. Black, *J. Neurosci.*, 2009, 29, 10995.
- [94] Maor-Nof, M., and Yaron, A. (2013). Neurite pruning and neuronal cell death: spatial regulation of shared destruction programs. *Current opinion in neurobiology*, 23(6), 990-996.
- [95] Herminia Pasantes-Morales, Karina Tuz, Volume changes in neurons: Hyperexcitability and neuronal death, *Contrib Nephrol.* 2006;152:221-40.
- [96] Pramod A. Pullarkat, Paul Dommersnes, Pablo Fernandez, Jean-Francois Joanny, and Albrecht Ott, Osmotically driven shape transformations in axons, *PRL* 96, 048104 (2006)
- [97] Pablo Fernandez and Pramod A. Pullarkat, The role of the cytoskeleton in volume regulation and beading transitions in PC12 neurites, *Biophysical Journal Volume 99 December 2010* 3571–3579
- [98] Pike CJ, Cummings BJ, Cotman CW, beta-Amyloid induces neuritic dystrophy in vitro: similarities with Alzheimer pathology, *Neuroreport.* 1992 Sep;3(9):769-72
- [99] NC Berchtold et CW Cotman, Evolution in the conceptualization of dementia and Alzheimer's disease: Greco-Roman period to the 1960s, *Neurobiol. Aging*, vol. 19, no 3, 1998, p. 173-189. (PMID 9661992, DOI 10.1016/S0197-4580(98)00052-9)
- [100] ROGER B. KNOWLES, CLAIRE WYART, SERGEY V. BULDYREV, LUIS CRUZ, BRIGITA URBANC, MICHAEL E. HASSELMO, H. EUGENE STANLEY, AND

-
- BRADLEY T. HYMAN, Plaque-induced neurite abnormalities: implications for disruption of neural networks in Alzheimer's disease, *Proc. Natl. Acad. Sci. USA Vol. 96*, pp. 5274–5279, April 1999 *Neurobiology*
- [101] Miguel Angel Riudavets, Diego Iacono, Susan M. Resnick, Richard O'Brien, Alan B. Zonderman, Lee J. Martin, Gay Rudow, Olga Pletnikova, and Juan C. Troncoso, Resistance to Alzheimer's pathology is associated with nuclear hypertrophy in neurons, *Neurobiol Aging*. 2007 October ; 28(10): 1484–1492. doi:10.1016/j.neurobiolaging.2007.05.005
- [102] Diego Iacono, Richard O'Brien, Susan M. Resnick, Alan B. Zonderman, Olga Pletnikova, Gay Rudow, Yang An, Mark J. West, Barbara Crain, and Juan C. Troncoso, Neuronal Hypertrophy in Asymptomatic Alzheimer Disease, *J Neuropathol Exp Neurol*. 2008 June ; 67(6): 578–589
- [103] Ksiezak-Reding, H., Liu, W.K., Hardsky, J. and Yen, S.H. (1990) Phosphate analysis of different τ preparations from normal and Alzheimer disease brains, *J. Cell Biol*. 111,435.
- [104] Rosenblum, J.S., Bramblett, G.T. and Lee, V.M.Y. (1990) The selective phosphorylation of sites near the microtubule (MT) binding domain in normal τ may be an initial event leading to the formation of Alzheimer disease (AD) paired helical filaments (PHF), *J Cell Biol* 111, 435.
- [105] Stieler JT, Bullmann T, Kohl F, Tøien Ø, Brückner MK, et al. (2011) The Physiological Link between Metabolic Rate Depression and Tau Phosphorylation in Mammalian Hibernation. *PLoS ONE* 6(1): e14530. doi:10.1371/journal.pone.0014530
- [106] Paula VJR, Guimarães FM, Diniz BS, Forlenza OV. Neurobiological pathways to Alzheimer's disease: amyloid-beta, Tau protein or both?. *Dement. Neuropsychol*. 2009;3(3):188-194
- [107] Antonio Currais, Oswald Quehenberger, Aaron M Armando, Daniel Daugherty, Pam Maher and David Schubert, Amyloid proteotoxicity initiates an inflammatory response blocked by cannabinoids, *npj Aging and Mechanisms of Disease* (2016) 16012
- [108] Alexandre B Roland¹, Ana Ricobaraza, Damien Carrel, Benjamin M Jordan, Felix Rico, Anne Simon, Marie Humbert-Claude, Jeremy Ferrier, Maureen H McFadden, Simon Scheuring, Zsolt Lenkei, Cannabinoid-induced actomyosin contractility shapes neuronal morphology and growth, *eLife* 2014;3:e03159. DOI: 10.7554/eLife.03159
- [109] John F Cryan and Andrew Holmes. The ascent of mouse: advances in modelling human depression and anxiety. *Nature reviews Drug discovery*, 4(9):775–790, 2005. 16
- [110] Benson, D. L., Watkins, F. H., Steward, O., & Banker, G. (1994). Characterization of GABAergic neurons in hippocampal cell cultures. *Journal of neurocytology*, 23(5), 279-295.
- [111] Carlos G. Dotti, Christopher A. Sullivan, and Gary A. Banker, The establishment of polarity by hippocampal neurons in culture, *The Journal of Neuroscience*, April 1988, 8(4): 1454-1468
- [112] Claire Wyart, Christophe Ybert, Laurent Bourdieu, Catherine Herr, Christelle Prinz, Didier Chatenay, Constrained synaptic connectivity in functional mammalian neuronal networks grown on patterned surfaces, *Journal of Neuroscience Methods* 117 (2002) 123–131

-
- [113] G.D. Fischbach, and P. G. Nelson (1977), Cell culture in neurobiology, *In Handbook of Physiology, Sect. 1: The Nervous System, Part 2*, pp. 719-774, American Physiological Society, Bethesda, MD.
- [114] P.G. Nelson, and M. Lieberman (1981), Excitable Cells in Tissue Culture, *Plenum Press, New York*.
- [115] Graves, A. R., Moore, S. J., Bloss, E. B., Mensh, B. D., Kath, W. L., & Spruston, N. (2012). Hippocampal pyramidal neurons comprise two distinct cell types that are countermodulated by metabotropic receptors. *Neuron*, 76(4), 776-789.
- [116] Chen, C. S., Mrksich, M., Huang, S., Whitesides, G. M., & Ingber, D. E. (1997). Geometric control of cell life and death. *Science*, 276(5317), 1425-1428.
- [117] Manuel Théry, Micropatterning as a tool to decipher cell morphogenesis and functions, *Journal of Cell Science* 123, 4201-4213, doi:10.1242/jcs.075150
- [118] Hol, F. J., & Dekker, C. (2014). Zooming in to see the bigger picture: microfluidic and nanofabrication tools to study bacteria. *Science*, 346(6208), 1251821.
- [119] Zhang, Q., & Austin, R. H. (2012). Applications of microfluidics in stem cell biology. *BioNanoScience*, 2(4), 277-286.
- [120] FIONA M. WATT, PETER W. JORDAN, AND CHARLES H. O'NEILL, Cell shape controls terminal differentiation of human epidermal keratinocytes, *Proc. Natl. Acad. Sci. USA* Vol. 85, pp. 5576-5580, August 1988 Cell Biology
- [121] Singhvi, R., Kumar, A., Lopez, G., Stephanopoulos, G. N., Wang, D. I. C., Whitesides, G. M., and Ingber, D. E. (1994) Engineering cell shape and function. *Science* 264,696-698.
- [122] Christopher S. Chen, Milan Mrksich, Sui Huang, George M. Whitesides, and Donald E. Ingber, Micropatterned surfaces for control of cell shape, position, and function, *Biotechnol. Prog.* 1998, 14, 356-363
- [123] Matthieu Piel, Manuel Théry, Micropatterning in Cell Biology, *Methods in Cell Biology*, 2014
- [124] Théry M, Racine V, Piel M, Pépin A, Dimitrov A, Chen Y, Sibarita JB, Bornens M, Anisotropy of cell adhesive microenvironment governs cell internal organization and orientation of polarity, *Proc Natl Acad Sci U S A*. 2006 Dec 26;103(52):19771-6. Epub 2006 Dec 18
- [125] Pouthas, F., Girard, P., Lecaudey, V., Ly, T. B., Gilmour, D., Boulin, C., Pepperkok, R. and Reynaud, E. G. (2008). In migrating cells, the Golgi complex and the position of the centrosome depend on geometrical constraints of the substratum. *J. Cell Sci.* 121, 2406-2414
- [126] Théry M, Pépin A, Dressaire E, Chen Y, Bornens M., Cell distribution of stress fibres in response to the geometry of the adhesive environment, *Cell Motil Cytoskeleton*. 2006 Jun;63(6):341-55.
- [127] Ravi A. Desai, Lin Gao, Srivatsan Raghavan, Wendy F. Liu, and Christopher S. Chen, Cell polarity triggered by cell-cell adhesion via E-cadherin, *Journal of Cell Science* 122 (7)

-
- [128] Tseng Q, Wang I, Duchemin-Pelletier E, Azioune A, Carpi N, Gao J, Filhol O, Piel M, Théry M, Baland M, A new micropatterning method of soft substrates reveals that different tumorigenic signals can promote or reduce cell contraction levels, *Lab Chip*. 2011 Jul 7;11(13):2231-40. doi: 10.1039/c0lc00641f. Epub 2011 Apr 26
- [129] Jun Nakanishi, Yukiko Kikuchi, Satoshi Inoue, Kazuo Yamaguchi, Tohru Takarada, and Mizuo Maeda, Spatiotemporal Control of Migration of Single Cells on a Photoactivatable Cell Microarray, *J. Am. Chem. Soc.*, 2007, 129 (21), pp 6694–6695, DOI: 10.1021/ja070294p
- [130] Angela Katrin Vogt, Fernando Daniel Stefani, Andreas Best, Gabriele Nelles, Akio Yasuda, Wolfgang Knoll, Andreas Offenhäusser, Impact of micropatterned surfaces on neuronal polarity, *Journal of Neuroscience Methods* 134 (2004) 191–198
- [131] Rita Fricke, Peter D. Zentis, Lionel T. Rajappa, Boris Hofmann, Marko Banzet, Andreas Offenhäusser, Simone H. Meffert, Axon guidance of rat cortical neurons by microcontact printed gradients, *Biomaterials* 32 (2011) 2070e2076
- [132] Roth S, Bisbal M, Brocard J, Bugnicourt G, Saoudi Y, et al. (2012) How Morphological Constraints Affect Axonal Polarity in Mouse Neurons. *PLoS ONE* 7(3): e33623. doi:10.1371/journal.pone.0033623
- [133] Sophie Roth, Ghislain Bugnicourt, Mariano Bisbal, Sylvie Gory-Fauré, Jacques Brocard, and Catherine Villard, Neuronal architectures with axo-dendritic polarity above silicon nanowires, *small* 2012, DOI: 10.1002/sml.201102325
- [134] Caterina Tomba, Céline Braïni, Beilun Wu, Nir S. Gov and Catherine Villard, Tuning the adhesive geometry of neurons: length and polarity control, *Soft Matter*, 2014, 10, 2381
- [135] S. Halldorsson, E. Lucumi, R. Gómez-Sjöberg, R. M. T. Fleming, Advantages and challenges of microfluidic cell culture in polydimethylsiloxane devices, *Biosensors and Bioelectronics* 63(2015)218–231
- [136] Sudong Kim, Hyunjae Lee, Minhwan Chunga and Noo Li Jeon, Engineering of functional, perfusable 3D microvascular networks on a chip, *Lab Chip*, 2013, 13, 1489
- [137] A. M. Taylor, M. Blurton-Jones, S. W. Rhee, D. H. Cribbs and C. W. Cotman, et al. A microfluidic culture platform for CNS axonal injury, regeneration and transport, *Nat. Methods*, 2005, 2, 599–605.
- [138] Jean-Michel Peyrin, Bérangère Deleglise, Laure Saias, Maéva Vignes, Paul Gougis, Sébastien Magnifico, Sandrine Betuing, Mathéa Pietri, Jocelyne Caboche, Peter Vanhoutte, Jean-Louis Viovy and Bernard Brugg, Axon diodes for the reconstruction of oriented neuronal networks in microfluidic chambers, *Lab Chip*, 2011, 11, 3663–3673 | 3663
- [139] Ngoc-Duy Dinh, Ya-Yu Chiang, Heike Hardelauf, Jenny Baumann, Emily Jackson, Sarah Waide, Julia Sisnaiske, Jean-Philippe Frimat, Christoph van Thriel, Dirk Janasek, Jean-Michel Peyrin and Jonathan West, Microfluidic construction of minimalistic neuronal co-cultures, *Lab Chip*, 2013, 13, 1402–1412
- [140] Ayako Yamada, Maéva Vignes, Cécile Bureau, Alexandre Mamane, Bastien Venzac, Stéphanie Descroix, Jean-Louis Viovy, Catherine Villard, Jean-Michel Peyrin, and Laurent

-
- Malaquin, In-mold patterning and actionable axo-somatic compartmentalization for on-chip neuron culture, *Lab on Chip* 2016
- [141] Renaud Renault, Jean-Baptiste Durand, Jean-Louis Viovy, Catherine Villard, Asymmetric axonal edge guidance : a new paradigm for building oriented neuronal networks, *Lab on Chip* 2016
- [142] Ling Gu, Bryan Black, Simon Ordonez, Argha Mondal, Ankur Jain and Samarendra Mohanty, Microfluidic control of axonal guidance, *SCIENTIFIC REPORTS* | 4 : 6457 | DOI: 10.1038/srep06457
- [143] Stephan K. W. Dertinger, Xingyu Jiang, Zhiying Li, Venkatesh N. Murthy, and George M. Whitesides, Gradients of substrate-bound laminin orient axonal specification of neurons, *PNAS* October 1 2002 vol. 99 no. 20 12543, www.pnas.org/cgi/doi/10.1073/pnas.192457199
- [144] Thibault Honegger, Moritz I. Thielen, Soheil Feizi, Neville E. Sanjana and Joel Voldman, Microfluidic neurite guidance to study structure-function relationships in topologically-complex population-based neural networks, *SCIENTIFIC REPORTS* | 6:28384 | DOI: 10.1038/srep28384
- [145] Ewa Zlotek-Zlotkiewicz, Sylvain Monnier, Giovanni Cappello, Mael Le Berre, and Matthieu Piel, Optical volume and mass measurements show that mammalian cells swell during mitosis, *J. Cell Biol.* Vol. 211 No. 4 765–774 www.jcb.org/cgi/doi/10.1083/jcb.201505056
- [146] Son, S., J. Ho Kang, S. Oh, M.W. Kirschner, T.J. Mitchison, and S.R. Manalis. 2015. Resonant microchannel volume and mass measurements show that suspended cells swell during mitosis. *J. Cell Biol.* <http://dx.doi.org/10.1083/jcb.201505058>
- [147] Carl D. Bortner, John A. Cidlowski, Apoptotic volume decrease and the incredible shrink- ing cell, *Cell Death and Differentiation* (2002) 9, 1307 - 1310
- [148] Carl D. Bortner, John A. Cidlowski, The role of apoptotic volume decrease and ionic home- ostasis in the activation and repression of apoptosis, *Pflugers Arch - Eur J Physiol* (2004) 448: 313–318
- [149] D. A. Hill, S. Chiosea, S. Jamaluddin, K. Roy, A. H. Fischer, D. D. Boyd, J. A. Nickerson and A. N. Imbalzano, Inducible changes in cell size and attachment area due to expression of a mutant SWI/SNF chromatin remodeling enzyme, *J. Cell Sci.*, 2004, 117, 5847–5854
- [150] Boucrot, E., and T. Kirchhausen. 2008. Mammalian cells change volume during mitosis. *PLoS One*. 3:e1477. <http://dx.doi.org/10.1371/journal.pone.0001477>
- [151] Habela, C.W., and H. Sontheimer. 2007. Cytoplasmic volume condensation is an integral part of mitosis. *Cell Cycle*. 6:1613–1620. <http://dx.doi.org/10.4161/cc.6.13.4357>
- [152] S. Schneider, P. Pagel, C. Rotsch, T. Danker, H. Oberleithner, M. Radmacher and A. Schwab, Volume dynamics in migrating epithelial cells measured with atomic force mi- croscopy, *Pflugers Arch.–Eur. J. Physiol.*, 2000, 439, 297–303.
- [153] Martin M, Benzina O, Szabo V, Vegh A-G, Lucas O, et al. (2013) Morphology and Nanome- chanics of Sensory Neurons Growth Cones following Peripheral Nerve Injury. *PLoS ONE* 8(2): e56286. doi:10.1371/journal.pone.0056286

-
- [154] Benzina O, Szabo V, Lucas O, Saab MB, Cloitre T, Scamps F, Gergely C, Martin M, Changes induced by peripheral nerve injury in the morphology and nanomechanics of sensory neurons, *J Biomed Opt.* 2013 Oct;18(10):106014. doi: 10.1117/1.JBO.18.10.106014
- [155] Y. E. Korchev, J. Gorelik, M. J. Lab, E. V. Sviderskaya, C. L. Johnston, C. R. Coombes, I. Vodyanoy and C. R. W. Edwards, Cell volume measurement using scanning ion conductance microscopy, *Biophys. J.*, 2000, 78, 451–457.
- [156] Bryan, A.K., A. Engler, A. Gulati, and S.R. Manalis. 2012. Continuous and long-term volume measurements with a commercial Coulter counter. *PLoS One*. 7:e29866. <http://dx.doi.org/10.1371/journal.pone.0029866>
- [157] Gregg, E.C., and K.D. Steidley. 1965. Electrical counting and sizing of mammalian cells in suspension. *Biophys. J.* 5:393–405. [http://dx.doi.org/10.1016/S0006-3495\(65\)86724-8](http://dx.doi.org/10.1016/S0006-3495(65)86724-8)
- [158] S. Z. Hua and T. Pennell, A microfluidic chip for real-time studies of the volume of single cells, *Lab Chip*, 2009, 9, 251–256.
- [159] Bryan AK1, Hecht VC, Shen W, Payer K, Grover WH, Manalis SR, Measuring single cell mass, volume, and density with dual suspended microchannel resonators, *Lab Chip*. 2014 Feb 7;14(3):569-76. doi: 10.1039/c3lc51022k.
- [160] P. Marquet, C. Depeursinge and P.J.Magistretti, Exploring Neural Cell Dynamics with Digital Holographic Microscopy, *Annu. Rev. Biomed. Eng.* 2013. 15:407–31, doi: 10.1146/annurev-bioeng-071812-152356
- [161] Barer R. 1952. Interference microscopy and mass determination. *Nature* 169:366–67
- [162] DunnGA, ZichaD. 1993. Phase-shifting interference microscopy applied to the analysis of cell behavior. *Symp. Soc. Exp. Biol.* 47:91–106
- [163] Gabor D. 1948. A new microscopic principle. *Nature* 161:777–78
- [164] P. Marquet et al., 2005, Digital holographic microscopy: a noninvasive contrast imaging technique allowing quantitative visualization of living cells with subwavelength axial accuracy, *Optics Letters*, Vol. 30, No. 5, 468-470.
- [165] Benjamin Rappaz, Alexander Barbul, Annick Hoffmann, Daniel Boss, Rafi Korenstein, Christian Depeursinge, Pierre J. Magistretti, Pierre Marquet, Spatial analysis of erythrocyte membrane fluctuations by digital holographic microscopy, *Blood Cells, Molecules, and Diseases* 42 (2009) 228–232
- [166] Kersti Alm, Helena Cirenajwis, Lennart Gisselsson, Anette Gjörlöf Wingren, Birgit Janicke, Anna Mölder, Stina Oredsson and Johan Persson (2011). Digital Holography and Cell Studies, *Holography, Research and Technologies*, Prof. Joseph Rosen (Ed.), ISBN: 978-953-307-227-2, InTech
- [167] Thomas A Zangle and Michael A Teitell, Live-cell mass profiling: an emerging approach in quantitative biophysics, *NATURE METHODS* | VOL.11 NO.12 | DECEMBER 2014
- [168] Benjamin Rappaz, Alexander Barbul, Yves Emery, Rafi Korenstein, Christian Depeursinge, Pierre J.Magistretti, Pierre Marquet, Comparative Study of Human Erythrocytes by Digital Holographic Microscopy, Confocal Microscopy, and Impedance Volume Analyzer, *Cytometry Part A* - 73A: 895-903, 2008

-
- [169] Benjamin Rappaz, Pierre Marquet, Etienne Cuche, Yves Emery, Christian Depeursinge and Pierre J. Magistretti, Measurement of the integral refractive index and dynamic cell morphometry of living cells with digital holographic microscopy, *14 November 2005 / Vol. 13, No. 23 / OPTICS EXPRESS* 9362
- [170] Gray, M.L., R.A. Hoffman, and W.P. Hansen. 1983. A new method for cell volume measurement based on volume exclusion of a fluorescent dye. *Cytometry*. 3:428-434. <http://dx.doi.org/10.1002/cyto.990030607>
- [171] Bottier, C., C. Gabella, B. Vianay, L. Buscemi, I.F. Sbalzarini, J.-J. Meister, and A.B. Verkhovsky. 2011. Dynamic measurement of the height and volume of migrating cells by a novel fluorescence microscopy technique. *Lab Chip*. 11:3855-3863. <http://dx.doi.org/10.1039/c1lc20807a>
- [172] Gabella, C., E. Bertseva, C. Bottier, N. Piacentini, A. Bornert, S. Jeney, L. Forró, I.F. Sbalzarini, J.-J. Meister, and A.B. Verkhovsky. 2014. Contact angle at the leading edge controls cell protrusion rate. *Curr. Biol*. 24:1126-1132. <http://dx.doi.org/10.1016/j.cub.2014.03.050>
- [173] Sophie Roth Thesis. Réseaux de Neurones modèles : Contrôle de la différenciation axonale par micropatterns. *Université Joseph Fourier - Grenoble 1*. 2009
- [174] Ghislain BUGNICOURT Thesis. Adhésion, croissance et polarisation de neurones sur substrats micro- et nano-structurés. *UNIVERSITÉ DE GRENOBLE*. 2006
- [175] Caterina Tomba Thesis. Primary brain cells in in vitro controlled microenvironments : single cell behaviors for collective functions. *Université de Grenoble*, 2014.
- [176] Thomas Fath, Yazı D Ke, Peter Gunning, Jürgen Götz, and Lars M Ittner. Primary support cultures of hippocampal and substantia nigra neurons. *Nature protocols*, 4(1):78–85, 2008.
- [177] Caterina Tomba, Céline Braïni, Beilun Wu, Nir S. Gov and Catherine Villard, Tuning the adhesive geometry of neurons: length and polarity control, *Soft Matter*, 2014, 10, 2381–2387
- [178] D. Seetapun and D. J. Odde, Cell-length-dependent microtubule accumulation during polarization, *Curr. Biol.*, 2010, **20**, 979-988.
- [179] H. Yamamoto, T. Demura, M. Morita, G. A. Banker, T. Tanii and S. Nakamura, Differential neurite outgrowth is required for axon specification by cultured hippocampal neurons, *J. Neurochem.*, 2012, **123**, 904-910.
- [180] Barer, R. *Determination of dry mass, thickness, solid and water concentration in living cells*. *Nature* 172, 1097-1098 (1953).
- [181] Schoch et al., Nuclear transport receptor binding avidity triggers a self-healing collapse transition in FG-nucleoporin molecular brushes, *PNAS - October 16, 2012 - vol. 109 - no. 42 - 16911–16916*
- [182] R. Barer, 1952, Interference Microscopy and Mass Determination, *Nature* vol 169, 366-367
- [183] H.G.Davies, M.H.F.Wilkin, 1952, Interference microscopy and mass determination, *Nature* vol 169, 541

-
- [184] Popescu, G. et al. Optical imaging of cell mass and growth dynamics. *Am. J. Physiol. Cell Physiol.* 295, C538-C544 (2008).
- [185] Zhao, H., Brown, P.H. and Schuck, P. On the distribution of protein refractive index increments. *Biophys. J.* 100, 2309-2317 (2011).
- [186] Barer, R. and Joseph, S. Refractometry of living cells. *Q. J. Microsc. Sci.* s3-95, 399-423 (1954).
- [187] Wen, J. and Arakawa, T. Refractive index of proteins in aqueous sodium chloride. *Anal. Biochem.* 280, 327-329 (2000).
- [188] Armstrong, S.H., Budka, M.J.E., Morrison, K.C. and Hasson, M. Preparation and properties of serum and plasma proteins. XII. The refractive properties of the proteins of human plasma and certain purified fractions. *J. Am. Chem. Soc.* 69, 1747-1753 (1947).
- [189] Barer, R. and Tkaczyk, S. Refractive index of concentrated protein solutions. *Nature* 173, 821-822 (1954).
- [190] Chincholi, B.S., Havlik, A.J. and Vold, R.D. Specific refractive index increments of polymer systems at four wavelengths. *J. Chem. Eng. Data* 19, 148-152 (1974).
- [191] Brown, G.L., McEwan, M.B. and Pratt, M.I. Macromolecular weight and size of deoxyribose nucleic acids. *Nature* 176, 161-162 (1955).
- [192] Northrop, T.G., Nutter, R.L. and Sinsheimer, R.L. Refractive increment of thymus nucleic acid. *J. Am. Chem. Soc.* 75, 5134-5135 (1953).
- [193] Northrop, T.G. and Sinsheimer, R.L. Light scattering by tobacco mosaic virus nucleic acid. *J. Chem. Phys.* 22, 703-707 (1954).
- [194] Davies, H.G. in *General Cytochemical Methods* (ed. Danielli, J.F.) 55-161 (Academic Press, 1958).
- [195] Hayes, W.M. *CRC Handbook of Chemistry and Physics* 94th edn. (CRC Press, 2013).
- [196] Erbe, A. and Sigel, R. Tilt angle of lipid acyl chains in unilamellar vesicles determined by ellipsometric light scattering. *Eur. Phys. J. E* 22, 303-309 (2007).
- [197] T. Zangle, M. Teitell, 2014, Live-cell mass profiling: an emerging approach in quantitative biophysics, *Nature methods*, Vol 11, 1221-8
- [198] Prescher, J.A. and Bertozzi, C.R. Chemistry in living systems. *Nat. Chem. Biol.* 1, 13-21 (2005)
- [199] Gabriel Popescu, YoungKeun Park, Niyom Lue, Catherine Best-Popescu, Lauren Deflores, Ramachandra R. Dasari, Michael S. Feld, and Kamran Badizadegan, Optical imaging of cell mass and growth dynamics, *Am J Physiol Cell Physiol* 295: C538-C544, 200
- [200] A. Mershin et al., Tubulin dipole moment, dielectric constant and quantum behavior: computer simulations, experimental results and suggestions, *BioSystems* 77 (2004) 73-85
- [201] H. Sato et al., 1975, Microtubular origin of mitotic spindle form birefringence: demonstration of the applicability of Wiener's equation. *J. Cell Biol.* 67:501-517.

-
- [202] A. Ehrlicher et al., Guiding neuronal growth with light, *PNAS* vol. 99 no. 25 16024–16028, 2002
- [203] R. Oldenbourg et al., Birefringence of Single and Bundled Microtubules, *Biophysical Journal* Volume 74 January 1998 645–654
- [204] K. Katoh et al., Birefringence Imaging Directly Reveals Architectural Dynamics of Filamentous Actin in Living Growth Cones, *Molecular Biology of the Cell*, Vol. 10, 197–210, January 1999
- [205] SHARWAN K. KAKAR and FREDERICK A. BETTELHEIM, Birefringence of Actin, *Biopolymers*, Vol. 31, 1283-1287 (1991)
- [206] R. Hard et al., 1985, Flow birefringence of microtubules and its relation to birefringence measurements in cells. *Cell Motil.* 5:31–51.
- [207] B. Rappaz et al., Noninvasive characterization of the fission yeast cell cycle by monitoring dry mass with digital holographic microscopy, *Journal of Biomedical Optics* 14(3), 034049 May/June 2009
- [208] M. P. VIOLA-MAGNI et al., Postnatal Variations of the Dry Mass of Neuronal Nuclei of the Spinal Cord in Rat and Guinea-Pi, *Experientia*. 1966 May 15;22(5):328-9.
- [209] Watson WE (1969) The response of motor neurones to intramuscular injection of botulinum toxin. *J Physiol* 202:611-630
- [210] J.A. Russell, Changes in Nucleolar Dry Mass of Neurones of the Paraventricular and Supraoptic Nuclei in the Rat During Pregnancy and Lactation, *Cell Tissue Res.* 208, 313-325 (1980)
- [211] Albert J. Saubermann and Vicky L. Scheid, 1985, Elemental Composition and Water Content of Neuron and Glial Cells in the Central Nervous System of the North American Medicinal Leech (*Macrobdella decora*), *J. Neurochem.*, Vol. 44, No. 3.